PROCESSING OF SYNTHETIC APERTURE RADAR DATA AS APPLIED TO THE
CHARACTERIZATION OF LOCALIZED DEFORMATION FEATURES

A Dissertation presented to
the Faculty of the Graduate School
at the University of Missouri-Columbia

In Partial Fulfillment
of the Requirements for the Degree

Doctor of Philosophy

by
RICHARD A. COFFMAN, MSE, PE, PLS

Dr. J. Erik Loehr, PE, Dissertation Supervisor
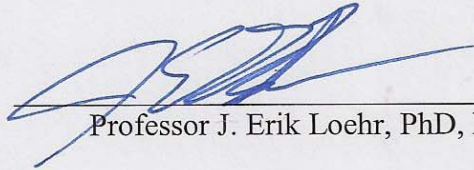
JULY 2009

The undersigned, appointed by the Dean of the Graduate School, have examined the dissertation entitled

PROCESSING OF SYNTHETIC APERTURE RADAR DATA AS APPLIED TO THE CHARACTERIZATION OF LOCALIZED DEFORMATION FEATURES
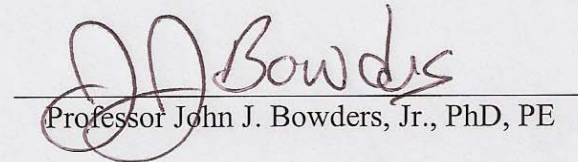
Presented by Richard A. Coffman, MSE, PE, PLS,

a candidate for the degree Doctor of Philosophy in Civil Engineering,

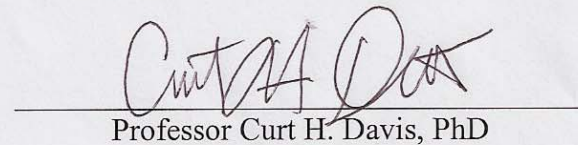and herby certify that, in their opinion, it is worthy of acceptance.
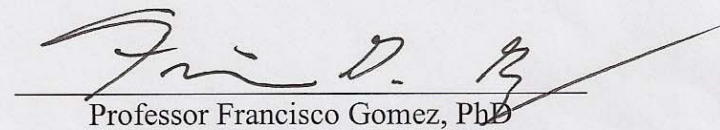
Professor J. Erik Loehr, PhD, PE

Professor John J. Bowders, Jr., PhD, PE

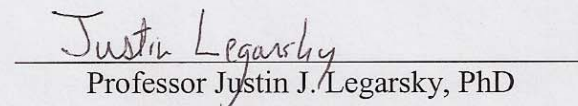Professor Curt H. Davis, PhD
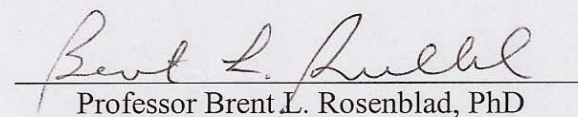
Professor Francisco Gomez, PhD

Professor Justin J. Legarsky, PhD

Professor Brent L. Rosenblad, PhD

DEDICATION

To my parents,

Peggy and Glen Coffman,

For their love and support in making my dreams become reality.

Also to my brothers,

Bryan and Todd Coffman,

For instilling a "don't back down" mentality.

To my wife,

Ashley Renee Coffman

For your love, compassion, strength, and beauty.

Sonnet XVIII: Shall I Compare Thee to a Summer's Day?
By William Shakespeare
Shall I compare thee to a summer's day?
Thou art more lovely and more temperate.
Rough winds do shake the darling buds of May,
And summer's lease hath all too short a date.
Sometime too hot the eye of heaven shines,
And often is his gold complexion dimm'd;
And every fair from fair sometime declines,
By chance or nature's changing course untrimm'd;
But thy eternal summer shall not fade
Nor lose possession of that fair thou ow'st;
Nor shall Death brag thou wander'st in his shade,
When in eternal lines to time thou grow'st:
So long as men can breathe or eyes can see,
So long lives this, and this gives life to thee.

ACKNOWLEDGEMENTS

TABLE OF CONTENTS

LIST OF FIGURES

x

LIST OF TABLES

ABSTRACT

Satellite-based Interferometric Synthetic Aperture Radar (InSAR) has been used by the Geoscience community for many years to obtain ground deformation measurements of large-scale spatial features. Researchers have also begun applying InSAR to detect small-scale spatial features associated with geotechnical engineering applications. However, there is a significant lack of understanding on how to obtain ground deformation measurements associated with civil infrastructure because of the generally large spatial resolution of the imagery as compared with the limited spatial scale of the deformation features.

In this study, InSAR processing techniques were evaluated for two demonstration sites to enhance the understanding of detection of small-scale spatial features. The sites consist of a predominately urban site (Los Angeles, California, USA) and a predominately rural site (outside of Mosul, Iraq). Both sites are known to have experienced localized deformation associated with construction of the Los Angeles Red Line subway tunnel system and deformation associated with gypsum dissolution causing subsidence of Mosul Dam.

A parametric study was conducted using the Los Angeles site to evaluate spatial phase unwrapping parameters. Thirty-three combinations of parameters (multi-looking, filter size, filter type, and coherence mask threshold) were investigated. The combination of parameters that provided the least amount of filtering (least amount of multi-looking, smallest filter size, and no coherence mask threshold) produced output in which the feature associated with the Los Angeles Red Line construction deformation was most

readily observable. In addition to minimal filtering, stacking image pairs that just spanned the time of construction provided the best results.

Three spatial ("traditional", "spatial", and "enhanced spatial") and two time-dependent ("Interferometric Point Target Analysis (IPTA)" and "multiple baseline") InSAR processing techniques were evaluated for the Los Angeles site. The "spatial", "enhanced spatial", and "multiple baseline" InSAR processing techniques were also evaluated for the Mosul Dam site.

The "enhanced spatial" processing technique using minimal multi-looking (1 and 5 looks), a very small filtering window size (2), and no coherence mask produced the best output for the Los Angeles Red Line site. The "multiple baseline" technique produced images in which the progression of the tunnel boring with time was detected but these images contain more speckle than those produced using the enhanced spatial method. The "spatial" processing technique using minimal multi-looking (1 and 5 looks), a small window size (8), and a coherence mask threshold of 50 percent produced the best output for the Mosul Dam site. In addition to the subsidence feature associated with the movement of the dam displayed in the "spatial" processing output, subsidence features associated with sinkholes around the dam were detected using the "enhanced spatial" processing technique.

InSAR coverage allows for the detection of small movements (<1 cm) covering small spatial extents (<100 meters) by scanning large areas (100 km^2) instead of or in addition to current surveying practices which provide spatially limited point measurements. This coverage and the ability to conduct deformation investigations on civil infrastructure using archived InSAR data make the use InSAR well suited for geotechnical engineering applications.

Chapter 1: Introduction

1.1   Introduction

Synthetic Aperture Radar (SAR) studies have been used since the early 1970's for topographic studies of the Earth, the moon, and Venus. Repeat-pass, satellite based SAR platforms enable the detection of millimeter scale displacements of the Earth's surface from satellite platforms flying approximately 780 km above the earth. Unlike the visible band wavelengths, radar band wavelengths facilitate wave penetration through cloud cover, allowing for imaging in most weather conditions. Radar is also an active source, which transmits and receives self-generated waves, promoting both day and night time operations. Some of the current commercial SAR satellites have been collecting data of the Earth's surface at regular intervals since 1991. The collected data have been archived, permitting investigation of events that have occurred in the past. A typical satellite based SAR image covers 100 km by 100 km.

Multiple synthetic aperture radar images can be used to perform Interferometric Synthetic Aperture Radar (InSAR) analyses. During InSAR processing, the phase value for each pixel within one image is subtracted from the phase value for the identical pixel in the other image, allowing for the detection of movement between image acquisitions. InSAR processing provides vast spatial coverage (100 km by 100 km images in comparison to traditional terrestrial point source surveying measurement). In addition to InSAR providing better spatial coverage than point source surveying, the InSAR approach may be more economically feasible in some cases.

SAR processing techniques, which have been in use for the past 40 years, are currently being applied to geotechnical engineering applications. However, because typical geotechnical engineering structures are small in scale compared with features commonly observed in Earth resource observations (ground water extraction, oil extraction, post-seismic deformations, and glacier movements), the InSAR processing techniques need refinement, as the signal of interest may appear to be noise in the image.

1.2   *Importance and Significance*

Tunneling and dam construction operations are common in the geotechnical engineering community. For many years, research has been conducted to investigate the effects of tunneling construction on surrounding infrastructure (Monsees, 2007) and dam settlement/movement (Charlwood, 2007). However, these investigations are typically conducted using modeling programs and spatially limited point data, obtained using traditional surveying methods (levels, global positioning systems), from before and while the structures are being built.

The ability to purchase archived data acquired from up to 17 years ago allows for post-construction analysis since 1991. Whereas most infrastructure is instrumented and monitored during construction, the instrumentation is often removed after construction and the infrastructure is no longer monitored. InSAR is one way to monitor movements associated with past, present, and future infrastructure construction. The InSAR technique allows for the detection of small movements over large areas instead of or in addition to current practices which provide spatially limited point measurements.

1.3   *Problem Statement*

For this research, two civil infrastructure sites with known deformation - the Los Angeles Redline Subway System in California and Mosul Dam in Iraq - were selected for study of InSAR processing techniques for civil infrastructure applications. Current SAR processing techniques were applied to study these sites. However, masking and speckle in the resulting images precluded observation of deformations at these two sites. Modified processing techniques were therefore investigated to allow observation of the deformation features with limited spatial scale (20 feet) using the large spatial resolution (60 feet) of current imagery in order to detect small scale surface deformations caused by tunneling or grouting in the Los Angeles and Mosul applications, respectively.

Hypothesis:

Modifications to "traditional" Geoscience processing techniques are required to detect and spatially characterize ground movements due to geotechnical engineering infrastructure using InSAR because of the large spatial resolution of imagery as compared with the limited spatial scale of the deformation features.

1.4   *Research Objectives*

The research described in this dissertation concentrates on improving processing techniques to measure localized deformation features associated with geotechnical engineering applications. This work is part of a larger research project underway at the University of Missouri to detect and characterize ground movement induced by a variety of natural and human processes. Manjunath (2008) studied the effect of a limited data set (image quantity and quality) using the Interferometric Point Target Analysis (IPTA) processing technique. Legarsky et al. (2007) studied scatter informatics to determine the

optimal polarization to be used by satellite platforms when conducting geotechnical engineering related studies.

The following research objectives are outlined for this study:

1. Evaluate the effect of filtering, multi-looking, and masking of SAR data as applied to geotechnical engineering applications (e.g. subway construction, monitoring of dams).

2. Evaluate five different methods used to determine ground deformations for Earth resource applications, as applied to geotechnical engineering applications.

3. Rank the five different methods, according to their effectiveness for use in geotechnical engineering applications.

1.5   *Dissertation Overview*

This manuscript is comprised of seven chapters. Chapter 1 (current chapter) presents an introduction to the project research, provides a problem statement and lists research objectives. Chapter 2 contains information regarding satellite-based remote sensing platforms, the sensor hardware used to obtain deformation measurements from these platforms (Synthetic Aperture Radar), how deformation estimates are obtained using this sensor hardware (interferometry) and past applications of this technique.

For this study, two sites were selected for evaluation: the Los Angeles (USA) Red Line Subway System and Mosul Dam (Iraq). These two sites are discussed in detail in Chapter 3 including discussion of the location, geological properties, infrastructure properties, construction timeline, and subsidence timeline. Selection of these two sites was based on *a priori* knowledge of measurable and documented ground movement.

The data processing techniques used to process Interferometric Synthetic Aperture Radar (InSAR) data are presented in Chapter 4. These five processing techniques are referred to in this dissertation as "traditional InSAR", "spatial InSAR", "enhanced spatial InSAR", "interferometric point target analysis (IPTA)", and "multiple baseline InSAR". The data, software and processing flow (computational code) used to conduct this research and to achieve the research objectives are presented in Chapter 5. Results from the various processing techniques (discussed in Chapter 4) are presented and discussed in Chapter 6, including a ranking system used to discern which processing technique/s is/are recommended for use in geotechnical engineering applications. Conclusions derived from this research and recommendations are presented in Chapter 7.

Chapter 2: Overview of Satellite Based Radar Remote Sensing

2.1   Introduction

Satellite-based remote sensing using imaging radars for commercial purposes began in 1978 with the launch of the first Synthetic Aperture Radar (SAR), SeaSAT. SeaSAT's ability to remotely sense the Earth's oceans led to the desire to also remotely sense the earth's land masses. SARs have been used historically to develop digital elevation models (DEMs) of the entire earth surface, and monitor changes to the Earth's surface (volcanoes, earthquakes, ground water and oil extraction). Satellite-based synthetic aperture imaging radars are advantageous over satellite-based optical imaging because they can be used to monitor the Earth's surface at night and through cloud cover.

In this chapter, historical applications of interferometric synthetic aperture radar are presented followed by an overview of operation of the on-board, active microwave synthetic aperture radars. Discussions on interferometry and past and present radar remote sensing (imaging) platforms are also presented.

2.2   Past Applications of Interferometric Synthetic Aperture Radar (InSAR)

Interferometric Synthetic Aperture Radar (InSAR) dates back to 1972, using InSAR from the Earth to measure the topography of the Moon and Venus (Burgmann et. al, 2000). InSAR was implemented from satellite based platforms using the SeaSAT platform in 1978, and was able to detect vertical soil movement caused by swelling soils in the Imperial Valley, California (Burgmann et al., 2000) using the repeat pass technique. The repeat pass technique was used by many more satellites from 1978 until

2000, when the first one-pass interferometer (STS-99 SRTM) was used to collect topographic data of the whole Earth (Jensen, 2000).

Burgmann et al. (2000) mention many past applications of InSAR including: measuring topography, lava thickness and viscosity (MacKay et al., 1998), crustal deformation (Gabriel et al., 1989), earthquake deformation (Massonnet et al., 1993), post-seismic deformation (Massonnet et al., 1994), inter-seismic deformation (Peltzer et al., 1998), volcano deformation (Francis, 1999), land subsidence from coal mining (Carnec et al., 1996), and land subsidence from extraction of fluids (Massonnet et al, 1997, Galloway et al., 1998, Fielding et al., 1997). In addition to the Earth resources applications previously mentioned, InSAR is now beginning to be used for geotechnical engineering applications. Beaver and Marra (2006) used a form of InSAR called Interferometric Point Target Analysis (IPTA) to measure subsidence caused by tunneling. This application of InSAR to tunnel construction led to this research to gain better understanding of InSAR processing techniques for geotechnical engineering applications, as conducted on the Los Angeles Redline Subway system described in this dissertation.
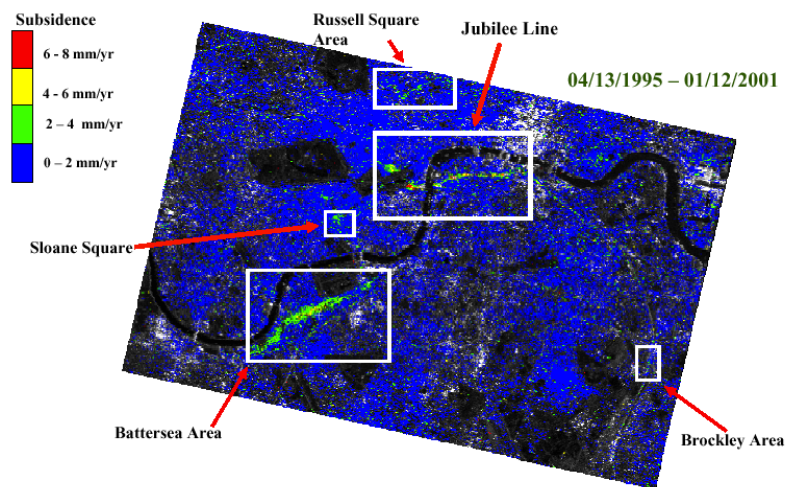
Figure 2.1. Subsidence Above the London Underground Subway System, Caused by Tunneling (from Beaver and Marra, 2006).

7

Satellite based InSAR has been used for landslide monitoring (Farina et al., 2006), which is a common concern in the geotechnical engineering profession. The use of InSAR as a dam monitoring tool, as a hypothesis presented by Coffman (2007), led to the research on the Mosul Dam discussed in this dissertation. The applications of InSAR in geotechnical engineering applications will begin to increase as the ground resolution of satellite imagery decreases. Current satellites (launched during 2007 and 2008) have ground cell resolutions of one meter as compared with the ERS-1 platform that has a ground cell resolution size of 25 meters. These resolutions will further the existing geotechnical engineering applications (tunneling, landslide monitoring, dam monitoring) and enable more research on additional geotechnical engineering applications (consolidation of small fill sites, expansive soils, etc.).

2.3   *Overview of Satellite Based Synthetic Aperture Radar*

As described in Section 2.2, satellite based Synthetic Aperture Radars (SAR) are used to image the Earth. *Active* satellite based radars image the Earth by sending pulses of electromagnetic energy (waves at certain frequencies) at the Earth's surface and receiving the corresponding backscattered pulses from the Earth's surface. Conversely, *passive* radars work by receiving only backscattered energy created by sources not located on the satellite platform (sun, moon, etc.). All of the SAR platforms discussed later in Section 2.5 are active radars, which allow for day and nighttime acquisition because they are not dependent upon another energy source. The term *synthetic* is used because a synthesized antenna length (length L in Figure 2.2) is produced by viewing the Earth's surface from multiple satellite viewing geometries (positions a through g in Figure 2.2) using a *real* (actual size) aperture antenna length (length D in Figure 2.2).

The synthesized antenna is created using the forward motion of the satellite to simulate a much larger antenna (e.g. the ERS-1 satellite platform real aperture radar antenna is a 1 meter by 10 meter planar array; the synthesized antenna size is 1 meter by 4000 meters). Synthesizing a large antenna array from a small real aperture radar antenna is necessary, because a 4000 meter antenna cannot be transported to space, and because resolution cell size in the direction of flight (azimuth direction) is inversely proportional to antenna size.
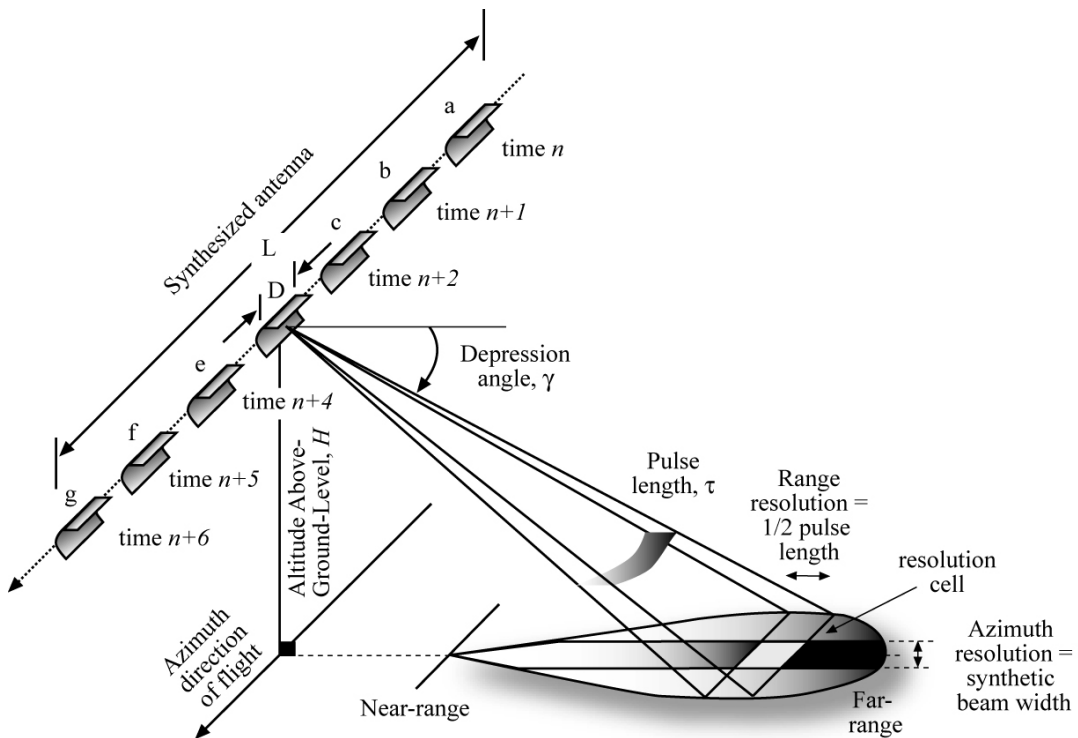
Figure 2.2. Schematic showing satellite based synthetic aperture radar concept (from Jensen, 2000).

As the satellite platform travels through space, the direction in which the satellite travels (flight direction, along-track) is referred to as the azimuth direction, and the direction of radar pointing is the range direction (cross-track). The range direction is commonly perpendicular to the azimuth direction. The radar transmits energy towards the ground, creating a tear-dropped shape commonly referred to as the radar footprint.

The radar footprint is created by the radar scanning/sweeping in the range direction as the radar travels in the azimuth direction. As is illustrated in Figure 2.2, the tear-drop shape is smallest in the near-range (closest to the satellite) and largest in the far-range (farthest from the satellite). Because the depression angle changes as the radar scans, the range resolution (size of the resolution cell in the direction perpendicular to the flight direction) changes from the near-range to the far-range, with the near-range range resolution cell being larger than the far-range range resolution cell. The range and azimuth resolution cell sizes for a real aperture radar are calculated as:

$$R_r = \frac{\tau \cdot c}{2 \cdot \cos(\gamma)} \qquad \textbf{Equation 2.1}$$

$$R_a = \left(\frac{H}{\sin(\gamma)}\right)\frac{\lambda}{D} \qquad \textbf{Equation 2.2}$$

where R_r is the range resolution, τ is the pulse length, c is the speed of light, γ is the depression angle, R_a is the azimuth resolution, H is the height of the satellite above ground level, λ is the wavelength, and D is the length of the real aperture radar antenna. From Equation 2.1, the range resolution decreases as the pulse length is decreased. However, if the pulse length is too short, the power transmitted from the satellite and backscattered to the satellite, will be too small, which results in poor range resolution as per Equation 2.3 for the pulse-limited case (Richards, 2006).

$$P_r = \frac{P_t G^2 \lambda^2 \sigma^0 \Delta R \theta_3}{(4\pi)^3 R_o^{\ 3} L_s L_a (R_o) \cos(\delta)} \qquad \textbf{Equation 2.3}$$

where P_r is the received power, P_t is the transmitted power, G is the ratio of peak antenna power gain to isotropic gain, λ is the wavelength, σ^0 is the area reflectivity, ΔR is the

range resolution, R_o is the range distance, L_s is the system loss factor, L_a is the atmospheric loss factor, and δ is the depression angle.

The azimuth resolution in Equation 2.2 is for a real aperture radar. The synthetic aperture radar azimuth resolution is calculated using the Doppler-synthesis approach (frequency changes if the source and/or target are in motion relative to each other) discussed in Elachi and Van Zyl (2006). As the radar travels past a target on the Earth, the target will be viewed by multiple radar pulses. The echo of the target will have a positive Doppler shift (when the target enters the beam), followed by zero Doppler shift, followed by negative Doppler shift (when the target exits the beam). Therefore, the spectrum of echo frequency from the target is the transmitted center frequency plus/minus the Doppler frequency with the Doppler frequency being calculated as

$$f_d = \frac{v}{D} \qquad \qquad \textbf{Equation 2.4}$$

where f_d is the Doppler frequency, v is the satellite velocity and D is the antenna length. The shortest time span (t) that can be measured is

$$t = \frac{1}{2f_d} \qquad \qquad \textbf{Equation 2.5}$$

Substituting Equation 2.4 into Equation 2.5, the shortest time span that can be measured is a function of velocity of satellite platform (v) and length of the satellite antenna (D).

$$t = \frac{D}{2v} \qquad \qquad \textbf{Equation 2.6}$$

Combined with the basic equation for displacement ($X = v \cdot t$), the azimuth resolution cell size ($X = R_a$) is calculated as

$$R_a = v \cdot \left(\frac{D}{2v}\right) = \left(\frac{D}{2}\right)$$

Equation 2.7

To achieve the azimuth resolution cell size provided by Equation 2.7, at least one pulse must be sent by the SAR every time the satellite moves by one-half of the real aperture radar antenna length. Using a large synthesized antenna (length L) produces the effect of a very narrow beam with small azimuth resolution cells; as compared to the small real aperture radar (length D) with a large beam that produces large azimuth resolution cells. Also, using the Doppler principle, the azimuth resolution cell size does not vary across a scene like the range resolution cell size.

Different satellite platforms use different frequencies (wavelengths). All Synthetic Aperture Radar (SAR) platforms use radars with wavelengths in the microwave frequency range (K, Ka, X, C, S, L, and P) (Figure 2.3). These frequencies correspond to wavelengths that are not interfered with by atmospheric conditions (even rain clouds which block visible wavelengths from reaching the Earth) because the radar wavelength is much larger than the atmospheric molecules (Figure 2.4).
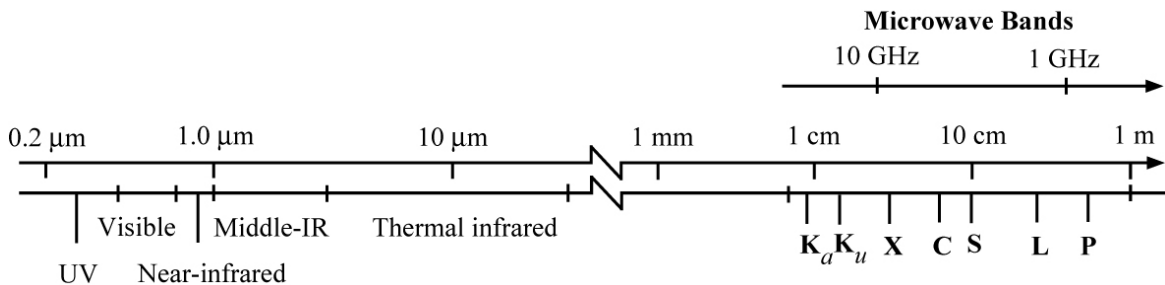
Figure 2.3. Wavelengths of commonly used microwave frequencies (from Jensen, 2000).
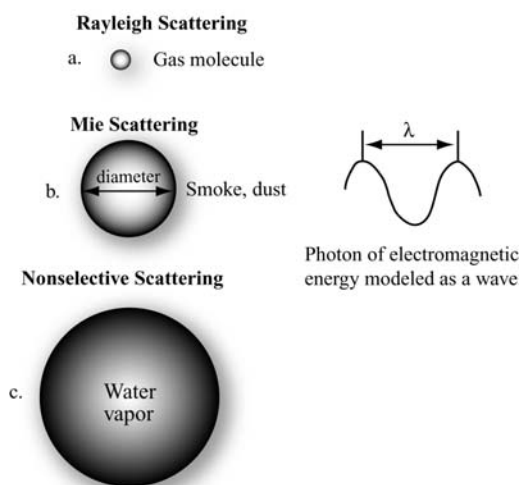
Figure 2.4. Penetration of radar waves due to wavelength being larger than atmospheric molecule diameter (from Jensen, 2000).

The different microwave bands, along with the respective wavelengths and frequencies are listed in Table 2.1. Note that most commercial SAR satellite platforms use X-band, C-band, or L-band radars. Wavelengths at these frequencies penetrate the atmosphere and provide better coherence than wavelengths at other band frequencies. These frequencies also produce wavelengths which penetrate into plant canopy and soil mass (longer wavelengths penetrate deeper), providing valuable information for Earth resource missions.

Table 2.1. Radar band wavelengths and frequencies.

Microwave Band Name	Wavelength (cm)	Frequency (GHz)
Ka	0.75 - 1.18	26.5 - 40.0
K	1.18 - 1.67	18.0 - 26.5
Ku	1.67 - 2.40	12.5 - 18.0
X	2.40 - 3.80	8.0 - 12.5
C	3.80 - 7.50	4.0 - 8.0
S	7.50 - 15.0	2.0 - 4.0
L	15.0 - 30.0	1.0 - 2.0
P	30.0 - 100.0	0.3 - 1.0

2.4   Interferometry

Merriam-Webster Dictionary defines interferometry as, "[the] utilization [of] the interference of waves for precise determination of distance." In radar interferometry, this is accomplished by using multiple radar images (each image encompassing the recording of multiple waves) of the same area. If these images are acquired at the same time using two radar antennas on one satellite platform (e.g. SRTM in Section 2.5.5), the interferometry is referred to as *single-pass interferometry*. If these images are acquired at different times using a single radar antenna on one satellite platform (i.e. ERS-1), it is referred to as *repeat pass interferometry*. *Tandem pass interferometry* consists of using two images acquired at different times (repeat pass) from different satellite platforms (i.e. ERS-1 and ERS-2).

Interferometry relies on the relative imaging geometry and location of each radar. For single-pass systems, the radars are separated by a short distance (60-meters for SRTM data) on the same platform moving in the same orbit around the Earth. For repeat-pass systems, the satellite orbit pattern changes slightly between each acquisition, resulting in a separation in distance between the locations of the radar for each image (approximately 0.5 meters to 1,000 meters). This separation is determined using satellite orbit (precise state vectors) information. The distance between the locations of the radars is referred to as *baseline* (B in Figure 2.5).
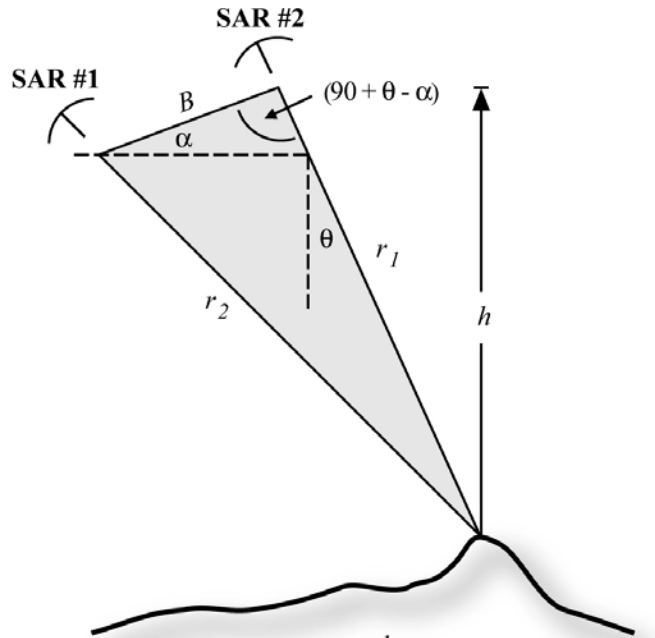
Figure 2.5. Relative viewing geometry of two synthetic aperture radars (from Jensen, 2007).

Using the geometry shown in Figure 2.5, the interferometric phase of a specific location on the ground is

$$\phi = -\frac{4 \cdot \pi}{\lambda}(r_1 - r_2)$$ **Equation 2.8**

where ϕ is the interferometric phase, π is the constant 3.14159, λ is the wavelength of the radar pulse, and r_1 and r_2 are the slant range distances between the radar and the ground location at two different times.

This equation utilizes the slant range distances between the radar and the ground location (r_1 and r_2) and the wavelength of the radar pulse (λ).

This interferometric phase (z) of each location in a radar image is used in conjunction with the radar image (range x and azimuth y) to produce a three-dimensional image. If the images are acquired at the same time, this image is used to produce a digital elevation model. If the images are acquired at different times, this image contains both

phase caused by topography and phase caused by deformation. To obtain only deformation phase information, the topographic phase is subtracted from the topography and deformation phase resulting in only the deformation phase component. According to Manjunath (2008), "deformation … can be derived by multiplying the complex phasors [sinusoid] of all pixels in one acquisition by the conjugate of the complex phasors of all corresponding pixels in the other acquisition. … The complex multiplication on a pixel by pixel basis is equivalent to differencing the phases representing each pixel in both the acquisitions while multiplying their respective amplitudes."

As depicted previously in Figure 2.5, the viewing geometry is different for each acquisition. Therefore, the location of the pixels may not be in the same place for each image. Prior to obtaining the interferometric phase, all pixels must be in the same location in both images. Moving pixel locations in one image to match pixel locations in another image is referred to as *co-registration*.

The baseline shown previously in Figure 2.5 is a vector comprised of two components. The components are in the along track (normal/parallel) and cross-track (perpendicular) directions. Image sets with longer perpendicular baselines are more sensitive to topography than image sets with shorter perpendicular baselines. The threshold at which an image set is not sensitive to topography is dependent upon the image geometry, the wavelength of the emitted pulse, and the perpendicular baseline. Manjunath (2008), indicates that the threshold is the perpendicular baseline ($B_{\perp}$) that will not cause a change in topographic height ($h_{ambiguity}$) which causes an interferometric phase change of one cycle (2π radians).

$$h_{ambiguity} = 2\pi \left(\frac{\delta h}{\delta \phi} \right) = \frac{\lambda \cdot r_1 \sin(\theta)}{2 \cdot B_\perp} \qquad \textbf{Equation 2.9}$$

Where $h_{ambiguity}$ represents the change in topographic height, λ is the wavelength of the radar pulse, and r_1 is the slant range distance between the radar and the ground location, q is the incidence angle, and $B_\perp$ is the perpendicular baseline. In Equation 2.9, the change in topographic height with respect to the change in interferometric phase is represented by $\left(\frac{\delta h}{\delta \phi} \right)$. As per Equation 2.9, larger perpendicular baselines may be used for satellite platforms with longer wavelengths. However, from Equation 2.9, longer wavelengths result in less phase difference, and therefore, less deformation resolution.

2.5   Overview of Radar Remote Sensing (Imaging) Platforms

From the launch of SeaSAT in 1978 until present, 21 satellites containing commercial synthetic aperture radars have been launched (Table 2.2). Each satellite is slightly different and is used to monitor the earth's surface in a different manner. The seven satellite platforms used predominately in research conducted at the University of Missouri are the ERS-1, ERS-2, RADARSAT-1, RADARSAT-2, ENVISAT, PALSAR, and SRTM platforms. These seven platforms are discussed in Sections 2.5.1-2.5.5; a brief overview of the other 14 satellite platforms is presented in Section 2.5.6.

Table 2.2. List of commercially available radar satellites, their operating agencies, and their launch dates.

Name	Operating Agency	Date Launched
ERS-1	European Space Agency	07/17/1991
ERS-2	European Space Agency	04/21/1995
ENVISAT	European Space Agency	03/01/2002
RADARSAT-1	Canadian Space Agency	11/04/1995
RADARSAT-2	Canadian Space Agency	12/14/2007
SRTM	National Aeronautics and Space Administration	02/11/2000
Sea-SAT		06/26/1978
SAR-LUPE 1	German Aerospace Agency	12/19/2006
SAR-LUPE 2		07/02/2007
SAR-LUPE 3		11/01/2007
SAR-LUPE 4		03/27/2008
SAR-LUPE 5		07/22/2008
TERRASAR-X		06/15/2007
JERS-1	Japan Aerospace Exploration Program	02/11/1992
COSMO-SkyMed-1	Italian Space Agency	06/08/2007
COSMO-SkyMed-2		12/09/2007
COSMO-SkyMed-3		10/25/2008
SIR-A	National Aeronautics and Space Administration	11/12/1981
SIR-B		10/05/1984
SIR-C/X-SAR		04/09/1994 09/30/1994
ALOS PALSAR	Japan Aerospace Exploration Program	01/24/2006

2.5.1   European Remote Sensing 1 and 2 (ERS-1, ERS-2) Satellites

The European Remote Sensing 1 (ERS-1) satellite was launched by the European Space Agency (ESA) from Kourou, French Guiana, on July 17, 1991 onboard an Ariane 4 expendable launch vehicle. The satellite platform houses multiple instruments for various scientific purposes that include (ESA, 2009a): a C-band (5.66 cm wavelength) active microwave synthetic aperture radar (SAR), a wind scatterometer, a radar altimeter (RA), an along track scanning radiometer (ATSR), a microwave sounder (MS), precise range and range-rate equipment (PRARE), and laser retro-reflectors (LRR). The 5.3 GHz

(C-band), 15.55 MHz bandwidth, linear vertical polarization, 4.8 KW, 37.12 micro-sec, active microwave SAR was the only equipment onboard the ERS-1 satellite that was used for this study. The SAR is comprised of a 1 meter by 10 meter rectangular planar array antenna divided into a 5 panel arrangement. The SAR is the heaviest piece of equipment on the ERS-1 platform, consuming approximately fifteen percent of the total mass of the ERS-1 satellite (ESA, 2009b).

Following the ERS-1 satellite launch, the satellite went through seven data collection phases, consisting of a commissioning phase (July 31, 1991 – December 28, 1991), an ice phase (December 28, 1991 – April 2, 1992), a multi-disciplinary phase (April 2, 1992 – December 23, 1993), an ice phase (December 23, 1993 – April 10, 1994), two geodetic phases (April 10, 1994 – March 21, 1995), and a multi-disciplinary phase (March 21, 1995 – June 2, 1996), respectively (Alaska SAR Facility, 2009). The ERS-1 satellite went into standby mode in June 2, 1996, and was retired on March 10, 2000. For this study, images obtained during the multi-disciplinary phases were used; therefore, ERS-1 imagery is available from April 2, 1992 to December 23, 1993 and from March 21, 1995 to June 2, 1996.

During the multi-disciplinary phases, in which the data used in this study was collected, the ERS-1 satellite platform was in a sun-synchronous, near-polar orbit at a mean altitude of 782 kilometers and an inclination of 98.542 degrees (ESA, 2009a). This altitude and inclination allow for 35-day repeat pass temporal resolution of individual locations. The data collected by the satellite are downloaded to ground stations when the ground station is within view of the orbiting satellite using an X-band Instrument Handling and Data Transmission (IHDT) system.

The satellite views the ground with a 23-degree incidence angle from nadir (vertical downward), allowing the satellite to image a 100-km strip of land, 250 km to the right of the projection of the flight line on the ground (Figure 2.6). Typically the 100 km data strips are cut into 100 km by 100 km images. For all acquisition phases, the spatial resolution is less than or equal to 30 meters in the along track (azimuth) direction and less than or equal to 26.3 meters in the across-track (range) direction. For the purposes of this study, the spatial resolution is often considered as 5.26 meters in the azimuth direction and 26.3 meters in the range direction. The data are commonly multi-looked by a factor of 5 in the azimuth direction, as compared to the range direction, to create square pixels. This multi-looking concept is discussed in detail in subsequent chapters. All ERS-1 data are available through the European Space Agency.
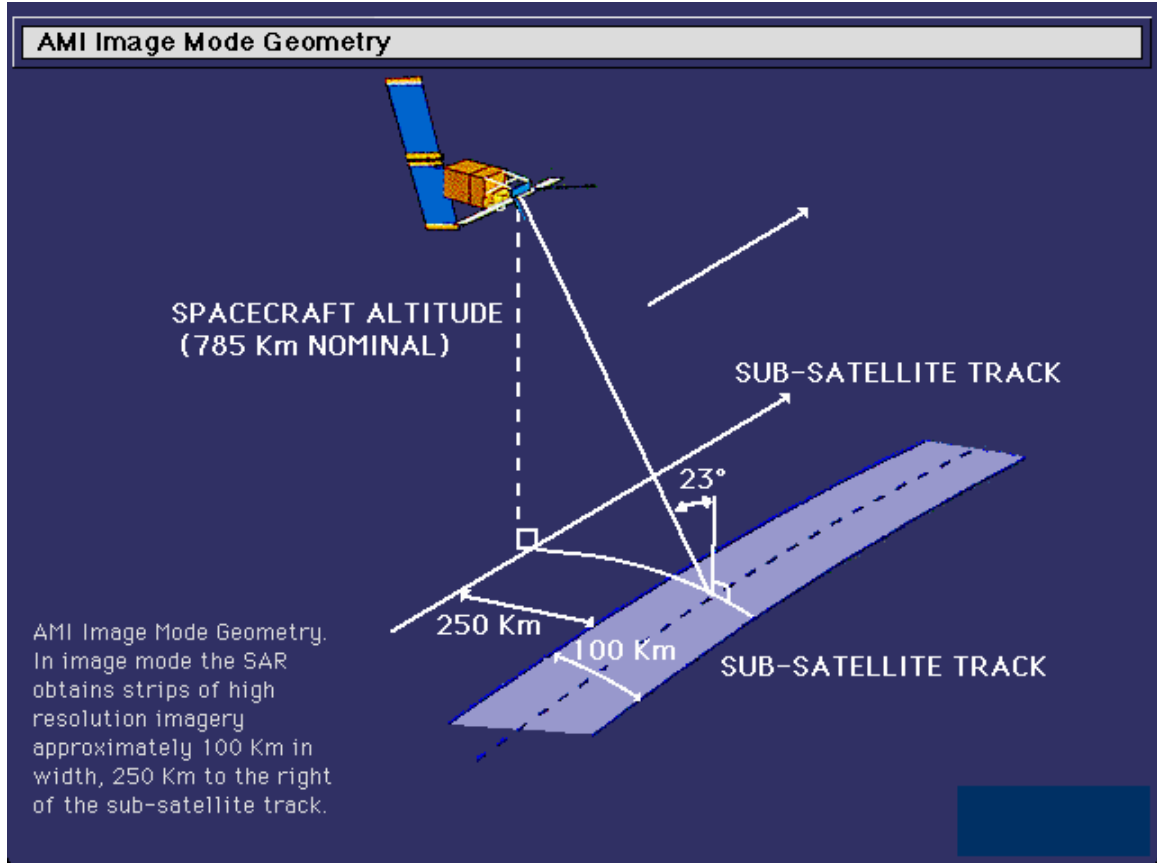
Figure 2.6. Imaging geometry for ERS-1 and ERS-2 satellites (from ESA, 2009b).

The European Remote Sensing 2 (ERS-2) satellite was launched by the ESA from Kourou, French Guiana, on April 21, 1995. Like the ERS-1 satellite launched previously, the ERS-2 satellite was launched onboard an Ariane 4 expendable launch vehicle. The ERS-2 platform contained replicas of the same instruments housed on the ERS-1 platform, along with Global Ozone Monitoring Equipment (GOME).

Following the launch of ERS-2, the platform was placed in the same orbit as the ERS-1 platform. The ERS-2 platform trailed the ERS-1 platform by 24 hours, allowing for one-day tandem images, in addition to the standard 35-day repeat pass temporal

resolutions of both satellites, until the ERS-1 went into standby mode on June 2, 1996 (Delft University Department of Earth Observation and Space Systems, 2009).

Although ERS-1 went into standby mode, ERS-2 continues to provide 35-day repeat pass temporal resolution of individual locations at present (2009). Unlike the ERS-1 platform, the ERS-2 platform did not go through ice or geodetic phases. Therefore, the satellite has only been, and is currently only used in the multi-disciplinary phase which is applicable to this research. Data obtained from the ERS-1 and ERS-2 satellite platforms were used to determine subsidence estimates above the Los Angeles Redline Subway System, as discussed in Chapter 6.

2.5.2   *Environmental Satellite (ENVISAT)*

The Environmental Satellite (ENVISAT) was launched by the ESA from Kourou, French Guiana, on March 1, 2002 onboard an Ariane 5 expendable launch vehicle. The satellite platform houses multiple instruments for various scientific purposes, which include: a C-band (5.66 cm wavelength) active microwave advanced synthetic aperture radar (ASAR), a radar altimeter 2 (RA-2), an advanced along track scanning radiometer (AATSR), a microwave radiometer (MWR), a Michelson interferometer for passive atmospheric sounding (MIPAS), a global ozone monitoring by occultation of stars (GOMOS), a scanning imaging absorption spectrometer for atmospheric chartography (SIAMACHY), a medium resolution imaging spectrometer (MERIS), a Doppler orbitography and radio-positioning integrated by satellite (DORIS), and laser retro-reflectors (LRR) (ESA, 2009c). The 5.3 GHz (C-band), dual-pol vertical and horizontal polarization, active microwave ASAR was the only piece of equipment onboard the ENVISAT satellite which was used for this scientific study. The ASAR antenna is a 1.3

meter by 10 meter rectangular planar array antenna divided into five 1.3 meter by 2 meter panels.

The ENVISAT satellite platform is in a sun-synchronous orbit at a mean altitude of 785 kilometers and an inclination of 98.6 degrees. This altitude and inclination allow for 35-day repeat pass temporal resolution of individual locations. The data collected by the satellite are downloaded to ground stations when the ground station is within view of the orbiting satellite using two X-band download links.

As summarized in Table 2.3 and shown in Figure 2.7, the ENVISAT ASAR has five viewing modes: global monitoring, wide swath, image, alternating polarization, and wave. The image mode is the mode used for this study. In image mode, six viewing modes are available allowing (IS1-IS7). The satellite views the ground with incidence angles from nadir ranging from 15.0-45.2 degrees, allowing the satellite to image 56 km to 105 km strips of ground, from 187 km to 671 km to the right of the projection of the flight line on the ground. Typically the 105 km data strips are cut into 100 km by 105 km images.

Table 2.3. List of ENVISAT viewing modes (ESA, 2009d).

Viewing Mode	Swath Width (km)	Incidence Angle (Degrees)	Ground Position from Nadir (km)
IS1	105	15.0-22.9	187-292
IS2	105	19.2-26.7	242-347
IS3	82	26.0-31.4	337-419
IS4	88	31.0-36.3	412-500
IS5	64	35.8-39.4	490-555
IS6	70	39.1-42.8	550-620
IS7	56	42.5-45.2	615-671

The spatial resolution is less than or equal to 30 meters in both the along track (azimuth) and across-track (range) direction. In order to do interferometry using these scenes, each scene must have the same track direction (all ascending or all descending) and must have the same incidence angle (imaging mode), i.e., all images must be collected using IS1 imaging mode, or all images must be collected using IS2 imaging mode, etc. as listed previously in Table 2.3. For the purposes of this study, the spatial resolution is often considered as 5 meters in the azimuth direction and 25 meters in the range direction. The data are commonly multi-looked by a factor of 5 in the azimuth direction, as compared to the range direction, to create square pixels. The multi-looking concept is discussed in detail in subsequent chapters. All ENVISAT data are available through the European Space Agency.

The ENVISAT platform was designed as a continuation of the ERS-1 and ERS-2 platforms. Therefore, cross-platform (ERS-1/ENVISAT, ERS-2/ENVISAT) interferometry can be conducted using scenes collected in the same imaging mode from each platform. Data obtained from the ENVISAT satellite platform were used to determine subsidence estimates of Mosul Dam, as discussed in Chapter 6.
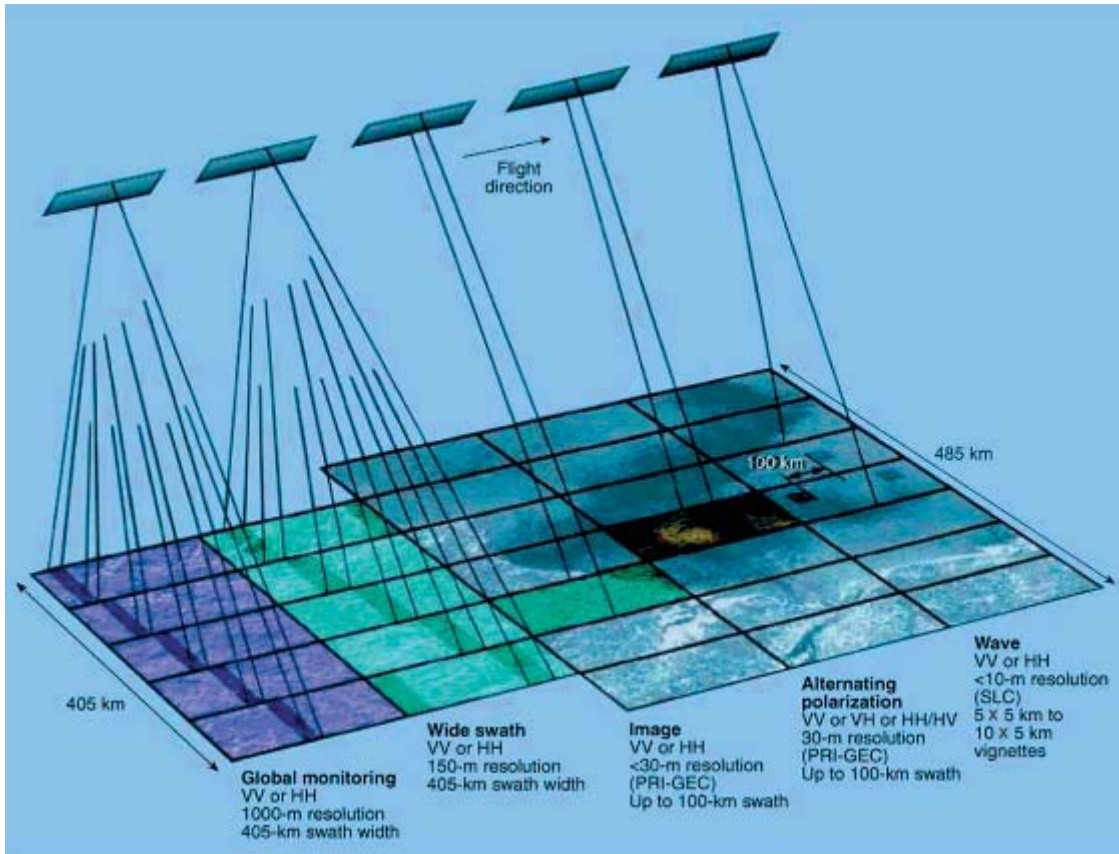
Figure 2.7. ENVISAT imaging modes (ESA, 2009e).

2.5.3   Radio Detection and Ranging Satellites 1 and 2 (RADARSAT-1, RADARSAT-2)

The Radio Detection and Ranging Satellite 1 (RADARSAT-1) was launched by the Canadian Space Agency from Vandenberg Air Force Base in California, on November 4, 1995 onboard a Delta 2 launch vehicle. The satellite platform is used only for data collection and dissemination from the 5.3 GHz (C-band), 11.6, 17.3, or 30 MHz bandwidth, linear horizontal polarization (horizontal transmitted waves and horizontal received waves), 5 KW, 1.5 meter by 15 meter rectangular planar array antenna active microwave SAR (Canadian Space Agency, 2009).

The RADARSAT-1 satellite platform is in a sun-synchronous orbit at a mean altitude of 798 kilometers and an inclination of 98.6 degrees. This altitude and inclination allow for 24-day repeat pass temporal resolution of individual locations. The

25

data collected by the satellite are downloaded to ground stations when the ground station is within view of the orbiting satellite using two X-band download links.

As shown in Figure 2.8 and listed in Table 2.4, RADARSAT-1 has six imaging modes: fine, standard, wide, ScanSAR narrow, ScanSAR wide, and extended beams (low and high incidence). In the ScanSAR mode, the satellite SAR images a 500 km strip of ground, 250 km to the right of the projection of the flight line on the ground. For processing conducted at the University of Missouri, fine beam mode images are used. In the fine beam mode, the satellite incidence angle may be varied to view five different 50 km locations within the outer 250 km of the ScanSAR wide 500 km beam footprint.
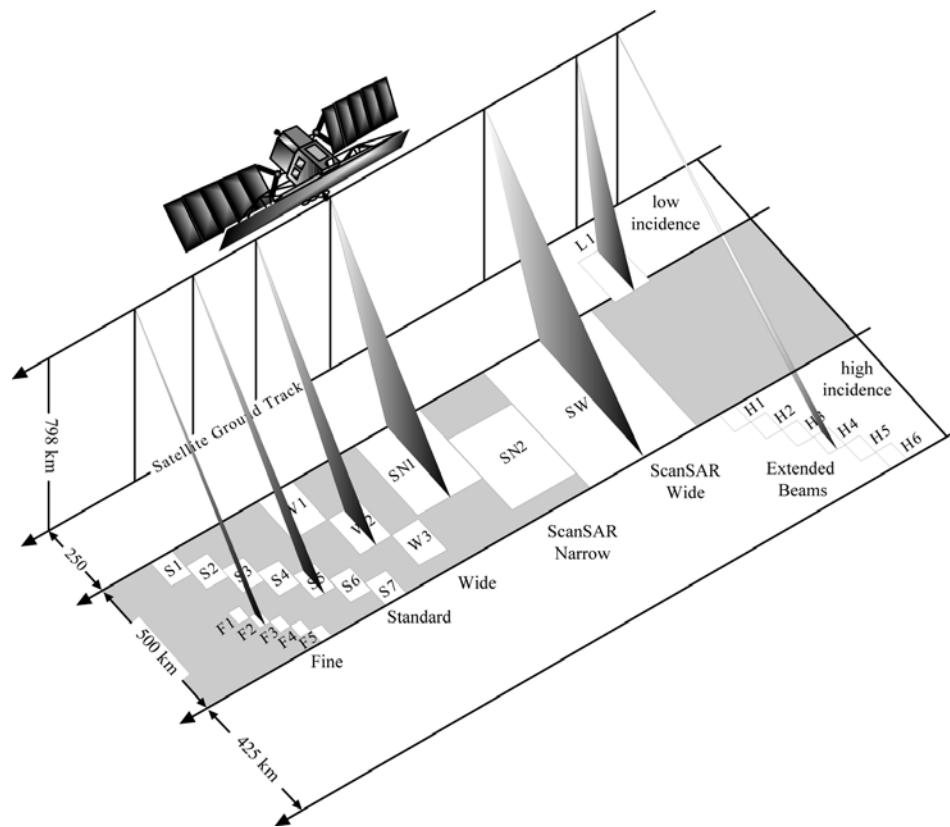
Figure 2.8. RADARSAT-1 imaging modes (from Jensen, 2000).

Table 2.4. RADARSAT-1 and RADARSAT-2 imaging mode characteristics (modified from Jensen, 2000 and MDA, 2009b).

Imaging Mode	Beam Position	Incidence Angle (Degrees)	Nominal Spatial Resolution (m)	Nominal Area (km)	Number of Processing Looks
Ultra-fine Multiple-look fine (RADARSAT-2 only)	-	30-40 30-50	3.0x2.0-3.4 7.9x7.4-9.1	20 x 20 50 x 50	1 x 1 >3
Fine (5 positions)	F1 F2 F3 F4 F5	37-40 39-42 41-44 43-46 45-48	8	50 x 50	1
Standard (7 positions)	S1 S2 S3 S4 S5 S6 S7	20-27 24-31 30-37 34-40 36-42 41-46 45-49	25	100 x 100	1 x 4
Wide (3-positions)	W1 W2 W3	20-31 31-39 39-45	30	165 x 165 150 x 150 135 x 135	1 x 4
ScanSAR Narrow (2 positions)	SN1 SN2	20-40 31-46	50	300 x 300	2 x 2
ScanSAR Wide	SW1	20-49	100	500 x 500	2 x 4
Extended High (6 positions)	H1 H2 H3 H4 H5 H6	49-52 50-53 52-55 54-57 56-58 57-59	26	75 x 75	1 x 4
Extended Low (RADARSAT-1 only)	L1	10-23	35	170 x 170	1 x 4
Fine Quad-Pol (RADARSAT-2 only)	-	20-41	12	25 x 25	1
Standard Quad-Pol (RADARSAT-2 only)	-	20-41	25	25 x 25	1

As shown and listed previously in Figure 2.8 and Table 2.4, respectively, the satellite incidence angles in the five different fine beam mode viewing geometries (F1, F2, F3, F4, and F5) are 37-40, 39-42, 41-44, 43-46, and 45-45 degrees from nadir, allowing the satellite to view the ground from 500-550, 550-600, 600-650, 650-700, 700-750 km to the right of the projection of the flight line on the ground, respectively. Images taken using the fine beam mode are 50 km by 50 km square images. In order to do interferometry using these images, each scene must have the same track direction (all ascending or all descending), and must have the same incidence angle (imaging mode); i.e., all images must be collected using F1 imaging mode, or all images must be collected using F2 imaging mode, etc. The nominal spatial resolution in fine beam mode is 10 meters. For the purposes of this study, the spatial resolution is often considered as 4 meters in the azimuth direction and 8 meters in the range direction. The data are commonly multi-looked by a factor of 2 in the azimuth direction, as compared to the range direction, to create square pixels. All RADARSAT-1 data are available through MacDonald, Dettwiler, and Associates Ltd.(MDA).

The Radio Detection and Ranging Satellite 2 (RADARSAT-2) was launched by the Canadian Space Agency from the Baikonur Cosmodrome in Kazakhstan, on December 14, 2007 onboard a Soyuz launch vehicle. The satellite platform is used only for data collection and dissemination from the 5.4 GHz (C-band), 11.6, 17.3, 30, 50, 100 MHz bandwidth, quad-polarimetric polarization (transmit and receive both horizontally and vertically polarized waves), 5 KW, 1.5 meter by 15 meter rectangular planar array antenna active microwave SAR (MDA, 2009a).

Like RADARSAT-1, the RADARSAT-2 platform is in a sun-synchronous orbit at a mean altitude of 798 kilometers and an inclination of 98.6 degrees. This altitude and inclination allow for 24-day repeat pass temporal resolution of individual locations. The data collected by the satellite are downloaded to ground stations when the ground station is within view of the orbiting satellite using two X-band download links.

As in shown in Figure 2.9 and listed previously Table 2.4, RADARSAT-2 has ten imaging modes: ultra-fine, standard, wide, fine, multi-look fine, standard quad-pol, fine quad-pol, ScanSAR narrow, ScanSAR wide, and extended high. RADARSAT-2 has the same imaging modes as RADARSAT-1 except for extended low, and also has ultra-fine, multi-look fine, standard quad-pol, and fine quad-pol. Like RADARSAT-1, RADARSAT-2 images a 500 km strip of ground, 250 km to the right of the of the projection flight line on the ground in the ScanSAR mode.
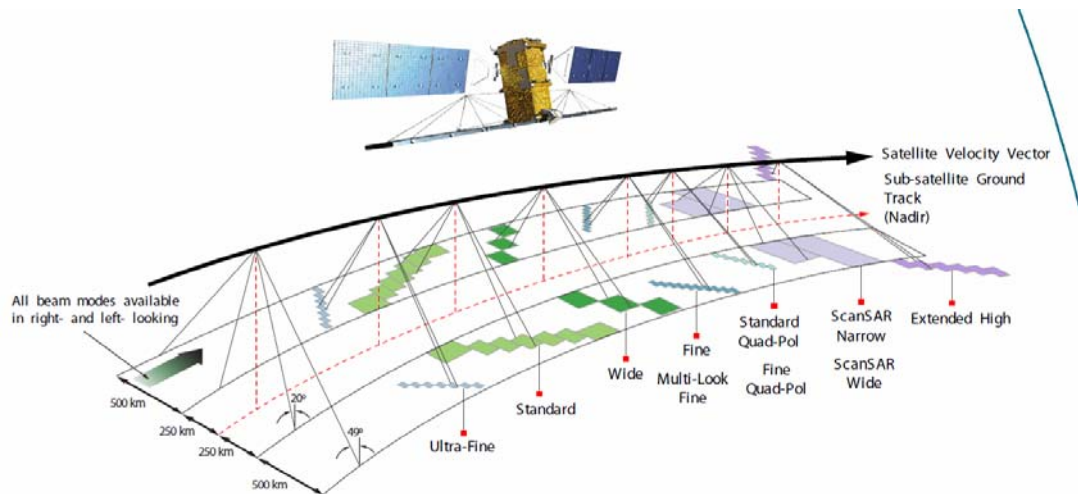
Figure 2.9. RADARSAT-2 imaging modes (from MDA, 2009b).

For processing conducted at the University of Missouri, RADARSAT-2 fine quad-pol beam mode images are used. The nominal spatial resolution in fine quad-pol beam mode is 12 meters (Table 2.4). In order to do interferometry using these scenes,

each scene must have the same track direction (all ascending or all descending), and imaging mode. Tandem pairs of images from RADARSAT-1 and RADARSAT-2 can not be used to do interferometry even if the RADARSAT-1 and RADARSAT-2 images have the same track direction and the same imaging mode because the frequency used by RADARSAT-1 (5.3 GHz) is different than the frequency used by RADARSAT-2 (5.4 GHz). All data are available through MDA.

According to MDA (2009c), RADARSAT-2 quad-pol polarization allows for "better discrimination of various surface types and improved object detection and recognition." RADARSAT-2 can transmit and receive radar waves in both the horizontal and vertical polarizations. RADARSAT-2 will transmit horizontally polarized waves and receive both horizontally (HH) and vertically (HV) polarized waves, and will transmit vertically polarized waves and receive both horizontally (VH) and vertically (VV) polarized waves. This allows for fully polarimetric (HH, HV, VH, and VV) datasets. Researchers at the University of Missouri are investigating the optimized polarization to improve localized feature detection and recognition. According to MDA (2009c), "The trick will be discovering the right combination of polarization to use. That's a quest that has consumed SAR experts at MDA and captured the interest of many researchers and users across the globe who have been conducting research to discover just what fully polarimetric and selective polarimetric data can offer."

Whereas the effects of polarization on InSAR are not discussed in this document, using multiple polarization is beneficial to InSAR because it allows for the identification of coherent points which would not have been identified using single polarization. By identifying these coherent points, more of a given scene is coherent. However, multiple

polarizations also reduce the bandwidth at which the radar performs, reducing the spatial resolution.

2.5.4   Advanced Land Observing Satellite (ALOS)

The Advanced Land Observing Satellite (ALOS) was launched by the Japan Aerospace Exploration Program from Tanegashima Space Center, located South of Kagoshima Prefecture, on January 24, 2006 onboard a H-IIA launch vehicle.   The satellite platform houses multiple instruments for various scientific purposes that include: a phased array type L-band synthetic aperture radar (PALSAR), a panchromatic remote-sensing instrument for stereo mapping (PRISM), and an advanced visible and near infrared radiometer type 2 (AVNIR-2) (Japan Aerospace Exploration Agency, 2009a). The 1270 MHz (L-band), 14 or 28 MHz bandwidth, single pol, dual-pol or quad-pol, 7 KW, active microwave SAR was the only piece of equipment onboard the ALOS satellite which was used for this study.   The PALSAR antenna is a 3.1 meter by 8.9 meter rectangular planar array antenna divided into a 4 panel arrangement.

The ALOS platform is in a sun-synchronous orbit at a mean altitude of 692 kilometers and an inclination of 98.2 degrees. This altitude and inclination allow for 46-day repeat pass temporal resolution of individual locations. The data collected by the satellite are downloaded to ground stations when the ground station is within view of the orbiting satellite at a rate of 240 Mbps.

As shown in Figure 2.10, ALOS PALSAR has three (3) imaging modes: fine resolution, ScanSAR, and polarimetric. In the ScanSAR mode, the satellite SAR images a 350 km strip of ground, 90 km to the right of the of the projection of the flight line on the ground. For processing conducted at the University of Missouri, ALOS PALSAR

fine beam mode 70 km by 70 km images with an incidence angle of 34.3 degrees are used. In order to do interferometry using these images, each scene must have the same track direction (all ascending or all descending) and must have the same imaging mode. The nominal spatial resolution in fine beam mode is 14 meters (Japan Aerospace Exploration Agency, 2009b). PALSAR data are available through the User Proposal Application Submission System (U-PASS) at the Alaska SAR facility.
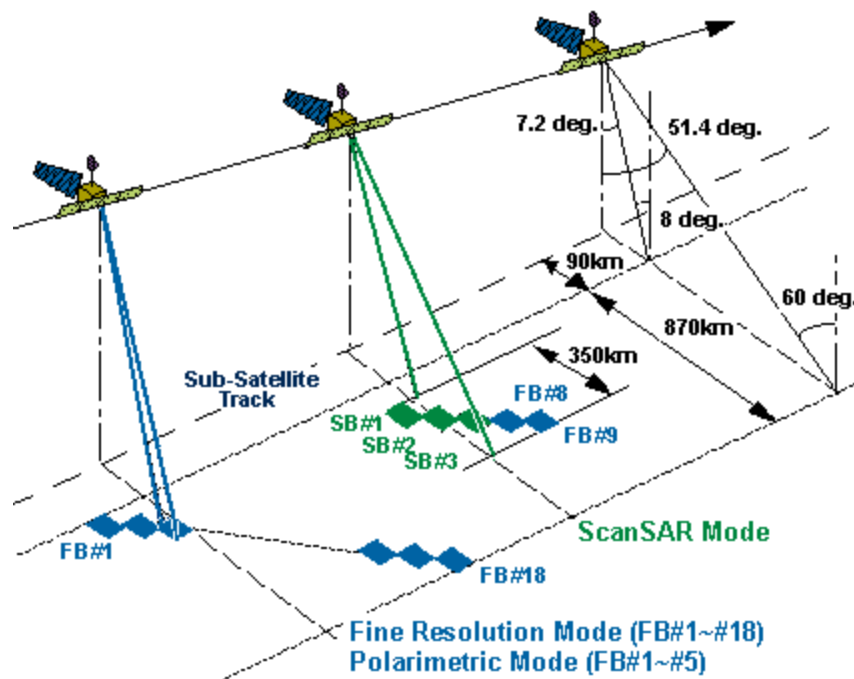
Figure 2.10. Imaging modes of ALOS PALSAR (from Japan Aerospace Exploration Agency, 2009b).

2.5.5 Shuttle Radar Topography Mission (SRTM)

The Shuttle Radar Topography Mission (SRTM) was launched by the National Aeronautics and Space Administration (NASA) from the Kennedy Space Center in Florida, on February 11, 2000 using the Space Transportation System (STS) 99 Space Shuttle Endeavour (NASA Jet Propulsion Laboratory (JPL), 2009a). The space shuttle

carried the Shuttle Imaging Radar-C (SIR-C) and the X-band Synthetic Radar (X-SAR),

both of which were carried by the space shuttle during two other missions in 1994 (STS-

59 in April and STS-68 in October). Unlike the other unmanned, continuous acquisition

synthetic aperture radar platforms and radars previously mentioned, the SRTM was an

11-day manned mission in which the platform and equipment returned to earth (in

operational form) after use (NASA JPL, 2009b).

The components of the SRTM mission consisted of three parts: the SIR-C/X-SAR

system (X-band, C-band, and L-band antenna) placed in the cargo bay of the space

shuttle (which transmitted and received signals), a 60-meter long mast, and a X-band and

C-band outboard antenna (which only received signals) placed at the end of a mast

(Figure 2.11).   The L-band antennas were used for the SIR-C mission, but were not used

for the SRTM mission.   Using two antennas (X-band or C-band), 60-meters apart,

allowed for single-pass interferometry (two images acquired at the same time).
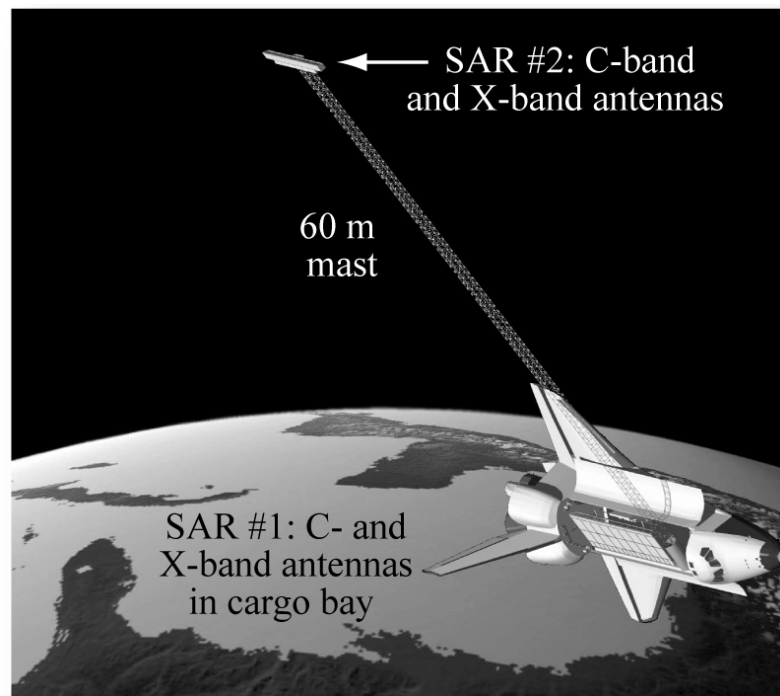
Figure 2.11. SRTM antennas and mast (Jensen, 2007).

The SIR-C/X-SAR antenna is a phased array antenna consisting of three planar array antennas (C-band 5.8-cm wavelength, L-band 23.5-cm wavelength, X-band 3.1-cm wavelength) on a nominally sized twelve-meter by four-meter structure (Figure 2.12) (NASA JPL, 2009c). The C-band and L-band antennas transmitted and received horizontally and vertically polarized waves on two separate channels allowing for quad-polarization. The X-band antenna transmitted horizontally polarized waves and received horizontally polarized waves. The space shuttle orbited at an elevation of 225 km, with an incidence angle from nadir ranging from 17 to 63 degrees, allowing for 15 to 90 km swath widths for C-band, and 15 to 40 km swath widths for the X-band data. The ground resolution is approximately a 30 meter by 30 meter pixel.
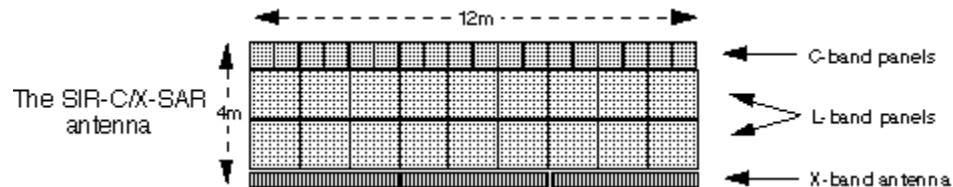
Figure 2.12. SIR-C/X-SAR antenna structure (NASA JPL, 2009c).

Unlike the antennas discussed previously which unfolded after deployment, the SIR-C/X-SAR antenna did not have to unfold as it was housed in the space shuttle cargo bay behind the cargo bay doors during launch. While orbiting, the cargo bay doors were opened, allowing the SIR-C/X-SAR radar to image the earth. The SRTM 60-meter mast and outboard C-band and X-band antennas were deployed in a fashion similar to the deployment of the satellite antennas discussed previously (ERS-1, ERS-2, ENVISAT, RADARSAT-1, and RADARSAT-2). The major differences between the satellite deployments and the SRTM deployment were that the SRTM deployment was controlled by the space shuttle crew, the SRTM mast is the largest structure ever flown in space, and the SRTM mast was retracted for travel back to Earth (NASA JPL, 2009d).

SRTM data was used in this study for the development of digital elevation maps (DEM). Topographic phase is estimated using digital elevation maps, and that phase is subtracted from the interferogram in order to determine the component of phase corresponding to deformation. SRTM data are available through the Earth Explorer System of the United States Geological Survey (USGS).

2.5.6   Other SAR Platforms

Sea Satellite (SeaSAT), the first SAR used for earth observation (as the name indicates, the platform was designed for observation of the sea), was launched by the National Aeronautics and Space Administration (NASA) from Vandenberg Air Force Base in California, on June 26, 1978 using an Atlas launch vehicle. The satellite platform was used only for data collection and dissemination from the 1.275 GHz (L-band), linear horizontal polarization, 2.16 meter by 10.7 meter corporate feed antenna active microwave SAR (Jensen, 2000). The platform was in a sun-synchronous orbit at a mean altitude of 791 kilometers and an inclination of 108 degrees for 105 days, before a short circuit drained all the satellite's power. This altitude and inclination allowed for 17-day repeat pass temporal resolution of individual locations using a 100 km swath width with 25 meter spatial resolution.

Shuttle Imaging Radar-A (SIR-A) was launched by the NASA from the Kennedy Space Center, on November 12, 1981 using the Space Transportation System (STS) 2 Space Shuttle Columbia. The space shuttle carried the SIR-A radar on a two and one-half (2.5) day manned mission. The radar is a 1.275 GHz (L-band), 6 MHz bandwidth, linear horizontal polarization, 1 KW, 2.16 meter by 9.35 meter rectangular planar array antenna active microwave SAR. The space shuttle orbited at an elevation of 254 km, with a 47

degree incidence angle from nadir ranging, allowing for a 54.6 km swath. The ground resolution is approximately 40 meters (Jensen, 2000; EO Sharing Earth Observation Resources, 2009a). No repeat pass data were collected because interferometry was not of interest to this mission.

Shuttle Imaging Radar-B (SIR-B) was launched by the National Aeronautics and Space Administration from the Kennedy Space Center in Florida, on October 5, 1984 using the Space Transportation System (STS) 41G Space Shuttle Columbia. The space shuttle carried the SIR-B radar on an eight (8) day manned mission. The radar is a 1.275 GHz (L-band), 12 MHz bandwidth, linear horizontal polarization, 1.12 KW, 2.16 meter by 10.7 meter rectangular planar array antenna active microwave SAR. The space shuttle orbited at multiple elevations of 225, 272, 352 km, with an incidence angle from nadir ranging from 15 to 60 degrees, allowing for swath widths ranging from 20 to 55 km. The ground resolution ranged from approximately 17 to 58 meters (Jensen, 2000; Sharing Earth Observation Resources, 2009b). No repeat pass data were collected because interferometry was not of interest to this mission.

As discussed previously, the SIR-C/X-SAR radar was flown by the space shuttle for three different missions (STS-59 April 9-20, 1994, STS-68 September 30-October 11, 1994, and STS-99 (SRTM) February 11-22, 2000). During the first mission, commonly referred to as Shuttle Radar Laboratory-1 (SRL-1 on STS-59), interferometry was not of interest. However, for the second (SRL-2 on STS-68) and third (SRTM on STS-99) missions, repeat passes were collected. According to NASA JPL (2009e), "A few interferometric pairs were collected by repeating the same orbit in the April SRL1 and

October SRL2 flights, all the other pairs were collected during days 7 through 10 of SRL2."

Japanese Earth Resource Satellite 1 (JERS-1) was launched by the National Space Development Agency (NASDA) of Japan from Tanegashima Space Center, located South of Kagoshima Prefecture, on February 11, 1992 onboard an H-I launch vehicle. The satellite platform was used only for data collection and dissemination from the 1.275 GHz (L-band), linear horizontal polarization, 1.3 kW, 2.4 meter by 11.9 meter rectangular planar array antenna (divided into an 8 panel arrangement) active microwave SAR and from the OPS optical sensor (Jensen, 2000). The platform was in a sun-synchronous orbit at a mean altitude of 568 kilometers and an inclination of 39 degrees until the platform's operation was terminated on October 12, 1998. This altitude and inclination allowed for 44-day repeat pass temporal resolution of individual locations using a 75 km swath width with 18 meter by 6 meter spatial resolution. (Japanese Aerospace Exploration Agency, 2009c). Antenna deployment problems occurred upon initial orbit of this platform. After two months, the antenna deployed properly and the satellite SAR performed the required mission lasting six and one-half years, much longer than the anticipated two year mission life.

Terra Synthetic Aperture Radar X (TerraSAR-X) was launched by the German Aerospace Agency from the Baikonur Cosmodrome in Kazakhstan, on June 15, 2007 onboard a Dnepr-1 launch vehicle. The satellite platform is used only for data collection and dissemination from the 9.6 GHz (X-band), linear horizontal or vertical or dual polarization, 2.3 kW, 0.7 meter by 4.8 meter rectangular phased array antenna (divided into a 3 leaf arrangement) active microwave SAR (Suess et al., 2009). The platform is in

a sun-synchronous orbit at a mean altitude of 514 kilometers and with an inclination of 97.44 degrees. This altitude and inclination allow for 11-day repeat pass temporal resolution of individual locations using a 20 to 55 degree incidence angle from nadir, producing a 10 to 100 km swath width with 1 meter to 16 meter spatial resolution (Hatfield Consultants, 2009).

The constellation of SARs named Synthetic Aperture Radar Lupe 1-5 ("Lupe" is German for magnifying glass) were launched by the German Aerospace Agency from the Plesetsk Cosmodrome in Arkhangelsk Oblast, Russia on December 19, 2006, July 2, 2007, November 1, 2007, March 27, 2008, and July 22, 2008 using the Cosmos-3M launch vehicle. The radars are able to obtain 5.5 by 5.5 km square scenes with a spatial resolution of 0.5 meters or a 60 km by 8 meter swath with 1.0 meter spatial resolution (COSMO-SkyMed, 2009).

Satellites 1, 2, and 3 of the constellation of small satellites for the Mediterranean Basin observation (COSMO-SkyMed) were launched by the Italian Space Agency from Vandenberg Air Force Base in California on June 8, 2007, December 9, 2007, and October 25, 2008, using the Delta 2 launch vehicle. The satellite platforms are used only for data collection and dissemination from the 9.6 GHz (X-band), linear horizontal or vertical or dual polarization, 3.6 kW, 1.4 meter by 5.7 meter rectangular planar array antenna active microwave SAR (Earth Observation Satellites and Sensors for Risk Management, 2009). The platform is in a sun-synchronous orbit at a mean altitude of 620 kilometers and with an inclination of 97.86 degrees. This altitude and inclination allow for 16-day repeat pass, 1-day tandem pass, temporal resolution of individual locations

using a 25 to 50 degree incidence angle from nadir, producing a 10 to 620 km swath width with 1 meter to 100 meter spatial resolution (COSMO-SkyMed, 2009).

A summary of all of the satellites discussed in this section (Section 2.5) is presented in Table 2.5. Satellite data currently being used by the University of Missouri were collected from the ERS-1, ERS-2, ENVISAT, RADARSAT-1, RADARSAT-2, SRTM, and PALSAR. Analyses on data collected from the ERS-1, ERS-2 and ENVISAT satellites are presented in Chapter 6 of this dissertation.

Table 2.5. List of commercially available radar satellites and their attributes.

Name	SAR Polarization	Altitude [km]	Band	Date Launched	Temporal Resolution [days]
ERS-1	VV	782	C	07/17/1991	35
ERS-2	VV	782	C	04/21/1995	35
ENVISAT	VV/HH	785	C	03/01/2002	35
RADARSAT-1	HH	798	C	11/04/1995	24
RADARSAT-2	Quad-Pol	798	C	12/14/2007	24
SRTM	Quad-Pol (C) VV (X)	223	C/X	02/11/2000	0
Sea-SAT	HH	791	L	06/26/1978	17/3
SAR-LUPE 1	Unknown	500	X	12/19/2006	Unknown
SAR-LUPE 2	Unknown	500	X	07/02/2007	Unknown
SAR-LUPE 3	Unknown	500	X	11/01/2007	Unknown
SAR-LUPE 4	Unknown	500	X	03/27/2008	Unknown
SAR-LUPE 5	Unknown	500	X	07/22/2008	Unknown
TERRASAR-X	VV/HH	514	X	06/15/2007	11
JERS-1	HH	570	L	02/11/1992	44
COSMO-SkyMed-1	HH,HV,VH,VV	619	X	06/08/2007	16 (1)
COSMO-SkyMed-2	HH,HV,VH,VV	619	X	12/09/2007	16 (1)
COSMO-SkyMed-3	HH,HV,VH,VV	619	X	10/25/2008	16 (1)
SIR-A	HH	222	L	11/12/1981	-
SIR-B	HH	352/272/225	L	10/05/1984	-
SIR-C/X-SAR	Quad-Pol (L,C)	215	L/C/X	04/09/1994	-
	VV (X)	215	L/C/X	09/30/1994	7-10, 174
ALOS PALSAR	VV/HH	692	L	01/24/2006	46

2.6   *Summary*

Researchers at the University of Missouri are currently using data from seven of twenty-one commercial satellite-based synthetic aperture radar (SAR) satellite platforms. All twenty-one platforms were introduced, along with basic properties about each platform. Of the seven platforms (ERS-1, ERS-2, RADARSAT-1, RADARSAT-2, ENVISAT, ALOS PALSAR and SRTM), data obtained from ERS-1 and ERS-2 were used in the investigation of subsidence above the Los Angeles Redline Subway System, and data obtained from ENVISAT were used in the investigation of the subsidence of Mosul Dam.

The principles of viewing geometry, baseline, and wavelength were introduced in relation to satellite based SAR. Satellite based SAR provides the ability to acquire images through all weather conditions, day and night, using a standard repeat pass. Using the images obtained from satellite based SAR, interferometric phase calculations are conducted which provide information about topography (single-pass interferometry) or deformation and topography (repeat-pass interferometry).

Satellite based SAR interferometry has been commonly used since the 1970's for Earth resource applications. Recently (2006-present) SAR interferometry has been used in geotechnical applications such as subsidence above tunneling, movement of dams, and landslide monitoring. With new high resolution satellite based SARs, more geotechnical engineering applications of InSAR will develop.

Chapter 3: Overview of Sites

3.1   Introduction

Two sites were chosen for this study. The sites are the Los Angeles Metro Red Line subway tunnel located in Los Angeles California, and Mosul Dam, located outside the city of Mosul, Iraq. These sites both contain spatially localized features and are known for historically measured and documented ground movements. The Los Angeles County Metropolitan Transit Authority (LACMTA) Red Line, hereinafter referred to as the LA Red Line, is an underground subway system not directly visible to satellites, while Mosul Dam is an above ground site directly visible to satellites. This chapter discusses both sites (LA Red Line and Mosul Dam) and documents the movements of each as reported in the "open" literature.

3.2   Los Angeles Metropolitan Transit Authority Red Line

The LA Red Line is a 17.4 mile portion of the Los Angeles County Metropolitan Transit Authority heavy rail system (Figure 3.1). It is comprised of three minimal operating segments (MOS shown in Figure 3.2), MOS-1, MOS-2a and MOS-2b, and MOS-3, which opened in January 1993, June 1996, June 1999, and June 2000, respectively (FTA, 2009). MOS-1 consists of 4.4 miles of heavy rail and five stations (Union Station, Civic Center, Pershing Square, 7th Street/Metro Center and Wilshire/McArthur Park). MOS-2a consists of 2.1 miles of heavy rail and three stations (Wilshire/Vermont, Wilshire/Normandie, and Wilshire/Western). MOS-2b consists of 4.6 miles of heavy rail and five stations (Vermont/Beverly, Vermont/Santa Monica, Vermont/Sunset, Hollywood/Western, and Hollywood/Highland). MOS-3 consists of 6.3

miles of heavy rail and three stations (Hollywood/Vine, Universal City, and North

Hollywood).

Figure 3.1. Aerial image (Google Earth) of LA Red Line site with the LA Red Line Subway path delineated in red (modified from Manjunath, 2008).
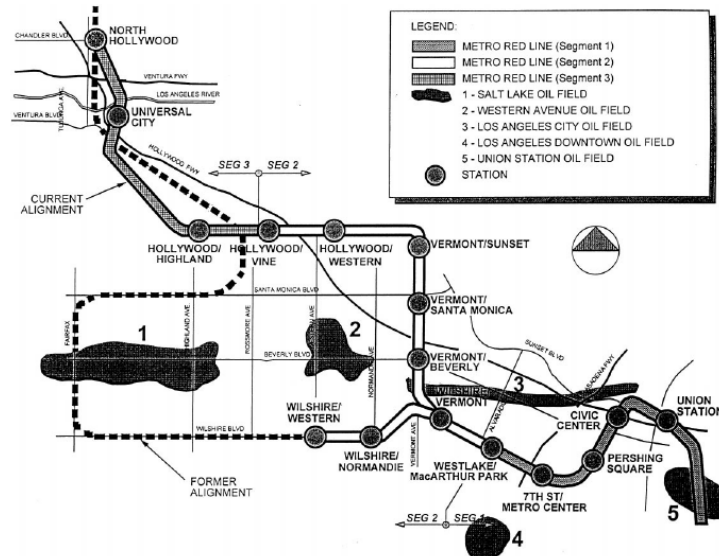
Figure 3.2. Minimal operating segments (MOS) of the LA Red Line Subway system (Stirbys et al., 1999).

MOS-1 construction began at Union Station and finished at Westlake/McArthur Park station. MOS-2a construction began at the previously constructed MOS-1 Westlake/McArthur station and finished at the Wilshire/Western station. MOS-2b was constructed in two directions, with construction for both directions beginning at the project's central entry point adjacent to Barnsdall Park in Hollywood and finishing at the Hollywood/Vine station (in the east/west direction), and at the previously constructed MOS-2a Wilshire/Vermont station (in the north/south direction) (MTA, June 1995). MOS-3 was constructed from three directions and two access points. Construction began at the previously constructed Hollywood/Vine station and went west toward the Universal City station, past the Hollywood/Highland station, ending at the southern base of the Santa Monica Mountains. Construction also started at the Universal City station and bored south 2.4 miles under the Santa Monica Mountains to tie in with the MOS-3 line previously constructed (Hollywood/Vine to southern base of Santa Monica Mountains), and also went from the Universal City station north to the North Hollywood station (Middleton, 2002).

The construction sequence for the LA Red Line is displayed in Figure 3.3 along with sources listing construction dates. Construction began on MOS-1 in 1986; however, contaminated soils (see Figure 3.2) forced realignment and delays so that actual construction of tunnels on this segment began in 1987 (LA Times, June 18, 2000). MOS-2a construction started in 1992 (LA Times, June 18, 2000). Construction of MOS-2b began in 1993; however, problems associated with water leakage with the MOS-2a section caused suspension of construction until the MOS-2b tunneling began in May of 1993 (LA Times, June 18, 2000). Construction of the MOS-2a tunnels extending south

along Vermont Avenue from the central entry point (Barnsdall Park) to the Wilshire/Vermont station finished in May 1994 (MTA, June 1995).
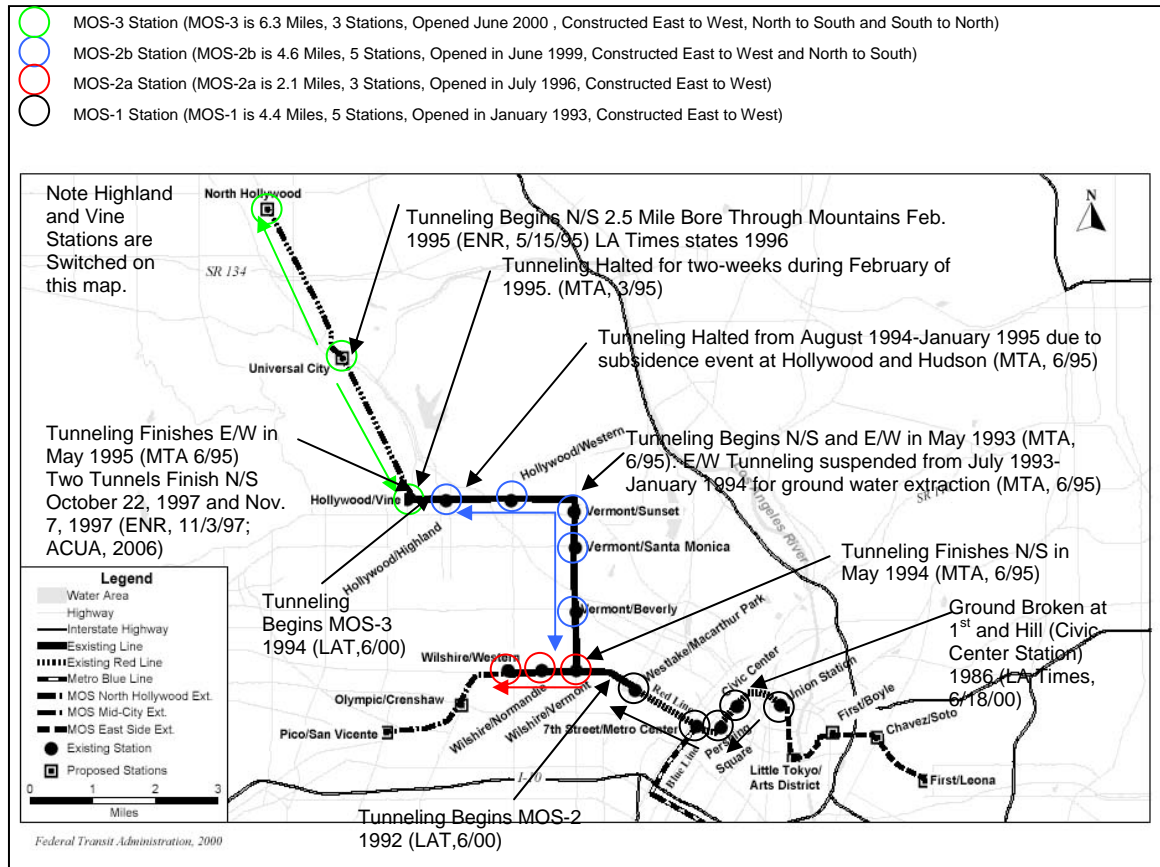
Figure 3.3. LA Red Line tunnel construction sequence (modified From Federal Transit Administration, 2009).

Construction of the MOS-2a tunnels extending from the central entry point (Barnsdall Park) to the west along Hollywood Boulevard finished in May 1995. The construction of MOS-3 began in Universal City, north of the Santa Monica Mountains in 1994; however, problems associated with settlement during the first 80-feet of tunneling near Universal City caused delays until the MOS-3 tunneling began in February of 1995 (ENR, May 15, 1995). The MOS-3 tunneling between Hollywood and Vine and the southern side of the Santa Monica Mountains finished on May 24, 1995 (MTA, June 1995). Construction of the first twin 2.5-mile-long tunnels began in North Hollywood on

February 13, 1995 (ENR, May 15, 1995).   On October 22, 1997 the first of the two 2.5-mile long, 22-foot 8-inch diameter tunnels holed through the Santa Monica Mountains (ENR, Nov. 3, 1997). The second of the 2.5-mile long, 22-foot 8-inch diameter tunnels finished drilling through the mountains on November 7, 1997 (AUCA, 2009).

This study focuses on the MOS-2b tunnels extending south and west from the central entry point near the intersection of Hollywood Boulevard and Vermont Avenue. This portion of the LA Red Line (MOS-2b) was selected because of the available imagery over the duration of construction, knowledge of construction problems associated with this portion of the LA Red Line, and the geology through which this portion of the LA Red Line was constructed (discussed later in this chapter). Construction problems are associated with all MOS segments of the LA Red Line as shown in Figure 3.4 and summarized in Table 3.1, Table 3.2, and Table 3.3. The most applicable problems to this study are the August 20, 1994, 10-inch subsidence event at Hollywood and Hudson and the July 22, 1995, 70-foot sinkhole located between Berendo and Edgemont along Hollywood Blvd.
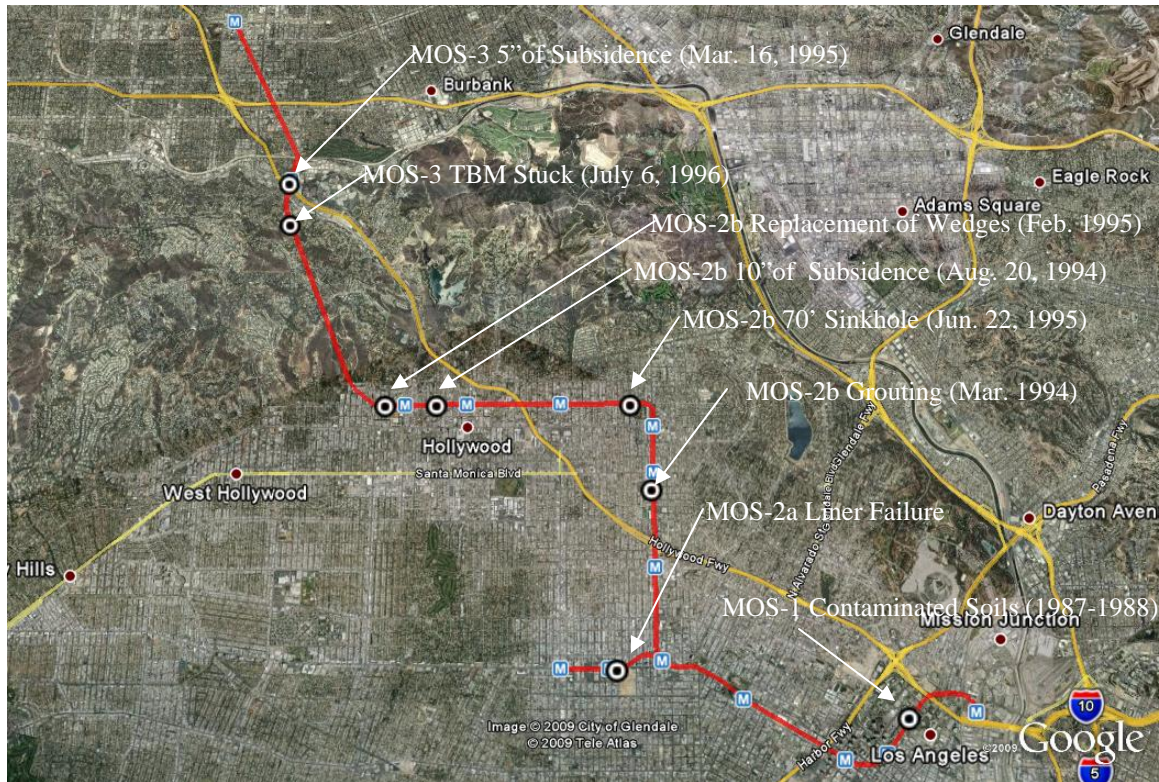
Figure 3.4. Aerial image (Google) with locations of construction problems associated with the LA Red Line.

Table 3.1. Summary of construction problems associated with MOS 1 and MOS 2-a LA Red Line.

MOS Number	Description of Problem	Source
	Tunnel liner built thinner than specified due to tunnel misalignment.	Waxman (2009)
	HDPE liner to prevent gas migration contains numerous holes.	Waxman (2009)
MOS 1	Work delayed for almost six months in 1987 because of contaminated groundwater and land acquisition delays.	LA Times (June 18, 2000)
	In 1988, realignment needed because of contaminated soil at Union Station which forces delays to construction.	LA Times (June 18, 2000)
	In 1990 timber lagging caught fire, causing a portion of the tunnel to collapse.	Middleton (2002)
MOS 2-a	"Water leakage caused millions of dollars in damage to the subway because a costly protective liner was poorly designed, installed, and inspected"	LA Times (June 18, 2000)

46

Table 3.2. Summary of construction problems for MOS 2-b LA Red Line.

Event	Location	Description	Source
Groundwater Extraction	Hollywood and Edgemont	Six month suspension in East/West Hollywood Blvd. tunneling for groundwater extraction from July 1993-January 1994	MTA (June, 1995)
		Rising groundwater caused August 199410-inch subsidence event.	LA Business Journal (2009)
		Tunnel construction caused street and surrounding buildings to settle as much as 10 inches.	Office of Inspector General (2009)
		Ten inches of subsidence shown west of Hudson in subsidence profile.	cottonshires.com (2009)
		August of 1994, 5 to 6 inches of subsidence with maximum of 10 inches in 6500 block of Hollywood Blvd.	Bell (2009)
Subsidence Event	Hollywood and Hudson	August 20, 1994 MTA reported nine inches of subsidence along a nine-block area of Hollywood Boulevard.	Waxman (2009)
		August 1994, water-saturated earth at Hollywood and Hudson caused subsidence 280 feet north of the tunnel.	MTA (June 1995)
		Tunneling at Hollywood and Hudson caused total loss of building (MTA believes damage is caused by 1994 Northridge earthquake).	Rackham (Dec. 12, 1994)
		Subway construction on August 20, 1994 caused Hillview Building at 6533 Hollywood Blvd. to suddenly drop 9 inches.	Pool (March 10, 2000)
		During initial construction in May 1993, the water table was lowered, however, during realignment work in June, 1995 the groundwater table was 20 feet higher than during initial construction.	LA Business Journal (2009)
		In 1995, 70-foot sinkhole formed during correction of tunnel misalignment.	Office of Inspector General (2009)
Sinkhole Event	Hollywood between Berendo and Edgemont	June 22, 1995, 80-foot-wide sinkhole within the 6300 block of Hollywood Blvd [Note: wrong location but right time].	Bell (2009)
		June 22, 1995, re-mining of 80-foot section of tunnel caused 70-square foot sinkhole after removing previously placed liner.	MTA (July 1995)
		"70-foot wide sinkhole opens on Hollywood Blvd. sending 20 workers scrambling for their lives."	LA Times (June 18, 2000)
Wooden Strut Replacement	Hollywood Blvd.	February 1995, two week delay in construction to replace wooden struts with steel struts.	MTA (March 1995)
Grouting along Vermont	Vermont Ave.	March 1994, contact grouting required along Vermont section, after 1/3 of the tunnel was constructed without grout.	Waxman (2009)

Table 3.3. Summary of construction problems associated with MOS 3 LA Red Line.

	Initial Tunneling	ENR (May 15, 1995)
	MTA suspended tunneling on March 16, 1995 due to 5.5 inches of subsidence after advancing only 200 feet from start of construction.	
MOS 3	**Bore through Mountains**	Middleton (2002)
	Work was stopped for six weeks on July 6, 1996, after the tunnel boring machine was stuck following the Fourth of July weekend break.	

The two main problems for MOS-2b presented in Table 3.2 are the subsidence event and the sinkhole event. Most sources attribute both of these construction problems to groundwater. However, some of the sources have suggested the 1994 Northridge earthquake caused the 10-inch deformation at Hollywood and Hudson. Other possible causes for the MOS-2b ground movement are soil densification caused by tunneling operations, stress reduction caused by tunnel boring, and crushing of wood wedges placed between the tunnel wall and liner (Cotton and Shires, 2009). Cotton, Shires, and Associates (2009) conducted a post-subsidence investigation which included collecting and testing soil samples, installing and monitoring inclinometers, extensometers, and piezometers, and floor level surveying. The conclusions drawn from the investigation and these analyses indicate that hydro-densifiable soils consolidated during construction (caused by construction equipment vibrations) developing the settlement profile shown in (Figure 3.5). Note the 10 inches of settlement located west of Hudson Street.
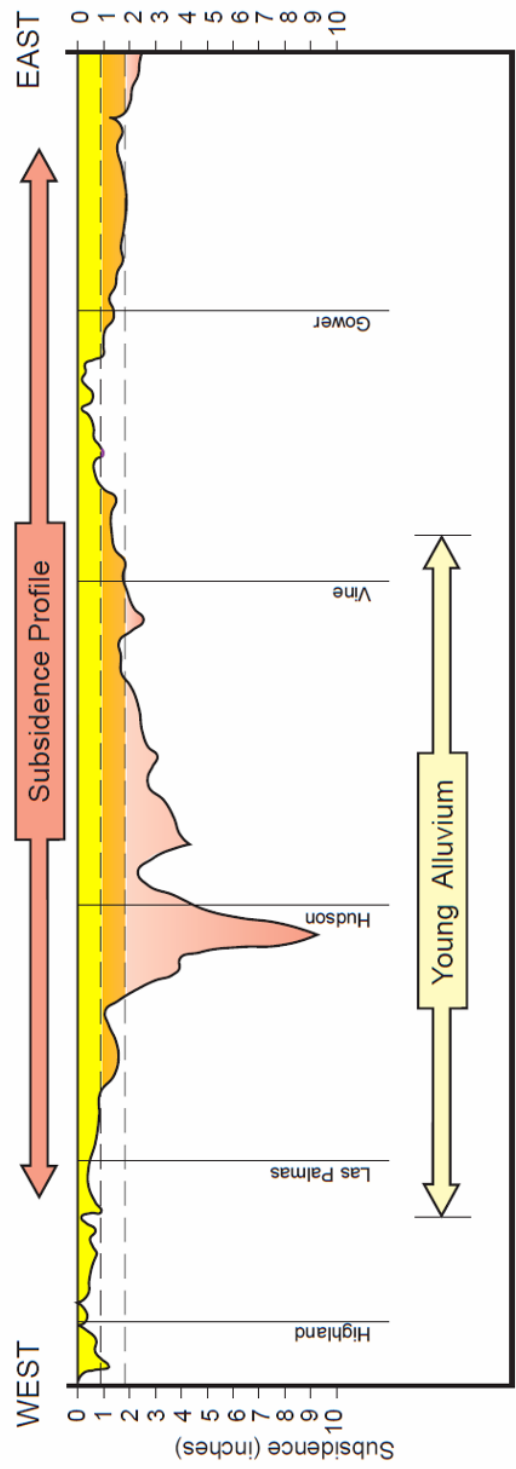
Figure 3.5. Subsidence profile along the MOS-2b Hollywood Boulevard section (Cotton and Shires, 2009).

A geological cross-section is presented in Figure 3.6. The tunnel profile goes through Upper Miocene to Plio-Pleistocene sandstone, siltstone, and claystone bedrock, and through alluvial deposits (old alluvium, young alluvium, and fill) ranging in age from the Pleistocene to Holocene (Manjunath, 2008). The section in which the Hollywood and Hudson subsidence event occurred is within the young alluvium (hydrodensifiable according to Cotton and Shires, 2009). The groundwater table varies significantly along the profile and is very high at the location of the sinkhole event between Berendo and Edgemont along Hollywood Boulevard, and very low in the location of the subsidence event at Hollywood and Hudson. As previously noted, the water table was drawn down near the central access point along Hollywood Boulevard during initial construction of the MOS-2b LA Red Line in 1993, however, during remining to correct the alignment in 1995, the water table was 20 feet higher than during the initial construction. Although the water table is low at the location of the Hollywood and Hudson subsidence event, Cotton and Shires indicated the soil had access to water. The section of the LA Red Line running north and south along Vermont Avenue appears to be constructed almost entirely in rock. The section of the LA Red Line running east and west along Hollywood Boulevard appears to be constructed in the young and old alluvium. Thus, tunneling boring machines proceeding east/west faced very different soil/rock conditions than tunnel boring machines proceeding north/south.
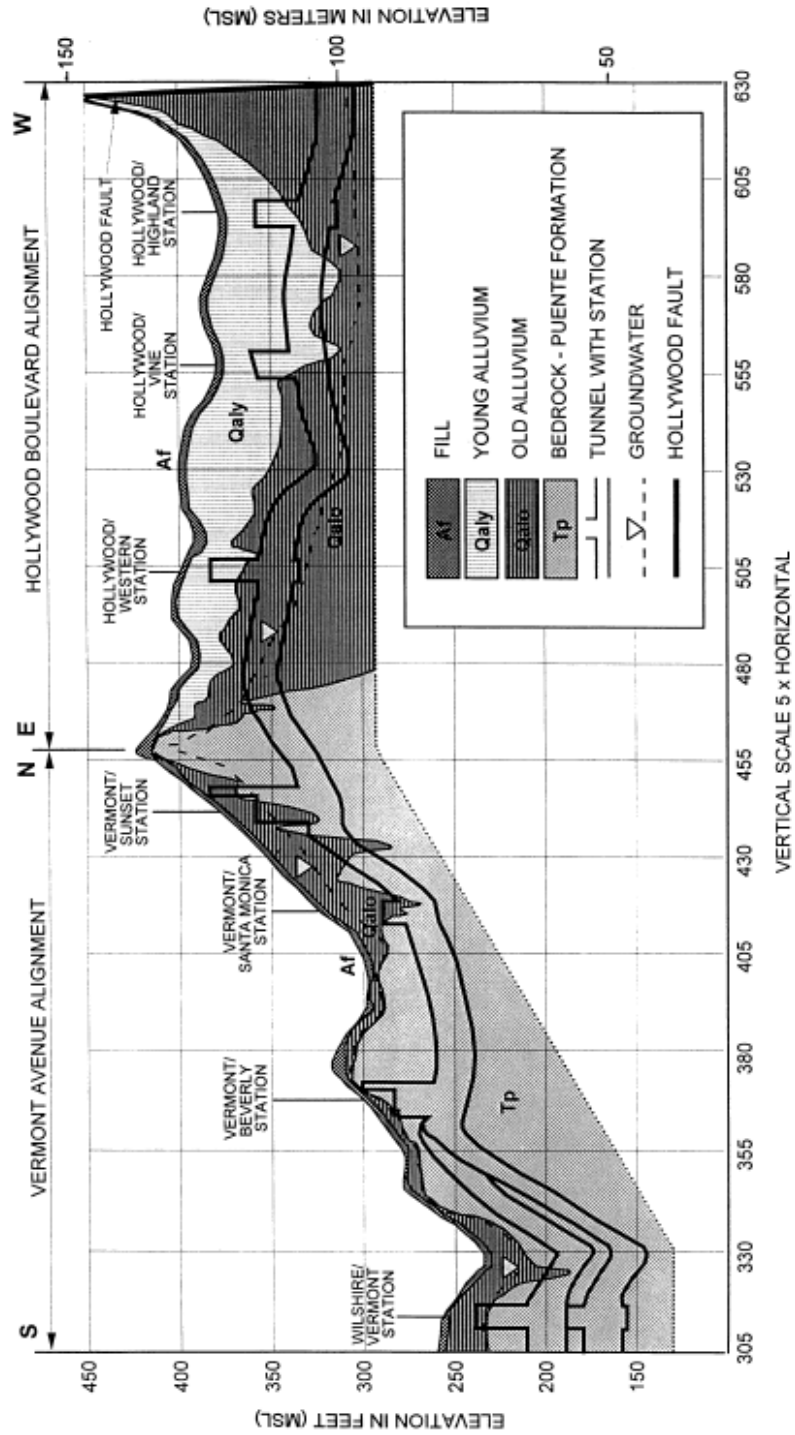
Figure 3.6. Geologic cross-section along MOS-2 of LA Redline (Stirbys et al., 1999).

3.3   Mosul Dam

Mosul Dam (Figure 3.7), located 45 km northwest of the city of Mosul, Iraq on the Tigris River, is the largest dam in Iraq and fourth largest dam in the Middle East by reservoir capacity (BBC Website, 2009a). The dam (Figure 3.8) is a 113-meter high by 2,100-meter long (3,400 meters including the main and emergency spillways) earth-fill structure holding back 12 billion cubic meters of water and is used for irrigation and power generation purposes. Power is generated using four 200 MW turbines. The dam has been reported to be producing less than full power capacity, varying somewhere between 320 MW (Daly, 2009) and 630 MW (Wright, 2003).
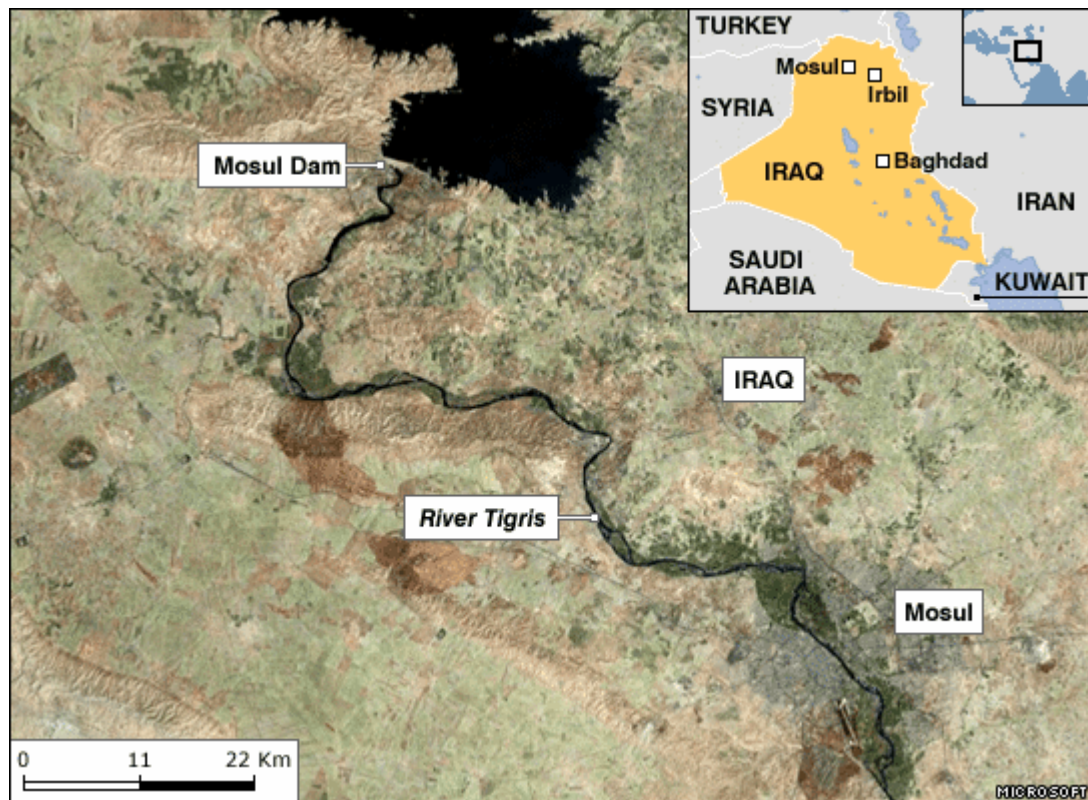
Figure 3.7. Annotated aerial image of the Mosul Dam study area (from BBC, 2009b).

52

Figure 3.8. Aerial image of Mosul Dam (from BBC, 2009c).

The four turbines are located on the downstream side of an inlet structure (Figure 3.9) that consists of risers leading to four tunnels located under the dam. The tunnels transfer the water from the top of the lake to the generator turbines. Two diversion tunnels are located under the dam and collect water through the diversion structure. The diversion tunnels, main spillway, and emergency spillway are used to draw down the reservoir level and to control the water balance of the reservoir (Figure 3.8 and Figure 3.9).
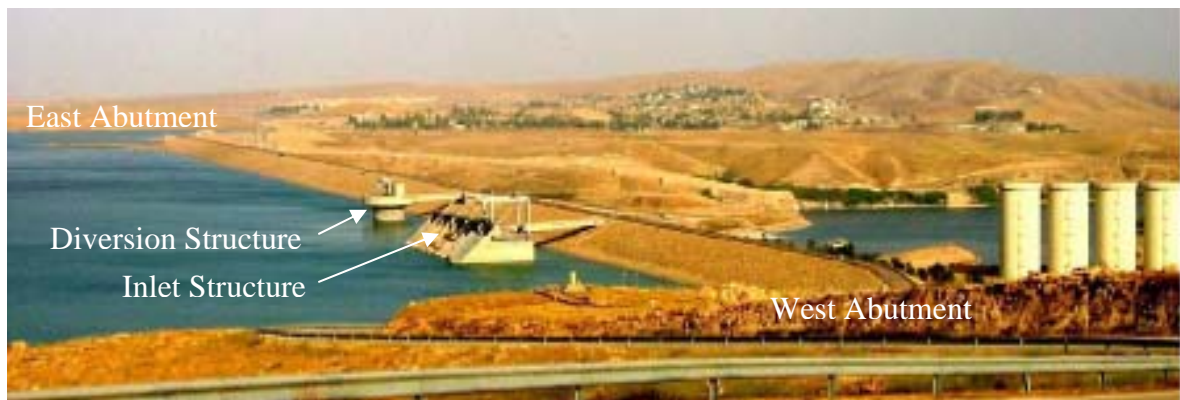
Figure 3.9. Oblique photo of Mosul Dam study area (from Theriot, 2009).

The dissolution of the highly soluble bedrock upon which Mosul Dam is constructed has caused historic subsidence of the dam and will continue to cause subsidence of the dam. During an on-site study of the dam, consultants from Washington Group International and Black and Veatch concluded, "the decision to locate such a major and important dam on the foundation rock mass which exists at the Mosul dam site was fundamentally flawed" (Water Power and Dam Construction, 2008). According to Kelley et al. (2007), "The dam was constructed on alternating highly variable units of gypsum, anhydrite, marl, and limestone, each of which is soluble in water under the environmental and hydrogeologic conditions of the dam." A horizontal geologic section showing the foundation material just below the grouting gallery of the dam is presented in Figure 3.10. The horizontal geologic section displays the complexity of the geology, due to dipping layers at different locations within the cross-section (Wakeley et al., 2007).

The seeping of reservoir water into the soluble foundation material causes the foundation material to dissolve, leading to larger open spaces. Larger open spaces lead to larger quantities of water seeping into the foundation material, leading to more dissolution. At Mosul Dam, dissolution began prior to construction, and although noticed during construction (Figure 3.11), the preventative measures (blanket grouting to 25 meters and the construction of a central deep grout curtain beneath the main dam and spillway to 150 meters) failed to reduce or prevent further dissolution. Therefore, upon dam completion and filling, safety issues led to the need for continuous grouting operations that continue to this day to control under-seepage and dissolution to maintain the integrity of the dam.
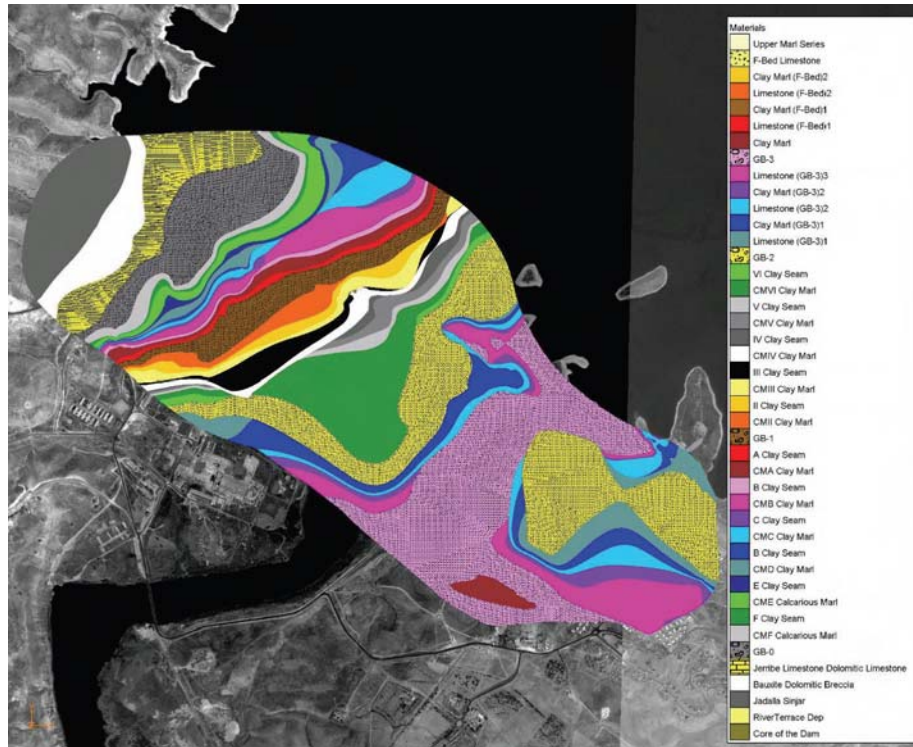
Figure 3.10. Horizontal geologic section of foundation material (at elevation 227 meters above sea level just below the grouting gallery) (from Wakeley et al., 2007).
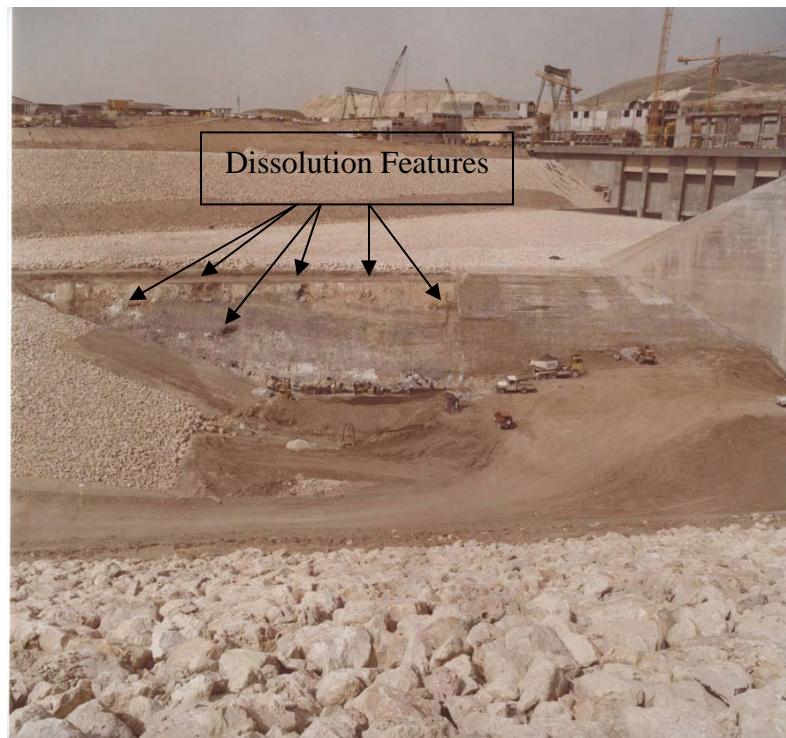
Figure 3.11. Photograph of Mosul Dam during construction (1982-1983) showing dissolution features prior to dam construction (Kelley et al., 2007).

Varying sources (Paley, 2007; Kelley, 2007; Wright, 2009) list the "grout take,"

or quantity of grout injected in a given amount of time, from continuous grouting

operations conducted from within the gallery of the dam. The locations of high grout

take alert engineers to problematic locations within the foundation material underneath of

the dam. These problematic locations are areas where suspected subsidence has occurred

in the past and will occur in the future. Paley (2007) lists the grout take as approximately

50,000 tons of material being grouted into the dam using 24 machines pumping grout 24

hours per day, six days per week since the dam opened in 1986. Wright (2009) states that

50 metric tons of grout per day, with as much as 250,000 tons of grout per day during

emergency sinkhole filling are required. According to Wright (2009), "mounted lines on

the gallery walls deliver bentonite, cement, water and air to make grout portable for

drilling machines." Wright (2009) also states that the, "grout injection wells are evenly

spaced approximately 10-20 m apart." Whereas grout is continuously pumped into the

dam, grout take records were not kept from 1986-2002. Grout take locations recorded

during normal grouting operations from 2002-2006 are reported in Kelley (2007), and

provide information about locations that required more grout. New automatic grout-

injection equipment and grouting techniques (Intelligrout) have been purchased by the

United States government for the Ministry of Water Resources to continuously grout and

monitor the dam. Although the equipment was purchased, the Special Inspector General

for Iraq Reconstruction (SIGIR) determined that the new equipment has not yet been

installed and has not yet improved the basic grouting capability at the dam (Reuters,

2007). This grout equipment may provide the ability to inject grout at the same rate of

dissolution, preventing further subsidence of the dam.

Following construction of the dam, water pressure tests were conducted to determine the amount of dissolution within the foundation material. Results from these tests were combined to determine the locations of highest dissolution. Kelley et al. (2007) combined knowledge of the regional and local geology with construction records, piezometric records, water pressure tests records, and grout take records to develop a geologic cross-section displaying locations of greatest dissolution. The areas of greatest dissolution in the foundation material correspond to the location of the historic river channel (Figure 3.12).
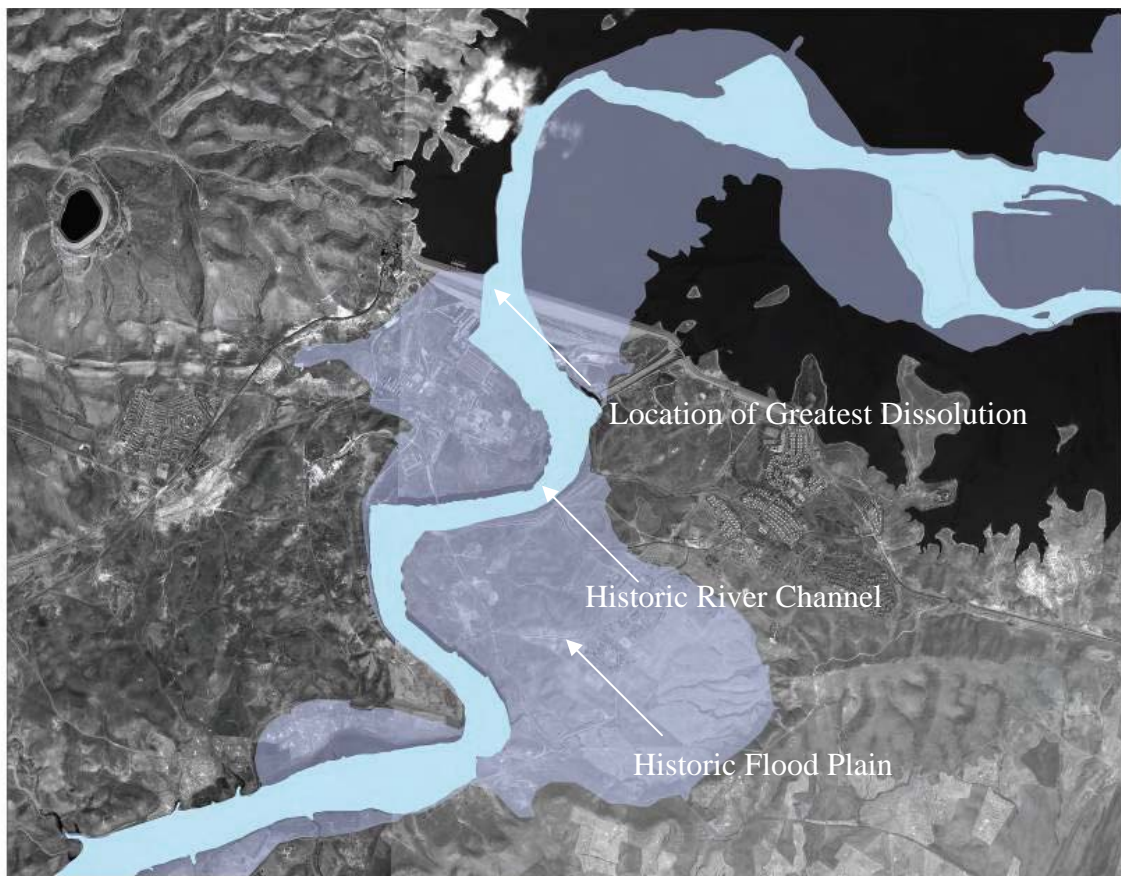
Figure 3.12. Aerial photo mosaic of Mosul Dam with pre-dam Tigris River channel overlay (from Kelley et al., 2007).

As shown in Figure 3.13, the location of the historic river channel within the foundation material corresponds to the length of the dam from stations 3+080 meters to

3+290 meters. This area was also the location of high dissolution as determined from water pressure tests performed following completion of the dam. During 2002-2006, this area of the foundation, identified as grout sections 78 to 93 in Figure 3.13, also required large quantities of grout where dissolution caused voids in the foundation material. Whereas other regions of the dam foundation are also shown as having historic dissolution from the water pressure tests following completion of the dam, the location of the historic river channel is the only location in which both large grout quantities and historic dissolution have occurred. According to Kelley et al. (2007) "the pattern of recent grouting activity indicates that Section 79 is in an advanced state of dissolution, and the front extends possibly as far as to the east as Section 69." The Eastern edges of grouting Sections 79 and 69 correspond to Stations 2+800 and 2+435, respectively, as displayed in Figure 3.13. These locations are approximately 600 and 965 meters from the diversion tunnels located at Station 3+400.

The information obtained from the grout take and water pressure tests is of importance because this information alerts the geotechnical engineers to where problems are located within the dam. Based on the data provided by the water pressure tests and grout take information, it is suggested that the area of concern and therefore areas of potential subsidence is located in between Station 3+400 and Station 2+435 along the dam's crest as displayed in Figure 3.13.
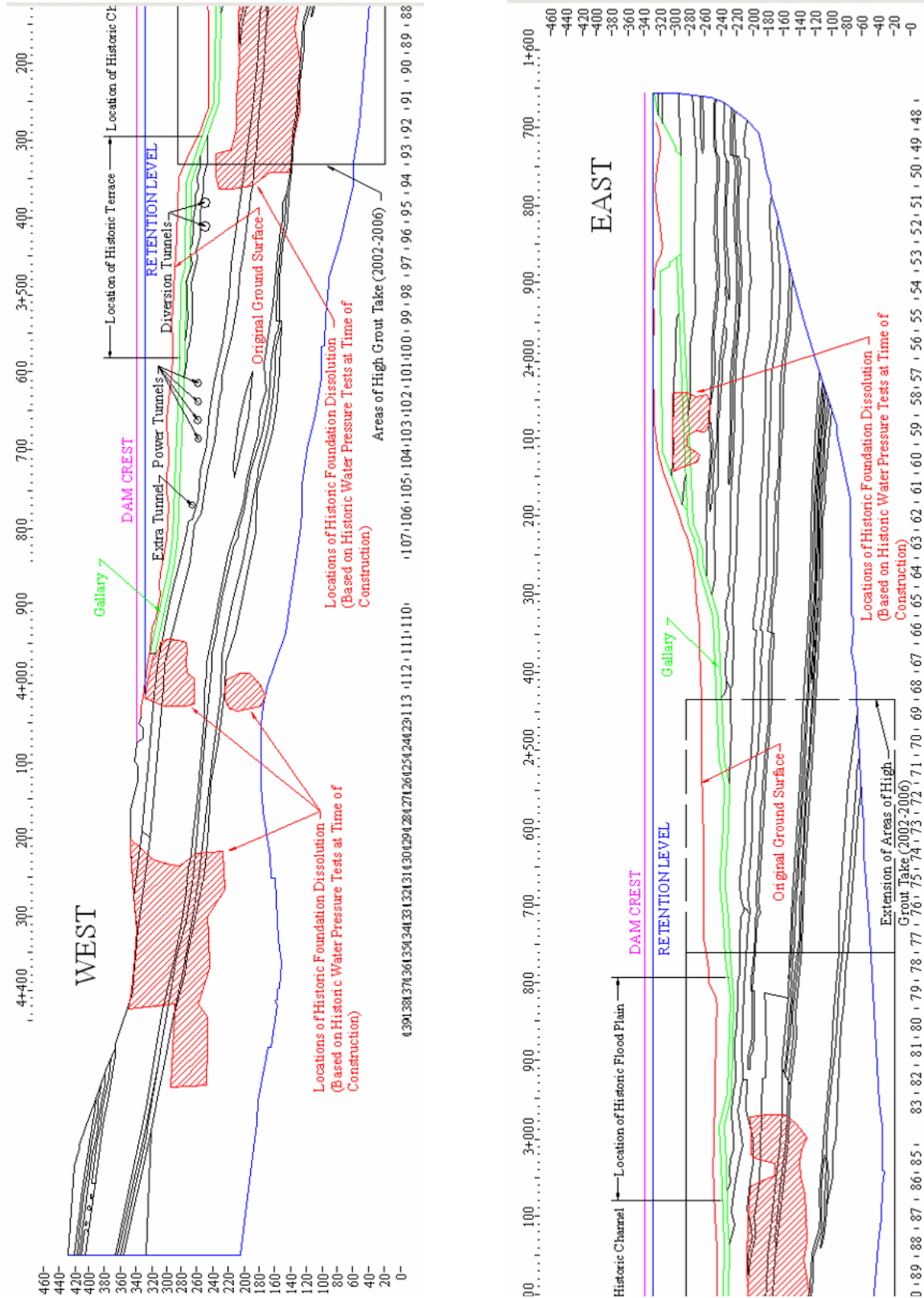
Figure 3.13. Geologic cross-Section of Mosul Dam showing locations of historic dissolution and areas of high grout take (Modified from Kelley, 2007).

3.4   Summary

The Los Angeles Metro Red Line (LA Red Line) and Mosul Dam were selected to be investigated in this study. Reported construction problems were associated with both of these spatially localized features. Brief overviews of each site were presented, consisting of the construction schedule, the geology of the site, and problems encountered during and after construction.

The LA Red Line subway tunnel was constructed in three sequential Minimal Operating Segments (MOS-1, MOS-2, and MOS-3), with MOS-2 consisting of two segments (MOS 2a and MOS 2b). The 4.4-mile long MOS-1 contains five stations beginning at Union Station and ending at Wilshire/McAurther Park station. The 2.1-mile long MOS-2a begins at Wilshire/McAurther Park station and ends at Wilshire/Western station and includes three stations.   The 4.6-mile long MOS-2b begins at Wilshire/Vermont station and ends at the Hollywood/Vine station and contains five stations. The 6.3-mile long MOS-3 begins at the Hollywood/Vine station and ends at the North Hollywood station and contains three stations.

Whereas construction problems occurred during construction of all Minimal Operating Segments (MOS), the construction problems associated with MOS-2b are highlighted here because imagery was collected during the time of construction, and because of the known subsidence events caused by poor tunnel construction techniques. These problems consist of a subsidence event which occurred on August 20, 1994 and a sinkhole event which occurred on July 22, 1995. The young alluvium and groundwater table may have contributed to these problems.

Mosul Dam is a 113-meter high, 2,100 meter long earth fill dam on the Tigris River, located 45 kilometers northwest of the city of Mosul, Iraq.   The dam was

constructed in the early 1980's for electrical generation and for irrigation. Prior to completion, dissolution of the foundation material was observed. To prevent this dissolution, extensive grouting operations have been conducted six days per week from initial filling of the reservoir behind the dam in 1986 to the present. The location of both the historic dissolution and current high quantities of "grout take" correspond to the historic river channel, located east of the diversion and power generation tunnels.

Chapter 4: Data Processing Techniques

4.1   *Introduction*

Interferometric Synthetic Aperture Radar (InSAR) processing for the work presented in this document was conducted using Gamma Remote Sensing software. In addition to Gamma Remote Sensing software, three other software programs were used to aid in processing. These software programs were MATLAB, ERMapper and DESC-W (Display Earth remote sensing Swath Coverage for Windows). Each of the four software programs used, and the computers on which they were used, is discussed in Section 4.2.

The processing flow used for this research is discussed in Section 4.3, while the five main processing techniques which follow this processing flow are discussed in Section 4.4. These InSAR processing approaches are referred to here as the: traditional processing technique, spatial processing technique, enhanced spatial processing technique, interferometric point target analysis (IPTA) processing technique, and multiple-baseline processing technique.

4.2   *Software and Computers Used in Study*

Multiple software programs were used for this study. The programs used include: DESC-W, The MathWorks MATLAB, GAMMA Remote Sensing Software, and ERDAS ERMapper. The use of these programs is broken down into three categories: pre-processing, processing and post-processing. DESC-W, MATLAB, and ERMapper were used for pre-processing, GAMMA Remote Sensing Software was used for processing, and ERMapper was used for post-processing.

Processing using these four software programs was conducted on two computers. One of the computers uses a Windows based operating system, while the other uses a Linux based operating system. DESC-W and ERMapper software were used on the computer using Windows, while MATLAB and GAMMA Remote Sensing Software were used on the computer using Linux.

4.2.1   Software

DESC-W (Display Earth Remote Sensing Swath Coverage for Windows) is a free program produced by the European Space Agency. It is available for download at http://earth.esa.int/descw/.   The program is used to determine the observations of a specific satellite. This program is used for ERS-1, ERS-2, LANDSAT-5, LANDSAT-7, JERS-1, TERRA/MODIS and, early ENVISAT images over a specific area (ESA, 2009). Output from the program is discussed in Section 4.3.1.1, and the commands for running the program are presented in Appendix A. The itab files (discussed in Section 4.4.4) used for the IPTA processing technique were generated using the information obtained from DESC-W.

ERDAS (Earth Resource Data Analysis System) ERMapper was used to modify the SRTM DEM data to create simulated SAR elevation images for both sites. The processing technique for developing a simulated SAR intensity image from a DEM is discussed in Section 4.3.1.2. ERMapper was also used in post-processing to present ortho-rectified images with scale bars and North arrows. The results obtained from ERMapper post-processing are presented in Chapter 6.

The MathWorks MATLAB (Matrix Laboratory) was used as a program development environment. Programs were developed in MATLAB to generate itab files

and histograms that are used for the enhanced spatial and multiple-baseline processing techniques to aid in processing large quantities of data (Gomez, 2009). These programs are discussed in Section 4.3, and the program code is presented in Appendix A.

For processing conducted with multiple-masters, MATLAB programs are utilized to develop the itab file based on: the RSLC_tab file (a list of the RSLC images created by the user in chronological order), the baselines between each RSLC image, and the maximum allowable baseline as selected by the user (Gomez, 2009). The MATLAB programs are bperp_plot.m, itab_bptime.m, and itab_hist.m. In addition to creating the itab files to be used during multiple-master processing, plots of how often images are used (discussed in Chapter 5) are generated using the MATLAB code. Plots displaying how images are paired to create interferograms are also generated using the MATLAB code. Examples of files created for different processing procedures (itab, RSLC_tab, DIFF_tab) are provided in Appendix A. Various arguments used in the prepared MATLAB programs are found in the MATLAB Users Manual.

For processing conducted with common-masters, the itab and RSLC_tab files are created by the user without the aid of automated processing through MATLAB. Note that there is one fewer interferogram generated than RSLC images used, as each image is paired with the one master image. Again, examples of files created for different processing procedures (itab, RSLC_tab, DIFF_tab) are provided in Appendix A.

GAMMA Remote Sensing Software contains multiple modules including:

- MSP (Modular SAR Processor),

- ISP (Interferometric SAR Processor),

- DIFF/GEO (Differential Interferometry/Geocoding),

- LAT (Land Application Tools),

- IPTA (Interferometric Point Target Analysis),

- DISP (Display Tools),

- and MOCOM (Motion Compensation).

For this study, only the MSP, ISP, DIFF/GEO, IPTA and DISP modules were used. Shell scripts were used to aid in the processing of large quantities of data (Gomez, 2009). These shell scripts are discussed in Sections 4.3.1, 4.4.4 and 4.4.5, and the code is presented in Appendix A.

4.2.2 *Computers*

Processing conducted using DESC-W and ERMapper was completed on a Dell Latitude D630 Laptop using an Intel Core2 Duo processor with a Windows XP operating system. Processing conducted using MATLAB and GAMMA Remote Sensing Software was completed using a Dell Precision 690 Workstation using an Intel Xeon processor with a Linux operating system.

4.3 *Processing Flow*

This section of the chapter focuses on the SAR data processing flow used for this research work. This section discusses the process of searching for available data, acquiring the archived data, uploading data to the server, and pre-processing, processing and post-processing of the data. The MATLAB and GAMMA remote sensing programs (shell scripts) discussed herein are presented in Appendix A (Gomez, 2009). The detailed ERMapper processing steps for development of a simulated SAR DEM are also presented in Appendix A. These scripts and processing steps allow for rapid processing of the SAR data.

4.3.1   Pre-Processing Flow

Data pre-processing consists of selecting and preparing radar (Section 4.3.1.1) and digital elevation model (Section 4.3.1.2) data by ingesting the data into the GAMMA Remote Sensing software program for focusing and resampling (Section 4.3.1.3).

4.3.1.1 Selection of Data

Processing conducted in the past has typically been conducted using data obtained from the European Space Agency (ESA) (ERS-1, ERS-2, and ENVISAT). The ease of finding archived data using DESC-W has contributed to the use of ESA data over other data (RADARSAT). The program is very easy to use and can be downloaded and updated from the ESA website (http://earth.esa.int/descw/). After opening the program, the user area definition icon is selected , the circle selection criteria is selected, and the coordinates of the location of interest are input. If the coordinates of the location of interest are known exactly, the search radius is set to 1 km, and if the coordinates are not known exactly, the search radius is set to 10 km. Following the selection of the area, the missions and filters icon is selected . Within the missions and filters window, ERS-1 is selected with both ascending and descending scenes selected and then added to the list. ERS-2 is also selected with both ascending and descending scenes selected and then added to the list. Finally, ENVISAT ASAR narrow swath is selected, with only Swath 2 ascending and descending scenes selected and then added to the list. Clicking on the scene selection icon will then display all of the tracks and frames which overlap the location of interest. When frames are selected in the list (on the left side of the program window), the image boundaries corresponding to that frame are highlighted in the graphical window of the program (on the right side of the program window). Tracks and

frames can be deleted by right clicking on the track or frame within the list. Typically, the track and frame with the most available images is selected. Double clicking on the track or frame in the list displays how many other scenes are contained within this track and frame, and also displays the lengths of the baselines the highlighted track and frame will make with the other images.

4.3.1.2 Digital Elevation Model Data Selection and Preparation

SAR data acquired during the Shuttle Radar Topography Mission are used to create 30 meter (1-arc second) spatial resolution digital elevation models (DEMs) of domestic sites and 90 meter (3-arc seconds) spatial resolution DEMs of foreign sites. These data are provided as one degree (latitude) by one degree (longitude) tiles. If the images acquired by the ERS 1, ERS 2 or ENVISAT platforms crossover the one degree by one degree tiles, several one degree square tiles can be stitched together to provide a DEM that covers the spatial extent of the images. ERMapper is used along with GAMMA Remote Sensing software to convert the DEM into a simulated SAR image that can be subtracted from an ERS 1, ERS 2, or ENVISAT interferometric pair. The ERMapper processing steps involved in this DEM conversion include:

1. ingesting the required one square degree SRTM data blocks,

2. creating an ERMapper algorithm (.alg) file,

3. creating an ERMapper earth resource mapping satellite image header (.ers) file,

4. geocoding the SRTM data using a map to map reprojection,

5. and rectifying the data.

Upon completion of the ERMapper processing steps, the *.ers and geocoded, rectified DEM files (e.g. la_redline_nutm11.ers, la_redline_nutm11) are processed in GAMMA to produce a height map (hgt_map). The processing commands used in GAMMA include the use of the following subroutines: swap_bytes, create_dem_par, gc_map, geocode, create_diff_par, init_offsetm, offset_pwrm, offset_fitm, and gc_map_fine. These GAMMA processing commands are contained in the geocoding_commands.txt file. An example of the ERMapper processing steps and GAMMA processing commands for geocoding are found in Appendix A.

4.3.1.3 Data Preparation and Image Registration Processing Flow

For this project, level zero data (raw data format) for the Los Angeles Red Line site were obtained from the Western North America Interferometric Synthetic Aperture Radar (WInSAR) consortium archive. Also, level zero data for the Mosul Dam site were obtained from the European Space Agency. Upon receipt of the data from various sources (e.g. European Space Agency, WInSAR archive, Alaska SAR Facility), the data are saved to hard drives, and read into Gamma Remote Sensing software using the Modular SAR Processor (MSP). Following the Modular SAR Processor, the data are then processed using the Interferometric SAR Processor (ISP). The MSP processing and the image registration and common band filtering step of the ISP processing are considered as "pre-processing" and discussed herein.

To transform the data from level 0 data to level 1 (Single Look Complex) data, Modular SAR Processor (MSP) processing is conducted using the GAMMA Remote Sensing software program. During the MSP processing steps, the ers_MSP_setup.sh and ers_MSP_batch.sh shell scripts are used for ERS 1 and ERS 2 data, and the

ev_MSP_setup.sh and ev_MSP_batch.sh shell scripts are used for ENVISAT data. The MSP_setup.sh scripts for both sensors create a text file (MSP_commands.txt) that contains commands that call built in routines within the GAMMA Remote Sensing software package. This text file containing the commands is run as a shell script using the MSP_batch.sh shell scripts. The GAMMA Remote Sensing routines that are called upon include: ERS_proc_ESA, DELFT_proc2, ERS_fix ESA/ESRIN, and ERS_PROC for ERS 1 and ERS 2 data, and ASAR_XCA, ASAR_IM_proc, DELFT_proc2, azsp_IQ, pre_rc, autof, az_proc, and multi_SLC for ENVISAT data. The syntax for the GAMMA Remote Sensing subroutines is found in the GAMMA Remote Sensing Users Manual. An example of the MSP_commands.txt file along with the correct GAMMA syntax is shown in Appendix A for one image used in processing the Mosul Dam site (image 06108).

The MSP conducts preprocessing and quality control to produce corrected raw data, a sensor parameter file, a processing parameter file and quality control data and plots (Figure 4.1). The corrected raw data, sensor parameter file and processing parameter file are then used in a range Doppler processing sequence in which the range compression, auto-focusing and azimuth compression are conducted (Figure 4.2). The outputs of the Doppler processing sequence are a single look complex (SLC) or a multi-looked intensity image (MLI). Examples of a SLC image and a MLI image are presented in Figure 4.3. This Doppler processing can be conducted on multiple images to produce multiple SLC or MLI images. All processing is conducted using SLC images, however, multi-looked images are useful for viewing because the files sizes are smaller and they contain square pixels.
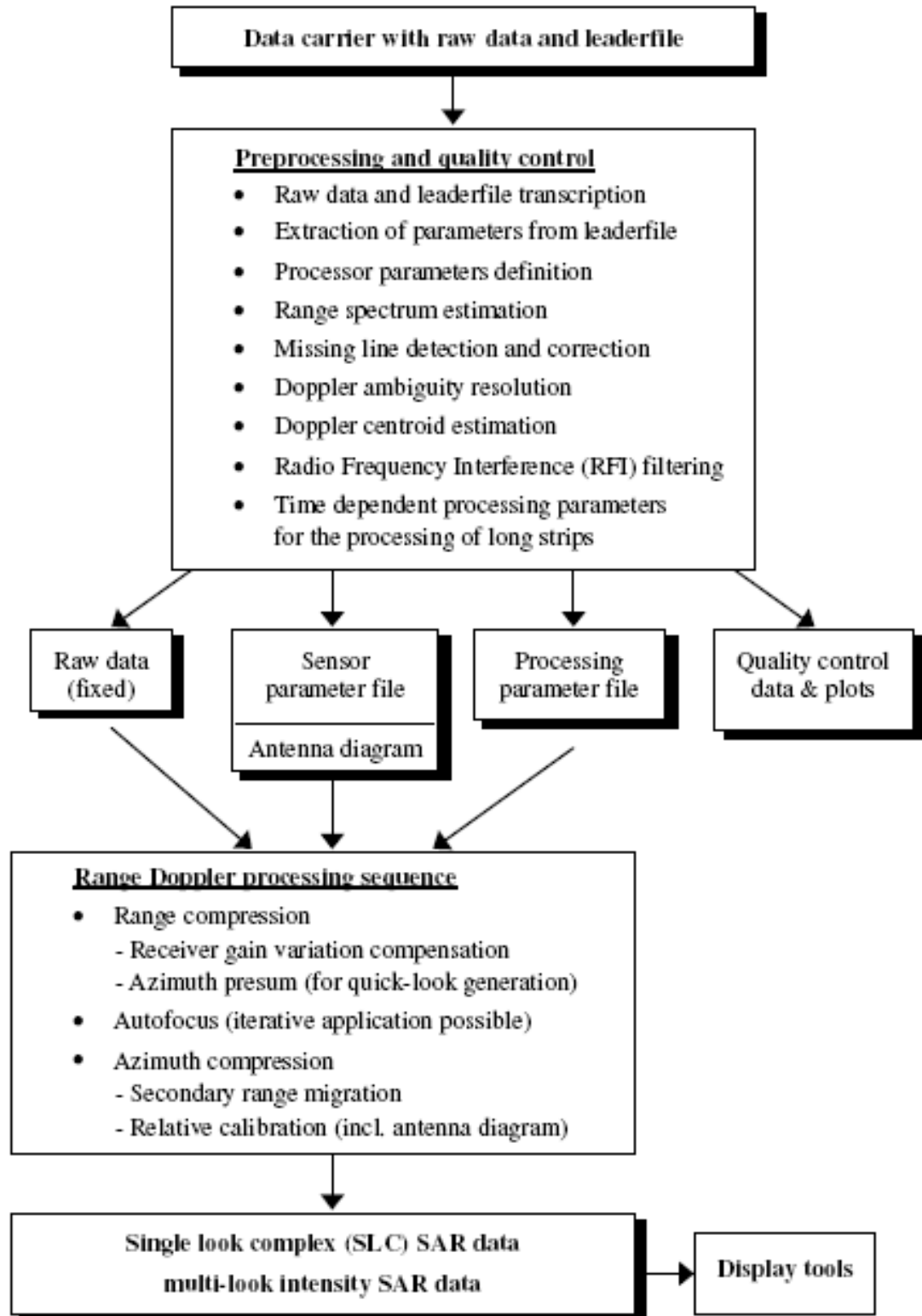
Figure 4.1. Gamma Remote Sensing MSP processing flow chart (from GAMMA, 2008).
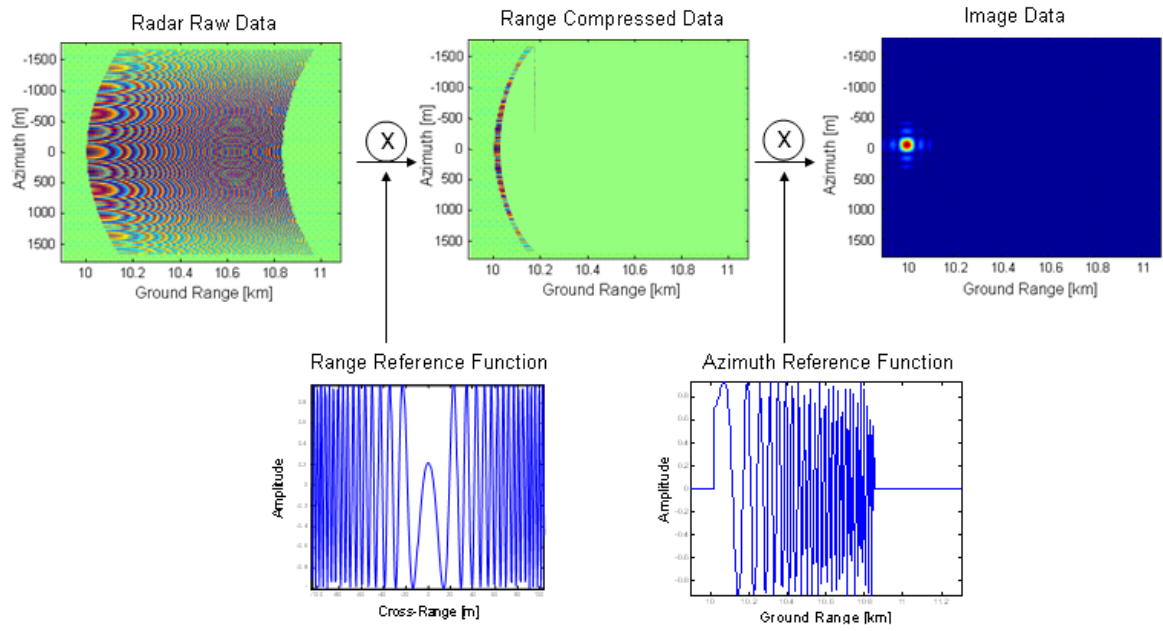
Figure 4.2. Range and azimuth compression of raw radar data (after GAMMA, 2008, modified from Richards, 2006).
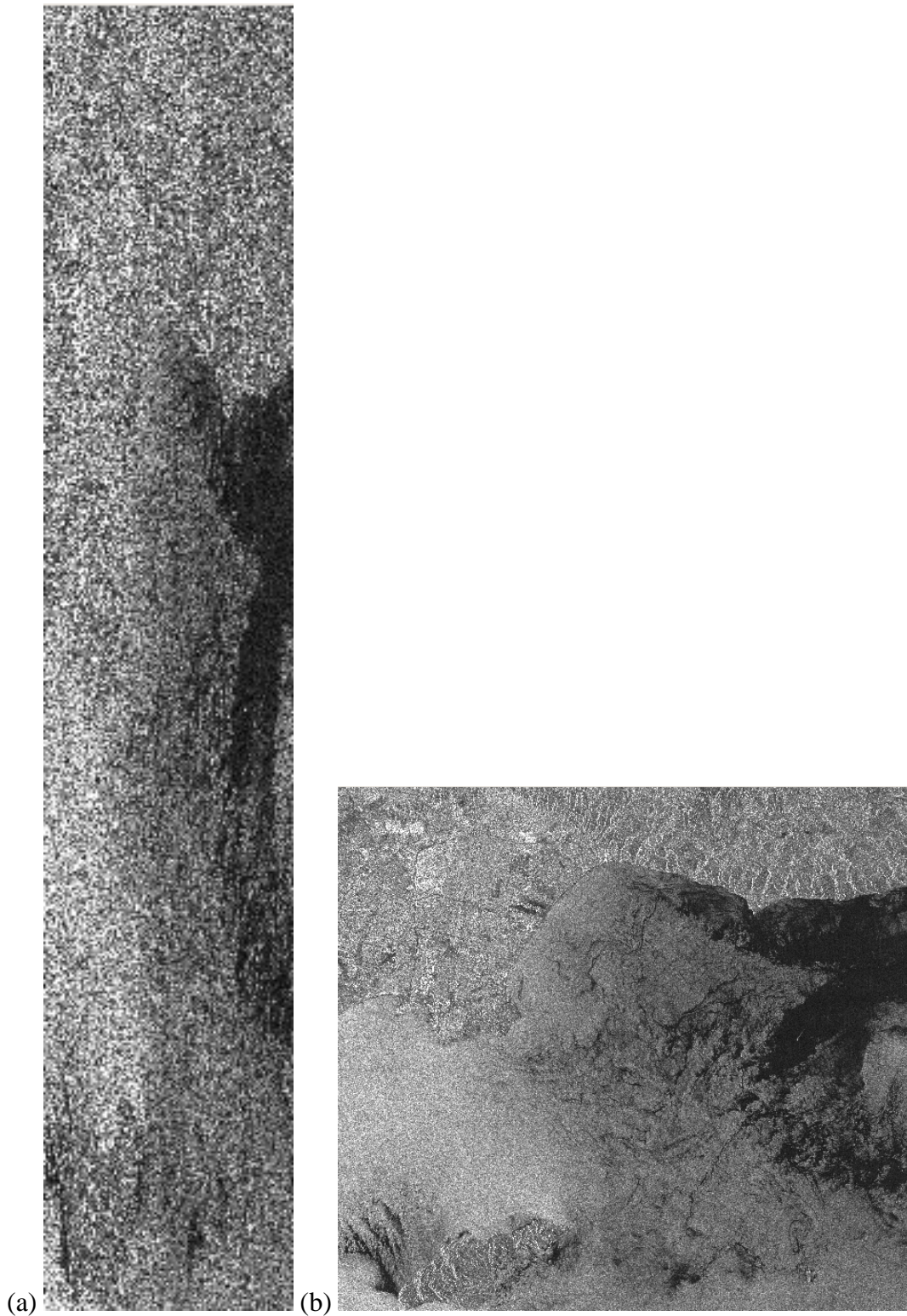
Figure 4.3. Example of (a) SLC and (b) MLI images of the 100 km by 100 km footprint of the Los Angeles Red Line site.

The SLC images and processing parameter file produced from the MSP processing steps are then imported into the Interferometric SAR Processor (ISP). Following creation of the Single Look Complex (SLC) images during MSP processing, the Interferometric SAR Processor (ISP) is used to shift/align whole images into a common viewing geometry (the first processing step found in the processing flow of the ISP is presented in Figure 4.4). One image is selected as a "master" and all of the other images ("slave" images) are transformed by shifting and aligning like pixels (resampled) into the viewing geometry of the master image. Three shell scripts are used to conduct the resampling of whole images. These three shell scripts are ISP_prep.sh, ISP_initoff.sh, and ISP_offsets.sh. Just as the MSP_setup creates a text file containing calls to GAMMA Remote Sensing software subroutines, the three ISP scripts also create text files that call GAMMA subroutines. The three text files created by the ISP_prep.sh, ISP_initoff.sh, and ISP_offsets.sh shell scripts are ISP_prep.txt, ISP_initoff.txt, and ISP_offsets.txt. The GAMMA subroutines called within these text files include: par_MSP, create_offset, init_offset, offset_pwr, offset_fit, and SLC_interp. These six subroutines:

1. create a scene parameter file,

2. create an offset file in which to store the offset polynomial values,

3. obtain multiple initial offsets estimate based on the orbit of the satellite for both image acquisitions,

4. estimate the offset between both images on a pixel by pixel basis,

5. cull those offsets to obtain a polynomial fit for how the images are to be aligned, and

6. resample the slave images into the master viewing geometry.
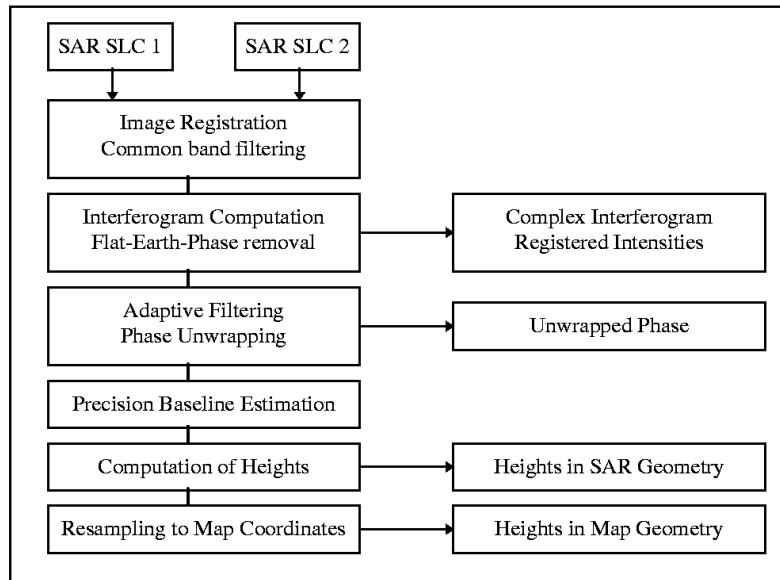
Figure 4.4. Interferometric SAR processor processing flow chart (from GAMMA, 2007).

4.3.2   Interferometric Synthetic Aperture Radar (InSAR) Processing Flow

As discussed in Section 4.3.1.3, data pre-processing consists of MSP processing and the first step of ISP processing. Using the results from the data pre-processing, the remainder of the ISP processing flow is conducted as a data processing flow. The data processing flow follows the model presented previously in Figure 4.4 and consists of image resampling (Section 4.3.2.1), interferogram computation (Section 4.3.2.2), flat-Earth-phase removal (Section 4.3.2.3), adaptive filtering and phase unwrapping (Section 4.3.2.4), and precision baseline estimation (Section 4.3.2.5).

Except for the IPTA processing technique, the commands used in the processing flow for the other four processing techniques (traditional, spatial, enhanced spatial, multiple-baseline) are the same. These commands consist of multiple shell script programs that execute subroutine programs within the GAMMA Remote Sensing software program (Gomez, 2009).

74

The shell script programs are executed in order, and that order is contained within the shell script entitled PROCESS_ALL2.sh. The shell script programs correspond to the major processing steps described in Section 4.3.2 subsections and include: translate_itab, CREATE_OFF, OFFSET_CALC, INTERF, BASEFLAT, FILTER, RASMPH, UNWRAPPER, and RASRMG. Note that all of the shell scripts with capitol letters contain matching GAMMA subroutines in lower case letters (Gomez, 2009). GAMMA subroutines contained within each of these programs include:

- create_off for CREATE_OFF,

- init_offset, offset_pwr, and offset_fit for OFFSET_CALC,

- interf_SLC for INTERF,

- base_init, phase_sim, and sub_phase for BASEFLAT,

- adf or adapt_filt and cc_wave for FILTER,

- rasmph for RASMPH,

- rascc_mask and mcf for UNWRAPPER,

- sub_phase (used to add phase values), extract_gcp, gcp_phase, base_ls, phase_sim and sub_phase (used to subtract phase values) for BASEREFINE, and

- rasrmg for RASRMG.

The syntax for each subroutine and computer code for each shell script is listed in Appendix A.

The outputs from the BASEREFINE program are unwrapped differential interferograms. These interferograms were obtained using a 50 percent coherence mask, and a spectral filter with a window size of 8. This type of mask and filter have been

proved to correctly unwrap interferograms; however, a substantial portion of the interferograms may be masked out (no phase values presented) or over smoothed (localized features are presented as being larger than they actually are). Therefore various other types of filters, multi-looking, coherence masks, and filter window sizes were investigated. The processing for each filter/multi-looking/coherence mask/filter size is conducted in separate folders using the shell script reunwrap_commands.txt. The various processing techniques use the outputs (.int, .sim_unw2 files) from the BASEREFINE program and use the REUNWRAP and RASRMG programs to generate differential interferograms that may contain the signal of interest (i.e. the signal was not over filtered or masked out). The REUNWRAP program uses the following GAMMA subroutines: sub_phase (to subtract phase), adf or adapt_filt, cc_wave, rascc_mask, and mcf. The RASRMG program uses the rasrmg GAMMA subroutine.

4.3.2.1 Image Registration and Common Band Filtering

Because the SLC images developed during the MSP processing were not acquired from exactly the same viewing geometry, the images do not image exactly the same area on the ground. "Slave" images are first co-registered into a common "master" scene. This co-registration enables viewing of the same area (the master scene viewing area) within all of the scenes. After co-registration, the scenes are referred to as resampled single look complex (RSLC) images. Varying viewing geometry between satellite passes not only causes the SLC images to view different areas of the ground, it also causes the SLC images to contain different frequency spectra. The portion of the frequency spectra that does not overlap among the SLC images must be filtered to prevent de-correlation in the interferograms computed using various RSLC images. Just as the RSLC images

76

contain the image viewing area of the master scene, the RSLC images also contain the frequency spectra of the interferometric master scene.

4.3.2.2 Interferogram Computation

Combinations of two resampled single look complex (RSLC) images are used in the interferogram computation. As discussed in Section 2.4, deformation is obtained by multiplying the complex sinusoids of each pixel in one image by the conjugate of the complex sinusoids of the corresponding pixel in the other image. The complex multiplication on a pixel by pixel basis is equivalent to differencing the phases for each pixel in both acquisitions while multiplying their respective amplitudes (Manjunath, 2008). The following equation is used to calculate the interferometric phase (Hanssen, 2001):

$$y_1 y_2^* = | y_1 || y_2 | \exp(j(\psi_1 - \psi_2)) \qquad \textbf{Equation 4.1}$$

with y_1 and y_2 being the complex sinusoids for a common pixel within each SLC, and ψ_1 and ψ_2 being the phase for the common pixel within each SLC. The interferometric phase (ϕ) as calculated is the sum of the phase due to Earth curvature ($\phi_{CurvedEarth}$), phase due to topography ($\phi_{Topography}$), phase due to deformation ($\phi_{Deformation}$), phase due to atmosphere ($\phi_{PathDelay}$), and phase due to noise (ϕ_{Noise}):

$$\phi = \phi_{CurvedEarth} + \phi_{Topography} + \phi_{Deformation} + \phi_{PathDelay} + \phi_{Noise} \qquad \textbf{Equation 4.2}$$

Note this phase is calculated for all pixels within the overlapping area of both SLC images. The output from the interferometric computations are complex interferogram data and registered intensity data (GAMMA, 2007).

4.3.2.3 Flat-Earth-Phase Removal

After completing the interferometric calculations, the flat-Earth-phase removal step is conducted. This step consists of calculating the baseline(s) between SLC images and determining the component of phase caused by earth curvature and topography using a simulated SAR image generated from a digital elevation model and the following equation:

$$\frac{\partial \phi}{\partial R} = -\frac{4\pi}{\lambda R \tan \theta} B_n$$

Equation 4.3

where $\frac{\partial \phi}{\partial R}$ is the change in phase with respect to the range direction from topography and earth curvature, λ is the wavelength, R is the distance in the range direction, θ is the compliment of the incidence angle from nadir, and B_n is the normal component of the baseline (GAMMA, 2007). The remaining phase is referred to as the flat-Earth-phase (consisting only of deformation phase, path delay phase, and noise phase) after removing the components of the phase caused by earth curvature and topography.

4.3.2.4 Adaptive Filtering and Phase Unwrapping

The next step in processing is adaptive filtering and phase unwrapping. In this step, coherence between the SLC images is calculated and filtering of the wrapped interferogram is completed. Coherence is defined as the "normalized complex correlation coefficient of the complex backscatter intensities" (Werner et al., 2002). Coherence is visualized as shown in Figure 4.5, and is calculated using a sliding estimation window on a pixel by pixel basis (GAMMA, 2007):

$$|\hat{\gamma}| = \frac{|\sum_{i=1}^{N} g_{1,i} g_{2,i}^{*} e^{-j\varphi_i}|}{\sum_{i=1}^{N} |g_{1,i}|^2 \sum_{i=1}^{N} |g_{2,i}|^2}$$

Equation 4.4

where $|\hat{\gamma}|$ is the coherence at the ith pixel, g_1 and g_2 are the complex backscatter intensities of the ith pixels in each SLC (master and slave), and $e^{-j\varphi}$ is a correction term related to the local topography at the ith pixel. Because of the local topography correction term, a better estimate of coherence is obtained using the phase obtained from a digital Elevation Model (DEM) than the estimate obtained using an Earth model represented as a mathematical function (constant, linear, quadratic, etc.) (GAMMA, 2007).
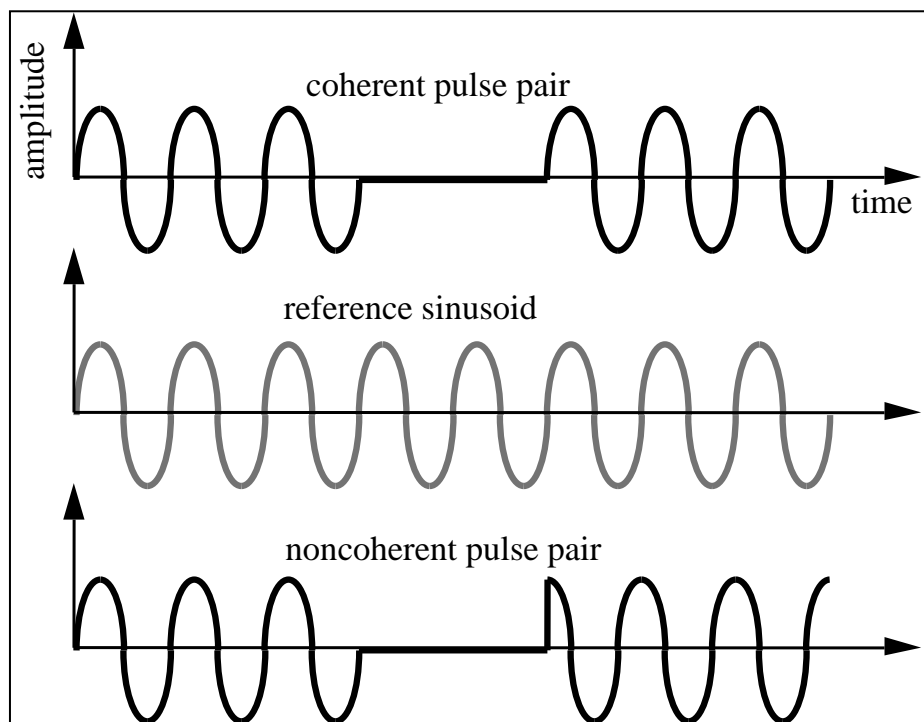
Figure 4.5. Schematic displaying coherent and noncoherent pulse pairs relative to a reference sinusoid. (from Richards, 2006).

As mentioned previously, de-correlation is observed in the portions of the images which do not overlap. If the images are co-registered to within one-tenth of a pixel, 96% of the coherence in the interferograms is preserved (Hanssen, 2001).

Coherence not only depends upon the co-registration, but also on characteristics of the individual scenes. Changes in the image properties such as: dielectric constant, infrastructure development, canopy growth, and large displacement may cause loss of coherence between images. The resulting loss in coherence will result in adverse effects (portions of the image being eliminated) on the generated interferograms. Therefore, coherence thresholds may be used to prevent non-coherent phase from affecting the interferogram calculation and unwrapping of phase values. Examples of different coherence masks are presented in Figure 4.6. A 50% coherence mask is used in Figure 4.6(a) while no coherence mask is used in Figure 4.6(b). Portions of the scene which are black have been eliminated from the scene and contain null data.

(a)   (b)
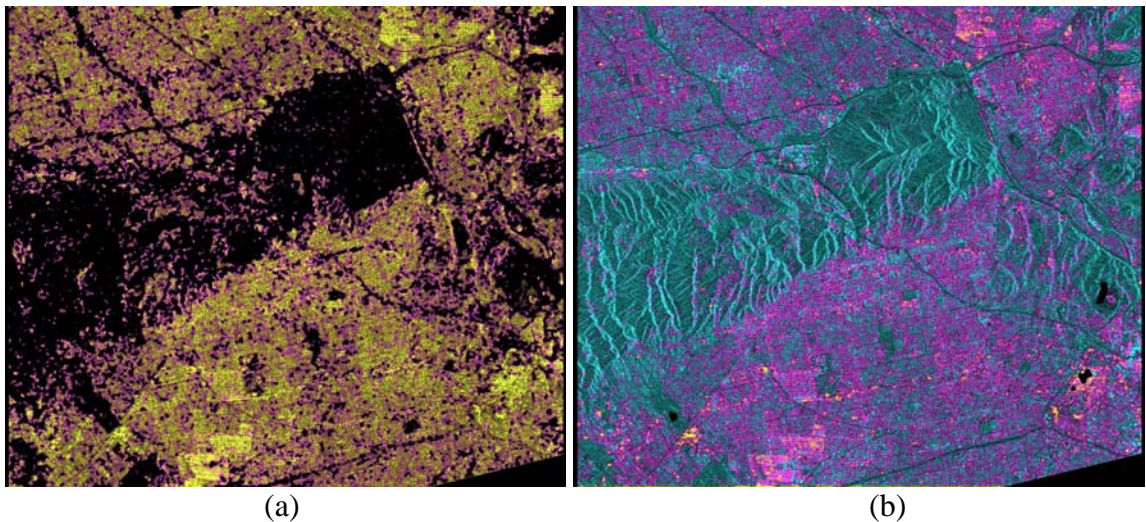
Figure 4.6. Different types of coherence masks (a) 50% coherence mask, (b) no coherence mask.

In addition to coherence thresholds, filtering is also an important component of the unwrapping process. Filtering can be accomplished using multi-looking, spectral

filtering, or slope adaptive filtering. The radiometric spectrum is averaged for multiple pixels (multi-looking) within a certain window size (typically 1 pixel by 5 pixels or 2 pixels by 10 pixels for ERS and ENVISAT imagery) and the value of each pixel is replaced with the average value of the window of pixels. Image multi-looking (Figure 4.7) increases the radiometric (i.e. measurement) resolution while decreasing the spatial resolution.   Spatial resolution is decreased because the individual pixel values are replaced with average values over the window (in other words, the value for a one-meter pixel will be averaged with values for 5 other one-meter pixels, and the average value will replace the individual pixel values effectively creating one five-meter average value pixel.   However, multi-looking technique reduces phase noise between pixels by averaging values of individual outlier pixels with those of surrounding stable pixels. As seen in Figure 4.7, multi-looked images generally become smoother (more in focus) as the "salt-and-pepper" or "speckled" appearance disappears with more looks. Whereas the intensity image looks smoother, the phase values of multiple pixels have been replaced with the average value of surrounding pixels, leading to larger spatial resolution.
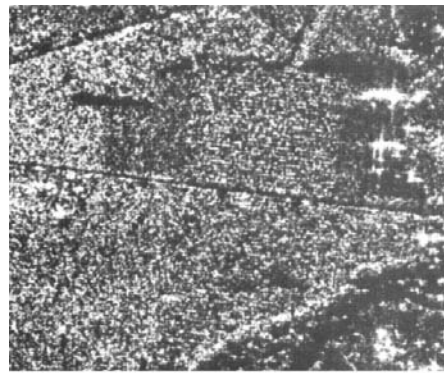
a. 1-look radar image.
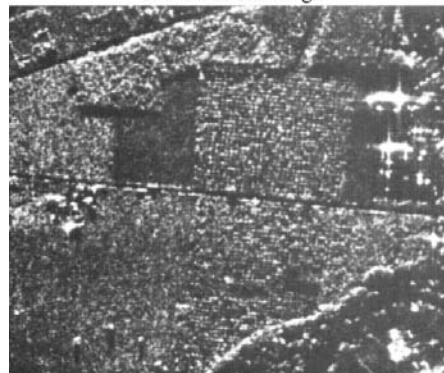
b. 4-look radar image.
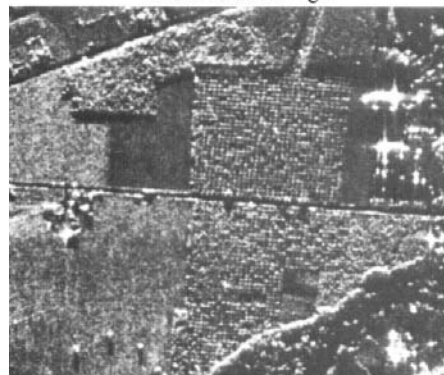
c. 16-look radar image.

Figure 4.7. Multi-looking of SAR radar image using (a) 1–look, (b) 4-looks, (c) 16-looks (from Jensen, 2001).

4.3.2.4.1   Filtering

Filtering reduces or removes thermal noise from a wrapped interferogram in order to allow unwrapping to take place. An example of unfiltered and filtered interferograms is presented in Figure 4.8. Two filter types were investigated in this study. These two filter types (spectral filter and slope adaptive filter) are described below.
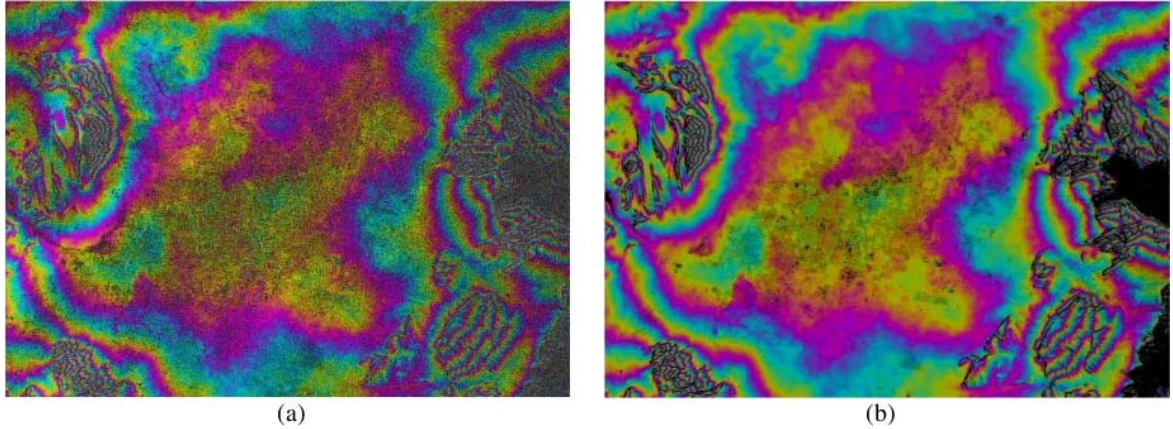
Figure 4.8. Interferogram (a) before filtering, and (b) after filtering (from GAMMA, 2007).

Spectral filters, based on the algorithm presented by Goldstein and Werner (1998), determine the local power spectrum of the wrapped interferogram, design a filter for this spectrum, and filter the interferogram (GAMMA, 2006). The filter is referred to as an adaptive spectral filter because it adapts the filter based on the power spectrum (Figure 4.9) of the interferogram. The spectral adaptive filter is used to reduce phase noise, and the number of residues or locations in the interferogram where the phase difference between pixels around a closed path is not 0.0 (GAMMA, 2006). Residues present problems during unwrapping from the wrapped phase component ($-\pi$ to π) as displayed in to the unwrapped phase component (multiples of 2π) as displayed in Figure 4.10 and Figure 4.11.
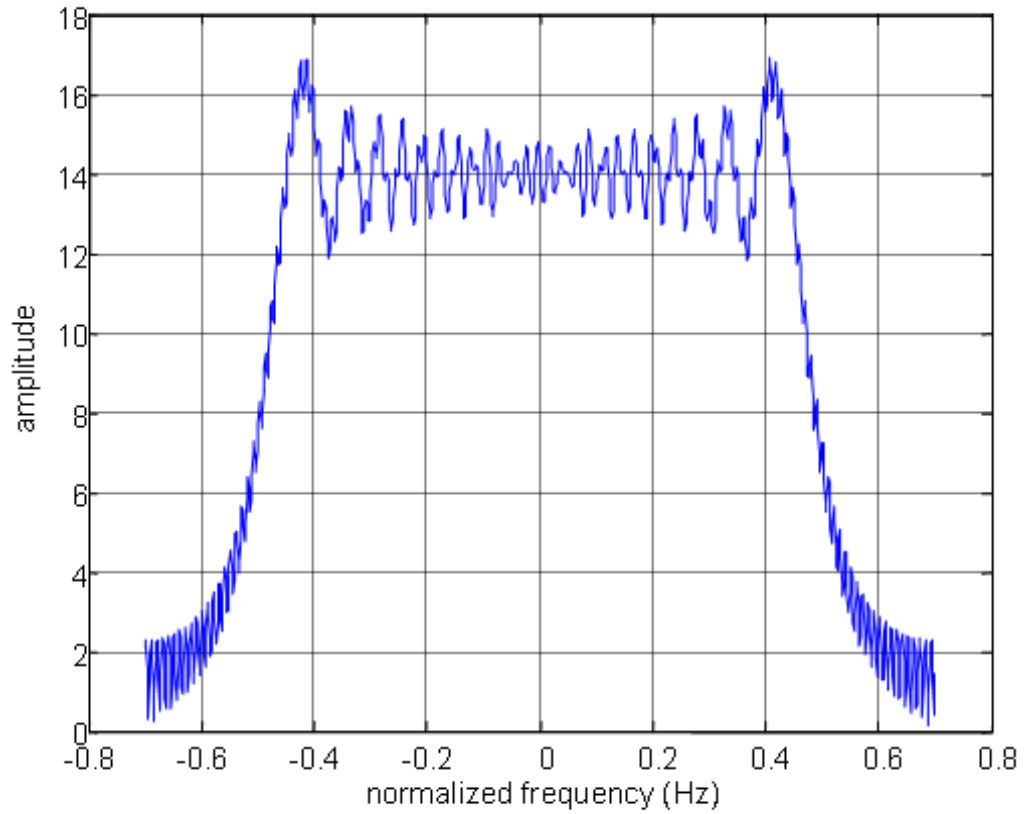
Figure 4.9. Power spectrum of a Linear Frequency Modulation (LFM) waveform (from Richards, 2006)

(a)   (b)
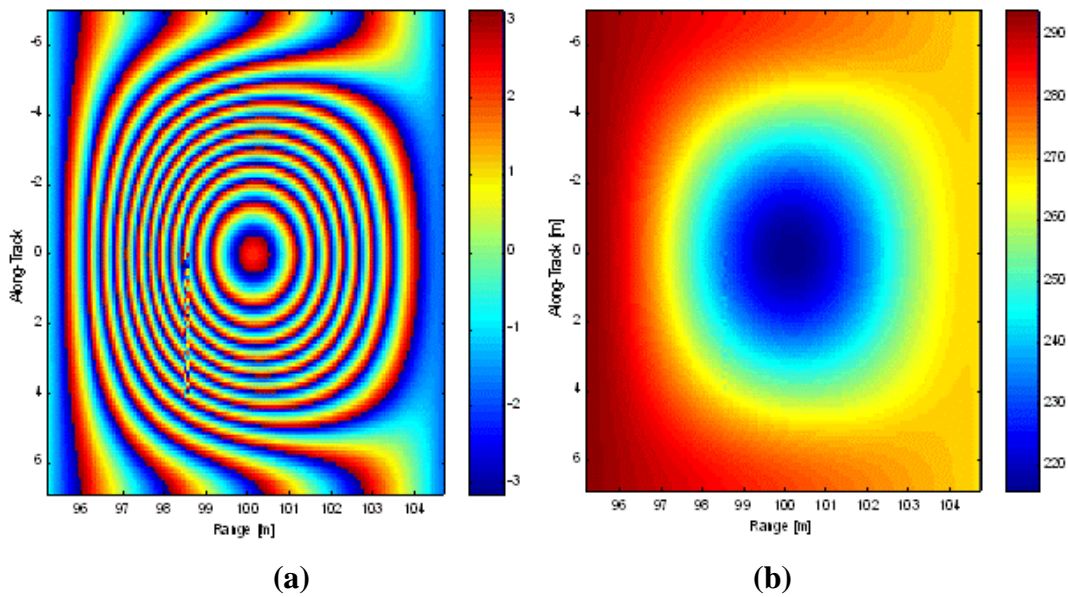
Figure 4.10. Example of (a) unwrapped and (b) wrapped phase (from Richards, 2007).
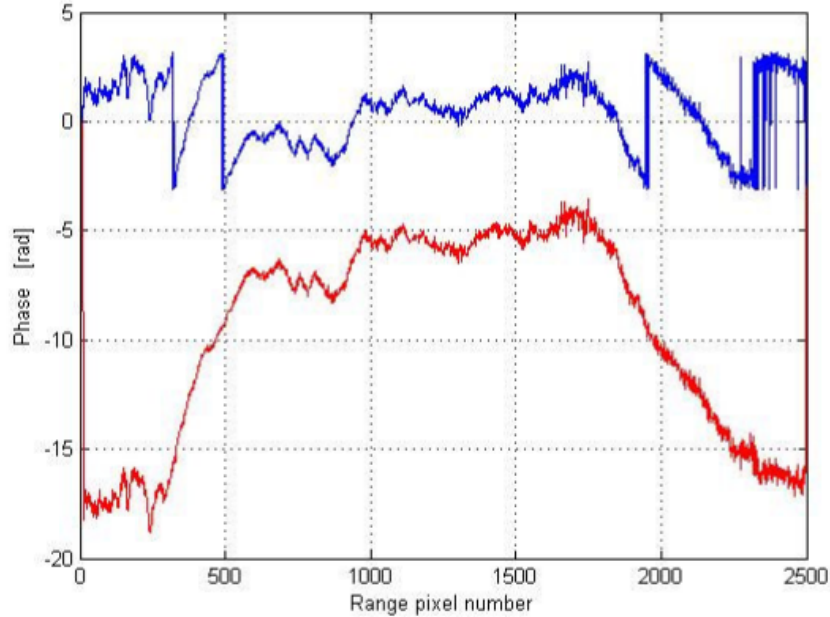
Figure 4.11. Wrapped (blue line) and unwrapped (red line) flattened interferogram for one range bin (from GAMMA, 2007).

At locations where residues are present, phase unwrapping problems occur (GAMMA, 2006). Multi-looking (as discussed in Section 4.3.2.4) and filtering (as discussed previously in this section) reduce the number of residuals to improve unwrapping. The size of the filter used may also cause problems during phase unwrapping. Common window sizes for adaptive spectral filters are multiples of eight beginning with 8 (8, 16, 32, and 64). Using small Fast Fourier Transform (FFT) window sizes (8,16) for scenes with rapidly changing phase caused by topographic features (rough terrain), and using large Fast Fourier Transform (FFT) window sizes (32, 64) for scenes with gradually changing phase caused by limited topographic features (smooth terrain) is suggested in the GAMMA Reference Manual (2006). Small window size values (8,16) lead to smoother filtered output, but take longer to process, whereas large window sizes (32,64) lead to less smooth filtered output, but do not take as long to process, and take up less disk space. The affect of various filter window sizes on stacked interferograms is discussed in Chapter 6.

Slope adaptive filters determine the local slope of the phase, and average the phase along the slope, using a Kaiser window. Like the adaptive spectral filter, the slope adaptive filter is used to reduce phase noise, and the number of residues Common window sizes for slope adaptive filters are multiples of two beginning with 2 (2, 4, and 8). For processing conducted at the University of Missouri, phase unwrapping is usually conducted using an adaptive spectral filter. Because the slope adaptive filter is typically applied after unwrapping, small "clipped" images are typically used, resulting in the use of smaller window sizes.

Different filters and coherence masks (Figure 4.12) affect the results obtained from differential interferogram processing (Figure 4.13). Processing conducted for Earth observation studies (ground water extraction, oil extraction, post-seismic deformations, and glacier movements) have traditionally utilized adaptive spectral filtering with local fringe spectrum (spectral filter) and a phase unwrapping validity mask (coherence mask). Proposed modified processing techniques discussed in Chapter 6 utilize slope adaptive filtering and no phase unwrapping validity mask. As discussed in Chapter 6, it was determined that the adaptive spectral filtering with fringe spectrum and phase unwrapping validity mask (Figure 4.12 (a)) often removed the signal of interest, while the slope adaptive filtering with no phase unwrapping validity mask (Figure 4.12 (b)) does not remove the localized deformation features. Note that the results shown in Figure 4.12 and Figure 4.13 are for one differential interferogram of the Los Angeles Red Line site with a 20 meter baseline and 688 day temporal resolution. The (a) images in Figures 4.12 and 4.13 correspond to processing using an adaptive spectral filter with window size of 8 and 50 percent coherence mask, while the (b) images in Figures 4.12

and 4.13 correspond to processing using a slope adaptive filter with a window size of 2 and no coherence mask.
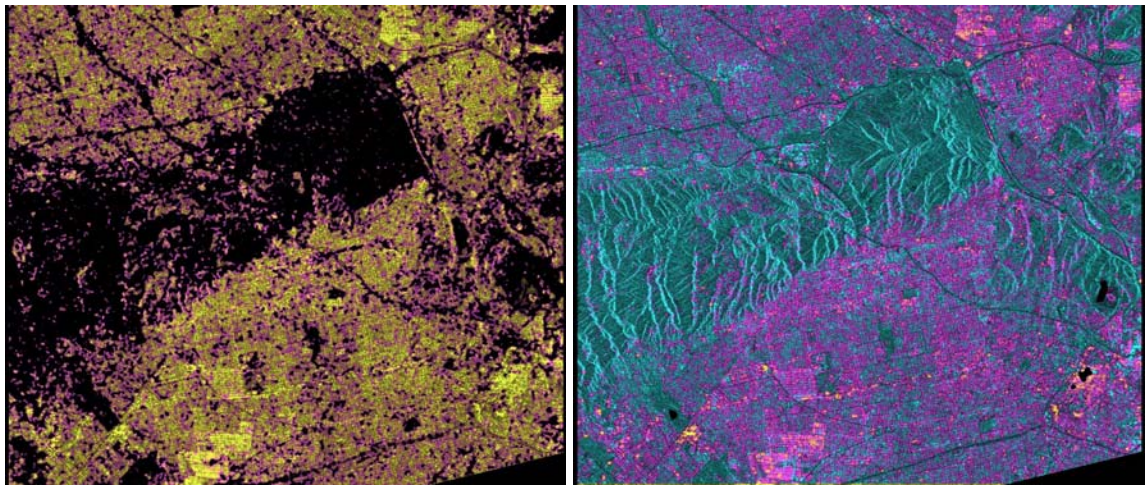
<center>(a) (b)</center>

Figure 4.12. Different types of filtering and coherence masks (a) adaptive spectral filter with window size of 8 and 50% coherence mask, (b) slope adaptive filter with window size of 2 and no coherence mask.
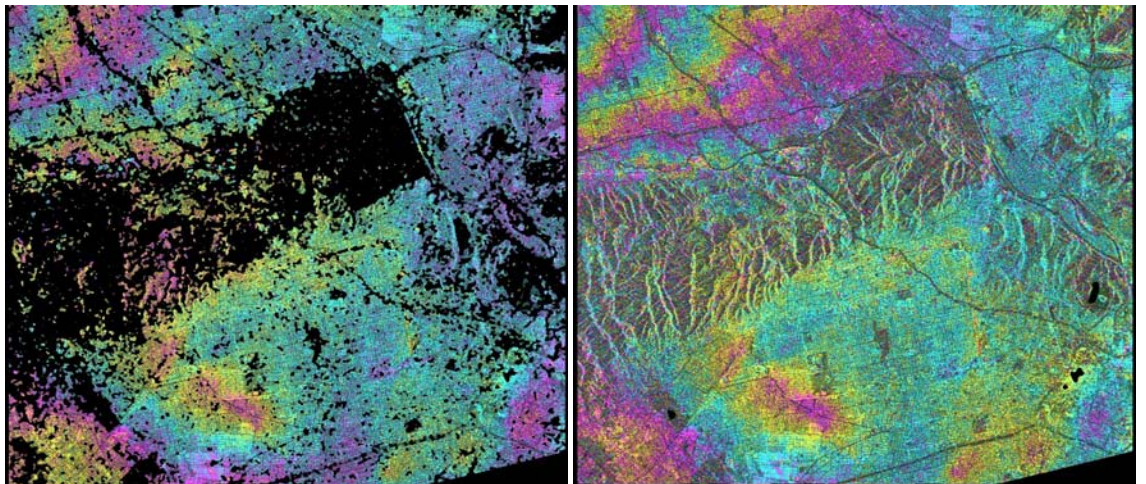
<center>(a) (b)</center>

Figure 4.13. Effect of filtering and coherence masks types on unwrapped differential interferograms (a) adaptive spectral filter with window size of 8 and 50% coherence mask, (b) slope adaptive filter with window size of 2 and no coherence mask.

Phase unwrapping is used to convert the wrapped phase (–π to π) to unwrapped phase (multiples of 2 π) relative to a reference point within the interferogram as displayed previously in Figures 4.10 and 4.11. Phase unwrapping is the most complicated step in the interferometric SAR processing sequence. Problematic areas within the wrapped interferogram such as areas with rugged topography, low coherence, and geometric effects (layover, radar shadow, etc) are very difficult to unwrap because some areas of the interferogram may be disconnected from other areas of the interferogram, resulting in an artificial phase jump across the problematic areas (Figure 4.14).
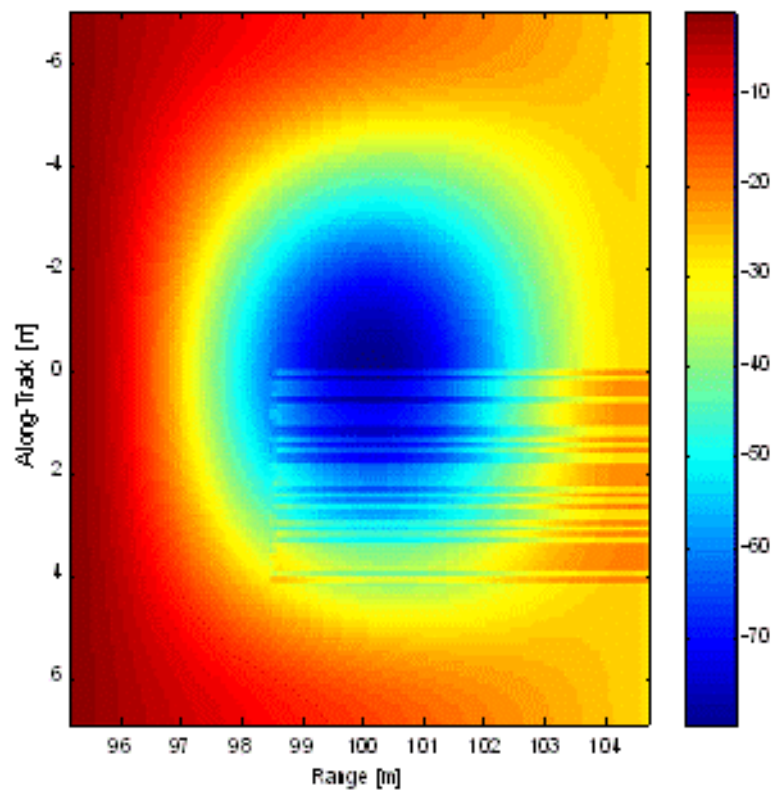
Figure 4.14. Phase jump across, and caused by, area with low coherence (from Richards, 2007).

As previously discussed, wrapped interferograms are easier to unwrap using digital elevation models (DEMs), filtering, and coherence masking produces because the

interferograms are flatter (smaller topography component of phase) and smoother (smaller noise component of phase).

Two methods of unwrapping are commonly used. These methods consist of the branch-cut region growing algorithm (Rosen et al., 1994), and the minimum cost flow algorithm (Constantini, 1998). For processing conducted for this work, the minimum cost flow algorithm was used. This algorithm is more computationally and time intensive, but is more robust and can be used to unwrap very large scenes. The minimum cost flow algorithm consists of generating a triangulation network in which areas with low coherence values are specified using a validity mask (GAMMA, 2008). Different regions within the interferogram have different cost within the minimum cost flow. Areas where phase discontinuities (rugged topography, low coherence, geometric effects) are present tend to be associated with areas of low cost, which have low weight, indicating network flow is needed in these areas within the minimum cost flow. Conversely, areas where phase is continuous tend to be associated with areas of high cost, which have high weight, indicating flow from this area within the minimum cost flow.

A positive residue (point in the interferogram where the phase difference around a closed path is positive), as calculated by integrating the phase around the triangle, indicates contributing flow to the network, whereas a negative residue (point where phase difference is negative) indicates accepting flow from the network (GAMMA, 2006). The network is solved to minimize the net cost using the successive shortest path. Because processing conducted for this study is conducted on small "clipped" images, unwrapping is performed over the whole scene, and unwrapped phase values are calculated relative to a reference point with an initial phase value.

4.3.2.5 Precision Baseline Estimation

Following phase unwrapping, the unwrapped phase is used to refine the initial baseline estimates obtained from orbit data. Whereas this estimate is sufficient for correcting for Earth curvature and topography to produce the flat-Earth-phase, the estimate is not sufficient for development of topographic heights from the unwrapped differential interferometric phase (GAMMA, 2008). The topographic phase that was subtracted from the wrapped interferometric phase to produce the flat-Earth-phase is added to the unwrapped interferogram to develop an image including topography. Initial baselines are then refined using ground control points within the interferogram with known elevations and the unwrapped interferometric phase (including topographic and earth curvature phases) using:

$$B_n = \frac{\lambda R \sin\theta}{4\pi z}\phi_{topo}$$ **Equation 4.5**

where B_n is the normal baseline, λ is the wavelength, R is the range distance, θ is the incidence angle, z is the elevation of the ground control points, and ϕ_{topo} is the unwrapped topographic phase (GAMMA, 2008). A least squares adjustment is conducted in which the baselines corresponding to the locations of the ground control points are calculated from the unwrapped interferometric phase and the ground control point elevations by reducing the squared elevation errors. Conditions that may lead to poor performance of the least squares adjustment include: poor initial baseline estimate, poor selection of ground control points, too many free parameters specified for the least squares fitting, or too small of an area specified for averaging the phase values from multiple pixels (GAMMA, 2008).

Using the refined baselines calculated using unwrapped phase including topography and ground control points, the differential interferograms are obtained by subtracting the simulated intensity topographic phase from the interferometric phase. The resulting phase after subtraction of the simulated topographic phase is the deformation phase component in radar coordinates.

4.3.2.6 Summary of Processing Flow

The InSAR data processing flow consists of image registration and common band filtering, interferogram computation, flat-Earth-phase removal, adaptive filtering, phase unwrapping, and precision baseline estimation as discussed in Sections 4.3.2.1 through 4.3.2.5. This processing flow produces individual or multiple unwrapped interferogram(s) displaying displacement in radar viewing geometry.

4.3.3 Post-Processing Flow

Following the development of the interferograms, post-processing is conducted to transform the images from radar viewing geometry to map viewing geometry. Multiple interferograms are also stacked to produce one interferogram displaying the average displacement of the stack of multiple images. This stacking procedure is used to enhance the deformation features which are common to all images.

4.3.3.1 Stacking of Radar Data

Stacking is a procedure in which the phase components from multiple interferograms are averaged together using a time-weighted average to produce a "stacked" interferogram displaying the components of phase common to all of the

interferograms. Atmospheric phase is not constant over time and therefore, the averaging procedure (stacking) tends to reduce the effect of atmospheric phase.

Stacking is conducted after the interferograms have been unwrapped using spatial unwrapping techniques. Stacking is typically conducted on images obtained using multiple masters (multiple-baseline), but can also be conducted on images using a common master. Stacking is typically conducted using a file entitled stacking_commands.txt. This text file draws upon the GAMMA subroutine entitled stacking. A diff_tab is required for the stacking command to compute a stacked differential interferogram. The interferograms used within the stacking command and the amount of time between the images (in days) are contained within the diff_tab. The time difference is used as a weighting factor (multiplied by the phase) and neglected if the subsidence event of interest was a one-time rapid subsidence event (as opposed to a gradual subsidence event). A time weighting factor was not used for this research. The diff_tab is called diff_tab_eq_weight if the subsidence event was a one-time event, and diff_tab_weighted if the subsidence event is a gradual event. Only the interferograms containing images surrounding the time of interest are stacked, as images which are not around the time of interest and do not contain subsidence will skew the average. Examples of the stacking_commands.txt, and the diff_tab_eq_weight files for the Los Angeles Red Line site are provided in Appendix A.

4.3.3.2 Development of Ortho-rectified Displacement Image Product

Following the generation of interferograms during processing the GAMMA Remote Sensing and ERMapper software programs are both used in post-processing to convert the image from average or cumulative phase in the satellite viewing geometry to

ground deformations in the ortho-rectified viewing geometry. The disp_map GAMMA subroutine is used to convert the interferograms from average or total cumulative phase to displacement heights. The geocode_back subroutine in GAMMA is used to do the ortho-rectification transformation. The ERMapper program is used to display the ground deformation interferograms with Latitude and Longitude bounding boxes, and horizontal and vertical scales.

4.4   Interferometric Synthetic Aperture Radar (InSAR) Processing Techniques

The five interferometric synthetic aperture radar processing techniques which were investigated for this study are introduced in Sections 4.4.1 through 4.4.5. These procedures include: traditional processing, spatial processing, enhanced spatial processing, interferometric point target processing and multiple-baseline processing.

4.4.1   Traditional Interferometric Synthetic Aperture Radar (InSAR) Processing

The traditional interferometric synthetic aperture radar approach has been used by different investigators at different locations to provide an overview of different sites as discussed in Section 2.2. The traditional application is very useful for obtaining knowledge about the coherence of images for different site, and for gathering information about large scale deformation features (e.g. due to post-seismic earthquake analyses, groundwater withdrawal, and oil extraction). The traditional approach is usually the first approach utilized in all InSAR studies because of the limited processing and data storage requirements. It also allows investigators the opportunity to determine the locations of localized features that can be clipped out of the larger image and further processed.

Typically, traditional processing is conducted on the entire scene (100 square kilometers for ERS 1, ERS 2, and ENVISAT imagery; 50 square kilometers for

RADARSAT-1 Fine Beam Mode imagery). Interferograms are typically multi-looked at 2 looks in the range direction and 10 looks in the azimuth direction for ERS 1, ERS 2, and ENVISAT imagery to form an approximately square 40 meter by 40 meter pixel. Interferograms are typically multi-looked at 4 looks in the range direction and 8 looks in the azimuth direction for RADARSAT-1 imagery to form an approximately square 32 meter by 32 meter pixel. These levels of multi-looking generally cause the radiometric resolution to increase at the expense of the spatial resolution as discussed in Section 4.3.2.4 and shown previously in Figure 4.7. However, the traditional approach is used to gain an understanding of the coherence of the images for a given site, not to identify localized features, so the radiometric resolution of the interferogram is more important than the spatial resolution of the interferogram.

Following the creation of the wrapped interferogram and prior to unwrapping the interferogram, the interferogram is filtered using an adaptive spectral filter and low coherence points are masked. For processing conducted for this work, an adaptive spectral filter with a window size of 32 is commonly used along with a 50 percent coherence mask (Figure 4.15).
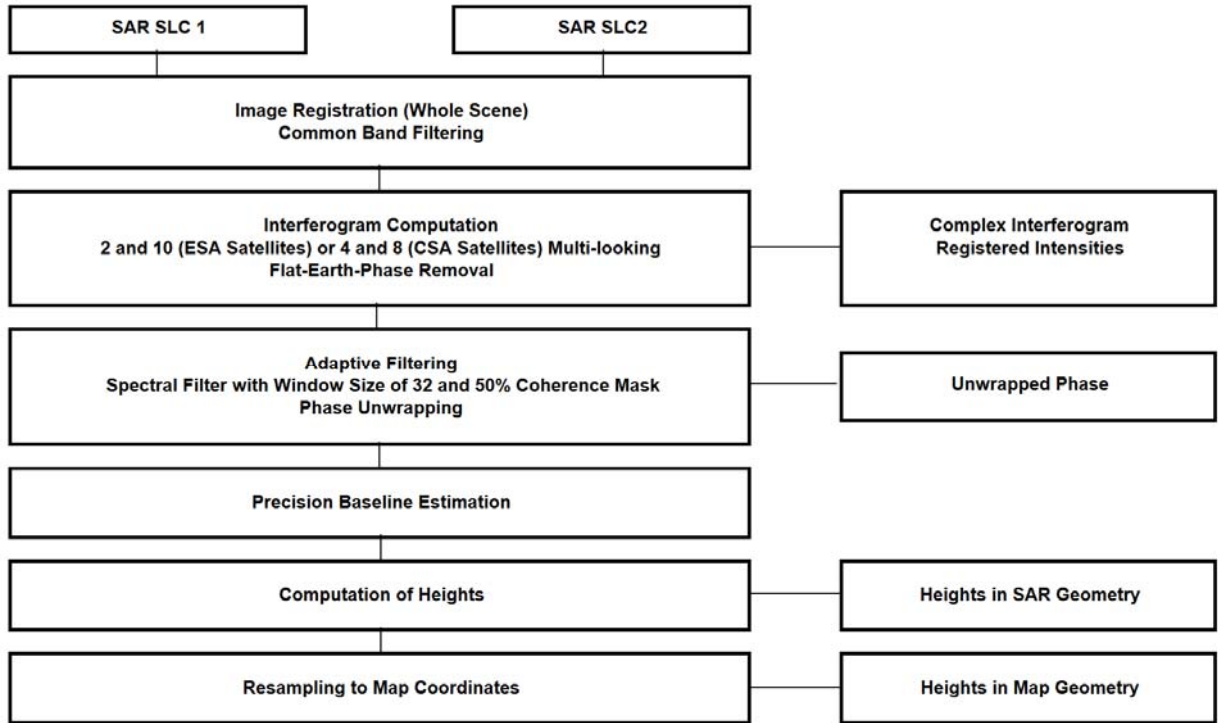
Figure 4.15. Traditional processing flow.

Typically, traditional processing is conducted on relatively few scenes, using a small selection of scenes as determined by initial baseline lengths. Multiple master-slave pairs are selected to produce interferograms and determine the coherence of the scenes. The selected combinations are determined by using a matrix containing baselines estimates between image pairs. As shown in Table 4.1, the SLC orbit numbers (identification numbers providing information about the location and date of each scene) are listed in the first horizontal row and in the first vertical column. Because the SLC orbit numbers are listed in this manner, a symmetric (magnitude) matrix is produced with the baseline between the same SLC images being zero (i.e. zero values along the diagonal). The other values in the table correspond to the baseline values for pairs of images. For example, the baseline for the SLC pair of 4595 and 7100 is 90 meters,

obtained by either starting with 4595 in the horizontal row or vertical column and going

down or across to 7100 in the vertical column or horizontal row, respectively.

Table 4.1. Example SLC imagery table used for the ad-hoc selection of SLC pairs based on baseline length.

Orbit/Orbit	4595	6098	6599	7100
4595	0	-361	388	-90
6098	361	0	749	271
6599	-388	-749	0	-478
7100	90	-271	478	0

Values in table correspond to baseline length between SLC orbits (in meters).

Post-processing is not typically conducted during traditional processing as traditional processing is typically only conducted to provide initial information about site characteristics. The individual interferograms are usually viewed in radar viewing geometry without stacking or ortho-rectification.

4.4.2   Spatial Interferometric Synthetic Aperture Radar (InSAR) Processing

The spatial interferometric synthetic aperture radar, or spatial InSAR, approach is a modified version of the traditional interferometric approach to provide higher spatial resolution. Interferograms produced using spatial InSAR are multi-looked at 1 look in the range direction and 5 looks in the azimuth direction for ERS 1, ERS 2, and ENVISAT imagery to form an approximately square 20 meter by 20 meter pixel. Interferograms are produced at 2 looks in the range direction, and 4 looks in the azimuth direction for RADARSAT-1 imagery to form an approximately square 16 meter by 16 meter pixel. Decreasing the number of looks increases the spatial resolution, at the expense of decreasing the radiometric resolution as discussed in Section 4.3.2.4 and displayed previously in Figure 4.7. For characterization of localized deformation features, this decrease in radiometric resolution for an increase in spatial resolution is necessary

because the localized deformation features are smaller in size than the pixel size of SAR when multi-looked at 1 and 5 looks.

Following the creation of the wrapped interferogram and prior to unwrapping the interferogram, the interferogram is filtered using a spectral filter and low coherence points are masked. For processing conducted for this study, an adaptive spectral filter with a window size of 32 is commonly used with a 50 percent coherence mask (Figure 4.16).
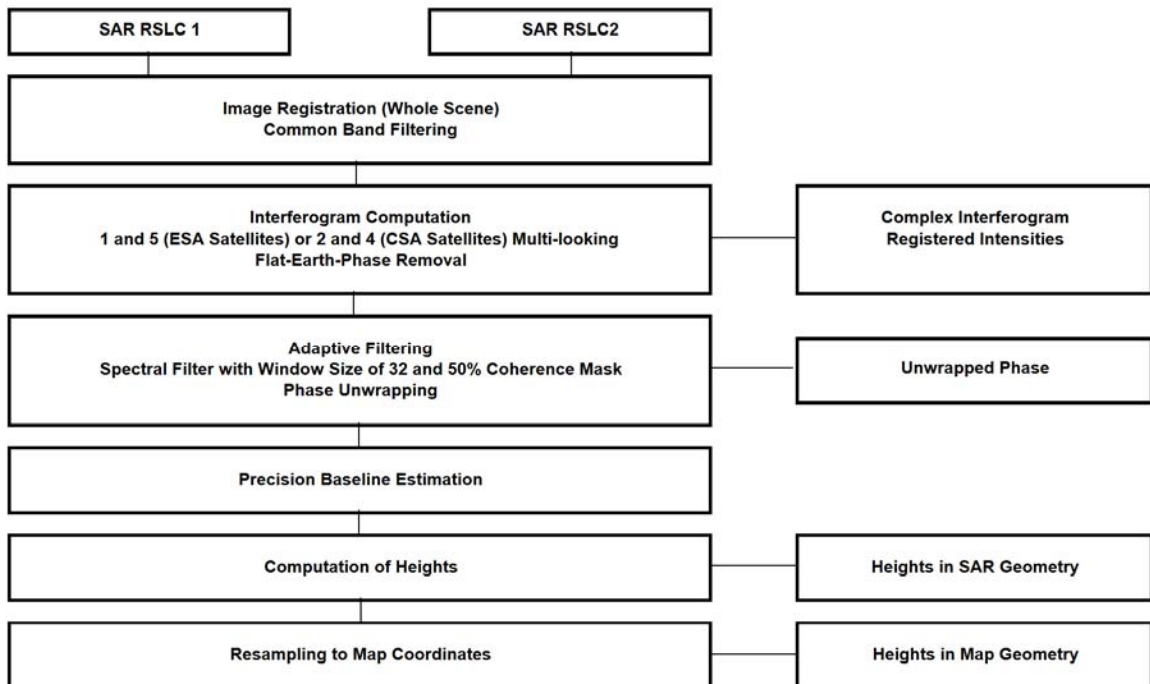
Figure 4.16. Spatial processing flow.

Instead of using multiple master-slave pairs, all of the images are co-registered to one master. The master selected can either be the first (oldest) scene or the scene that has the smallest average baseline with the other images. The scene with the smallest baseline average (as compared to the other scenes) is often selected because small baselines help to facilitate unwrapping. Unlike the approaches listed in Sections 4.4.3 through 4.4.5, co-registration is overseen by the operator instead of being automated. The reason for

operator oversight is to co-register the scenes within one-tenth of one pixel in the range direction and one-seventh of one pixel in the azimuth direction as recommended by Manjunath (2008). The computer control will ensure one-seventh of one pixel in both the range and azimuth directions. Also, the resampled SLC (RSLC) images created in the spatial processing technique are also used, albeit clipped, in the remaining processing techniques described in Sections 4.4.3 through 4.4.5.

Post-processing is not typically conducted during spatial processing as spatial processing is typically only conducted to provide initial information about site characteristics. The individual interferograms are usually viewed in radar viewing geometry without stacking or ortho-rectification.

4.4.3 *Enhanced Spatial Interferometric Synthetic Aperture Radar (InSAR) Processing*

Like the spatial InSAR, the enhanced spatial InSAR approach is a modified version of the traditional interferometric approach. The processing uses the same processing flow described in Section 4.4.2 (spatial), except the processing is conducted on the clipped RSLC images which were co-registered during the spatial processing flow. Also, the difference between the enhanced spatial and the traditional and spatial approaches is that the unwrapped interferogram to which the simulated topographic phase has been added is filtered using a slope adaptive filter with a window size of 2, and no coherence mask is applied to produce the final differential interferogram, instead of using a spectral filter with a window size of 8, and a coherence mask of 50 as done in the spatial processing flow (Figure 4.17).

```
┌─────────────────────┐          ┌─────────────────────┐
│     SAR RSLC 1      │          │     SAR RSLC2       │
└─────────────────────┘          └─────────────────────┘
            │                              │
┌─────────────────────────────────────────────────────┐
│        Image Registration (Clipped Scene)            │
│              Common Band Filtering                   │
└─────────────────────────────────────────────────────┘
                        │
┌─────────────────────────────────────────┐   ┌─────────────────────────┐
│          Interferogram Computation      │   │  Complex Interferogram  │
│ 1 and 5 (ESA Satellites) or 2 and 4     │───│  Registered Intensities │
│   (CSA Satellites) Multi-looking        │   │                         │
│        Flat-Earth-Phase Removal         │   └─────────────────────────┘
└─────────────────────────────────────────┘
                        │
┌─────────────────────────────────────────┐   ┌─────────────────────────┐
│             Adaptive Filtering          │   │                         │
│ Slope Adaptive Filter with Window Size  │───│    Unwrapped Phase      │
│   of 2 and no Coherence Mask            │   │                         │
│           Phase Unwrapping              │   └─────────────────────────┘
└─────────────────────────────────────────┘
                        │
┌─────────────────────────────────────────┐
│        Precision Baseline Estimation    │
└─────────────────────────────────────────┘
                        │
┌─────────────────────────────────────────┐   ┌─────────────────────────┐
│          Computation of Heights         │───│  Heights in SAR Geometry│
└─────────────────────────────────────────┘   └─────────────────────────┘
                        │
┌─────────────────────────────────────────┐   ┌─────────────────────────┐
│                Stacking                 │───│   Stacked Interferogram │
└─────────────────────────────────────────┘   └─────────────────────────┘
                        │
┌─────────────────────────────────────────┐   ┌─────────────────────────┐
│       Resampling to Map Coordinates     │───│  Heights in Map Geometry│
└─────────────────────────────────────────┘   └─────────────────────────┘
```

Figure 4.17. Enhanced spatial processing flow.

The enhanced spatial technique uses the RSLC images (resampled into one common master), however, only a clip of the image is used. The clip is a small area in which the deformation is expected to occur located within the 100 kilometer by 100 kilometer image. Like the spatial technique, to provide higher spatial resolution, the interferograms produced using enhanced spatial approach are multi-looked at 1 look in the range direction and 5 looks in the azimuth direction for ERS 1, ERS 2, and ENVISAT imagery and at 2 looks in the range direction and 4 looks in the azimuth direction for RADARSAT-1 imagery.

After clipping the images, the RSLCs are again re-sampled to ensure the images are registered in the same way they were before clipping. During this resampling, automated registration is used to ensure that the co-registration of the images is within

one-tenth of one pixel (note: the RSLC images from the spatial processing technique were overseen by the user, therefore, the clipped RSLC images will be co-registered within one-tenth of a pixel). Multiple master-slave pairs of images are selected using all possible combinations with baselines less than a certain threshold (125 meters for the LA Red Line site). The computer was used to select the images with baselines less than 125, rather than the user selecting the scenes using the selection method described in Section 4.4.1.

Post-processing is typically conducted during enhanced spatial processing to provide detailed information about site characteristics. The individual interferograms are usually viewed in radar viewing geometry, then stacked and ortho-rectified.

4.4.4 *Interferometric Point Target Analysis (IPTA) Processing*

As mentioned previously, the IPTA processing technique uses itab and RSLC_tab files that are generated by the user, and not by MATLAB. IPTA processing is typically conducted using a file entitled ipta_commands.txt. This text file draws upon the following GAMMA subroutines: mk_msr_pt, mk_sp_all, thres_im_pt, ras_pt, merge_pt, data2pt, base_orbit_pt, base_par_pt, dis_ipta, qc_pt, multi_def_pt, pdisdt_pwr24, prasdt_pwr24, def_mod_pt, lin_comb_pt, phase_sim_pt, sub_phase_pt, msk_pt, ras_pt, base_ls_pt, spf_pt, tpf_pt, vu_disp, and prt_pt and follows the processing flow displayed in Figure 4.18. Manjunath (2008) extensively discusses the IPTA processing conducted on the 52 Los Angeles Red Line RSLC images and variations thereof. Note that the image size used for IPTA processing (500 pixels) was smaller than that used for the other processing techniques (1000 pixels) for the Los Angles Red Line site because it is very

difficult to unwrap the images correctly using temporal unwrapping techniques across portions of the image that have few coherent scatters (e.g. the Santa Monica Mountains).

The Interferometric Point Target Analysis approach utilizes the same MSP processing steps and the same ISP co-registration and resampling process as the traditional interferometric approach. However, after the SLC's are resampled into one common master only a clip of the RSLC images are used. The clip size for IPTA (500 pixels) is smaller than the clip size used in the enhanced spatial processing technique (1000 pixels) because it is more difficult to unwrap large images using the IPTA processing technique. Also, after a clip is taken, the RSLC images are again resampled to ensure the images are precisely co-registered. Following re-sampling of the RSLC image clips, the clipped images are converted from the pixel domain to the point domain, in which every pixel is taken to be one point. Using these point domain RSLC images, the interferograms are temporally unwrapped in the point domain, by selecting points in the image which do not change with time, instead of spatially unwrapped. By using temporal unwrapping, the individual components of the phase (topography, deformation, atmosphere, and noise) can be separated. This analysis method also produces time-rate of deformation plots by selecting on individual points (pixels) within the image. This approach is not limited by short time period, short baseline interferograms as the correctly unwrapped short baseline interferograms are used as an unwrapping model to unwrap long baseline interferograms.
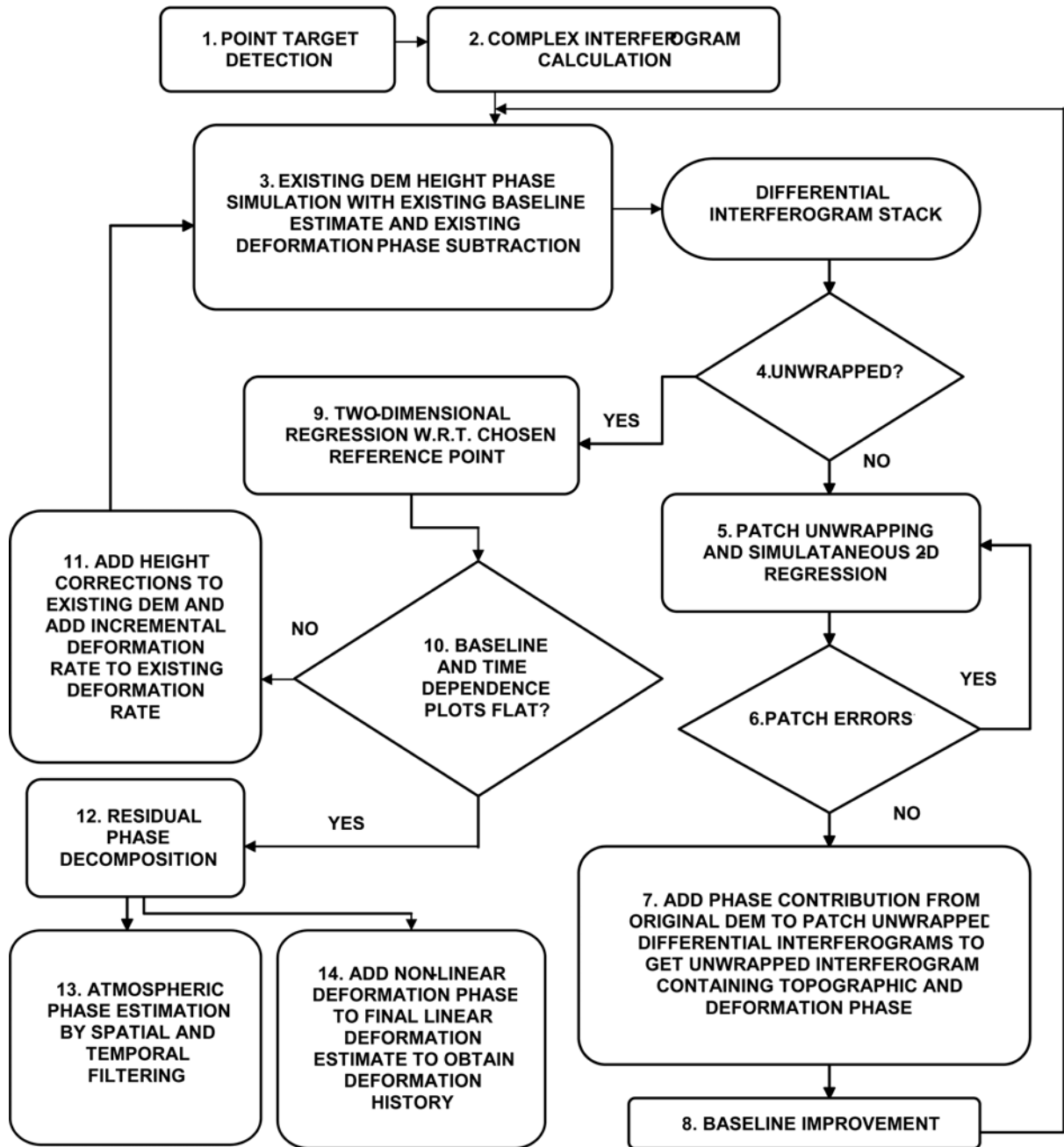
Figure 4.18. IPTA processing flow (from Manjunath, 2008).

4.4.5   Multiple-Baseline Interferometric Synthetic Aperture Radar (InSAR) Processing

The over-constrained multi-baseline linear decomposition regression analysis uses interferogram images obtained from the enhanced spatial processing. However, unlike stacking which was conducted on the enhanced spatial images the multiple-baseline

102

technique creates an interferogram showing the total cumulative phase at various time steps (the time steps correspond to each RSLC image). For the analysis to be over-constrained, each image must be used at least twice to create baselines with other images less than a certain threshold. Because each RSLC image is used at least twice, and multiple images overlap each time step (one time step per RSLC image), the differential interferometric phase is calculated at each time step using a single value decomposition.

The processing flow for multiple-baseline processing is depicted in Figure 4.19. The processing flow is conducted using GAMMA remote sensing commands in a file entitled mb_commands.txt. This text file draws upon the mb GAMMA subroutine. A diff_tab file is required for the mb command to compute multiple differential interferograms. Like the stacking procedure, the diff_tab used for the mb procedure corresponds to the interferograms used to conduct the processing, and the time difference between the RSLC images used to make each interferogram. However, unlike the stacking procedure, only weighted, time dependent, non-equal time diff_tab files are used. Examples of the mb_commands.txt, and the diff_tab files for the Los Angeles Red Line site are provided in Appendix A.
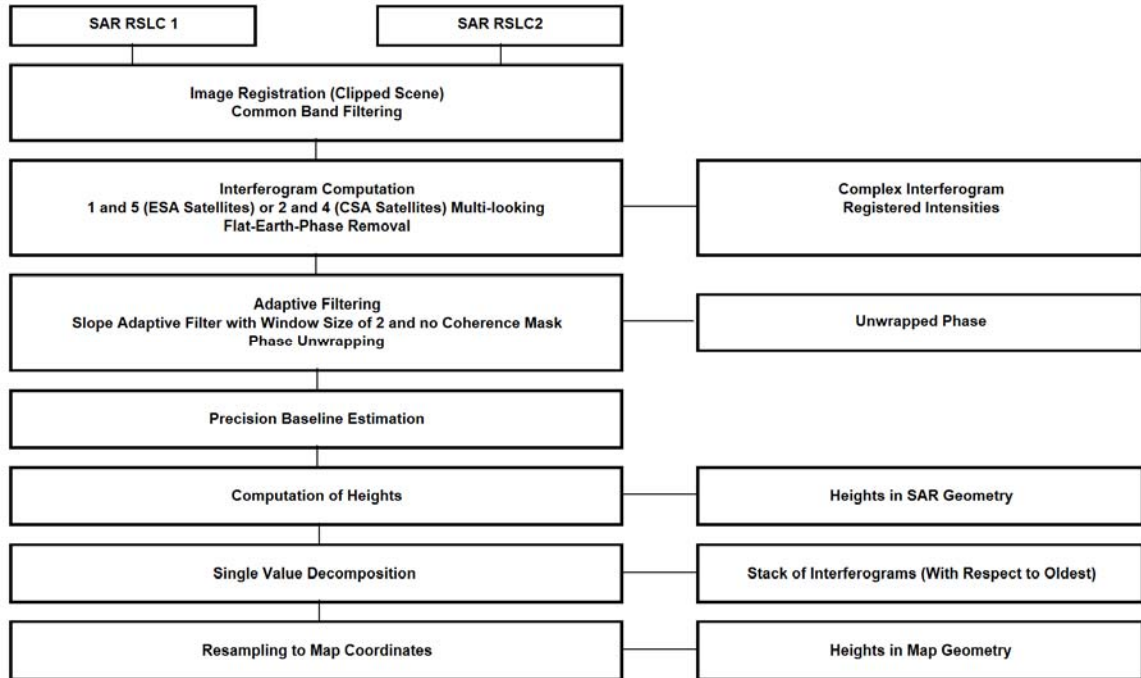
Figure 4.19. Multiple-baseline processing flow.

Post-processing is typically conducted during multiple-baseline processing to provide detailed information about site characteristics. The individual interferograms corresponding to each time step are usually viewed in radar viewing geometry then ortho-rectified.

4.5   Summary

Four different software programs were used for processing conducted for this research. The DESC-W, ERMapper, MATLAB, and GAMMA Remote Sensing software programs were utilized for pre-processing, processing, and post-processing of the obtained satellite-based SAR data.

The processing flow (and command line code) used to obtain estimates of subsidence using the aforementioned software programs was presented. This code enables users to identify available data, modify the data for use in detecting subsidence,

and quantify the amount of subsidence for a given site. Complete programming code (Gomez, 2009) that was modified as needed by the author is listed in Appendix A for completeness.

Five different processing techniques were utilized to produce estimates of deformation for various sites. These InSAR processing approaches include the: traditional processing technique, spatial processing technique, enhanced spatial processing technique, interferometric point target analysis (IPTA) processing technique, and multiple baseline processing technique. The specifics of the processing techniques are summarized in Table 4.2.

In addition to common pre-processing, several of the processing techniques use results from other processing techniques as well. For example, the IPTA, enhanced spatial, and multiple baseline techniques use clipped RSLC images produced using the spatial processing technique.

Table 4.2. Summary of different processing techniques.

	Multi-looking	**Filter Type**	**Filter Size**	**Scene Size (km)**	**Stacking**	**Time History**
Traditional	2 and 10	Spectral	32	100 x 100	No	No
Spatial	1 and 5	Spectral	32	100 x 100	No	No
Enhanced Spatial	1 and 5	Slope Adaptive	2	20 x 20	Yes	No
IPTA	1 and 1	Temporal	-	10 x 10	No	Yes
Multiple-Baseline	1 and 5	Slope Adaptive and Temporal	2	20 x 20	No	Yes

Chapter 5: Data and Data Processing Analyses

5.1   Introduction

Data obtained from the ERS-1, ERS-2, and ENVISAT satellites were used in analyzing the Los Angels Red Line and Mosul Dam sites. The manner in which the data was used for the traditional, spatial, ad-hoc enhanced spatial, enhanced spatial, IPTA and multiple-baseline processing techniques conducted on the Los Angeles Red Line and the traditional and enhanced spatial processing techniques conducted on the Mosul Dam site is discussed. Data for each site is described in Sections 5.2 and 5.3 for the Los Angeles Red Line Site and the Mosul Dam site, respectively. Various multi-looking, filtering, coherence masking and stacking combinations used to aid in spatial unwrapping of interferograms are discussed in Section 5.4.

5.2   Los Angeles Red Line Site Data

The Los Angeles California Metro Red Line site was analyzed to prove the concept of using various InSAR processing techniques to measure small and localized deformations. The semi-arid climate of this geographic location, the heavily populated (many coherent scatters) location, the sandy-gravelly geologic condition, and the large amount of satellite data are advantageous attributes for detecting subsidence.

As discussed in Chapter 3, the Los Angeles Red Line tunnel construction began in 1986 and finished in 1997. The area of interest to this study is MOS-2b, the portion of the LA Red Line that runs north/south along Vermont Avenue and east/west along Hollywood Boulevard. This section was constructed between May 1993 and May 1995. Known deformation of the tunnels occurred during construction from 1993 to 1995.

Excavation work to construct the tunnels resulted in large ground movements of known magnitude.

In order for the satellites to detect deformation, pre- and post-deformation images must be acquired. The earliest available satellite image of the site location is provided by the ERS-1 satellite image dated June 1, 1992, prior to the start of construction for MOS-2b. Post-tunneling subsidence may occur due to stress relaxation in the soils surrounding the tunnel. Therefore, although tunneling of the MOS-2b segment was completed in 1997, post-construction data collected from the ERS-2 satellite were acquired until November 2000, in order to ensure all post-construction deformation was monitored.

5.2.1 *Preliminary Data Characteristics*

Fifty-two, 100 kilometer by 100 kilometer, commercially available (ESA), C-Band ERS-1, and ERS-2 Synthetic Aperture Radar (SAR) images of the Los Angeles, California Area were acquired from the WInSAR consortium. This consortium is comprised of: the National Science Foundation (NSF), the United States Geological Survey (USGS), the European Space Agency (ESA), and the National Aeronautics and Space Administration (NASA).

Although the ESA archive contains over 120 images for the Los Angeles Area, 52 selected scenes from Track 442, Frame 2925 were acquired during the time span from June 1992 to November 2000, which overlaps the time of tunnel construction and post-construction. Of the 52 scenes, 20 of the scenes are ERS-1 images (Table 5.1) and 32 of the scenes are ERS-2 images (Table 5.2). The baselines shown in both tables are calculated with respect to the first orbit (Orbit 4595) in Table 5.1 (note the baseline for orbit 4595 is 0). The times shown in both tables are also shown with respect to the first

orbit (Orbit 4595) in Table 5.1 (note the time for orbit 4595 is 0). ERS-1 Orbits 22474, 22975, 23476, and 23977 correspond to the ERS-2 tandem pairs (i.e. ERS-2 passing one day after ERS-1) with ERS-2 Orbits 2801, 3302, 3803, and 4304, respectively. Negative baseline values indicate that the slave image was acquired to the right of the master image position, while positive values indicate the slave image was acquire to the left of the master image position (the master image for Table 5.1 and Table 5.2 is Orbit 4595). The values displayed in Tables 5.1 and 5.2 (Platform, Date, Orbit, Perpendicular Baseline, and Time) were obtained from the ESA program DESC-W discussed previously in Section 4.3.1.1.

Table 5.1. List of acquired ERS-1 data covering the Los Angeles Red Line Metro System.

Platform	Date	Orbit	Perpendicular Baseline (m)	Time (Days)
ERS-1	1992/06/01	04595	0	0
ERS-1	1992/09/14	06098	361	105
ERS-1	1992/10/19	06599	-388	140
ERS-1	1992/11/23	07100	90	175
ERS-1	1992/12/28	07601	-654	210
ERS-1	1993/08/30	11108	-547	455
ERS-1	1993/10/04	11609	-237	490
ERS-1	1993/11/08	12110	-29	525
ERS-1	1995/04/05	19468	-448	1038
ERS-1	1995/05/10	19969	-1217	1073
ERS-1	1995/06/14	20470	-316	1108
ERS-1	1995/07/19	20971	-123	1143
ERS-1	1995/08/23	21472	-224	1178
ERS-1	1995/09/27	21973	-22	1213
ERS-1	1995/11/01	22474	619	1248
ERS-1	1995/12/06	22975	-18	1283
ERS-1	1996/01/10	23476	-53	1318
ERS-1	1996/02/14	23977	437	1353
ERS-1	1996/04/24	24979	637	1423
ERS-1	1996/05/29	25480	-571	1458

Table 5.2. List of acquired ERS-2 data covering the Los Angeles Red Line Metro System.

Platform	Date	Orbit	Perpendicular Baseline (m)	Time (Days)
ERS-2	1995/11/02	02801	472	1249
ERS-2	1995/12/07	03302	-168	1284
ERS-2	1996/01/11	03803	-169	1319
ERS-2	1996/02/15	04304	457	1354
ERS-2	1996/07/04	06308	100	1494
ERS-2	1996/09/12	07310	-388	1564
ERS-2	1996/10/17	07811	192	1599
ERS-2	1996/11/21	08312	930	1634
ERS-2	1996/12/26	08813	-314	1669
ERS-2	1997/03/06	09815	-212	1739
ERS-2	1997/04/10	10316	417	1774
ERS-2	1997/05/15	10817	-183	1809
ERS-2	1997/06/19	11318	-282	1844
ERS-2	1997/07/24	11819	-161	1879
ERS-2	1997/11/06	13322	-950	1984
ERS-2	1997/12/11	13823	-869	2019
ERS-2	1998/01/15	14324	-451	2054
ERS-2	1998/02/19	14825	-541	2089
ERS-2	1998/08/13	17330	-171	2264
ERS-2	1998/09/17	17831	-1007	2299
ERS-2	1998/10/22	18332	-597	2334
ERS-2	1998/11/26	18833	-344	2369
ERS-2	1998/12/31	19334	-1051	2404
ERS-2	1999/02/04	19835	-630	2439
ERS-2	1999/03/11	20336	-270	2474
ERS-2	1999/07/29	22340	213	2614
ERS-2	1999/10/07	23342	-595	2684
ERS-2	1999/12/16	24344	278	2754
ERS-2	2000/05/04	26348	-255	2894
ERS-2	2000/06/08	26849	-446	2929
ERS-2	2000/08/17	27851	-339	2999
ERS-2	2000/11/30	29354	-326	3104

Different pairs of images were used during processing conducted using different processing techniques. For all of the processing techniques (traditional, spatial, enhanced spatial, IPTA, and multiple baseline), all images were initially resampled into the viewing geometry of Orbit 11609 creating resampled single look complex (RSLC) images. Orbit 11609 was selected because it produced the shortest average baselines with respect to the other images (Table 5.3). In producing the shortest average baseline, this master scene is

paired with fourteen other scenes to form interferometric pairs with baselines less than 100 meters and seven other scenes to form interferometric pairs with baselines between 100 and 200 meters. Thus, twenty-one interferometric pairs were formed with baselines less than 200 meters.

Table 5.3. Average baseline length for different master scenes for the L.A. Red Line.

Platform	Master Scene Orbit	Avg. Magnitude Perpendicular Baseline (m)	Platform	Master Scene Orbit	Avg. Magnitude Perpendicular Baseline (m)
ERS-1	04595	417	ERS-2	07811	417
ERS-1	06098	631	ERS-2	08312	631
ERS-1	06599	385	ERS-2	08813	520
ERS-1	07100	461	ERS-2	09815	1145
ERS-1	07601	529	ERS-2	10316	365
ERS-1	11108	459	ERS-2	10817	360
ERS-1	11609	359	ERS-2	11318	672
ERS-1	12110	405	ERS-2	11819	362
ERS-1	19468	408	ERS-2	13322	361
ERS-1	19969	1002	ERS-2	13823	366
ERS-1	20470	365	ERS-2	14324	755
ERS-1	20971	376	ERS-2	14825	691
ERS-1	21472	359	ERS-2	17330	410
ERS-1	21973	407	ERS-2	17831	455
ERS-1	22474	846	ERS-2	18332	364
ERS-1	22975	409	ERS-2	18833	804
ERS-1	23476	397	ERS-2	19334	489
ERS-1	23977	687	ERS-2	19835	371
ERS-1	24979	862	ERS-2	20336	844
ERS-1	25480	473	ERS-2	22340	360
ERS-2	02801	715	ERS-2	23342	440
ERS-2	03302	364	ERS-2	24344	532
ERS-2	03803	364	ERS-2	26348	487
ERS-2	04304	703	ERS-2	26849	575
ERS-2	06308	466	ERS-2	27851	407
ERS-2	07310	385	ERS-2	29354	736

Coordinates of the approximately 100 km by 100 km images (after resampling into Orbit 11609 viewing geometry) are presented in Table 5.4 in SAR and geographical coordinates. The intensity image is displayed in Figure 5.1, in which the image is

displayed in the SAR viewing geometry. SAR viewing geometry is flipped north-south for images which are imaged when the platform is in a descending orbit and flipped east-west when the platform is in an ascending orbit. Initial image registration was accomplished using the approximately 100 km by 100 km images for the traditional and spatial processing techniques (Sections 5.2.2 and 5.2.3, respectively). For the other processing techniques, portions (clips) of the images are used as discussed in Sections 5.2.4 through 5.2.7.

Table 5.4. Coordinates of RSLC images used for traditional and spatial InSAR processing for the L.A. Red Line.

Azimuth Pixel	Range Pixel	WGS84 Latitude (^{o})	WGS84 Longitude (^{o})
0	0	34.04	-117.98
0	4911	34.22	-119.03
28855	0	33.02	-118.24
28855	4911	33.20	-119.28
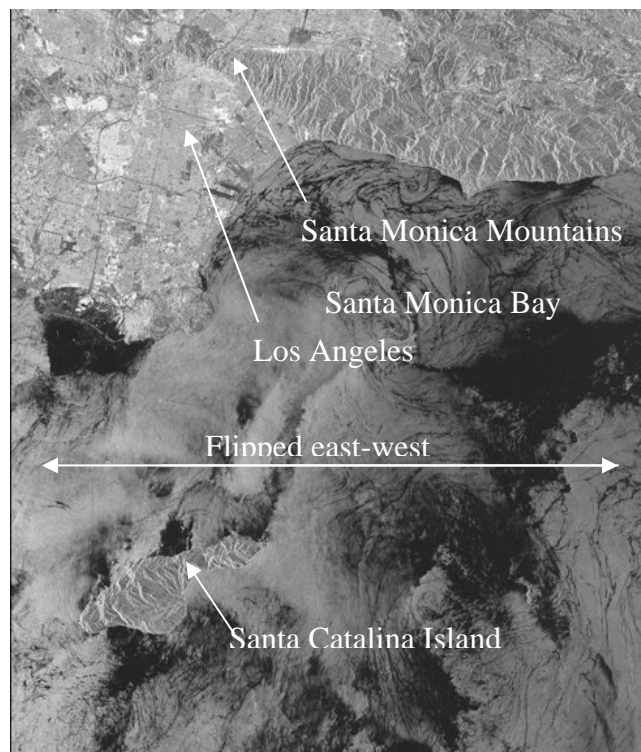
Figure 5.1. Multi-looked intensity image of the Los Angeles Red Line site (whole scene, 100 km by 100 km, Orbit 11609, 1 and 5 looks, SAR viewing geometry).

111

5.2.2   Traditional Processing

The first processing technique performed for the Los Angeles Red Line site was traditional processing. During this processing, all of the fifty-two 100 km by 100 km images were resampled into the viewing geometry of Orbit 11609 as discussed in Section 5.2.1. Twenty-one 100 km by 100 km interferograms with baselines less than 200 meters were also developed using a selection of the fifty-two resampled images for the traditional processing.

5.2.3   Spatial Processing

The second processing technique performed for the Los Angeles Red Line site was spatial processing. The same images fifty-two 100 km by 100 km images, which were resampled for during the traditional processing, were used for spatial processing. Just as with the traditional processing, twenty-one interferograms with baselines less than 200 meters were developed using a selection of the fifty-two resampled images for spatial processing

5.2.4   Ad-hoc Enhanced Spatial Processing

The third processing technique performed for the Los Angels Red Line site was ad-hoc enhanced spatial processing. Here, ad-hoc is used to refer to the user-defined image selection method used during processing. During processing conducted using the ad-hoc enhanced spatial processing technique, different interferometric pairs with varying masters were selected. The user-defined selection of images was ad-hoc because short baselines (less than 200 meters as with traditional and spatial processing) images were selected between the pairs of images, and because the images spanned the time of construction. All of the pairs contained one pre-construction or early-construction image

(pre August 1993), and one post-construction or late-construction image (post August 1993). The RSLC images used for the ad-hoc enhanced spatial processing technique are listed in Table 5.5 the baseline and time values listed in Table 5.5 are with respect to the first acquisition (Orbit 04595). These images are approximately 20 km by 20 km clips of the approximately 100 km by 100 km images used for the traditional and spatial processing techniques. After clipping, the images were again resampled to ensure that the clipping procedure did not cause the images to become unregistered. For the ad-hoc enhanced spatial processing technique, the images were again resampled relative to the Orbit 11609 viewing geometry during the after clipping resampling. The coordinates of the corners of the clipped image are presented in Table 5.6 and the RSLC intensity image for the master viewing geometry is shown in Figure 5.2. The interferograms produced using these resampled RSLC images and used for the ad-hoc enhanced spatial processing technique are presented in Table 5.7. These interferograms are identified using the orbit numbers corresponding to the images used to make the interferogram. The time listed is the time in days between the two image acquisitions for each interferogram. Note that the baseline magnitude for interferogram number 3 is larger than the 200 meters threshold. This pair was accidentally used for this processing. All of the other interferometric pairs have baselines less than the desired 200 meters, upon which the ad-hoc selection criteria was based.

Table 5.5. Resampled RSLC images used in the ad-hoc enhanced spatial processing technique for the LA Red Line.

RSLC #	Platform	Date	Orbit	Perpendicular Baseline (m)	Time
1	ERS-1	1992/06/01	04595	0	0
2	ERS-1	1992/09/14	06098	361	105
3	ERS-1	1992/10/19	06599	-388	140
4	ERS-1	1992/11/23	07100	90	175
5	ERS-1	1993/08/30	11108	-547	455
6	ERS-1	1993/10/04	11609	-237	490
7	ERS-1	1993/11/08	12110	-29	525
8	ERS-1	1995/04/05	19468	-448	1038
9	ERS-1	1995/06/14	20470	-316	1108
10	ERS-1	1995/07/19	20971	-123	1143
11	ERS-1	1995/08/23	21472	-224	1178
12	ERS-1	1995/09/27	21973	-22	1213
13	ERS-1	1995/12/06	22975	-18	1283
14	ERS-2	1995/11/02	02801	472	1249
15	ERS-2	1995/12/07	03302	-168	1284

Table 5.6. Coordinates of the approximately 20 km by 20 km RSLC images used for the ad-hoc enhanced spatial InSAR processing technique for the LA Red Line.

Azimuth Pixel	Range Pixel	WGS84 Latitude (^{o})	WGS84 Longitude (^{o})
0	0	34.20	-118.19
0	999	34.24	-118.41
4999	0	34.02	-118.23
4999	999	34.06	-118.46
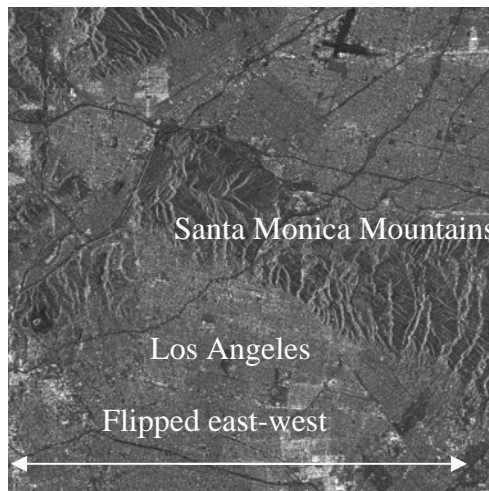
Figure 5.2. Multi-looked intensity image of the Los Angeles Red Line site (clipped scene, 20 km by 20 km, Orbit 04595, 1 and 5 Looks, SAR viewing geometry).

114

Table 5.7. Interferograms used for the ad-hoc enhanced spatial processing technique for the L.A. Red Line site.

Interferogram #	Interferogram ID	Perpendicular Baseline (m)	Time (Days)
1	19468-06599	-60	898
2	19468-11108	99	583
3	20470-04595	-316	1108
4	20470-06599	72	968
5	20470-11609	-79	618
6	20971-04595	-123	1143
7	20971-11609	114	653
8	20971-12110	-94	618
9	21472-06599	164	1038
10	21472-11609	13	688
11	21973-04595	-22	1213
12	21973-07100	-112	1038
13	21973-12110	7	688
14	22975-04595	-18	1283
15	22975-07100	-108	1108
16	22975-12110	11	758
17	02801-06098	111	1144
18	03302-04595	-168	1284
19	03302-12110	-139	759

5.2.5   Enhanced Spatial Processing

The fourth processing conducted for the Los Angeles Red Line was enhanced spatial processing. The scene selection process for the enhanced spatial processing technique was automated as opposed to the user-defined scene selection process for the ad-hoc enhanced spatial processing technique. As with the previous processing, during processing conducted using the enhanced spatial processing technique different interferometric pairs (combinations of images in which phase values are subtracted from one another) with varying masters were selected.   All of the selected pairs (interferograms) have baselines less than 125 meters. The pairs were selected using computer oversight and processed automatically.

Like the ad-hoc enhanced spatial processing, the images used for the enhanced spatial processing were clipped 20 km by 20 km images. However, unlike the ad-hoc enhanced

spatial processing, the images were resampled relative to the Orbit 04595 viewing geometry after clipping (Table 5.8). This viewing geometry was selected because Orbit 04595 is the first available image, and all images must be in sequential order with respect to the first image for processes requiring time weighting (as discussed later in this chapter). The baseline values and time differences presented in Table 5.8 are with respect to Orbit 04595. These baseline values are larger than the previously mentioned 125 meter baseline threshold used to select interferometric pairs. As discussed in Section 4.4.5, the forty-four images selected from the 52 available images and whose characteristic are presented in Table 5.8 were selected because each of the images must be used at least twice for the multi-baseline processing technique. Using these forty-four images, 207 multiple master-slave interferograms were produced with baselines between the RSLC images being less than 125 meters (Table 5.9). The interferograms presented in Table 5.9 are identified using the orbit numbers corresponding to the images used to make the interferogram. The time listed is the time in days between the two image acquisitions for each interferogram.

Table 5.8. Resampled RSLC images used in the enhanced spatial processing technique and the multiple-baseline processing technique for the LA Red Line.

RSLC #	Platform	Date	Orbit	Perpendicular Baseline (m)	Time (days)
1	ERS-1	1992/06/01	04595	0	0
2	ERS-1	1992/09/14	06098	361	105
3	ERS-1	1992/10/19	06599	-387	140
4	ERS-1	1992/11/23	07100	90	175
5	ERS-1	1992/12/28	07601	-653	210
6	ERS-1	1993/08/30	11108	-546	455
7	ERS-1	1993/10/04	11609	-236	490
8	ERS-1	1993/11/08	12110	-28	525
9	ERS-1	1995/04/05	19468	-447	1038
10	ERS-1	1995/06/14	20470	-315	1108
11	ERS-1	1995/07/19	20971	-122	1143
12	ERS-1	1995/08/23	21472	-223	1178
13	ERS-1	1995/09/27	21973	-21	1213
14	ERS-2	1995/11/02	02801	472	1249
15	ERS-1	1995/12/06	22975	-17	1283
16	ERS-2	1995/12/07	03302	-167	1284
17	ERS-1	1996/01/10	23476	-52	1318
18	ERS-2	1996/01/11	03803	-168	1319
19	ERS-1	1996/02/14	23977	437	1353
20	ERS-2	1996/02/15	04304	457	1354
21	ERS-1	1996/05/29	25480	-570	1458
22	ERS-2	1996/07/04	06308	100	1494
23	ERS-2	1996/09/12	07310	-387	1564
24	ERS-2	1996/10/17	07811	192	1599
25	ERS-2	1996/12/26	08813	-313	1669
26	ERS-2	1997/03/06	09815	-211	1739
27	ERS-2	1997/04/10	10316	417	1774
28	ERS-2	1997/05/15	10817	-182	1809
29	ERS-2	1997/06/19	11318	-281	1844
30	ERS-2	1997/07/24	11819	-160	1879
31	ERS-2	1998/01/15	14324	-450	2054
32	ERS-2	1998/02/19	14825	-540	2089
33	ERS-2	1998/08/13	17330	-170	2264
34	ERS-2	1998/10/22	18332	-596	2334
35	ERS-2	1998/11/26	18833	-343	2369
36	ERS-2	1999/02/04	19835	-629	2439
37	ERS-2	1999/03/11	20336	-269	2474
38	ERS-2	1999/07/29	22340	213	2614
39	ERS-2	1999/10/07	23342	-594	2684
40	ERS-2	1999/12/16	24344	278	2754
41	ERS-2	2000/05/04	26348	-254	2894
42	ERS-2	2000/06/08	26849	-445	2929
43	ERS-2	2000/08/17	27851	-338	2999
44	ERS-2	2000/11/30	29354	-325	3104

Table 5.9. Interferograms used in the enhanced spatial processing technique and the multiple-baseline processing technique for the L.A. Red Line.

#	Interfer. ID			Base.	Time	#	Interfer. ID			Base.	Time
1	4595	-	7100	-91	175	46	11609	-	21472	-13	688
2	4595	-	12110	29	525	47	11609	-	3302	-69	794
3	4595	-	20971	122	1143	48	11609	-	3803	-68	829
4	4595	-	21973	21	1213	49	11609	-	8813	77	1179
5	4595	-	22975	17	1283	50	11609	-	9815	-25	1249
6	4595	-	23476	52	1318	51	11609	-	10817	-54	1319
7	4595	-	6308	-100	1494	52	11609	-	11318	45	1354
8	6098	-	2801	-111	1144	53	11609	-	11819	-76	1389
9	6098	-	23977	-76	1248	54	11609	-	17330	-66	1774
10	6098	-	4304	-96	1249	55	11609	-	18833	108	1879
11	6098	-	10316	-57	1669	56	11609	-	20336	33	1984
12	6098	-	24344	83	2649	57	11609	-	26348	18	2404
13	6599	-	19468	60	898	58	11609	-	27851	102	2509
14	6599	-	20470	-72	968	59	11609	-	29354	89	2614
15	6599	-	7310	0	1424	60	12110	-	20971	94	618
16	6599	-	8813	-75	1529	61	12110	-	21973	-7	688
17	6599	-	11318	-106	1704	62	12110	-	22975	-12	758
18	6599	-	14324	63	1914	63	12110	-	23476	24	793
19	6599	-	18833	-44	2229	64	19468	-	25480	123	420
20	6599	-	20336	-119	2334	65	19468	-	7310	-60	526
21	6599	-	26849	58	2789	66	19468	-	14324	3	1016
22	6599	-	27851	-49	2859	67	19468	-	14825	92	1051
23	6599	-	29354	-63	2964	68	19468	-	18833	-104	1331
24	7100	-	12110	120	350	69	19468	-	26849	-3	1891
25	7100	-	21973	112	1038	70	19468	-	27851	-109	1961
26	7100	-	22975	108	1108	71	19468	-	29354	-123	2066
27	7100	-	6308	-9	1319	72	20470	-	21472	-92	70
28	7100	-	7811	-102	1424	73	20470	-	7310	72	456
29	7100	-	22340	-122	2439	74	20470	-	8813	-3	561
30	7601	-	11108	-106	245	75	20470	-	9815	-104	631
31	7601	-	25480	-82	1248	76	20470	-	11318	-34	736
32	7601	-	14825	-113	1879	77	20470	-	18833	28	1261
33	7601	-	18332	-57	2124	78	20470	-	20336	-47	1366
34	7601	-	19835	-24	2229	79	20470	-	26348	-61	1786
35	7601	-	23342	-59	2474	80	20470	-	27851	23	1891
36	11108	-	19468	-99	583	81	20470	-	29354	9	1996
37	11108	-	25480	24	1003	82	20971	-	21472	101	35
38	11108	-	14324	-96	1599	83	20971	-	21973	-101	70
39	11108	-	14825	-7	1634	84	20971	-	22975	-105	140
40	11108	-	18332	49	1879	85	20971	-	3302	45	141
41	11108	-	19835	82	1984	86	20971	-	23476	-70	175
42	11108	-	23342	48	2229	87	20971	-	3803	46	176
43	11108	-	26849	-102	2474	88	20971	-	9815	89	596
44	11609	-	20470	79	618	89	20971	-	10817	60	666
45	11609	-	20971	-114	653	90	20971	-	11819	38	736

Table 5.9. Interferograms used in the enhanced spatial processing technique and the multiple-baseline processing technique for the L.A. Red Line. (Cont.)

#	Interfer. ID			Base.	Time	#	Interfer. ID			Base.	Time
91	20971	-	17330	48	1121	136	25480	-	14825	-31	631
92	21472	-	3302	-56	106	137	25480	-	18332	25	876
93	21472	-	3803	-55	141	138	25480	-	19835	58	981
94	21472	-	8813	90	491	139	25480	-	23342	24	1226
95	21472	-	9815	-12	561	140	6308	-	7811	-93	105
96	21472	-	10817	-41	631	141	6308	-	22340	-113	1120
97	21472	-	11318	58	666	142	7310	-	8813	-74	105
98	21472	-	11819	-63	701	143	7310	-	11318	-106	280
99	21472	-	17330	-53	1086	144	7310	-	14324	63	490
100	21472	-	18833	121	1191	145	7310	-	18833	-43	805
101	21472	-	20336	46	1296	146	7310	-	20336	-118	910
102	21472	-	26348	31	1716	147	7310	-	26849	58	1365
103	21472	-	27851	115	1821	148	7310	-	27851	-49	1435
104	21472	-	29354	102	1926	149	7310	-	29354	-62	1540
105	21973	-	22975	-4	70	150	7811	-	22340	-20	1015
106	21973	-	23476	31	105	151	7811	-	24344	-85	1155
107	21973	-	6308	-122	281	152	8813	-	9815	-102	70
108	2801	-	23977	35	104	153	8813	-	11318	-31	175
109	2801	-	4304	15	105	154	8813	-	18833	31	700
110	2801	-	10316	55	525	155	8813	-	20336	-44	805
111	22975	-	23476	35	35	156	8813	-	26348	-58	1225
112	22975	-	6308	-117	211	157	8813	-	27851	26	1330
113	3302	-	23476	-115	34	158	8813	-	29354	12	1435
114	3302	-	3803	1	35	159	9815	-	10817	-29	70
115	3302	-	9815	44	455	160	9815	-	11318	71	105
116	3302	-	10817	15	525	161	9815	-	11819	-51	140
117	3302	-	11318	115	560	162	9815	-	17330	-41	525
118	3302	-	11819	-7	595	163	9815	-	20336	58	735
119	3302	-	17330	3	980	164	9815	-	26348	43	1155
120	3302	-	20336	102	1190	165	9815	-	29354	114	1365
121	3302	-	26348	88	1610	166	10817	-	11318	100	35
122	23476	-	3803	116	1	167	10817	-	11819	-22	70
123	23476	-	11819	108	561	168	10817	-	17330	-12	455
124	23476	-	17330	118	946	169	10817	-	20336	87	665
125	3803	-	9815	43	420	170	10817	-	26348	73	1085
126	3803	-	10817	14	490	171	11318	-	11819	-122	35
127	3803	-	11318	114	525	172	11318	-	17330	-111	420
128	3803	-	11819	-8	560	173	11318	-	18833	62	525
129	3803	-	17330	2	945	174	11318	-	20336	-13	630
130	3803	-	20336	101	1155	175	11318	-	26348	-27	1050
131	3803	-	26348	87	1575	176	11318	-	27851	57	1155
132	23977	-	4304	-20	1	177	11318	-	29354	43	1260
133	23977	-	10316	20	421	178	11819	-	17330	10	385
134	4304	-	10316	39	420	179	11819	-	20336	109	595
135	25480	-	14324	-120	596	180	11819	-	26348	95	1015

Table 5.9. Interferograms used in the enhanced spatial processing technique and the multiple-baseline processing technique for the L.A. Red Line. (Cont.)

#	Interfer. ID			Base.	Time	#	Interfer. ID			Base.	Time
181	14324	-	14825	89	35	195	18833	-	26849	101	560
182	14324	-	18833	-107	315	196	18833	-	27851	-5	630
183	14324	-	26849	-6	875	197	18833	-	29354	-19	735
184	14324	-	27851	-112	945	198	19835	-	23342	-35	245
185	14825	-	18332	56	245	199	20336	-	26348	-14	420
186	14825	-	19835	89	350	200	20336	-	27851	70	525
187	14825	-	23342	54	595	201	20336	-	29354	56	630
188	14825	-	26849	-95	840	202	22340	-	24344	-65	140
189	17330	-	20336	99	210	203	26348	-	27851	84	105
190	17330	-	26348	84	630	204	26348	-	29354	70	210
191	18332	-	19835	33	105	205	26849	-	27851	-106	70
192	18332	-	23342	-2	350	206	26849	-	29354	-120	175
193	18833	-	20336	-75	105	207	27851	-	29354	-14	105
194	18833	-	26348	-89	525						

The enhanced spatial processing technique and the ad-hoc enhanced spatial processing technique both used the same image size. The RSLC SAR coordinates and the geographical coordinates for the corners of the images used were previously presented in Table 5.6, and shown in Figure 5.2.

5.2.6 *Multiple-Baseline Processing*

The fifth processing performed for the Los Angeles Red Line was multiple-baseline processing. The multiple-baseline processing used the same forty-four 20 km by 20 km resampled images, and the same 207 interferograms produced in enhanced spatial processing. The histogram presented in Figure 5.3 displays how often each RSLC image is used during multiple-baseline processing (i.e. how many interferometric pairs each image makes with the other images).
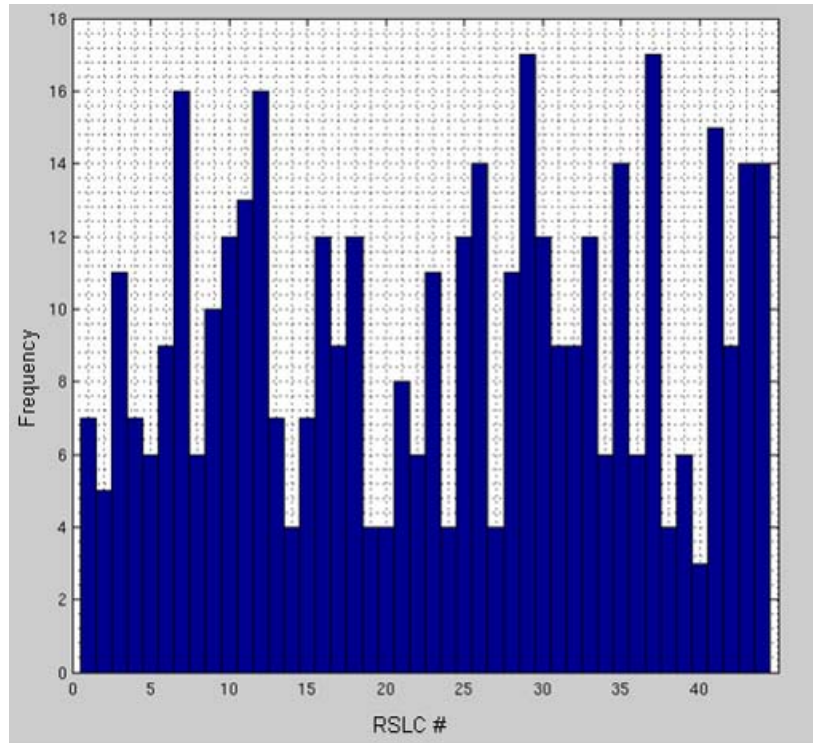
Figure 5.3. Histogram showing how frequently various RSLC images were used in the multi-baseline processing technique for the LA Red Line.

5.2.7   IPTA Processing

During processing conducted using the Interferometric Point Target Analysis (IPTA) processing technique, a smaller clip of the entire 100 kilometer by 100 kilometer images was used. The 10 kilometer by 10 kilometer clip only contains the MOS-2b segment of the Los Angeles Red Line site, and does not contain the Santa Monica Mountains and the Sacramento Valley like the 20 kilometer by 20 kilometer clip used for the ad-hoc enhanced spatial, enhanced spatial, and multi-baseline processing techniques. The RSLC SAR coordinates and the geographical coordinates for the corners of the images used for the IPTA processing technique are presented in Table 5.10 and shown in Figure 5.4.

121

Table 5.10. Coordinates of the approximately 10 km by 10 km RSLC images used for the IPTA processing technique for the LA Red Line.

Azimuth Pixel	Range Pixel	WGS84 Latitude (^{o})	WGS84 Longitude (^{o})
0	0	34.04	-118.29
0	499	34.06	-118.40
2499	0	33.95	-118.31
2499	499	33.97	-118.43
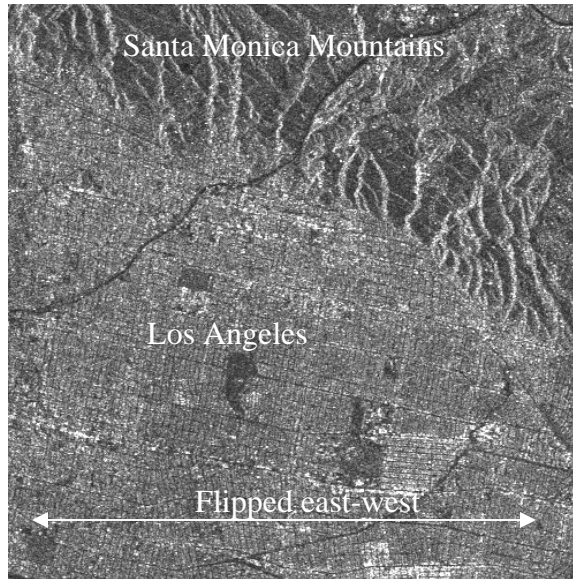
Figure 5.4. Multi-looked intensity image of the Los Angeles Red Line site (clipped scene, 10 km by 10 km, Orbit 04595, 1 and 5 Looks, SAR viewing geometry).

This portion (Table 5.10, Figure 5.4) of all 52 ERS-1 and ERS-2 RSLC images described previously in Table 5.1 and Table 5.2 were used for the IPTA processing technique. Similarly to how the RSLC images were resampled following clipping during the ad-hoc enhanced spatial processing technique, the RSLC images used for the IPTA processing technique were also resampled after clipping. Again, the clipped RSLC images were resampled into the viewing geometry of Orbit 11609 (the image with the shortest baseline average of the LA Red Line site) as was conducted with the as-hoc enhanced spatial processing technique. Although the same processing techniques were used, the clips of the scenes used for IPTA processing were 500 pixels by 500 pixels as

opposed to the 1000 pixels by 1000 pixel images used for ad-hoc enhanced spatial, enhanced spatial processing technique. Fifty-two interferograms, including the auto-interferogram (zero baseline and zero time span) were created using these 500 pixel by 500 pixel RSLC images (Table 5.11).

Table 5.11. Interferograms used in the IPTA processing technique for the LA Red Line.

#	Interfer. ID			Base.	Time	#	Interfer. ID			Base.	Time
1	11609	-	4595	-237	-490	27	11609	-	7811	-429	1109
2	11609	-	6098	-598	-385	28	11609	-	8312	-1167	1144
3	11609	-	6599	151	-350	29	11609	-	8813	77	1179
4	11609	-	7100	-327	-315	30	11609	-	9815	-25	1249
5	11609	-	7601	417	-280	31	11609	-	10316	-654	1284
6	11609	-	11108	310	-35	32	11609	-	10817	-54	1319
7	11609	-	11609	0	0	33	11609	-	11318	45	1354
8	11609	-	12110	-208	35	34	11609	-	11819	-76	1389
9	11609	-	19468	211	548	35	11609	-	13322	713	1494
10	11609	-	19969	980	583	36	11609	-	13823	632	1529
11	11609	-	20470	79	618	37	11609	-	14324	214	1564
12	11609	-	20971	-114	653	38	11609	-	14825	304	1599
13	11609	-	21472	-13	688	39	11609	-	17330	-66	1774
14	11609	-	21973	-215	723	40	11609	-	17831	770	1809
15	11609	-	22474	-856	758	41	11609	-	18332	360	1844
16	11609	-	2801	-219	793	42	11609	-	18833	107	1879
17	11609	-	22975	-184	828	43	11609	-	19334	814	1914
18	11609	-	3302	-674	863	44	11609	-	19835	393	1949
19	11609	-	23476	-874	933	45	11609	-	20336	33	1984
20	11609	-	3803	334	968	46	11609	-	22340	-450	2124
21	11609	-	23977	-709	759	47	11609	-	23342	358	2194
22	11609	-	4304	-69	794	48	11609	-	24344	-515	2264
23	11609	-	24979	-68	829	49	11609	-	26348	18	2404
24	11609	-	25480	-780	934	50	11609	-	26849	209	2439
25	11609	-	6308	-337	1004	51	11609	-	27851	102	2509
26	11609	-	7310	151	1074	52	11609	-	29354	89	2614

5.2.8 Digital Elevation Model Used for Processing

For all processing techniques conducted on the LA Red Line site, a Shuttle Radar Topography Mission (SRTM) Digital Elevation Model (DEM) was used to subtract topographic phase from the interferometric pairs. Domestic SRTM data are sampled at

123

one arc-second, corresponding to 30 meter by 30 meter pixels. Depending on the multi-looking of the RSLC images, the DEM image is either over-sampled or sub-sampled to form either 20 meter by 20 meter (1 and 5 look multi-look imagery) pixels or 40 meter by 40 meter (2 and 10 look multi-look imagery) pixels, respectively. The DEM image is clipped to match the RSLC images.

The DEM image was used for subtraction of the topographic phase and ortho-rectification of the radar images. A simulated SAR intensity image (projected DEM in SAR viewing geometry, with elevations values assigned different intensity values) derived from the Los Angeles Red Line Site SRTM DEM is presented in Figure 5.5. The simulated SAR SRTM DEM presented in Figure 5.5 is a 20 km by 20 km clip of the 100 km by 100 km simulated SAR intensity image which was used for the traditional and spatial processing techniques. The 20 km by 20 km simulated SAR intensity image shown in Figure 5.5 was used for the ad-hoc enhanced spatial, enhanced spatial, and multi-baseline processing techniques. A smaller 10 km by 10 km clip of the simulated SAR SRTM DEM was also used for IPTA processing.
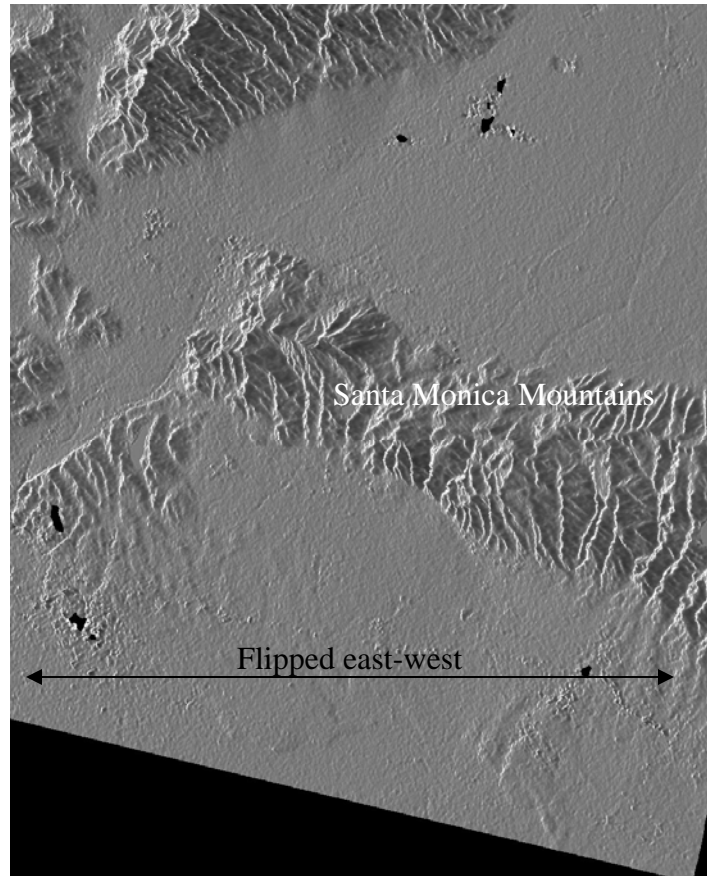
Figure 5.5. Simulated SAR intensity image of LA Red Line site derived from SRTM 1-arc second DEM (SAR viewing geometry).

5.3   Mosul Dam Site Data

The traditional and enhanced spatial processing techniques were utilized for analysis of the Mosul Dam site. The multiple-baseline processing technique was also attempted. The sixteen RSLC images (March 2003 through April 2007) used for the processing are listed in Table 5.12. All of these images were resampled into the viewing geometry of Orbit 24144 (Figure 5.6) because it produced the shortest average baselines with respect to the other images. However, during the enhanced spatial processing and the multiple-baseline processing techniques, the images were resampled (by the computer without user input) into the viewing geometry of Orbit 05607 because it is the first obtained image of the site, and the RSLC images must be in sequential order for these

processing techniques. This automated resampling results in the images being resampled twice. These 11.5 km by 20.5 km RSLC images (600 pixels by 1064 pixels when multi-looked at 1-look in the range direction and 5-looks in the azimuth) are a clip of the 100 km by 100 km SLC images.

Table 5.12. RSLC images used for the Mosul Dam site.

RSLC #	Platform	Date	Orbit	Perpendicular Baseline (m)	Time
1	ENVISAT	2003/03/27	05607	0	0
2	ENVISAT	2003/05/01	06108	-725	35
3	ENVISAT	2004/06/24	12120	272	455
4	ENVISAT	2004/07/29	12621	-232	490
5	ENVISAT	2004/09/02	13122	60	525
6	ENVISAT	2004/10/07	13623	-955	560
7	ENVISAT	2004/12/16	14625	847	630
8	ENVISAT	2005/01/20	15126	-539	665
9	ENVISAT	2005/05/05	16629	-869	770
10	ENVISAT	2005/07/14	17631	-494	840
11	ENVISAT	2005/10/27	19134	-616	945
12	ENVISAT	2005/12/01	19635	844	980
13	ENVISAT	2006/05/25	22140	181	790
14	ENVISAT	2006/10/12	24144	-250	1295
15	ENVISAT	2006/12/21	25146	402	1365
16	ENVISAT	2007/04/05	26649	-264	1470
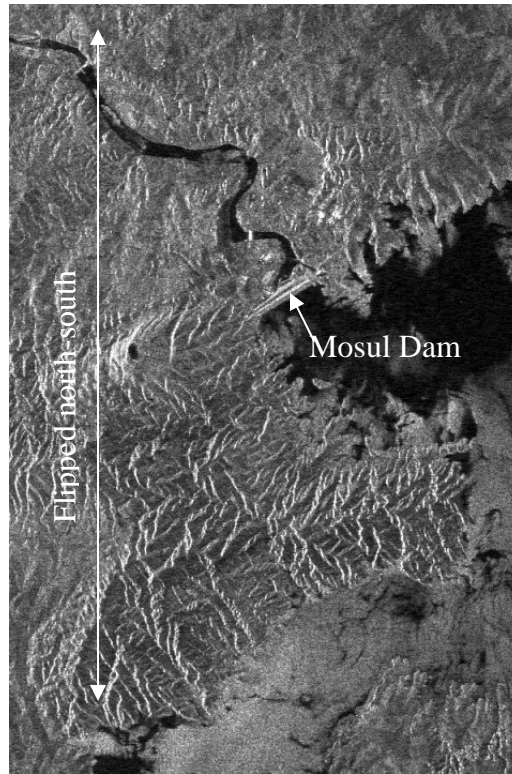
Figure 5.6. Multi-looked intensity image of the Mosul Dam site (clipped scene, 11.5 km by 20.5 km, Orbit 24144, 1 and 5 Looks, SAR viewing geometry).

For the enhanced spatial and multiple baseline processing, thirty-six interferograms with baselines less than 350 meters were created using multiple master and slave pair combinations of the 14 of 16 of RSLC images. Note RSLC images 7 (Orbit 14625) and 12 (Orbit 19635) were not used because these images did not make more than one interferometric pair with the other images (i.e. these two images only made on interferometric pair with each other which was less than 350 meters; each image must make at least two pairs in order to be used). The coordinates of the corners of the images are presented in Table 5.13, and the interferogram pairs are listed in Table 5.14. The histogram presented in Figure 5.7 displays how often each RSLC image was used (i.e. how many interferometric pairs each image makes with the other images).

Table 5.13. Coordinates of the approximately 11.5 km by 20.5 km RSLC images used for the enhanced spatial and multiple-baseline processing techniques for the Mosul Dam site.

Azimuth Pixel	Range Pixel	WGS84 Latitude (^{o})	WGS84 Longitude (^{o})
0	0	36.55	42.75
0	599	36.58	42.90
4499	0	36.71	42.70
4499	599	36.74	42.86

Table 5.14. Interferograms used in the enhanced spatial processing technique and the multiple-baseline processing technique for the Mosul Dam site.

#	Inter. ID			Base.	Time	#	Inter. ID			Base.	Time
1	5607	-	12120	-273	455	19	12621	-	26649	33	980
2	5607	-	12621	232	490	20	13122	-	22140	-121	630
3	5607	-	13122	-60	525	21	13122	-	24144	311	770
4	5607	-	22140	-181	1155	22	13122	-	25146	-342	840
5	5607	-	24144	251	1295	23	13122	-	26649	325	945
6	5607	-	26649	265	1470	24	13623	-	16629	-85	210
7	6108	-	13623	229	525	25	13623	-	19134	-339	385
8	6108	-	15126	-186	630	26	15126	-	16629	330	105
9	6108	-	16629	144	735	27	15126	-	17631	-45	175
10	6108	-	17631	-231	805	28	15126	-	19134	77	280
11	6108	-	19134	-109	910	29	15126	-	24144	-289	630
12	12120	-	13122	212	70	30	15126	-	26649	-275	805
13	12120	-	22140	91	700	31	16629	-	19134	-253	175
14	12120	-	25146	-130	910	32	17631	-	19134	122	105
15	12621	-	13122	-292	35	33	17631	-	24144	-244	455
16	12621	-	15126	307	175	34	17631	-	26649	-230	630
17	12621	-	17631	262	350	35	22140	-	25146	-221	210
18	12621	-	24144	18	805	36	24144	-	26649	14	175
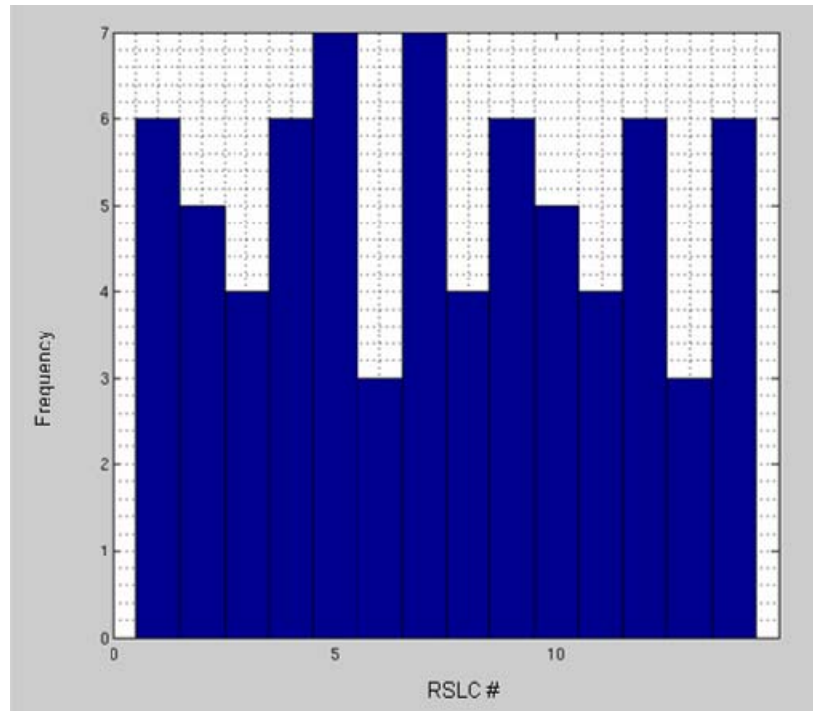
Figure 5.7. Histogram showing how frequently various RSLC images are used in the multi-baseline processing technique for the Mosul Dam site (disregarding image 7 and 12 from Table 5.12).

For all processing techniques conducted on the Mosul Dam site, a Shuttle Radar Topography Mission (SRTM) Digital Elevation Model (DEM) was used. Foreign SRTM data are sampled at 3 arc-second, corresponding to 90 meter by 90 meter pixels. All processing was conducted using 1-look in the range direction and 5-looks in the azimuth direction to create square 20 meter by 20 meter pixels. The DEM image was over-sampled to form 20 meter by 20 meter pixels, and clipped (11.5 km by 20.5 km) to match the RSLC images.

As with the Los Angeles DEM, the DEM image for the Mosul Dam site is used for subtraction of the topographic phase and ortho-rectification of the radar images. A simulated SAR intensity image of the Mosul Dam Site SRTM DEM is presented in Figure 5.8. This DEM was used for all the processing conducted on the Mosul Dam site (11.5 km by 20.5 km).

129
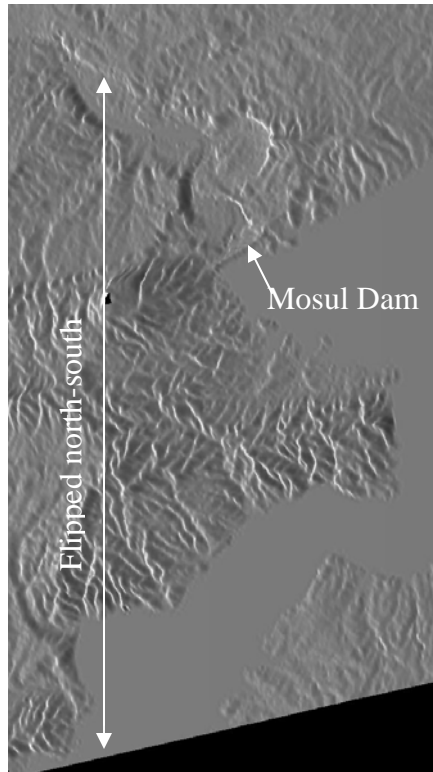
Figure 5.8. Simulated SAR image of Mosul Dam site SRTM three arc-second DEM (in SAR viewing geometry).

5.4   Spatial Unwrapping Processing Techniques

The four spatial processing techniques used in this work are identified as traditional, spatial, and enhanced spatial, and multiple-baseline. As discussed in Chapter 4, the variations in these processing techniques are the amount of multi-looking, the filter type and size, the scene size, and the amount of coherence masking and are summarized in Table 5.15.

Table 5.15. Summary of spatial processing technique parameters.

	Multi-looking	Filter Type	Coherence Mask (%)	Filter Size	Scene Size (km)
Traditional	2 and 10	Spectral	50	32	100 x 100
Spatial	1 and 5	Spectral	50	32	100 x 100
Enhanced Spatial	1 and 5	Slope Adaptive	0	2	20 x 20
Multiple-Baseline	1 and 5	Slope Adaptive and Temporal	0	2	20 x 20

Although processing for the traditional and spatial techniques are typically conducted on full 100 km by 100 km scenes, the techniques were applied to clipped images (similar to those created for enhanced spatial, multiple baseline) for comparison purposes. Whereas these names (traditional, spatial, enhanced spatial) have been applied to different combinations of multi-looking (2/10, 1/5 and 1/5), filter type (spectral, spectral, slope adaptive) and size (8, 8, 2) and coherence masks (50%, 50%, 0), respectively, a spectrum of multi-looking (1/5 and 2/10), filter type (spectral and slope adaptive), filter size (8, 16, 32 for spectral, 2, 4, 8 for slope adaptive), and coherence mask (0, 20%, 50%) possibilities were investigated to in additional to the traditional, spatial, and enhanced spatial processing to determine the advantages and disadvantages of varying combinations.

The combinations investigated are summarized in Table 5.16. The GAMMA reference numbers correspond to different combinations. The first number corresponds to the filter type (0=spectral, 1=slope adaptive), the second or second and third (if the filter size is greater than 10) number(s) correspond(s) to filter window size (2, 4, 8, 16, 32), the third or fourth (if the filter size is greater than 10) number(s) correspond(s) to the coherence mask size (0=0%, 2=20%, 5=50%), the fourth or fifth (if the filter size is

greater than 10) number corresponds to multi-looking in the range direction (1 or 2), and the fifth, or fifth and sixth (if the filter size is greater than 10), or sixth and seventh (if the filter size is greater than 10 and the multi-looking in the azimuth direction is 10) number(s) correspond(s) to the multi-looking in the azimuth direction (5 or 10). Spatial unwrapping can be conducted using a slope adaptive filter with no coherence mask, but cannot be conducted with a spectral filter with no coherence mask. Therefore, the spectral filter with no coherence mask was not evaluated. Also, some of the combinations in Table 5.16**Error! Reference source not found.** did not produce results because too much of the scene was masked. The combinations that did not produce results are indicated with an asterisk (*). Following the initial processing of the 30 combinations, two additional combinations (12315, 12415) were processed to determine which coherence threshold (increasing in value) causes too much of the image being masked when using the slope adaptive filter. One additional combination (081210) was processed to determine which coherence threshold (decreasing in value) allows for results to be obtained when using the spectral filter. The three additional combinations which were processed are indicated with a plus sign (+).

Table 5.16. Summary of processing parameters evaluated for spatial processing.

GAMMA Ref.	Filter Type	Filter Size (pixel)	Coherence Mask (%)	Multi-looking
12015	slope Adapt. (1)	2	0	1 by 5
14015	slope Adapt. (1)	4	0	1 by 5
18015	slope Adapt. (1)	8	0	1 by 5
12215	slope Adapt. (1)	2	20	1 by 5
14215	slope Adapt. (1)	4	20	1 by 5
18215	slope Adapt. (1)	8	20	1 by 5
12315+	slope Adapt. (1)	2	30	1 by 5
12415+	slope Adapt. (1)	2	40	1 by 5
12515*	slope Adapt. (1)	2	50	1 by 5
14515*	slope Adapt. (1)	4	50	1 by 5
18515*	slope Adapt. (1)	8	50	1 by 5
08215	spectral (0)	8	20	1 by 5
016215	spectral (0)	16	20	1 by 5
032215	spectral (0)	32	20	1 by 5
08515	spectral (0)	8	50	1 by 5
016515	spectral (0)	16	50	1 by 5
032515	spectral (0)	32	50	1 by 5
120210	slope Adapt. (1)	2	0	2 by 10
140210	slope Adapt. (1)	4	0	2 by 10
180210	slope Adapt. (1)	8	0	2 by 10
122210	slope Adapt. (1)	2	20	2 by 10
142210	slope Adapt. (1)	4	20	2 by 10
182210	slope Adapt. (1)	8	20	2 by 10
125210*	slope Adapt. (1)	2	50	2 by 10
145210*	slope Adapt. (1)	4	50	2 by 10
185210*	slope Adapt. (1)	8	50	2 by 10
081210+	spectral (0)	8	10	2 by 10
082210	spectral (0)	8	20	2 by 10
0162210	spectral (0)	16	20	2 by 10
0322210	spectral (0)	32	20	2 by 10
085210	spectral (0)	8	50	2 by 10
0165210	spectral (0)	16	50	2 by 10
0325210	spectral (0)	32	50	2 by 10

*Combinations which did not produce results.
+ Additional combinations processed for clarification of results.

For all of the variations presented in Table 5.16, 207 interferograms were computed from 44 images (as discussed in Section 5.2.5) for the Los Angeles Red Line

site.   For all of the variations evaluated, only a stack of eleven interferograms which span the time of construction (i.e. one image obtained before construction, one image obtained after construction) was used.   Each stack was obtained by determining the average phase rate from the weighted sum of the phases in each image. The stacks were developed using an equal weight of 365 days applied to each image.   The stacked interferograms, from 27 of the 33 combinations which could be stacked, as presented in Table 5.16, are displayed in Appendix B as Figures B.1 through B.27.

5.5   *Summary*

Data from two sites (Los Angeles Red Line Subway System and Mosul Dam) were acquired from three satellite-based SAR systems. For the LA Red Line site, twenty ERS-1 and thirty-two ERS-2 images ranging in time from June 1992 through November 2000 were obtained and processed. For the Mosul Dam site, sixteen ENVISAT images ranging in time from March 2003 through April 2007 were obtained and processed. SRTM data was also used to develop DEMs for both sites. One arc-second SRTM data was used for the LA Red Line site, and three arc-second SRTM data was used for the Mosul Dam site.

Chapter 6: Results and Discussion

6.1   Introduction

Detection and characterization of localized ground deformation features from space requires the correct combination of sensor resolution factors: spatial resolution (size of pixels), spectral resolution (size of spectral region in which data is acquired), temporal resolution (frequency of image acquisitions and quantity of images in data set), and radiometric resolution (detection of small differences in electromagnetic energy). As discussed in Chapter 4, multi-looking or averaging pixel values within an image increases the radiometric resolution by decreasing speckle at the expense of decreasing the spatial resolution. Different filter types and filter sizes also affect the radiometric resolution, which may make it difficult to detect and characterize localized ground deformations. Coherence masking is also used to eliminate noise within pairs of images. If the coherence is below a certain threshold, the pixel is masked, resulting in pixels with null values and potentially low spatial resolution if many pixels are masked. Various combinations of multi-looking, filter type and size, and coherence mask thresholds were investigated to determine the effect on generated interferograms.

In this chapter, results obtained from the various spatial processing techniques (traditional, spatial, enhanced spatial) are presented, followed by results obtained using time series analyses (IPTA, multiple-baseline) for the Los Angeles Red Line site. The results obtained from the enhanced spatial processing technique are also presented for the Mosul Dam site to show that the processing technique may be used for both urban (Los

Angeles Red Line) and non-urban (Mosul Dam) sites. The advantages and disadvantages of each processing technique are presented.

6.2   *Spatial Processing Techniques*

Discussion of how varying processing parameters affects the detection of localized deformation features is presented in the following subsections. The results from various combinations of processing parameters were used to determine the effect of multi-looking, filter type and size, and coherence masking. All of the variations were conducted with the Los Angeles Red Line data set because there is known deformation of the subway system, there was a large quantity of imagery obtained during construction, and because the subway system is in an urban environment, which promotes coherent images.

6.2.1   *Multi-looking Comparison*

As discussed previously in Chapter 4, multi-looking is a processing technique to reduce radiometric speckle. If speckle is present in an image, localized deformation features may be indistinguishable, as the speckle may form anomalies that appear to be localized deformation features. While multi-looking reduces speckle, it replaces the values of each pixel with the average value of the multiple pixels, resulting in reduced spatial resolution. Because multi-looking decreases speckle (advantage) but decreases spatial resolution (disadvantage), the correct amount of multi-looking is essential to the detection of localized deformation features.

For Earth resource observation studies using the ERS 1, ERS 2, and ENVISAT satellites, images are commonly multi-looked, or averaged using a moving window size of 2 pixels in the range direction and 10 pixels in the azimuth direction. This multi-

looking reduces the spatial resolution of the image from an approximately 4 meter by 20 meter pixel size to an approximately 40 meter by 40 meter pixel size. This amount of multi-looking reduces speckle at the expense of decreasing the spatial resolution by a factor of 10. For detection of localized deformation features, a 20 meter by 20 meter pixel is the smallest that can be used while applying some multi-looking to reduce radiometric speckle because the pixel is 20 meters in the range direction and that corresponds to 1 look. This approximately 20 meter by 20 meter pixel size results from multi-looking an approximately 4 meter by 20 meter pixel (standard size for ERS 1, ERS 2, and ENVISAT data) by 5 looks in the azimuth direction and 1 look in the range direction.

Comparisons among images using different values of multi-looking are presented in Figure 6.1 through Figure 6.8, and summarized in Table 6.1. For Figures 6.1 through 6.4, the same filter type (slope adaptive), filter window size (window size of 2), and coherence mask (no coherence mask applied) were applied to the data to isolate the effect of multi-looking on interferogram output. This filter type, filter window size and coherence mask combination is referred to as "enhanced spatial processing" in this work. For Figures 6.5 through 6.8, the same filter type (spectral), filter window size (window size of 8), and coherence mask (50% coherence mask applied) were applied to the data to focus only on the effect of multi-looking on interferogram output. This filter type, filter window size and coherence mask combination are referred to as "traditional" if the processing is conducted at 2 and 10 looks, and "spatial" if the processing is conducted at 1 and 5 looks. The "traditional" and "spatial" designations are usually reserved for processing conducted on full-scene (100 km by 100 km) images. However, 20 km by 20

137

km clipped images were used for consistency of comparison with other techniques, and these will be referred to as "traditional" and "spatial" within this chapter.

An interferogram stack multi-looked at 1 look in the range direction and 5 looks in the azimuth direction of the 20 km by 20 km clip (clip extents discussed in Chapter 5) is presented in Figure 6.1, while the same stack multi-looked at 2 looks in the range direction and 10 looks in the azimuth direction is presented in Figure 6.2. Note that all images were developed using equal time weighing of the 11 interferograms that span the time of construction; the effect of the number of images used in the stack will be discussed in Section 6.2.5. The effect of greater multi-looking (2 and 10 versus 1 and 5) is to reduce the sharpness of the images by reducing the spatial resolution. When viewing the full 20 km by 20 km clip (Figure 6.1 and Figure 6.2), more of the subsidence associated with the Los Angeles Red Line (Vermont Ave. and Hollywood Blvd.) is visually apparent (purple and blue fringes) in the interferogram stack multi-looked at 1 and 5 (Figure 6.1) than in the interferogram stack multi-looked at 2 and 10 (Figure 6.2). The interferogram stack multi-looked at 2 and 10 smoothes/smears the feature, making it look larger (spatially) in the vicinity of Barnsdall Park, as compared to the interferogram stack multi-looked at 1 and 5. This 2 and 10 smoothing/smearing reduces the visibility of feature along the Western edge of Hollywood Blvd., making the feature indistinguishable as compared with the surrounding pixels, and reduces the number of observed color fringe cycles representing deformation caused by oil extraction and post-seismic deformation.

138

6.2.1.1 Multi-looking Comparison using Spatial Filtering

The area showing the subsidence related to the Los Angeles Red Line construction as taken from the 20 km by 20 km interferogram stack displayed in Figure 6.1 and Figure 6.2 is enlarged for viewing and presented in Figure 6.3 (multi-looked at 1 and 5) and Figure 6.4 (multi-looked at 2 and 10), respectively. These images display the effect of multi-looking by enlarging the image to focus on the area of construction. Whereas the portion of the subsidence feature along Vermont Avenue is present in both figures, when the image is multi-looked at 2 and 10 looks (Figures 6.2 and 6.4), the feature appears blurred and not as focused as the image multi-looked at 1 and 5 looks (Figures 6.1 and 6.3).
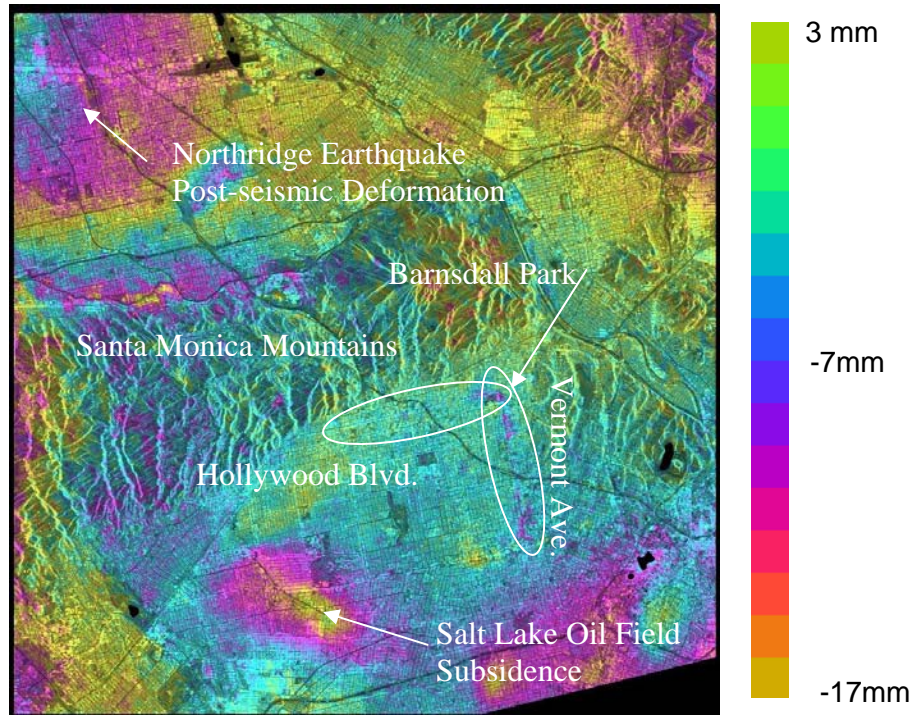
Figure 6.1. Interferogram stack (11 interferograms) of the Los Angeles Red Line site using 1 and 5 multi-looking, with slope adaptive filter, window size of 2, no coherence mask, and equal time weighting ("enhanced spatial technique").
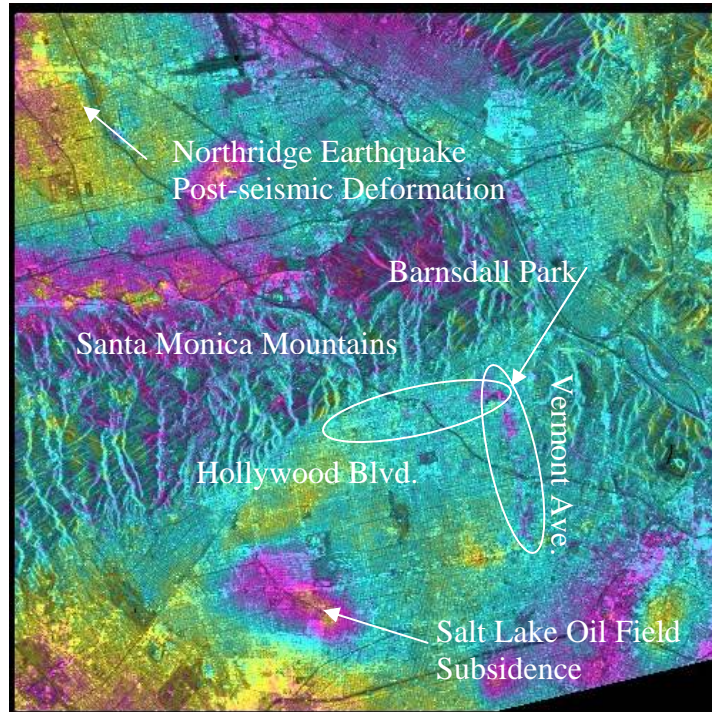
Figure 6.2. Interferogram stack of the Los Angeles Red Line site using 2 and 10 multi-looking, with slope adaptive filter, window size of 2 and no coherence mask.
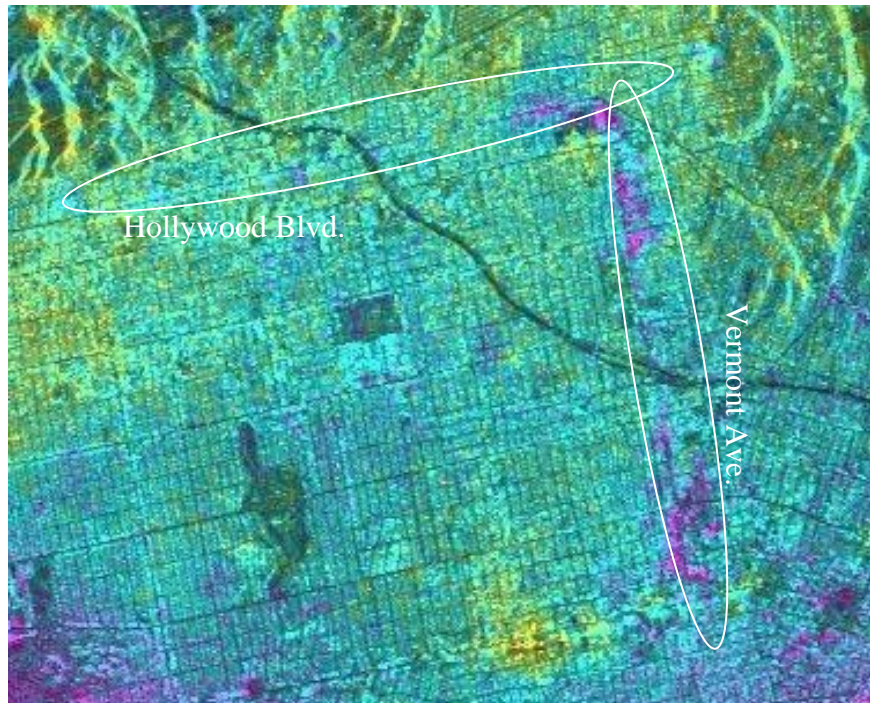
Figure 6.3. Interferogram stack (11 interferograms) showing area of subsidence related to the construction of the Los Angeles Red Line subway tunnels using 1 and 5 multi-looking, slope adaptive filter, window size of 2, no coherence mask, and equal time weighting ("enhanced spatial technique").
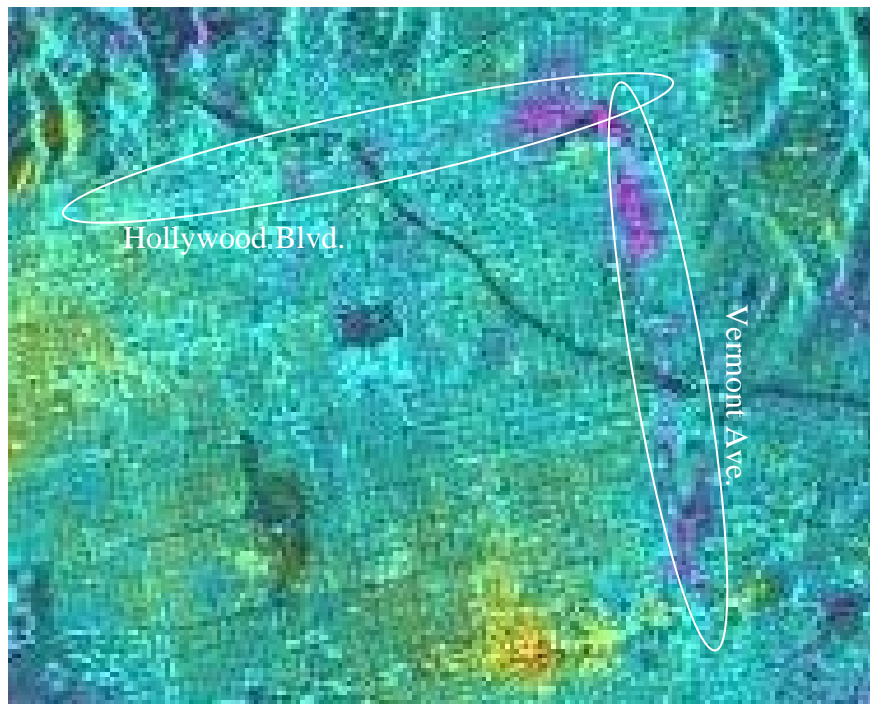
Figure 6.4. Interferogram stack showing area of subsidence related to the construction of the Los Angeles Red Line subway tunnels using 2 and 10 multi-looking, slope adaptive filter, window size of 2 and no coherence mask.

6.2.1.2 Multi-looking Comparison using Spectral Filtering

The 50 percent coherence mask more adversely affects (i.e. creates more null value portions of the image) the interferogram stack displayed in Figure 6.5 than the interferogram stack displayed in Figure 6.6. Additional multi-looks average more pixels within a given window size increasing the coherence of the window. Because the coherence mask eliminates (applies a null value which is represented as black in the image) pixels that have coherence below a certain threshold (50%), more pixels are eliminated in Figure 6.5 than Figure 6.6 because more averaging of pixels occurred in the processing prior to the development of Figure 6.6. Note that the Santa Monica Mountains are eliminated from both scenes as the coherence in mountainous areas is much less than in urban areas.

As in Figure 6.3 and Figure 6.4, the area of subsidence related to tunnel construction as taken from the stack of interferogram images displayed in Figure 6.5 and Figure 6.6 are enlarged for viewing and presented in Figure 6.7 (multi-looked at 1 and 5) and Figure 6.8 (multi-looked at 2 and 10), respectively. These images display the effect of multi-looking by enlarging the image to see the area of subsidence related to tunnel construction. The subsidence caused by tunneling construction is observed as linear null value strips along Vermont Avenue and Hollywood Boulevard in the image multi-looked at 1 and 5 looks. The subsidence feature is a combination of null value strips and color cycle fringes along Vermont Avenue and Hollywood Boulevard in the image multi-looked at 2 and 10 looks.

As with the interferograms with no coherence mask (presented in Figure 6.3 and Figure 6.4), when the image is multi-looked at 2 and 10 looks, the feature appears blurred and not as focused as the image multi-looked at 1 and 5 looks. However, unlike the

images presented in Figure 6.3 and Figure 6.4, much of the 1 and 5 looks image contains null values because of loss of coherence due to the coherence mask eliminating the effects of radar speckle, vegetation changes, and civil infrastructure changes (asphalt overlays, subsidence caused by tunneling, etc.). The areas with null values in Figure 6.8 correspond primarily to areas with changes in vegetation (parks and nature areas). The effect of increased multi-looking causes less decorrelation, and therefore less effect from the coherence mask. The effect of varying amounts of coherence masking is presented in Section 6.2.4.
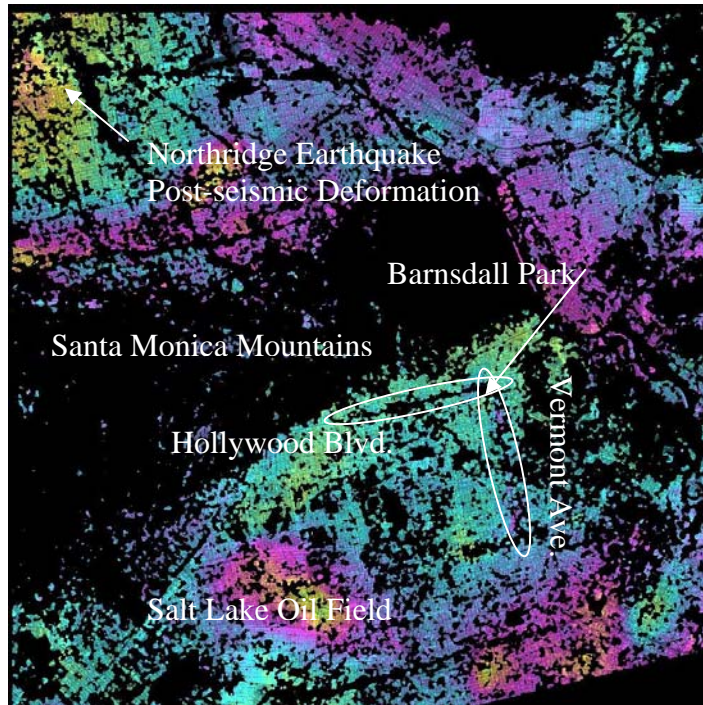
Figure 6.5. Interferogram stack (11 interferograms) of the Los Angeles Red Line site using 1 and 5 multi-looking, spectral filter, window size of 8, 50% coherence mask, and equal time weighting ("spatial technique").
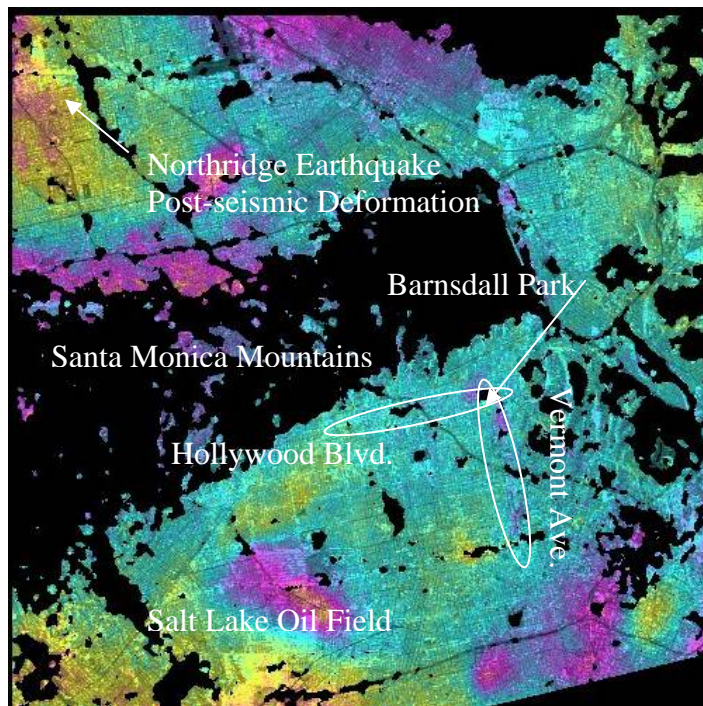
Figure 6.6. 2 Interferogram stack (11 interferograms) multi-looking of the Los Angeles Red Line site using 2 and 10, spectral filter, window size of 8, 50% coherence mask, and equal time weighting ("traditional technique").
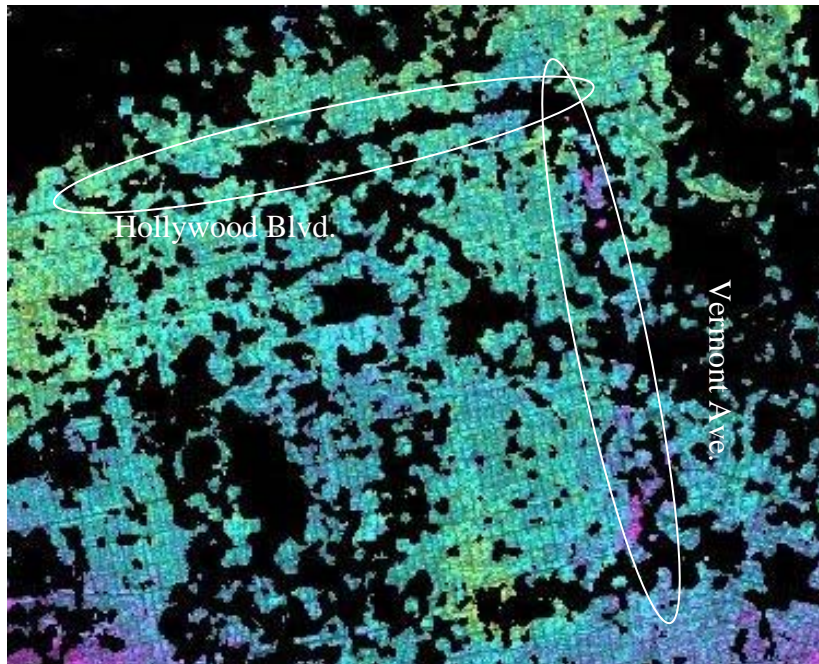
Figure 6.7. Interferogram stack (11 interferograms) showing area of subsidence related to the construction of the Los Angeles Red Line subway tunnels using 1 and 5 multi-looking, spectral filter, window size of 8, 50% coherence mask, and equal time weighting ("spatial technique").
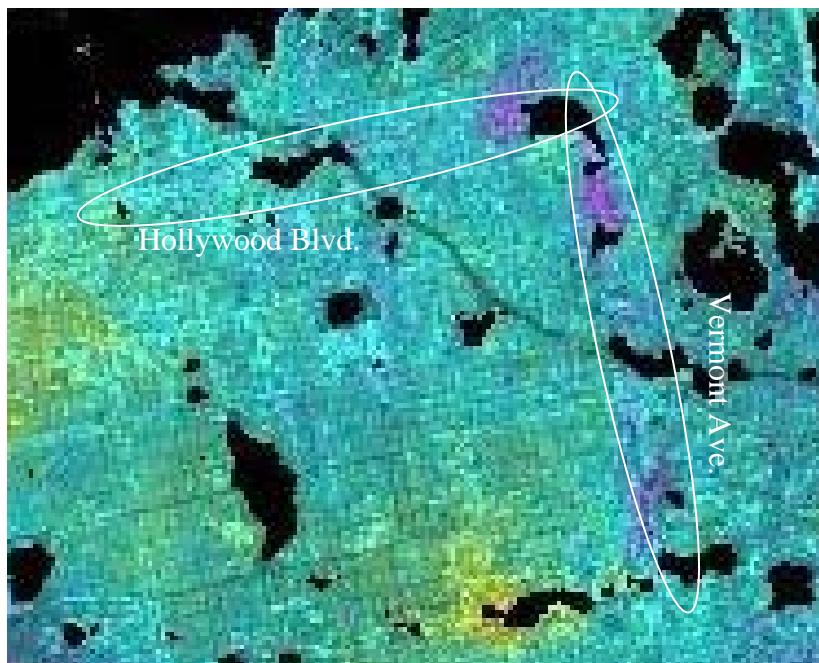
Figure 6.8. Interferogram stack (11 interferograms) showing area of subsidence related to the construction of the Los Angeles Red Line subway tunnels using 2 and 10 multi-looking, spectral filter, window size of 8, 50% coherence mask, and equal time weighting ("traditional technique").

145

Evaluating the images presented in Figures 6.1 through 6.8, the effect of multi-looking on images obtained using different filter types is presented in Table 6.1. The effect of multi-looking is smearing, therefore, this design parameter is of interest. However, the amount of masking is also of interest. As presented in Table 6.1, a rank is assigned to the various combinations based on the amount of smearing (higher ranking for decreased smearing). If multiple images are smeared by similar amounts, the amount of masking is also considered (lower ranking for increased masking).

Table 6.1. Summary of multi-looking results.

GAMMA Ref. #	Filter Type*	Filter Window Size	Coherence Mask Threshold	Multi-looking	Figure Number	LA Red Line Feature is Smeared	LA Red Line Feature is Masked	Ranking
12015	1	2	0	1x5	6.1 & 6.3	No	No	1
120210	1	2	0	2x10	6.2 & 6.4	Yes	No	2
08515	0	8	5	1x5	6.5 & 6.7	No	Yes	3
085210	0	8	5	2x10	6.6 & 6.8	Yes	No	4
* 0=Spectral, 1=Slope Adaptive								

6.2.2 Filter Type and Filter Window Size Comparison

As presented previously in Chapter 5, various filter types (spectral and slope adaptive) and filter window sizes were investigated to determine their effect on detection of localized ground deformation features. The spectral filter was investigated with window sizes of 8, 16, and 32 (Figure 6.9 a, b, and c). The slope adaptive filter was investigated with window sizes of 2, 4, and 8 (Figure 6.10 a, b, and c). A summary of the filter type and filter window size is presented in Table 6.2. As discussed in Section 6.2.1, 1 and 5 multi-looking retains less (masks more) of the image than 2 and 10 multi-looking

when using the spectral filter. Therefore, all of the images filtered using the spectral filter and used for filter comparison were processed using 2 and 10 multi-looking. Also, as discussed in Section 6.2.1, 1 and 5 multi-looking retains more sharpness of the features (less blurring) than 2 and 10 multi-looking when using the slope adaptive filter. Therefore, all of the images filtered using the slope adaptive filter and used for filter comparison were processed using 1 and 5 multi-looking.

A coherence mask of 20 percent was used for both filter types and all filter window sizes for comparison because some of the images could not be stacked due to decorrelation (loss in correlation caused by null values being applied to values with coherence values less than the threshold value) when using the 50 percent coherence mask.

6.2.2.1 Spectral Filter Window Size

As the spectral filter window size increases (Figure 6.9 a, b, and c) the coherence in low coherence areas (e.g. Santa Monica Mountains) increases. This effect is caused by more averaging of pixels within the filter window, causing better coherence in low coherence areas. This increase in coherence also alludes to using a spectral filter with large window for non-urban areas. By focusing on the area showing the subsidence related to the Los Angeles Red Line construction, as displayed in Figure 6.9 a, b, and c, the sharpness (number of color cycle fringes for a given feature) of the images decreases slightly with the increase in window size. This suggests that for images that contain areas prone to low coherence (non-urban areas) a larger filter window size should be used with the spectral filter to increase coherence in low coherence regions without significant adverse affects (loss in spatial resolution or sharpness) to the remainder of the scene.

6.2.2.2 Slope Adaptive Filter Window Size

As the slope adaptive filter window size increases (Figure 6.10 a, b, and c) coherence in low coherence areas (e.g. Santa Monica Mountains) remains practically constant. This filter is used to smooth small windows, and therefore, does not average enough pixels together to increase coherence using the window sizes investigated (2, 4, and 8). By focusing on the area showing the subsidence related to the Los Angeles Red Line construction, as displayed in Figure 6.12 a, b, and c, the sharpness of the images also remains constant, independent of the filter window size.
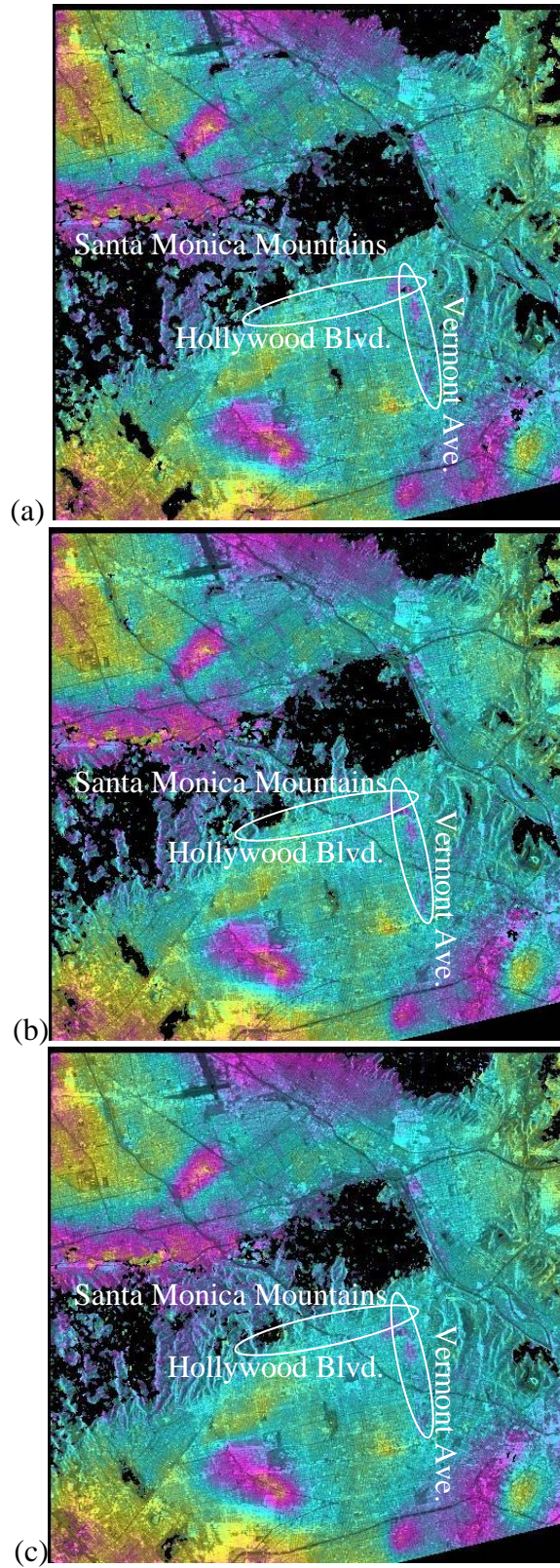
Figure 6.9. Interferogram stack (11 interferograms) of Los Angeles using a spectral filter, with 20% coherence mask, multi-looked at 2 and 10, equal time weighting, and window size of (a) 8, (b) 16, (c) 32.
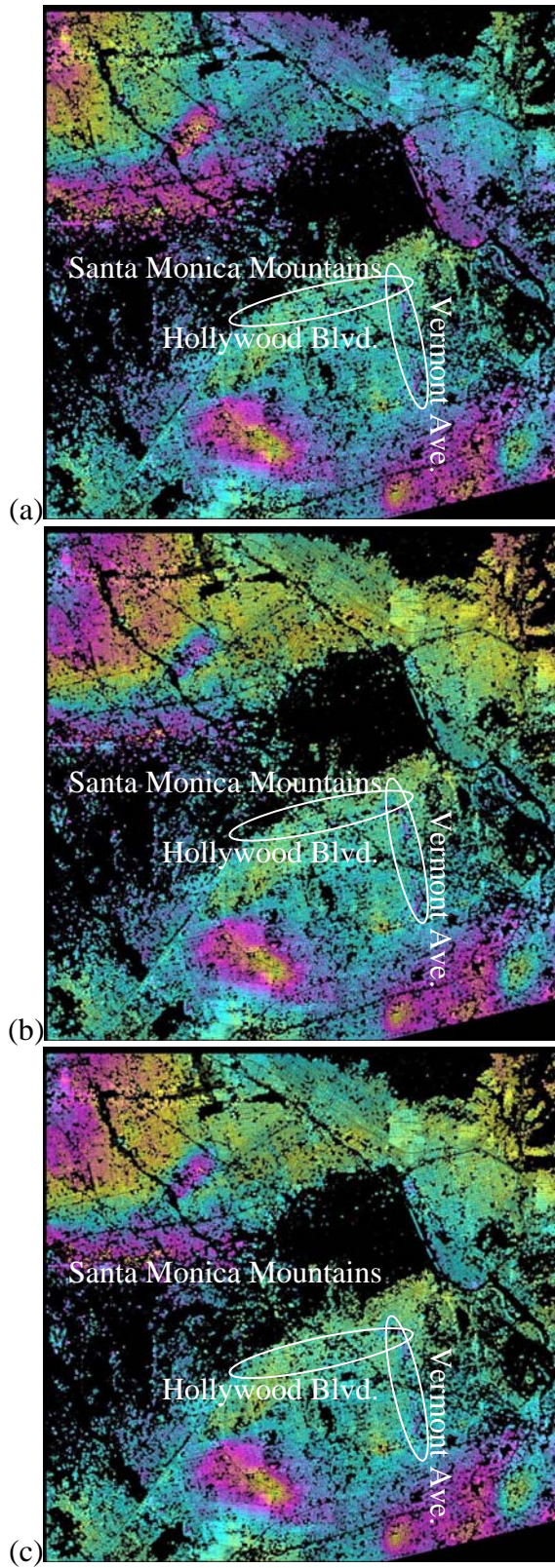
Figure 6.10. Interferogram stack (11 interferograms) of Los Angeles using a slope adaptive filter, 20% coherence mask, multi-looked at 1 and 5, equal time weighting, and window size of (a) 2, (b) 4, (c) 8.
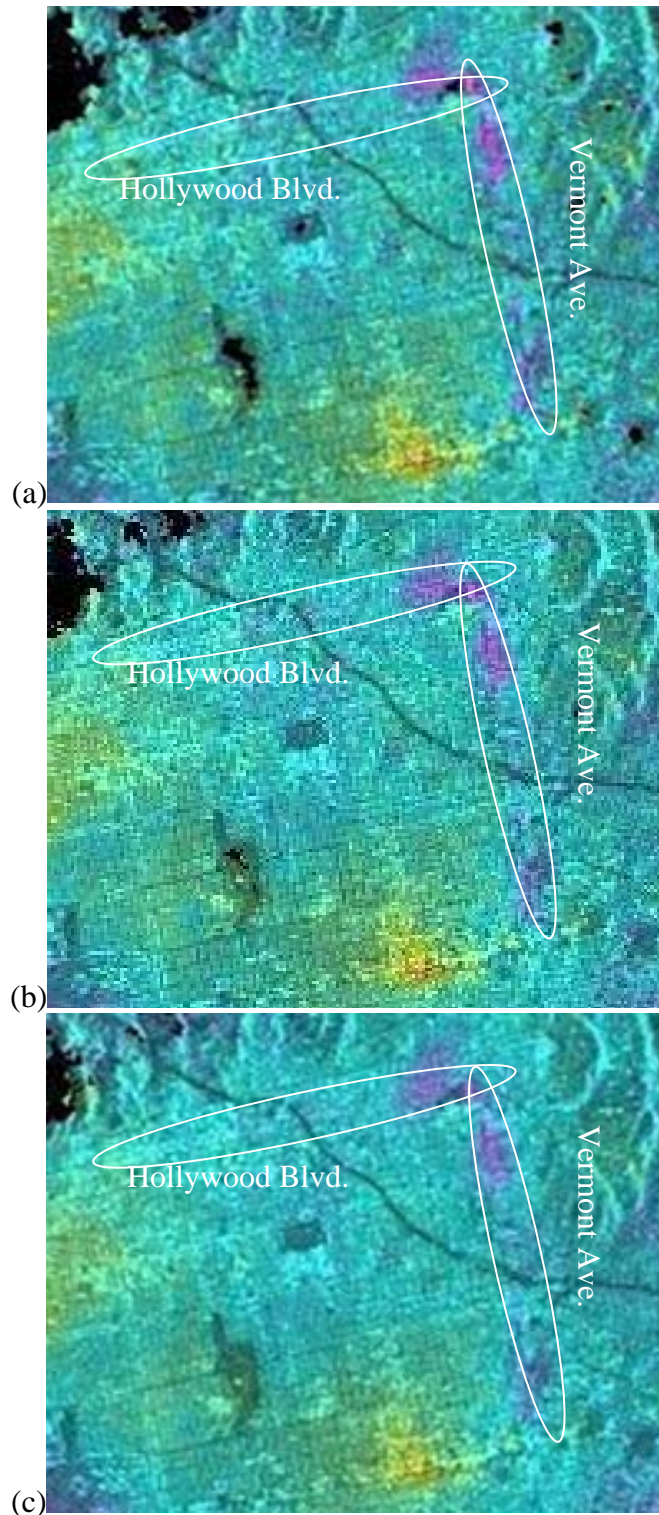
Figure 6.11. Interferogram stack (11 interferograms) showing area of subsidence related to the construction of the Los Angeles Red Line subway tunnels using a spectral filter, with 20% coherence mask, multi-looked at 2 and 10, equal time weighting and window size of (a) 8, (b) 16, (c) 32.
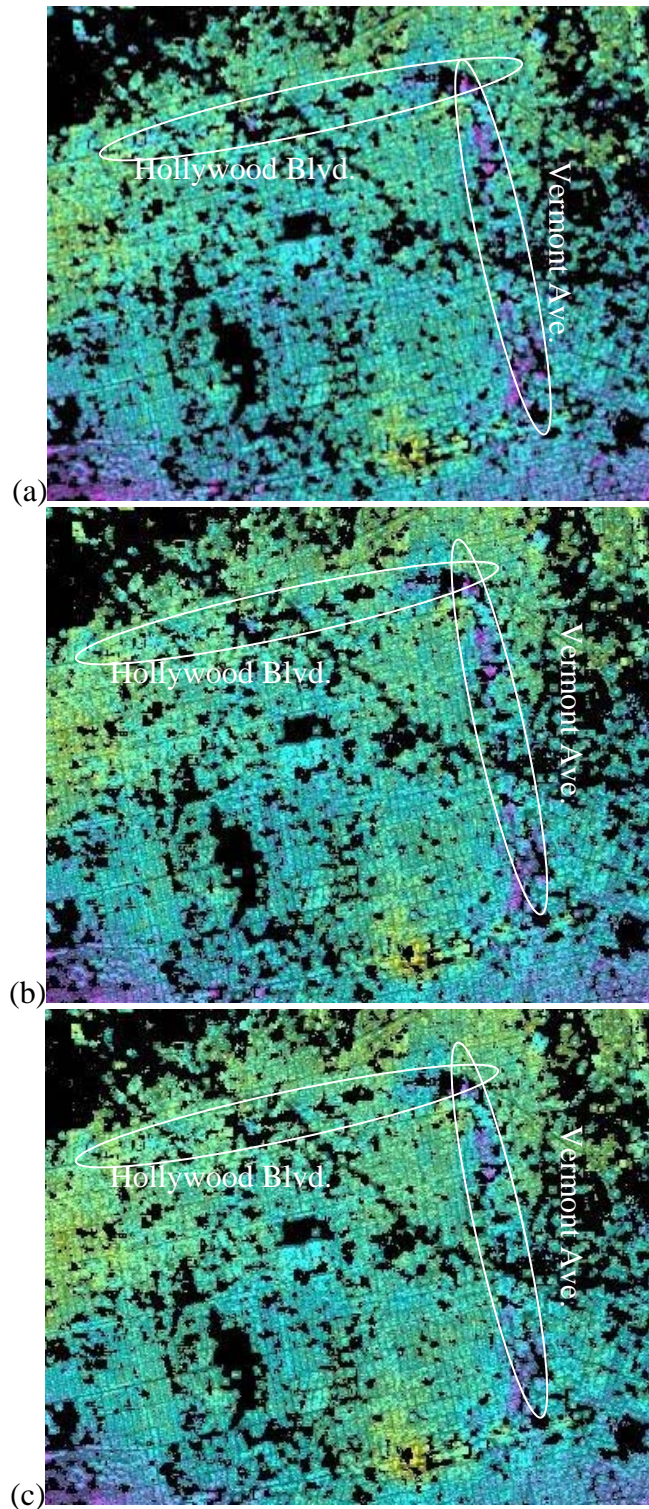
Figure 6.12. Interferogram stack (11 interferograms) showing area of subsidence related to the construction of the Los Angeles Red Line subway tunnels using a slope adaptive filter, 20% coherence mask, multi-looked at 1 and 5, equal time weighting, and window size of (a) 2, (b) 4, (c) 8.

6.2.2.3 Spectral and Slope Adaptive Filter Type Comparison

For the purpose of comparing the spectral and slope adaptive filter types, the interferometric stacks with the smallest filter window size for each filter type are compared. Therefore, this comparison is between the smallest filter window size for both filter types which are a window size of 8 for the spectral filter (previously displayed in Figure 6.11a) and a window size of 2 for the slope adaptive filter (previously displayed in Figure 6.12a). The interferogram stack produced using the spectral filter is more coherent than the interferogram stack produced using the slope adaptive filter. As discussed previously, these filters serve different purposes. The spectral filter is used to maintain coherence and the slope adaptive filter is used to maintain sharpness. Both of the images presented use a 20% coherence mask, which eliminates a majority of the image produced using the slope adaptive filter (Figure 6.12a), but only a small portion of the interferogram stack produced using the spectral filter (Figure 6.11a).

A coherence mask must be used for the spectral filter, but is not required for the slope adaptive filter. Therefore, when comparing the interferogram stack using the spectral filter with a 20 percent coherence mask and a window size of 8 (Figure 6.13) against the slope adaptive filter with no coherence mask and a window size of 2 (Figure 6.14), the interferogram stack image generated using the slope adaptive filter is sharper and apparently more coherent.

Images may be unwrapped using one filter type to ensure successful phase unwrapping, then unwrapped using a different filter type to filter the flattened interferogram containing unwrapped topographic phase, prior to the creation of the differential interferogram. Typically, the images are initially unwrapped using a spectral

153

filter and then a slope adaptive filter is used prior to the creation of the differential interferogram

It is recommended that a spectral filter with a window size of 8 be used to initially unwrap the interferograms (window size of 32 if image contains non-coherent areas), and then reunwrapped using a slope adaptive filter with a window size of 2 and no coherence mask. The interferogram stack image using this procedure is presented in both Figure 6.14 and Figure 6.15. Note that this image in Figure 6.15 has been post-processed and transformed from cumulative phase rate to deformation rate and the color scale has been modified to highlight the deformation.
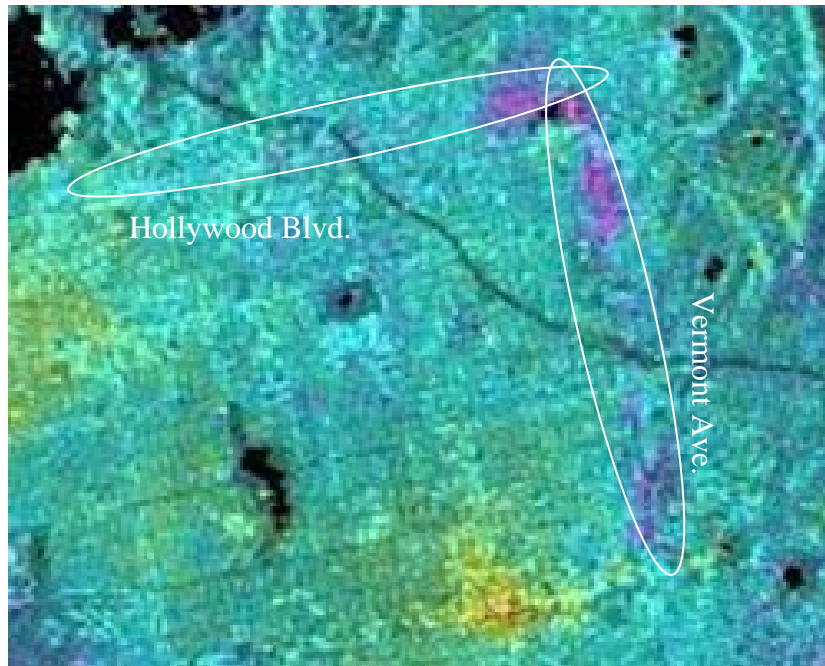
Figure 6.13. Interferogram stack (11 interferograms) showing area of subsidence related to the construction of the Los Angeles Red Line subway tunnels using spectral filter with window size of 8, 20% coherence mask, multi-looked at 2 and 10.
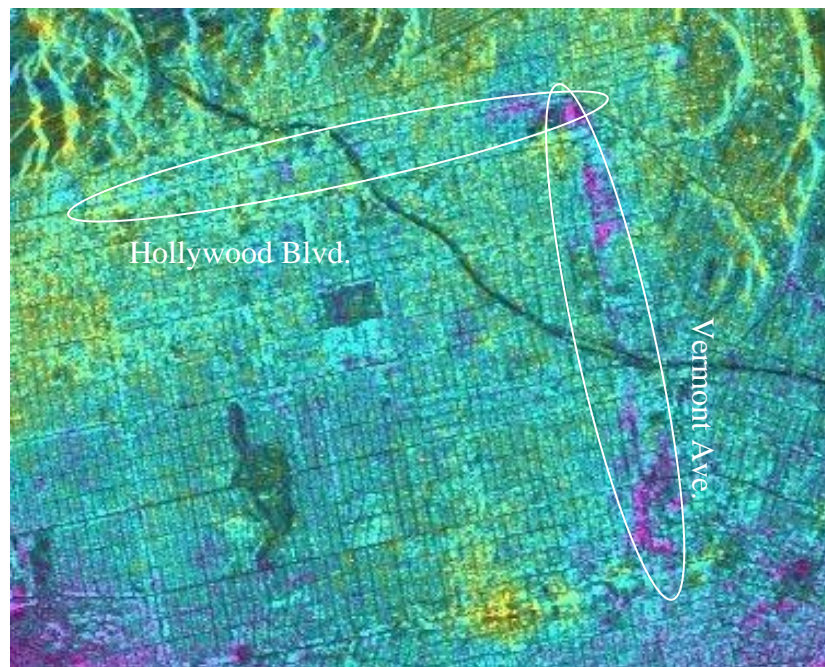
Figure 6.14. Interferogram stack (11 interferograms) showing area of subsidence related to the construction of the Los Angeles Red Line subway tunnels using slope adaptive filter with window size of 2, 0% coherence mask, multi-looked at 1 and 5, and equal time weighting "enhanced spatial technique".
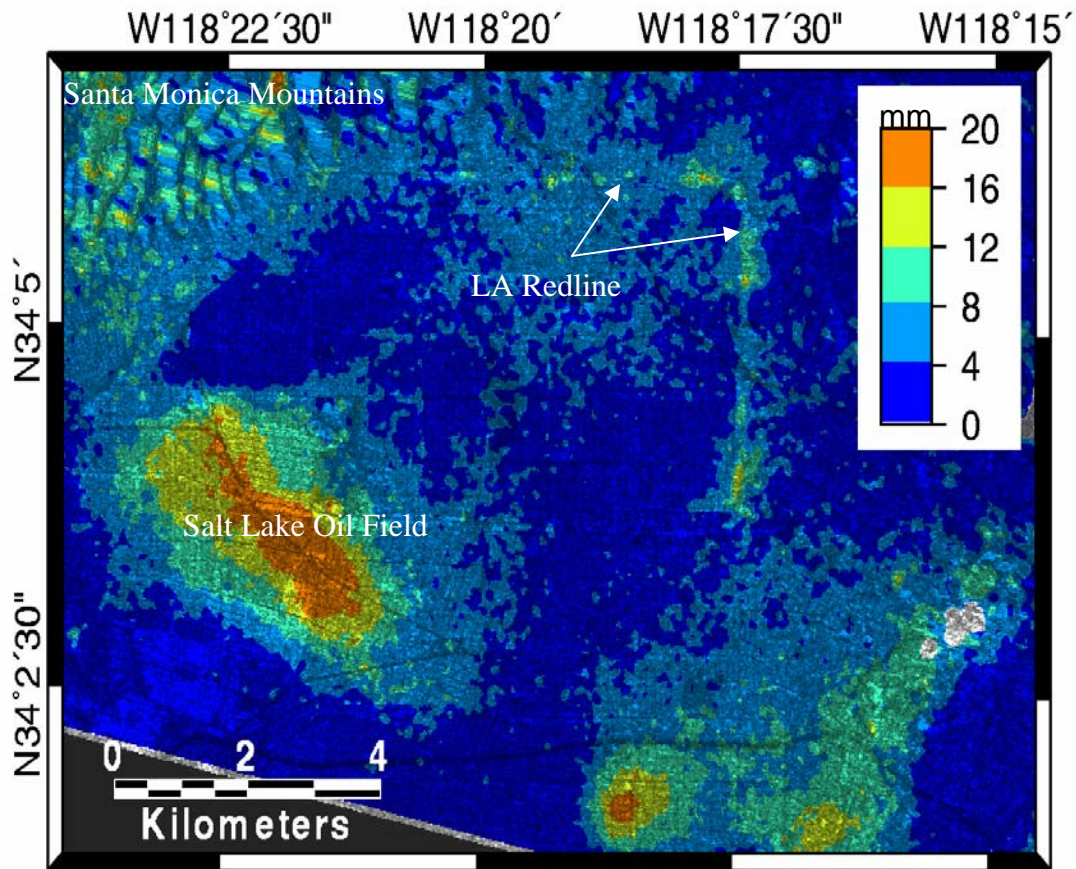
Figure 6.15. Area of subsidence related to the construction of the Los Angeles Red Line subway tunnels using 11 interferogram stack, slope adaptive filter with window size of 2, 0% coherence mask, multi-looked at 1 and 5, and equal time weighting, "enhanced spatial technique," deformation map (in UTM coordinates).

Evaluating the images presented in Figures 6.9 through 6.12, the effect of filter type and filter window size is presented in Table 6.2. The effect of multi-looking and filter window size is smearing. Therefore, this parameter is of interest. However, the amount of masking and filtering are also of interest. As presented in Table 6.2, a rank is assigned to the varying combinations based on the amount of smearing (higher ranking for decreased smearing) and the amount of masking. Because deformation estimates cannot be obtained if the signal associated with the deformation is masked, a lower ranking is assigned if the signal is masked even if it is not smeared.

156

For the 082210, 0162210, and 032210 combinations, the localized deformation feature associated with the L.A. Red Line is smeared, however, the feature is not masked. The 082210 combination is ranked higher than the 0162210 and 032210 combinations because the localized deformation feature becomes more smeared with increasing filter window size. For the 12215, 14215, and 18215 combinations, the localized deformation feature is not smeared but is masked. As mentioned previously, if the feature is masked, the combination is poorly ranked because a signal is required for deformation estimates. The 12215 combinations is ranked higher than the 14215, and 18215 combinations because the localized deformation feature becomes slightly more smeared with increasing filter window size. In summary, the localized deformation feature is smeared and not masked using the spectral filter and therefore ranked higher than the slope adaptive filter. Also, an increase window size results in an increase smearing assigning a lower ranking.

Table 6.2. Summary of filter type and filter window size results.

GAMMA Ref. #	Filter Type*	Filter Window Size	Coherence Mask Threshold	Multi-looking	Figure Number	LA Red Line Feature is Smeared	LA Red Line Feature is Masked	Ranking
082210	0	8	2	2x10	6.9a & 6.11a	Yes	No	1
0162210	0	16	2	2x10	6.9b & 6.11b	Yes	No	2
0322210	0	32	2	2x10	6.9c & 6.11c	Yes	No	3
12215	1	2	2	1x5	6.10a & 6.12a	No	Yes	4
14215	1	4	2	1x5	6.10b & 6.12b	No	Yes	5
18215	1	8	2	1x5	6.10c & 6.12c	No	Yes	6
* 0=Spectral, 1=Slope Adaptive								

6.2.3   Coherence Mask Threshold Comparison

Multiple coherence mask thresholds were evaluated to determine the effect of coherence masking on the Interferogram stacks. Three levels of coherence masks were

initially evaluated: 0, 0.2 (20%), and 0.5 (50%). The default value is 0.5 (GAMMA Remote Sensing Users Manual, 2006) when using the "adf" filtering command (spectral filter). During preliminary processing it was determined that the 0.5 threshold was masking too much of the scene; therefore, threshold values smaller than 0.5 were investigated. Although the 0 coherence threshold is acceptable for the slope adaptive filter, the spectral filter requires that the threshold is larger than 0. The spectral filter, 0 coherence mask combination was therefore not analyzed. A stack of interferograms was instead produced using a 10% coherence mask, using the spectral filter for comparison purposes. A stack of interferograms could not be produced for the slope adaptive filter with a window size of 2, 50% coherence mask, 1 and 5 multi-looking combination. Individual interferograms were produced using this processing combination, however, the coherence mask eliminated (provides null values for) too much of the image, causing problems during stacking and thereby making it impossible to stack the images together. Therefore, the combination of 40% coherence mask, window size of 2, 1 and 5 multi-looking was produced for comparison purposes.

Stacked interferograms produced using each of the coherence thresholds for the two filter types are presented in Figure 6.16. The corresponding ranking of processing combinations that produced these interferograms is presented in Table 6.3. These images correspond to 10% coherence mask spectral filter, 50% coherence mask spectral filter, 0% coherence mask slope adaptive filter, and 40% coherence mask slope adaptive filter, respectively. Just as with the filter types and sizes, the various coherence mask thresholds were used on images multi-looked at 2 and 10 looks for the spectral filter and 1 and 5 looks for the slope adaptive filter. For the spectral filter, all of the images were

produced using a filter window size of 8; for the slope adaptive filter, all of the images were produced using a window size of 2. These combinations of multi-looking and filter type and size produce the most coherent images for the spectral filter, and the sharpest images for the slope adaptive filter.

(a)   (b)

(c)   (d)
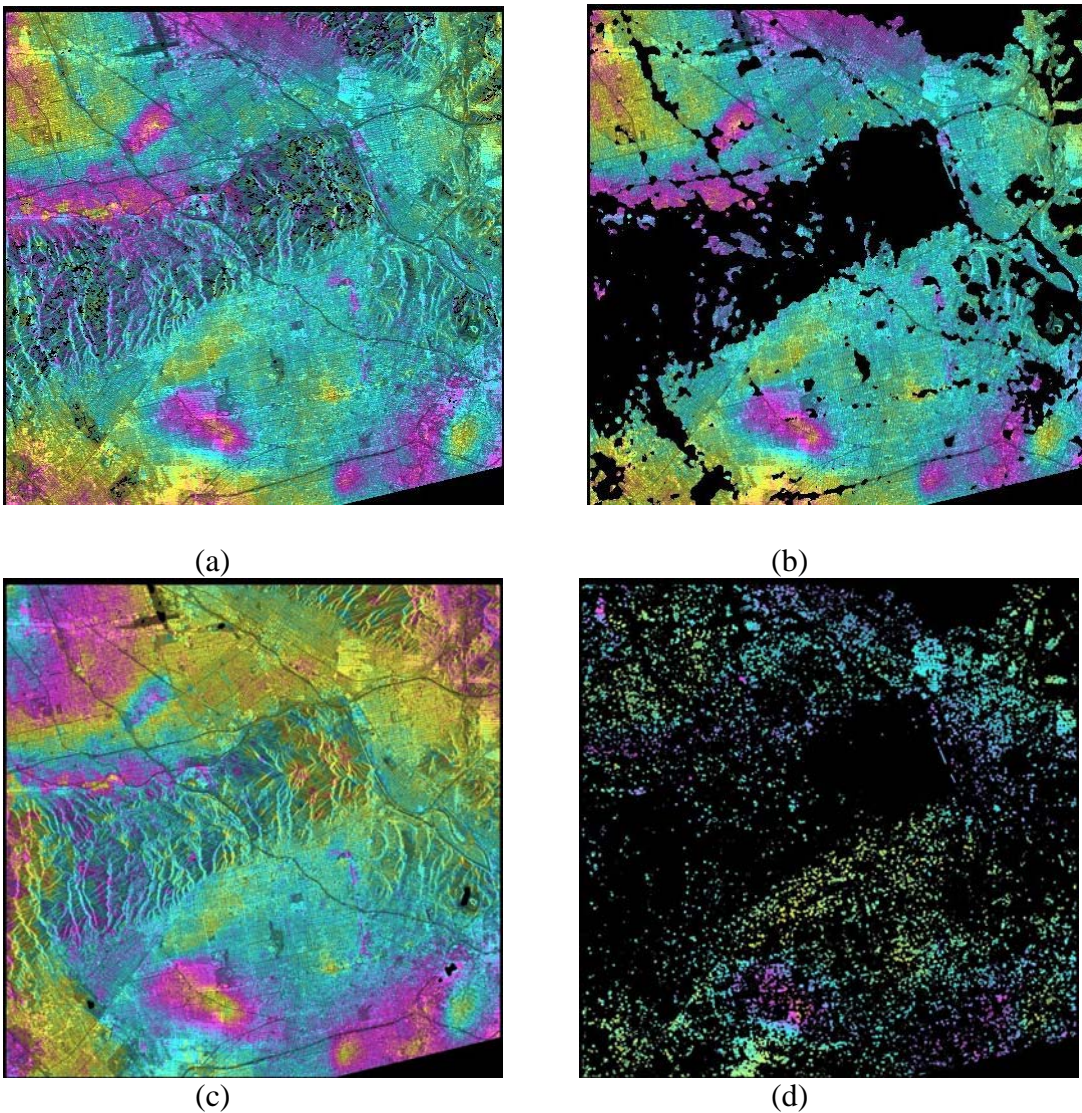
Figure 6.16. Interferogram stack (11 interferograms) using spectral filter with window size of 8, multi-looked at 2 and 10, and coherence mask threshold of (a) 10%, (b) 50%. Interferogram stack using slope adaptive filter with window size of 2, multi-looked at 1 and 5, equal time weighting, and coherence mask threshold of (c) 0%, (d) 40%.

For both filter types, as the coherence mask threshold is increased, low coherence points are eliminated. If the coherence mask is increased above 40% for the slope adaptive filter, the images cannot be stacked because too much of the image contains null values. It appears as if the images generated using the smaller coherence thresholds for both the spectral and slope adaptive filters, Figure 6.16 a and c, produce the images which contain the most data.

Because the second and fourth combinations in Table 6.3 (085210 and 12415) are masked these combinations received the lowest ratings (3 and 4), with 12415 containing the most null value data and therefore receiving the lowest rating. Of the two images that were not masked (081210 and 12015), the image produced using the slope adaptive filter and low coherence mask (12015) receives the highest ranking because it appears to be sharper than the image produced using the spectral filter and low coherence mask (081210).

Table 6.3. Summary of coherence masking results.

GAMMA Ref. #	Filter Type*	Filter Window Size	Coherence Mask Threshold	Multi-looking	Figure Number	LA Red Line Feature is Smeared	LA Red Line Feature is Masked	Ranking
081210	0	8	1	2x10	6.24	Yes	No	2
085210	0	8	5	2x10	6.25	Yes	Yes	3
12015	1	2	0	1x5	6.26	No	No	1
12415	1	2	4	1x5	6.27	No	Yes	4
* 0=Spectral, 1=Slope Adaptive								

6.2.4 *Stacking Comparison*

The number of images used in a stack directly affects the resulting image. If two SLC images are used in which both scenes are taken prior to or following the time of

construction, little or no deformation phase is being added to the interferogam stack. Similarly, if multiple interferograms that contain little or no deformation are added to the stack, the stack becomes biased by the interferograms that contain no deformaion. Three stacks of Los Angeles images are presented in Figure 6.17. These images are stacks of interferometric images that 1) include all images prior to 1996, 2) include all images from 1993 through 2000, and 3) include all images in which the first scene is before 1993 and the second scene is after 1993, but before 1996.

The images presented in Figure 6.17a, b, and c were developed using the enhanced spatial processing technique for comparison purposes (i.e the multi-looking, filter type, filter size and coherence mask variables were identical for the development of the three different images). The images are ranked in Table 6.4 based on how observable the localized deformation feature is in each image, as compared to one another. Within the interferogram stack produced using all images prior to 1996 (Figure 6.16 a), the localized deformation feature is observable, however, the feature is not as observable as it is in the interferogram developed using all images in which the first scene is before 1993 and the second scene is after 1993, but before 1996 (Figure 6.16 c). The localized deformation feature is not observable using the interferogram stack containing all images (Figure 6.16 b). Therefore, the interferogram stack generated using only the images which span the time of construction (images in which the first scene is before 1993 and the second scene is after 1993, but before 1996) is ranked higher than the interferogram stack using only images before 1996, and both are ranked higher than the interferogram image generated using all of the images.
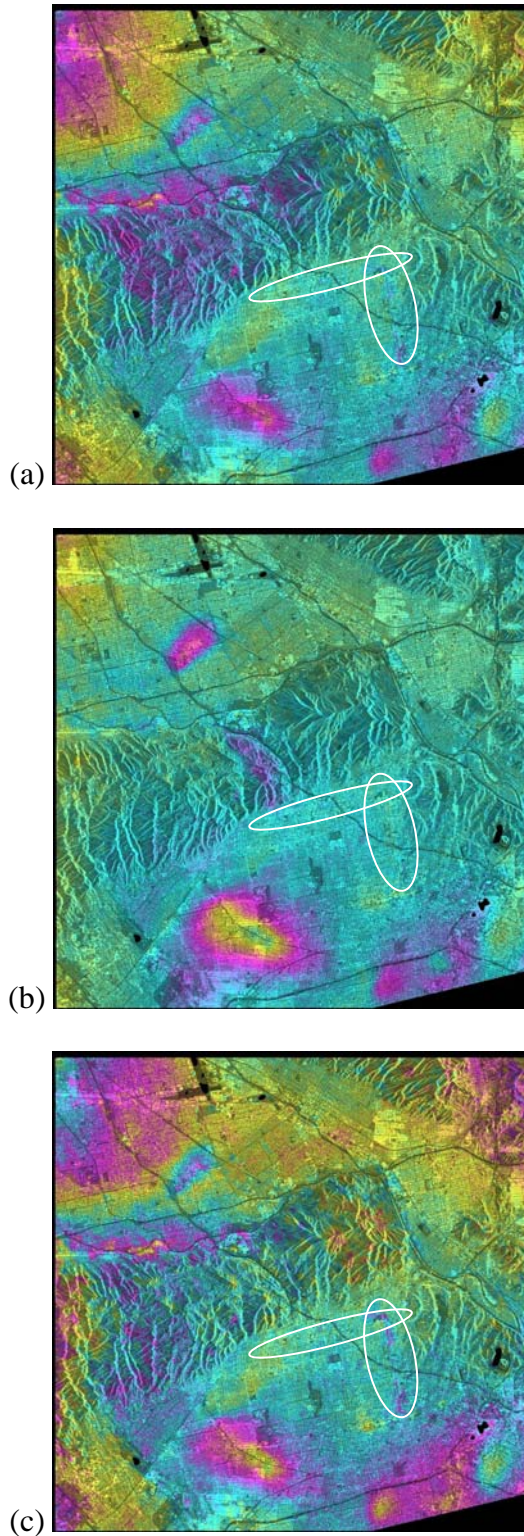
Figure 6.17. Interferogram stack (11 interferograms) using slope adaptive filter with window size of 2, 0% coherence mask, multi-looked at 1 and 5, and using (a) images before 1996, (b) all images, (c) using all images in which the first scene is before August 1993 and the second scene is after August 1993, but before 1996.

162

Table 6.4. Summary of stacking results.

Timeframe	Figure #	LA Red Line Feature is Observed	Ranking
Pre-1996	6.17a	Slightly	2
1992-2000	6.17b	No	3
Pre-1996 (pairs across August 1993)	6.17c	Yes	1

6.2.5   Summary of Evaluations

Results of the multi-looking, filter type and size, coherence mask and stacking comparisons are summarized as:

- Increased multi-looking (increased number of looks) decreased spatial resolution (increased smearing) and increased radiometric resolution (decreased speckle).

- Increased multi-looking increased coherence.

- Increased filter size increased smearing.

- The slope adaptive filter allows for the use of no coherence mask (all of the image can be unwrapped), while the spectral filter requires a coherence mask (only portions of the image with coherence values above the threshold can be unwrapped as the other values are replaced with null values).

- Increased coherence mask decreased signal for feature detection.

- The amount and quality of images used in a stack affect the results of the stack. Fewer high quality images surrounding the time span of the area of subsidence related to the construction of the Los Angeles Red Line subway tunnels allow for better detection of the subsidence.

Recommendations for which multi-looking, filter type and size and coherence mask, and stacking combination should be used for different site characteristics and feature detection requirements are provided in Section 6.7, based on the summarized results described above.

6.3   Time Dependent Processing Techniques

Two time dependent processing techniques were analyzed. These techniques include interferometric point target analysis (IPTA) and multiple-baseline analysis. As discussed in Chapter 4, these processing techniques develop images that display the total cumulative phase change (or displacement) for all points within the image(s). For the IPTA processing technique, the time-rate can also be displayed by selecting on individual points to display a time history (deformation versus time) for the selected points. For the multiple-baseline processing technique, one cumulative phase (or displacement) image is generated at each time step (one time step for each SLC image).

6.3.1   Interferometric Point Target Analysis (IPTA)

IPTA processing was conducted on a 500 pixel by 500 pixel clip of all fifty-two images obtained from the WInSAR archive (Tables 5.1 and 5.2). The total cumulative deformation (June 1992 through November 2000) for the area surrounding the Los Angeles Red Line is displayed in Figure 6.18. Plotting the cumulative deformation for each time step (one time step corresponds to the date of an SLC image) versus time allows for the determination of the rate of subsidence. The deformation rate for Point 19655 located along the Los Angeles Red Line (shown in Figure 6.18) is displayed in Figure 6.19.
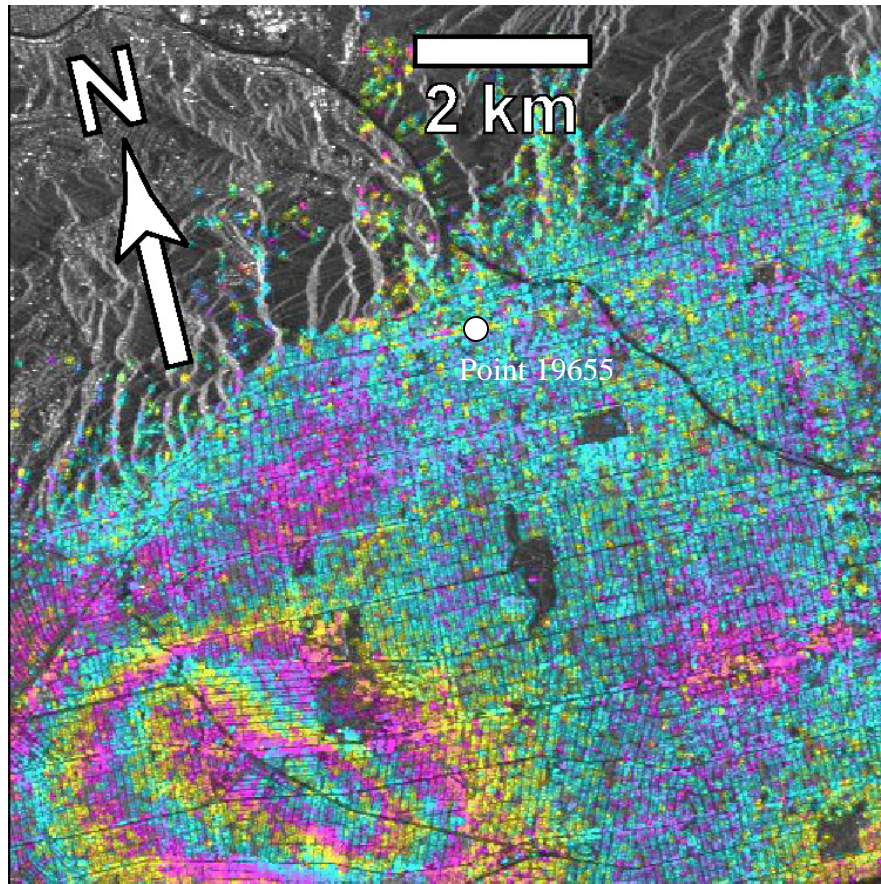
Figure 6.18. Total cumulative interferometric phase of the Los Angeles Red Line site using 52 Images (master SLC e1-11609).
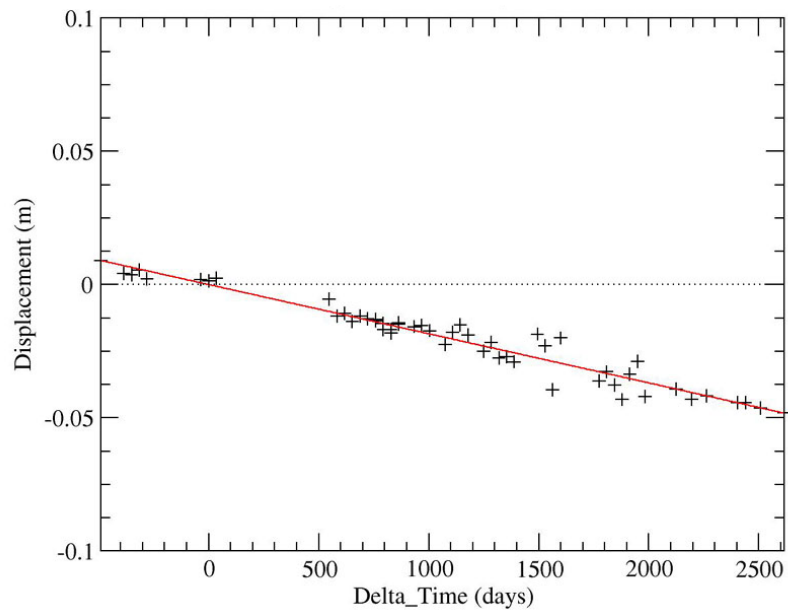
Figure 6.19. Deformation versus time plot of point 19655 (shown in Figure 6.31).

165

A linear deformation rate is presented (red trend line displayed in Figure 6.19) based on the cumulative deformation of the LA Red Line at Point 19655 within the scene. Note that the time line on the x-axis begins with negative values. These negative time values are caused by SLC e1-11609 being selected as the master scene. Six SLC images were acquired before SLC e1-11609; therefore, these images are presented in the negative time range. Manjunath (2008) presented an in- depth analysis of the factors affecting the IPTA processing techniques of the Los Angeles Red Line. Therefore, the presentation of IPTA analyses presented in the document is for processing technique comparison purposes.

6.3.2   Multiple-Baseline

Multiple-baseline processing was conducted on the same 1000 by 1000 pixel clip of the Los Angeles Area that was used for traditional, spatial, and enhanced spatial processing (Table 5.8). One interferogram displaying the total cumulative phase (with respect to the first scene in chronological order) is developed for each time step, with each time step corresponding to one image (44 images, 44 time steps). For the best performance of the multiple-baseline approach, multiple images with an equal time step between image acquisitions should be used (Schmidt and Burgmann, 2003). The time steps used for multiple-baseline processing on the L.A. data set are not equally spaced (35 days) as the images were acquired from the WInSAR archive, which contains images purchased by varying researchers for varying projects. The time between images ranges from 1 day (ERS1-ERS2 tandem pair) to 513 days (span in 1994 and 1995 in which ERS1 was not collecting images for interferometry).

The forty-four images (differential interferograms) produced using the multiple-baseline procedure are presented in Appendix C. The dates of the images span from June of 1992 to November of 2000. The differential interferogram images produced from December 28, 1999 (prior to construction) until August 23, 1995 (post construction) for the time steps surrounding construction are presented in Figures 6.21 through 6.28. Each figure contains the differential interferogram along with a schematic displaying MOS-2b of Los Angeles Red Line, and a time line displaying the number of months (individual boxes) that have passed since the time of the initial image acquisition (June 6, 1992). The white band along the timeline indicates how many months have elapsed since the initial image, while the red band indicates the time period when the ERS1 satellite was not acquiring interferometry imagery.

The cumulative differential interferogram from June 6, 1992 to December 28, 1992 is displayed in Figure 6.21. As shown on the timeline, both of these scenes were acquired prior to construction; therefore, no construction related deformation was expected, and none was observed. The differential interferograms displaying the total cumulative phase corresponding to August 30, 1993, October 4, 1993, and November 8, 1993 are displayed in Figures 6.22, 6.23, and 6.24, respectively. Because of construction stoppage along the Hollywood Boulevard corridor during 1993 for groundwater drawdown (as discussed in Chapter 3 and displayed above the timeline in Figure 6.21), only a small segment of the LA redline was constructed in the East-West direction along Hollywood Boulevard during this time. A significant amount of the North-South segment was constructed along Vermont Avenue. The location of construction (corresponding to the distance drawn by arrows indicating the extent of tunneling in the

167

schematic to the right of the differential interferogram) is noticeable, with the measured subsidence above the tunnel indicating the tunnel is progressing to the South.

The April 5, 1995 time step is just prior to completion of both the Hollywood and Vermont tunneling operations. This image (Figure 6.25) is somewhat distorted or speckled in nature, allowing for the line to be distinguished but not as discernable as the previous images. A correlation between the baseline length from the image of interest to the initial image (initial resampling) and speckled images was observed. Potential cause for the speckled appearance may be the number of times an image is used in the regression, how many image combinations gap the image of interest, atmospheric contamination, or improper phase unwrapping. The approximate location of the tunneling face, based on literature reports of the tunnel progress and inferred tunneling rate, is also displayed on the schematic showing the LA Red Line (green and blue arrows). The times over which construction was completed for both the Hollywood and Vermont branches of the line are displayed above the timeline.

The way in which the images are paired with other images may also affect the speckle. Gomez (2009) suggests ensuring that images are connected using triangles instead of lines in the baseline versus time graph (Figure 6.20). To accomplish this, interferograms with baselines larger than the selected threshold (125 meters for the Los Angeles Red Line) are required. This increased redundancy between images outweighs the effect of increased baseline (Gomez, 2009). For example, interferograms 1 and 2 in Figure 6.20 contain baselines less than the 125 meter threshold (25 and 125 respectively). Therefore, these interferograms would have been selected and processing conducted. Interferogram 3 in Figure 6.20 contains a baseline of 250 meters and would not have been

selected based on the 125 meter threshold. The inclusion of this interferogram may however reduce the speckle in multiple-baseline images by increasing the redundancy of the processed images.
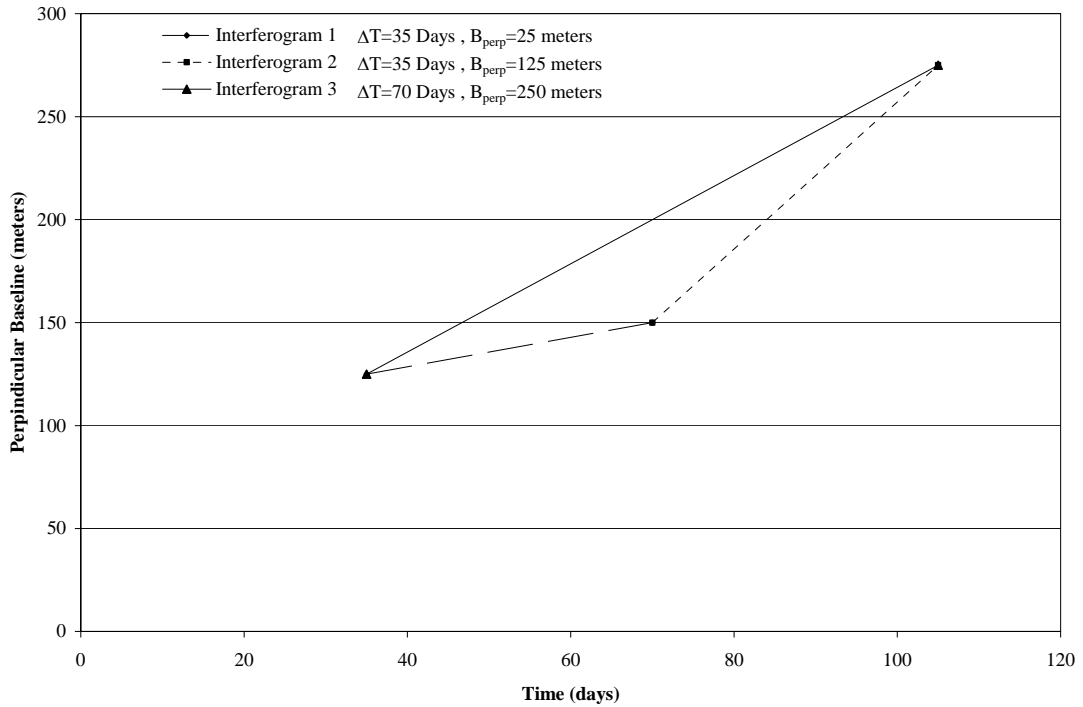
Figure 6.20. Baseline versus time plot example (not real data).

The June 14, 1995, July 19, 1995, and August 23, 1995 images are all post construction. Note that prior to the July 19, 1995 image, a section of the Hollywood Line was remined, causing additional settlement, which is observable in that image. Both the North-South Vermont line and the East-West Hollywood line are visible in the post-construction images; however, the North-South line is more readily apparent than the East-West lines. The increased spatial resolution North-South direction in the initial SLC images (4 meters multi-looked to 20 meters) is believed to be the cause for increased signal in the North-South direction as compared with the East-West direction (20 meters multi-looked to 20 meters).
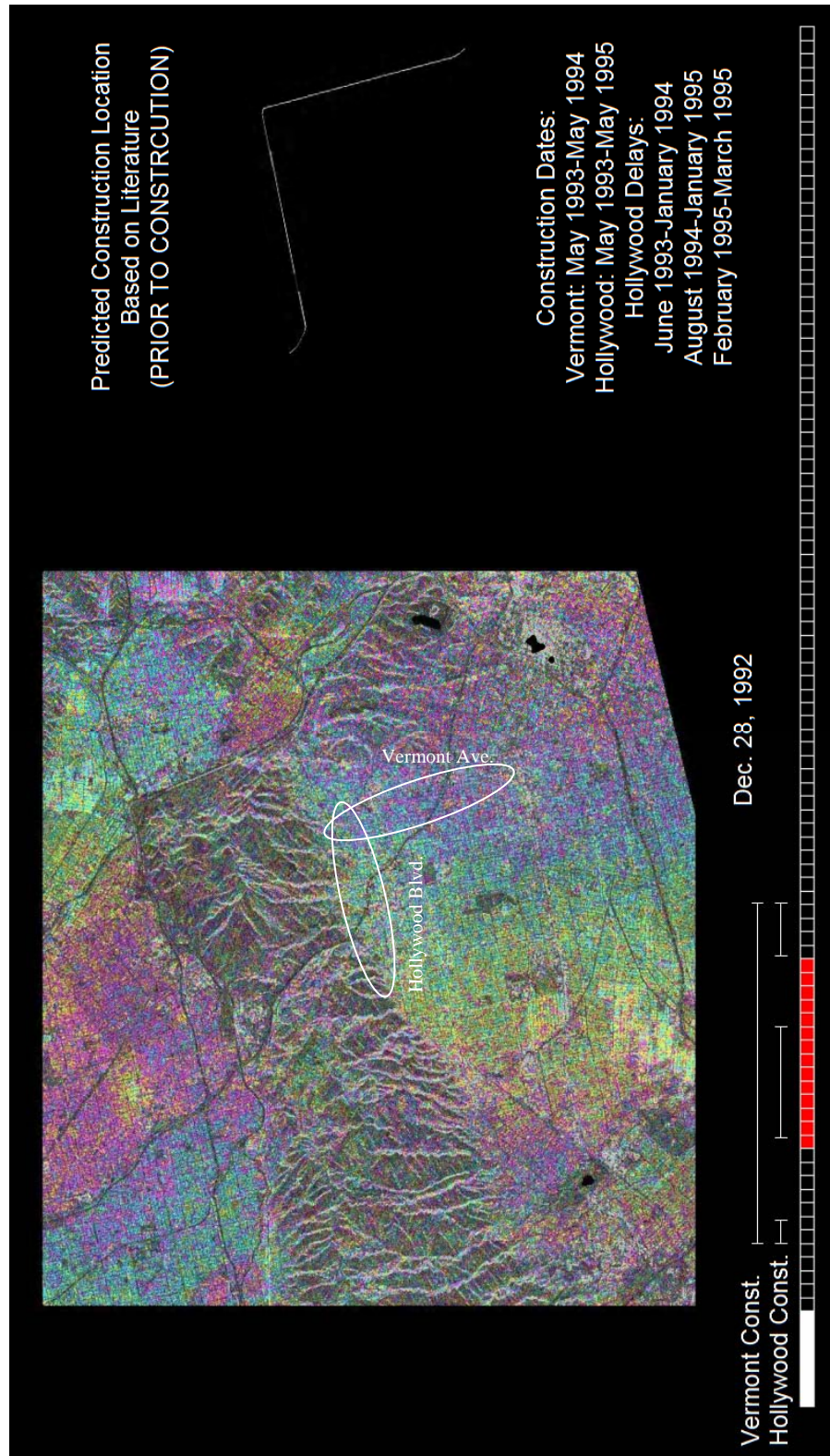
Figure 6.21. Multiple-baseline differential interferogram obtained for the December 28, 1992 time-step (prior to construction).
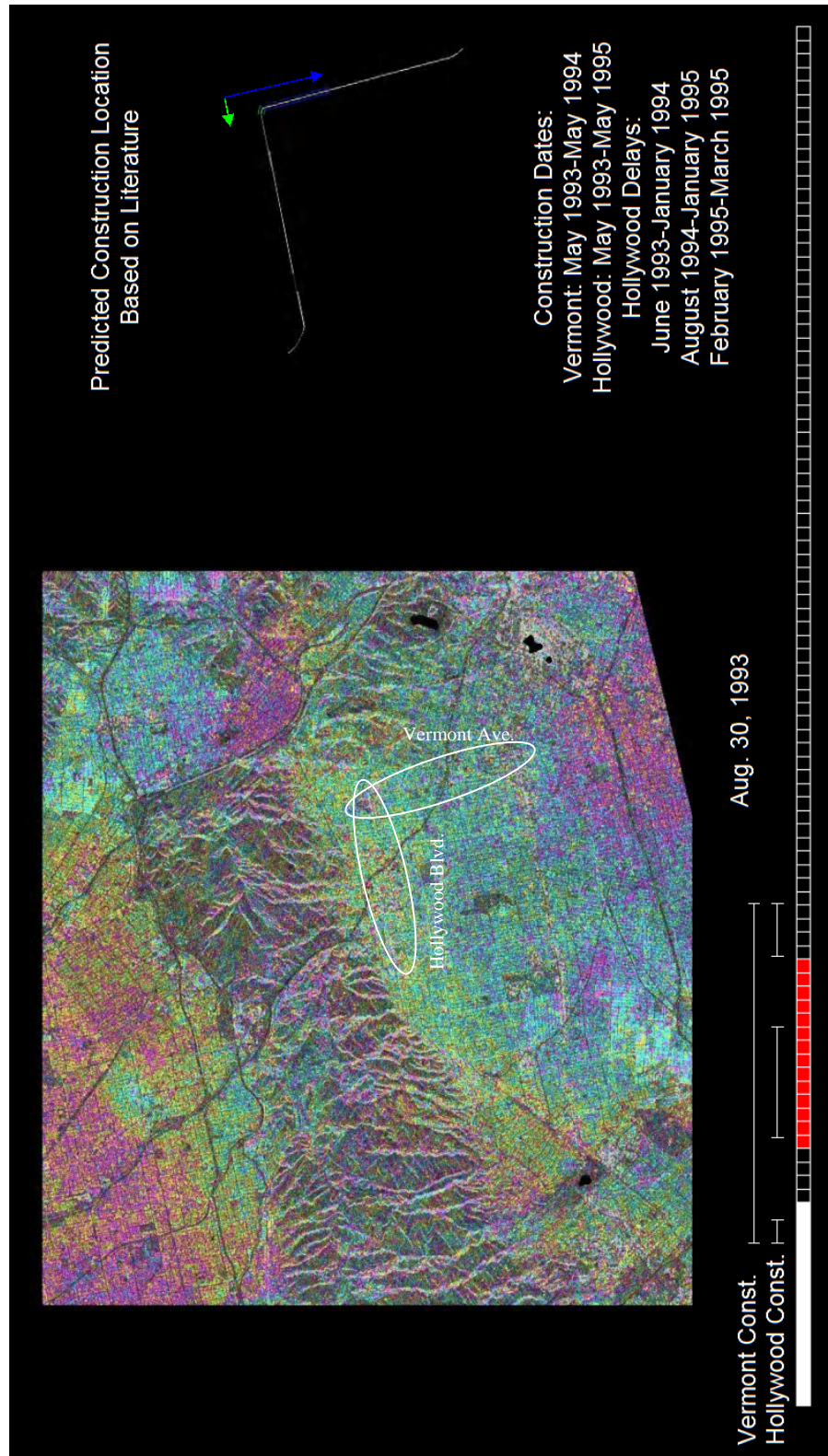
Figure 6.22. Multiple-baseline differential interferogram obtained for the August 30, 1993 time-step (during construction).

171
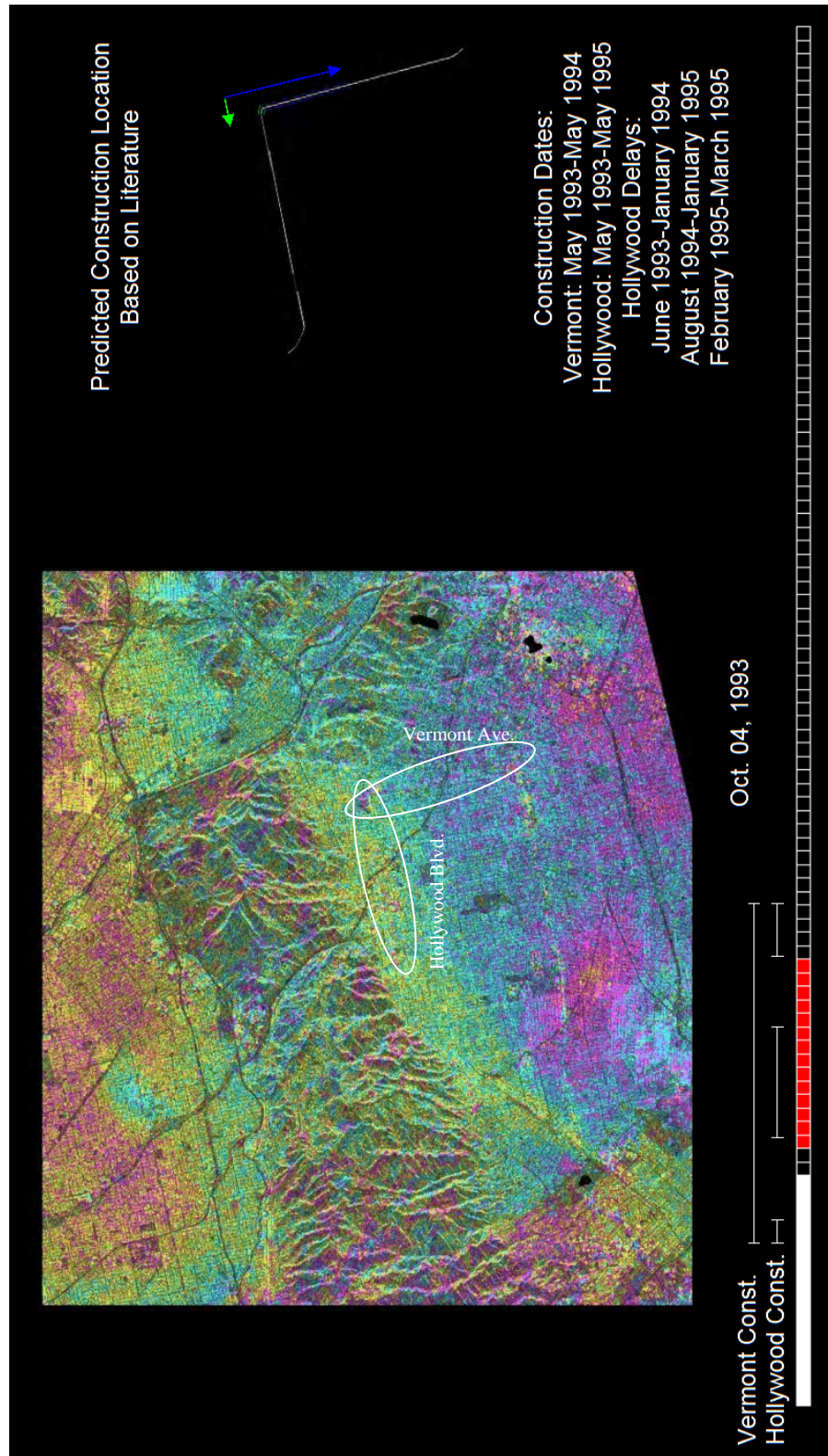
Figure 6.23. Multiple-baseline differential interferogram obtained for the October 4, 1993 time-step (during construction).

172
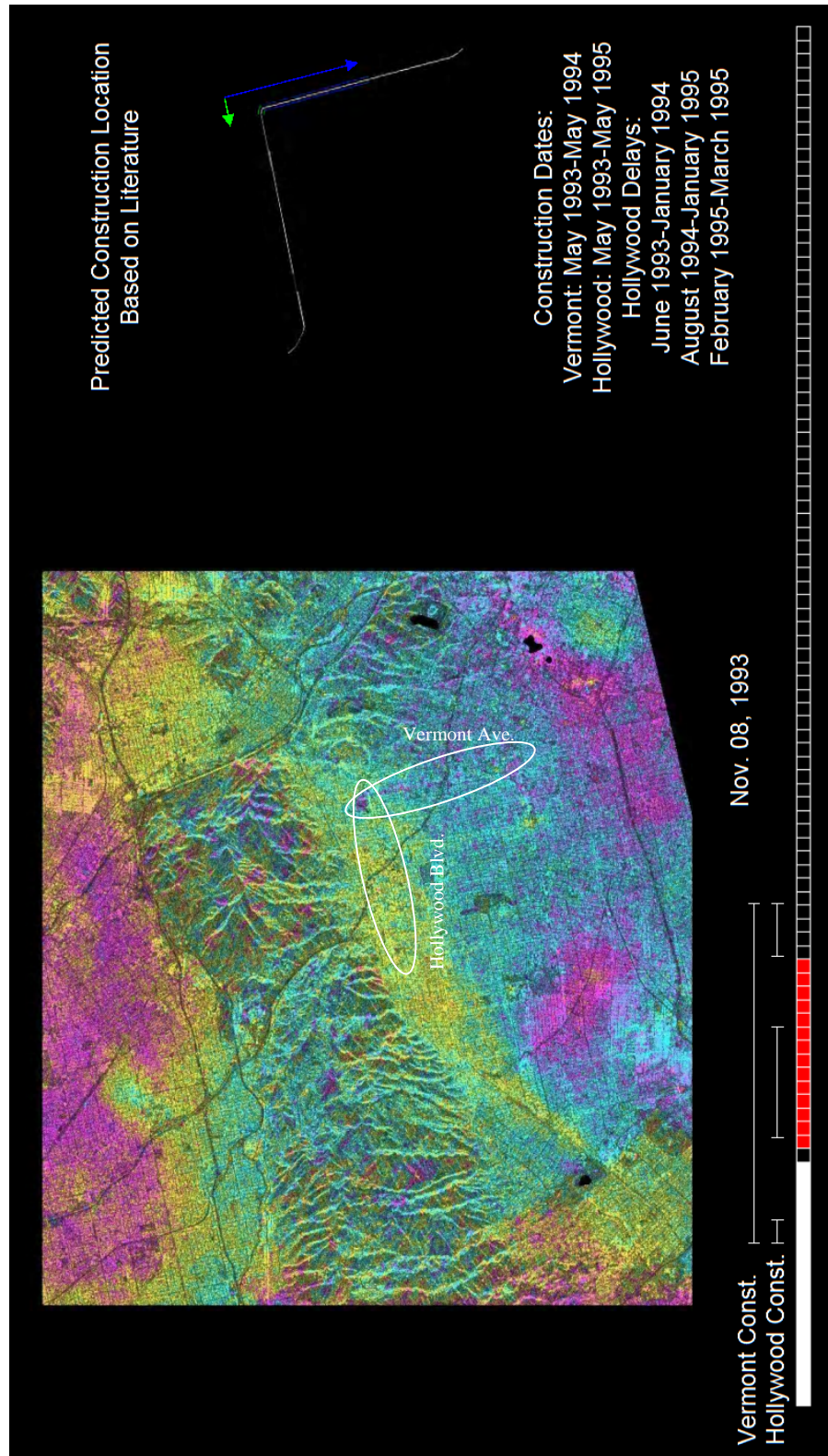
Figure 6.24. Multiple-baseline differential interferogram obtained for the November 8, 1993 time-step (during construction).
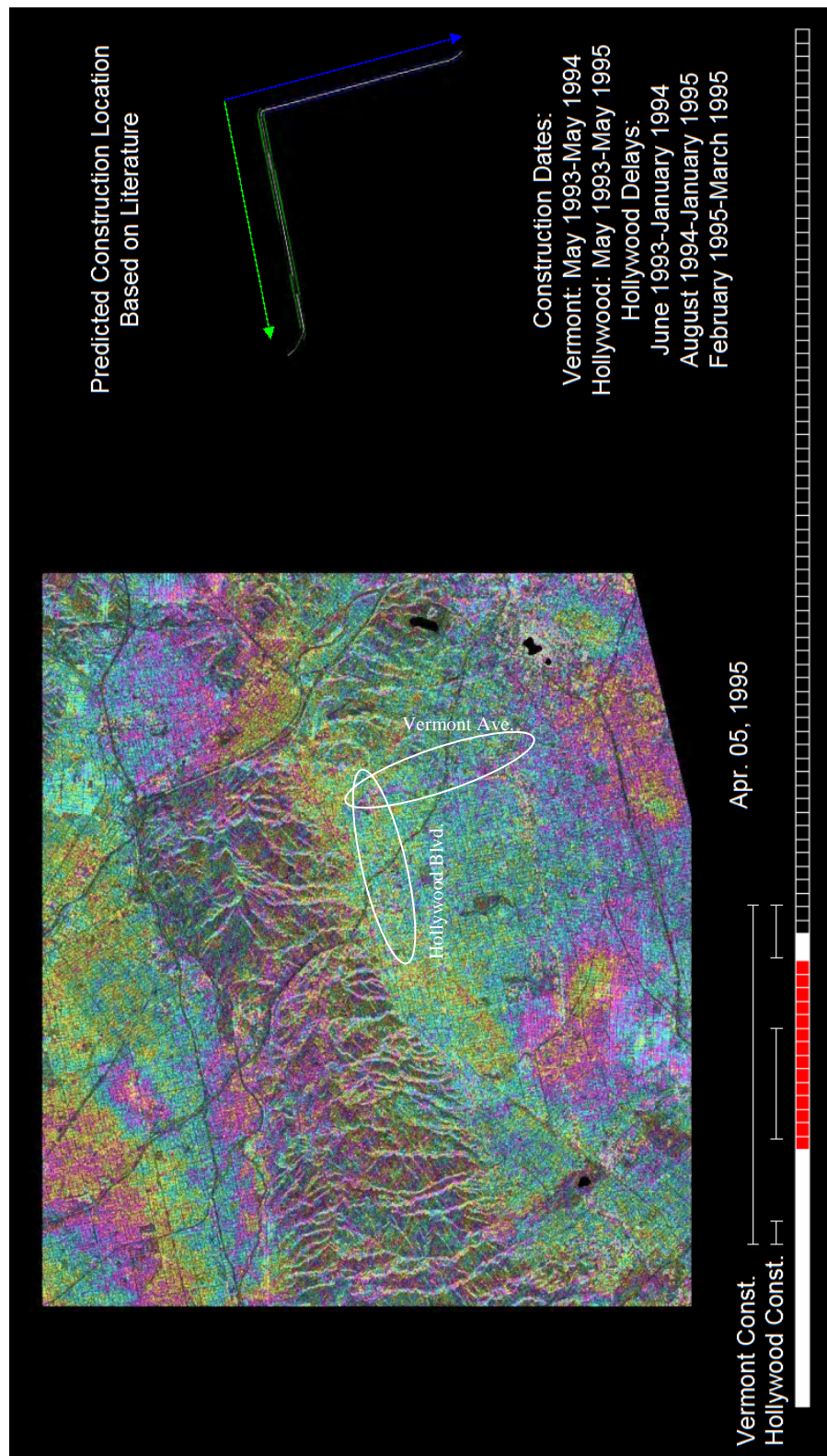
Figure 6.25. Multiple-baseline differential interferogram obtained for the April 5, 1995 time-step (during construction).

174
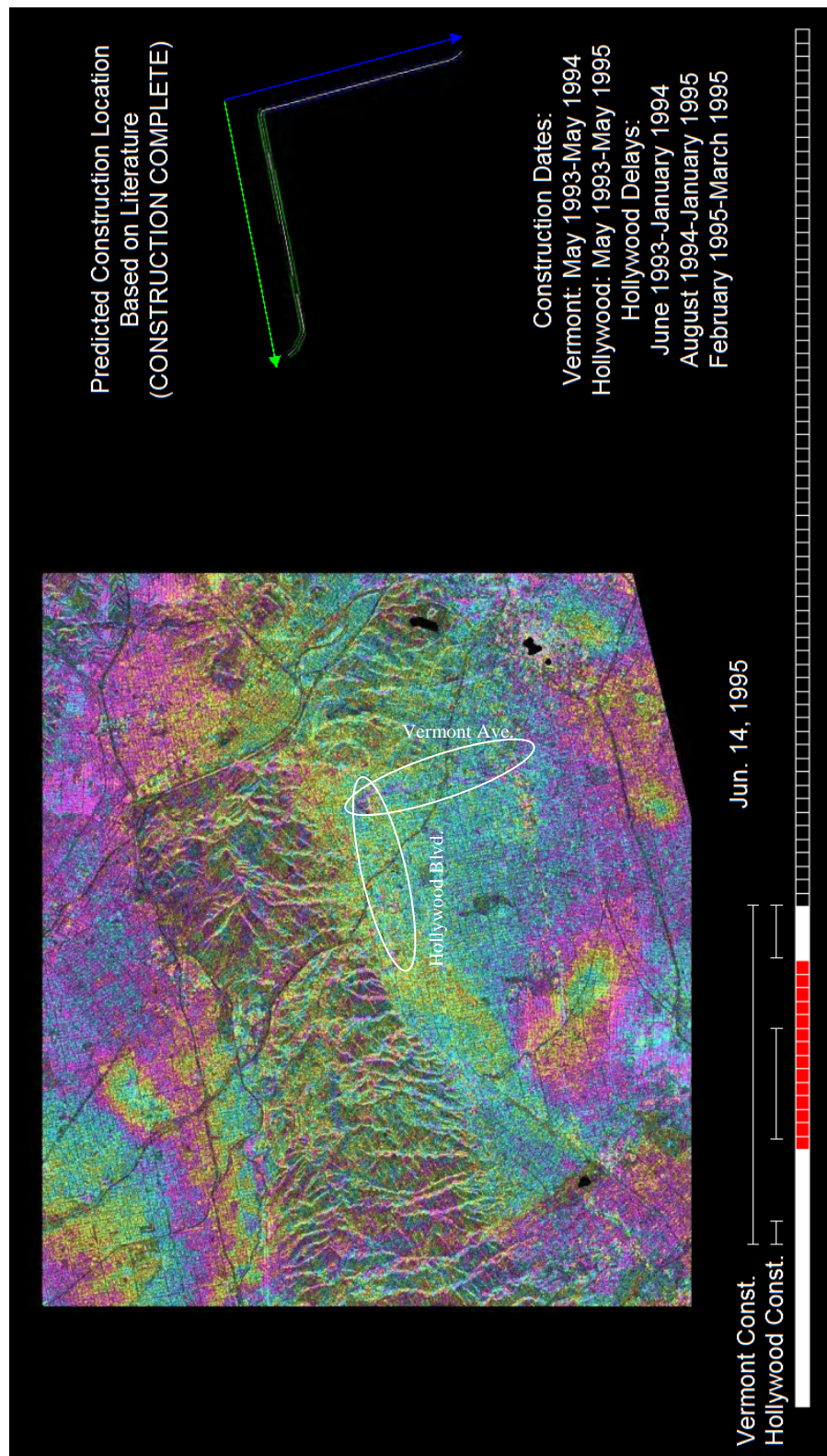
Figure 6.26. Multiple-baseline differential interferogram obtained for the June 14, 1993 time-step (after construction).

175
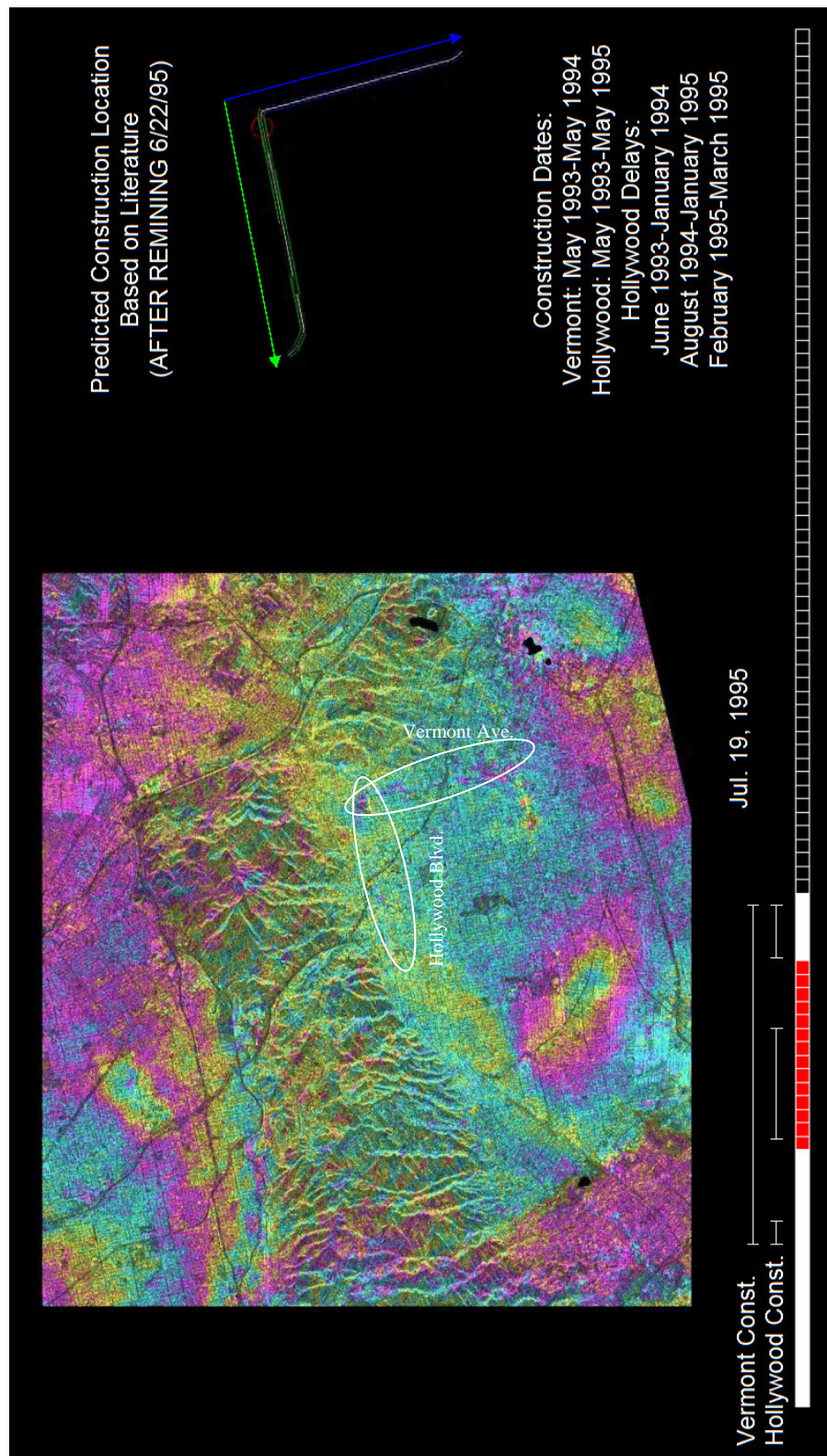
Figure 6.27. Multiple-Baseline differential interferogram obtained for the July 19, 1995 time-step (after construction and after post-construction remining).

176
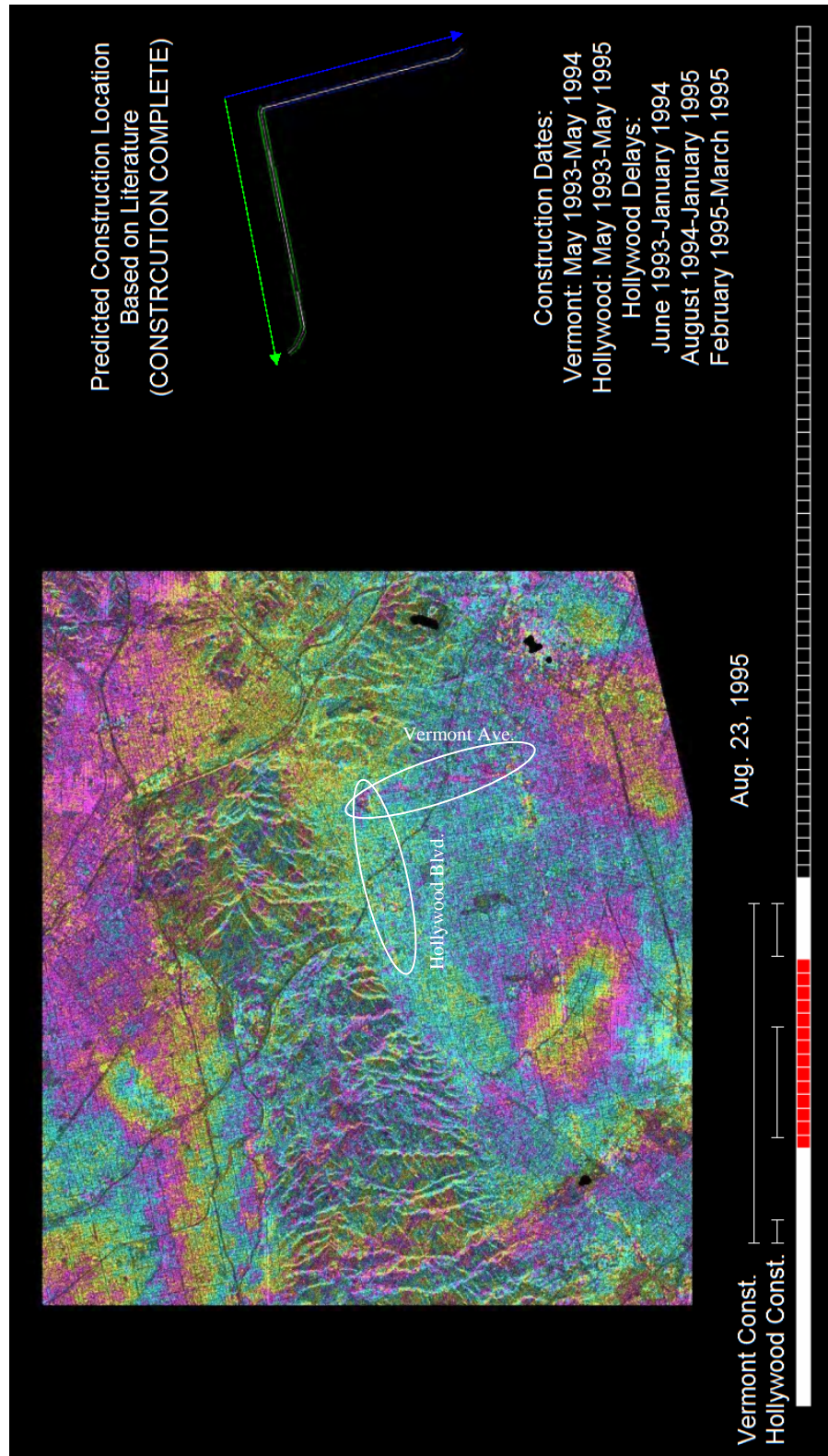
Figure 6.28. Multiple-baseline differential interferogram obtained for the August 23, 1995 time-step (after construction).

The multiple-baseline processing technique does not remove atmospheric contamination. Therefore, it is advisable to convert the multiple-baseline images into the multiple-baseline point domain (mb_pt) and conduct spatial and temporal filtering on the images to reduce the atmospheric phase contribution. Also, the phase unwrapping within the Santa Monica Mountains is not correct, as some unwrapping errors are present because of low coherence points adversely affecting this portion of the scene.

Using all of the scenes presented in Appendix C, the monotonic subsidence of the Salt Lake Oil Field is readily observable. The oil field appears to "grow" with time, as more subsidence is associated with increased compaction of the reservoir. Whereas the monotonic deformation in the oil field appears to grow with time, the episodic deformation of the L.A. redline appears to diminish with time as the pre-construction and post-construction phase do not continue to contribute to the phase difference.

6.4   *Ranking of Processing Techniques used on LA Red Line Site*

The advantages and disadvantages of the five processing techniques used on the Los Angeles Red Line Site are summarized in Table 6.5. These advantages and disadvantages include processing time, spatial resolution, radiometric resolution, portion of scene processed, time history, and feature detection.

Traditional processing is the fastest processing conducted, and contains the highest radiometric resolution and the lowest spatial resolution as compared with the other processing techniques. Traditional processing also enables processing of full scenes; however, the localized deformation features associated with the L.A. Red Line are typically masked or smeared in excess, preventing identification of the features.

Spatial processing is also rapid. However, because the spatial processing technique is typically conducted following traditional processing, and the results from traditional processing are used, spatial processing is slower than traditional processing. Because of decreased multi-looking in spatial processing, as compared with traditional processing, the radiometric resolution is lower and the spatial resolution is higher for spatial processing. This increased spatial resolution enabled detection of the localized deformation feature associated with the L.A. Red Line.

Enhanced spatial processing is quick. However, because the enhanced spatial processing technique is typically conducted following the spatial processing technique, and the results from spatial processing are used, enhanced spatial processing is slower than spatial processing and traditional processing. Like with spatial processing, decreased multi-looking in enhanced spatial processing, as compared with traditional processing, causes the radiometric resolution to be lower and the spatial resolution higher for enhanced spatial processing. Because a small filter is used and no coherence mask is used, and because the images are stacked, the localized deformation feature associated with the L.A. Red Line is detectable. In fact, the output image from the enhanced spatial processing technique best displays the localized deformation feature as compared with the output from the other processing techniques. However, the output image is a single stacked image, therefore, detection of the tunnel boring machine with time is not provided as it is with the multiple-baseline technique.

IPTA processing takes the longest of the processing techniques because the images have to be converted to the point domain. Although this technique requires the most time, it provides the highest radiometric and spatial resolution assuming stable

scatters, and enables detection of the localized deformation feature associated with the L.A. Red Line using a time-history plot. However, the feature is not discernable viewing the image generated containing total cumulative phase. Also, to enable unwrapping, this processing technique is conducted on the smallest image. Therefore, if the localized deformation feature associated with the L.A. Red Line was outside of the IPTA image footprint, processing would have to be conducted on another clip containing the localized deformation feature.

The multiple-baseline processing technique is a continuation of the enhanced spatial processing technique. Therefore, this processing technique takes longer than the traditional, spatial and enhanced spatial processing techniques. However, this technique enables detection of the localized deformation feature associated with the L.A. Red Line on a time dependent basis. Also, the progression of the tunnel face with time is discernable using this method.

Based on the above discussion of each processing technique and the advantages and disadvantages presented in Table 6.5, the enhanced spatial processing technique was selected as the best processing method for the Los Angeles Red Line site. Because the subsidence associated with the Los Angeles Red Line was best displayed in output from this processing method. Following the enhanced spatial method is the multiple-baseline method. Because the multiple-baseline method uses the enhanced spatial processing output, provides information about the amount of deformation over time, and enables the detection of the Los Angeles Red Line it was ranked ahead of the traditional, spatial and IPTA processing techniques. The spatial processing technique was ranked ahead of the IPTA processing technique for data processing conducted on the Los Angeles Red Line

site because the subsidence associated with the L.A. Red Line was detected in the spatial processing output image. The subsidence associated with the L.A. Red Line was not detected using the IPTA processing image, however the subsidence was detected using the IPTA processing time history. IPTA processing takes almost twice as long as spatial processing, therefore, spatial processing received the higher ranking. The traditional method was ranked last because the subsidence associated with the Los Angeles Red Line was not detected using this procedure. Additional variables that were taken into consideration in ranking the methods are presented in Table 6.6.

Table 6.5. Advantages and disadvantages of alternative processing techniques.

	Advantages	Disadvantages	Rank
Traditional	Fastest processing time. Low Speckle. 100 km^2 scene processed.	40 meter pixel. No time history. Feature smeared and masked in stacked image.	5
Spatial	Rapid processing time. 20 meter pixel Feature is detected but masked in stacked image. 100 km^2 scene processed.	Moderate speckle. No time history.	3
Enhanced Spatial	Quick processing time. 20 meter pixel LA Red Line subsidence is detected in stacked image covering the correct time-span.	Moderate speckle. No time history. 20 km^2 scene processed.	1
IPTA	Low speckle. 20 meter pixel Time history.	Slowest processing time. Temporal unwrapping. LA Red Line subsidence is not present in IPTA output image but can be interpreted in time history. 10 km^2 scene processed.	4
Multiple-baseline	20 meter pixel Time history. Feature is detected in output.	Slow processing time. Moderate to high speckle. 20 km^2 scene processed.	2

A ranking matrix using the advantages and disadvantages from .

Table 6.5. Advantages and disadvantages of alternative processing techniques.

is presented in Table 6.6. This matrix may be used to determine the proper processing technique to be used for various features and sites. Based on this table, the enhanced spatial and multiple-baseline processing techniques proved to be the most advantageous for the Los Angeles Red Line site, as these were the only processing techniques in which the feature was detected.

Table 6.6. Ranking matrix of five processing techniques as tested on the LA Red Line Site.

	Scene Size Processed	Time Required CPU/Human	Feature Observed	Spatial Smear Of Feature	Time-Series Produced
Traditional	100 km x 100 km	Hours/Day(s)	Slightly, Masked	High	No (Stack Only)
Spatial	100 km x 100 km	Hours/Day(s)	Slightly, Masked	Moderate	No (Stack Only)
Enhanced Spatial	20 km x 20 km	Hours/Week(s)	Yes	Low	No (Stack Only)
IPTA	10 km x 10 km*	Day(s)/Month(s)	Slightly	Low	Yes
Multiple-Baseline	20 km x 20 km	Day(s)/Week(s)	Yes	Low	Yes
*The IPTA processing technique is the only technique which cannot be conducted on a full scene. Smaller scene size for IPTA enables proper 3-D unwrapping and faster processing time.					

6.5   Processing of Mosul Dam Site

Based on the ranking of the processing techniques used on the Los Angeles Red Line, the top three processing techniques (spatial, enhanced spatial and multiple-baseline) were applied on the Mosul Dam site. Results and discussion of the processing techniques is presented in Sections 6.5.1 through 6.5.3. Discussion of the subsidence measured using these processing techniques as compared with historical subsidence (discussed in Chapter 3) is discussed in Section 6.5.4, and a ranking of the processing techniques is presented in Section 6.5.5.

6.5.1   Spatial Processing

Spatial processing was conducted using the 16 Envisat scenes acquired from March 2003 through April 2007. The processing was conducted on the 11.5 by 20.5 clipped RSLC images using the interferogram combinations described in Chapter 5. The spatial processing technique was used because, as previously recommended in this chapter, the spectral filter is recommended for use when a subsidence feature is located in mountainous areas.

This site proved to have low correlation (gray shaded areas) in the mountainous areas as displayed in the interferogram stack presented in Figure 6.29. Unlike the Los Angeles Red Line site where the localized deformation feature was located in the urban area, the localized deformation feature associated with the subsidence of Mosul Dam is located in a non-urban area. Whereas the same coherence mask threshold (50%) used during spatial processing on the Los Angeles Red Line site was applied to the Mosul Dam site, the Mosul Dam site was interpolated across the masked null values to produce an interferogram. The areas which were black in the Santa Monica Mountain for the Los Angeles site are gray for the Mosul Dam site because of the use of an interpolator. The interpolator aided in allowing more of the image to be displayed, but did not contribute to boosting the stacked phase. The interferogram stack displaying only the area surrounding Mosul Dam is presented in Figure 6.34. In this image the subsidence feature associated with Mosul Dam is distinguishable.
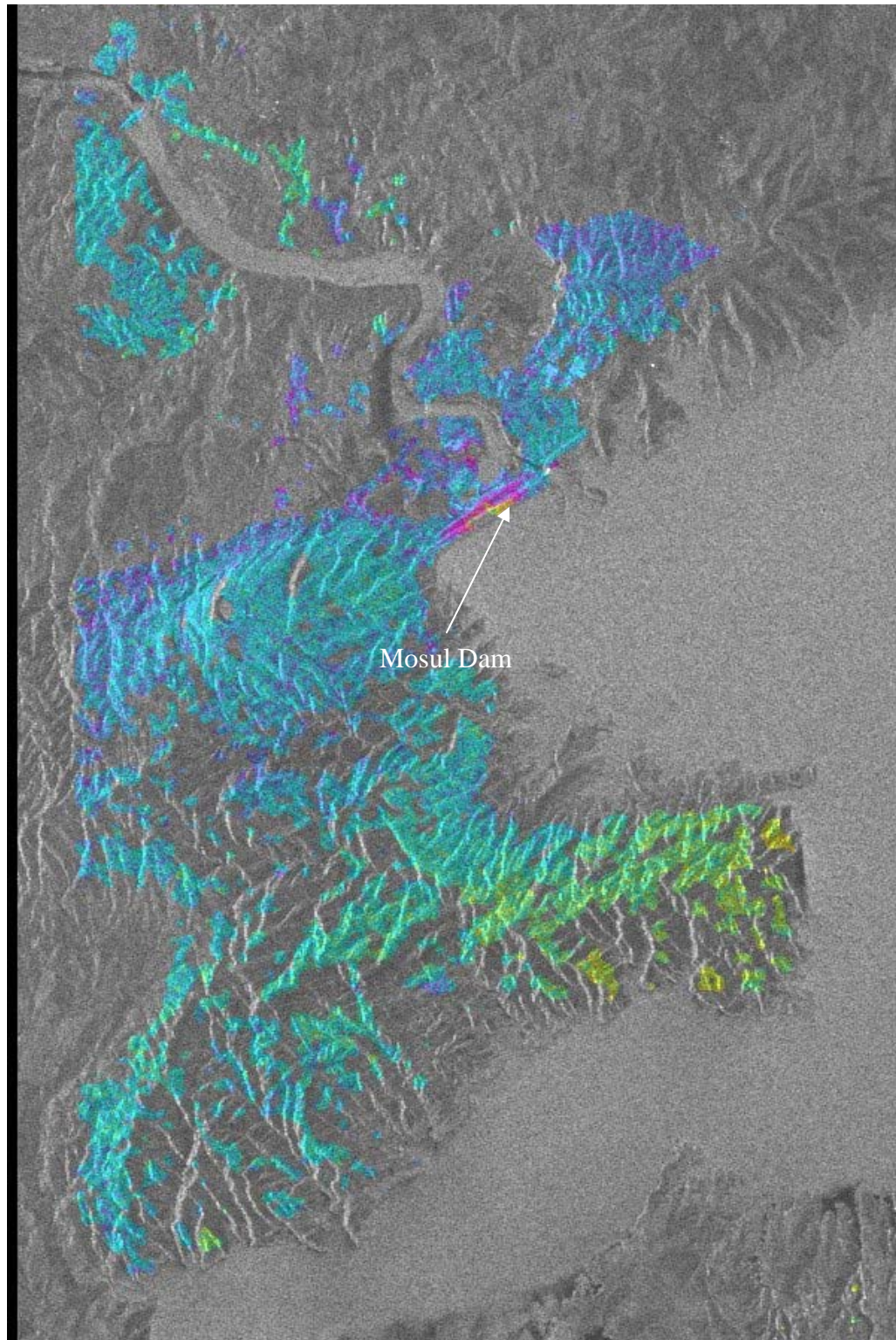
Figure 6.29. Interferogram stack (19 interferograms) of Mosul Dam Site using spectral filter with window size of 8, 20% coherence mask, multi-looked at 1 and 5 in SAR viewing geometry (Gomez, 2009).
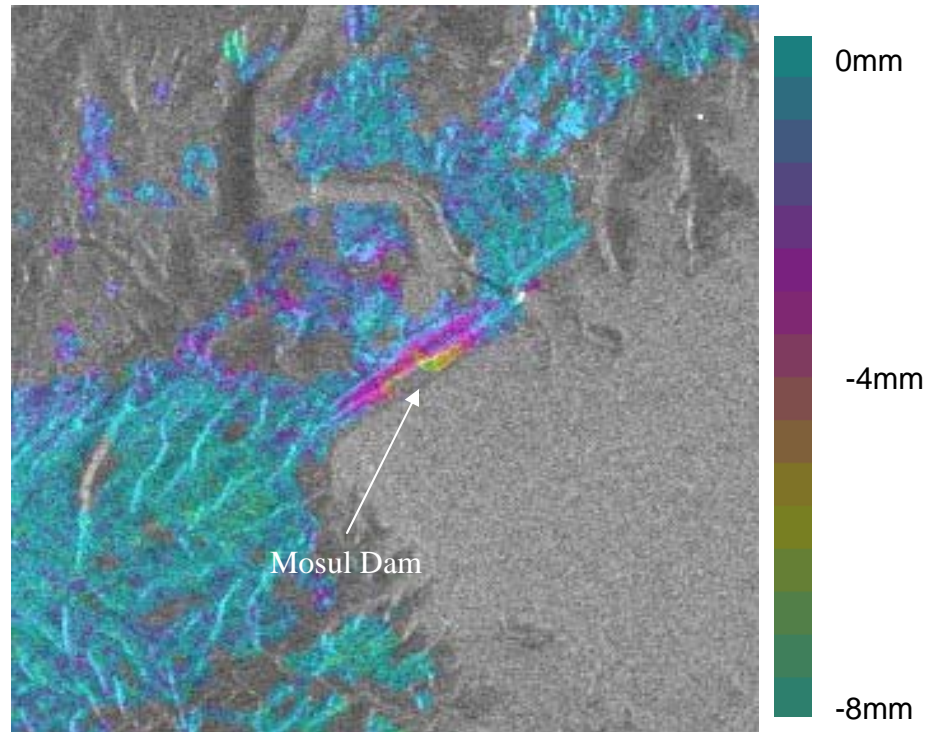
Figure 6.30. Interferogram stack (19 interferorams) showing area of subsidence related to the dissolution of foundation materials within Mosul Dam using spectral filter with window size of 8, 20% coherence mask, multi-looked at 1 and 5 in SAR viewing geometry (Gomez, 2009).

6.5.2   Enhanced Spatial Processing

Like the spatial processing technique, the enhanced spatial processing was conducted using the 16 Envisat scenes acquired from March 2003 through April 2007. The processing was conducted on the 11.5 by 20.5 clipped RSLC images using the interferogram combinations described in Chapter 5.   The enhanced spatial processing technique was used because it, as previously displayed in this chapter, provided the best results for the Los Angeles Red Line.

This site proved to have low correlation in the mountainous areas.   This poor coherence led to unwrapping errors during enhanced-spatial because a coherence mask threshold was not used.   Therefore, a small coherence mask was used (20%).   However, unwrapping errors occurred even when using this small coherence mask as presented in

Figure 6.31. Unlike the Los Angeles Red Line site where the localized deformation feature was located in the urban area with high coherence, the localized deformation feature associated with the subsidence of Mosul Dam is located in a non-urban area with low coherence. The interferogram stack displaying only the area surrounding Mosul Dam is presented in Figure 6.32. In this image the subsidence feature associated with Mosul Dam is distinguishable.

In addition to the dissolution below the dam, sinkholes have also developed in the right abutment and downstream from the dam by the power station (Emerson, 2009). Subsidence is observed in these areas in the images developed using the slope adaptive filter (Figure 6.32). Subsidence is not observed in these areas in the images developed using the spectral filter because too strong of a coherence mask was used (Figure 6.30 presented previously).
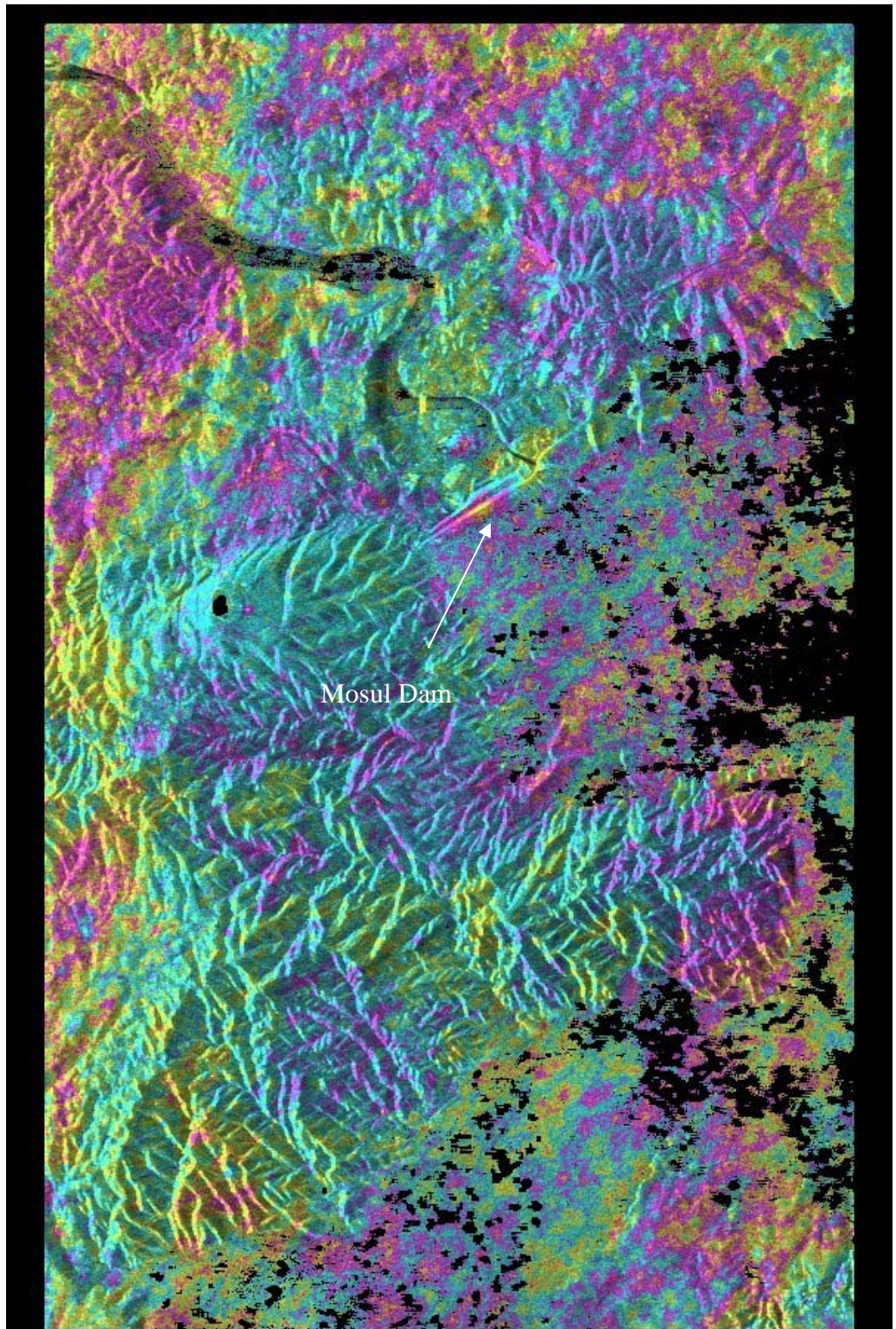
Figure 6.31. Interferogram stack (19 interferograms) of Mosul Dam Site using slope adaptive filter with window size of 2, no coherence mask, multi-looked at 1 and 5 in SAR viewing geometry.
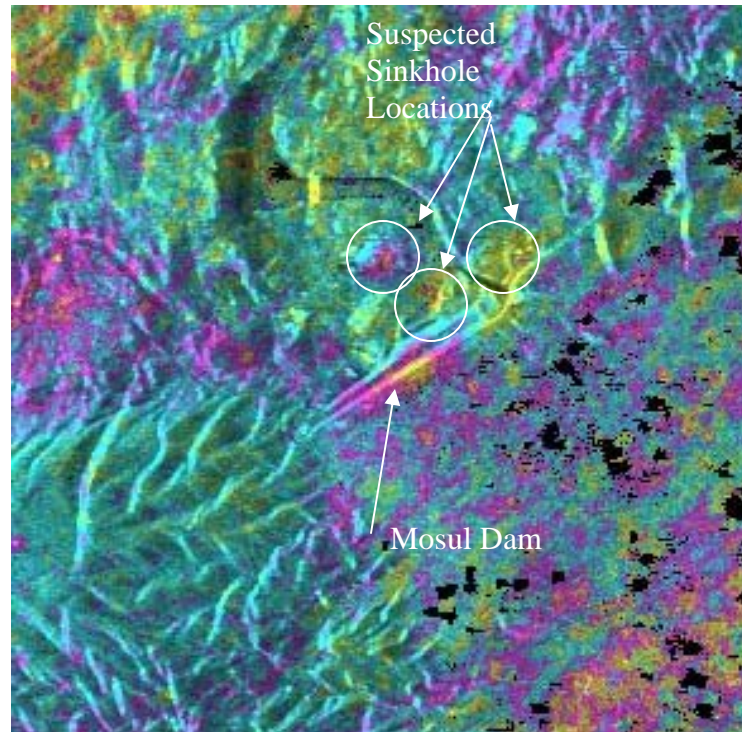
Figure 6.32. Interferogram stack (19 interferograms) showing area of subsidence related to the dissolution of foundation materials within Mosul Dam using slope adaptive filter with window size of 2, no coherence mask, multi-looked at 1 and 5 in SAR viewing geometry.

6.5.3   Multiple-Baseline

The multiple-baseline processing technique was attempted on the Mosul Dam site, however, low coherence prevented successful use. If any portion of the image has null values the GAMMA multiple-baseline program will not compute an interferogram time series for the interferogram stack. The null values may be interpolated across to allow for successful multiple-baseline processing. For the Mosul Dam site however, the coherence was so low in the mountainous areas that even after interpolating across the null value data, the multiple-baseline program would not perform. Therefore, the multiple-baseline processing technique did not work for the Mosul Dam site.

6.5.4   Ranking of Processing Techniques used on Mosul Dam

Based on the processing results acquired from each of the three processing techniques used on the Mosul Dam site, the spatial processing technique is the fastest to process and produced the image which displayed the localized deformation feature the best. However, the masking and interpolating used in this procedure prevented the observation of the sinkhole features presented in the enhanced spatial image. If small features are expected in non-urban areas both the spatial and enhanced spatial processing techniques should be used.

Table 6.7. Ranking matrix of five processing techniques as tested on the LA Red Line Site.

	Scene Size Processed	Time Required CPU/Human	Feature Observed	Spatial Smear Of Feature	Time-Series Produced	Rank
Spatial	11.5 km x 20.5 km	Hours/Day(s)	Yes Masked	Moderate, Interpolated	No (Stack Only)	1
Enhanced Spatial	11.5 km x 20.5 km	Hours/Week(s)	Yes	Low	No (Stack Only)	2
Multiple-Baseline	11.5 km x 20.5 km	Day(s)/Week(s)	No	-	No	3

6.5.5   Comparison of InSAR Subsidence with Historical Subsidence

The location of historical dissolution of the dam foundation causing subsidence of the dam crest was discussed in Chapter 3. Locations of high grout take and loss of water in water pressure tests indicate the location voids under the dam. For Mosul Dam, these locations correspond to the position of the historic river channel prior to construction of the dam. The position of the historic river channel as presented in Figure 3.12 is represented in Figure 6.33 for convenience. When compared with the interferogram stack generated using the spatial processing technique, the location of greatest subsidence

189

corresponds with the location of the historic river channel, on the up-steam face of the dam.
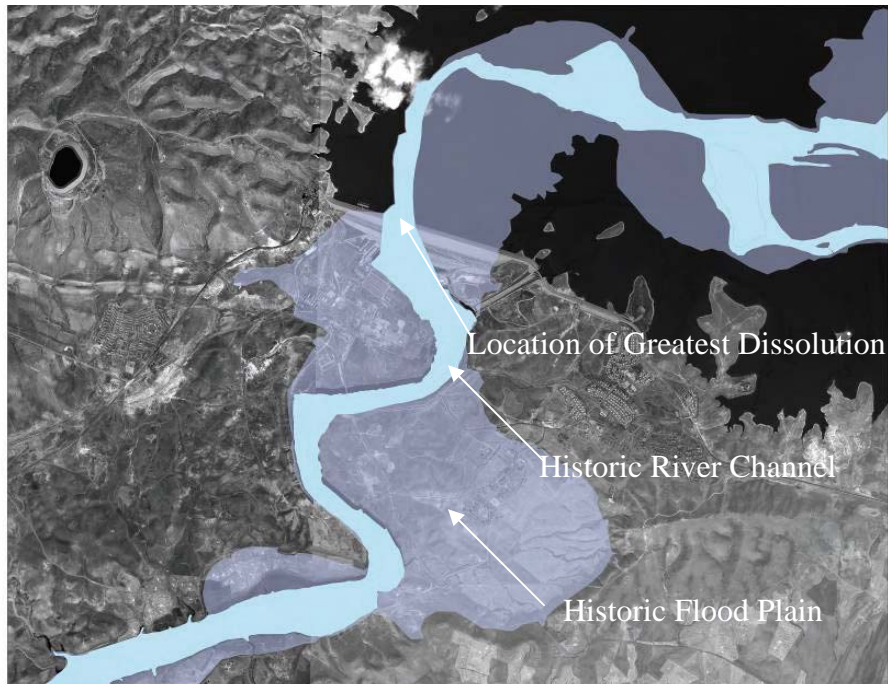
Figure 6.33. Aerial photo mosaic of Mosul Dam with pre-dam Tigris River channel overlay (from Kelley et al., 2007).
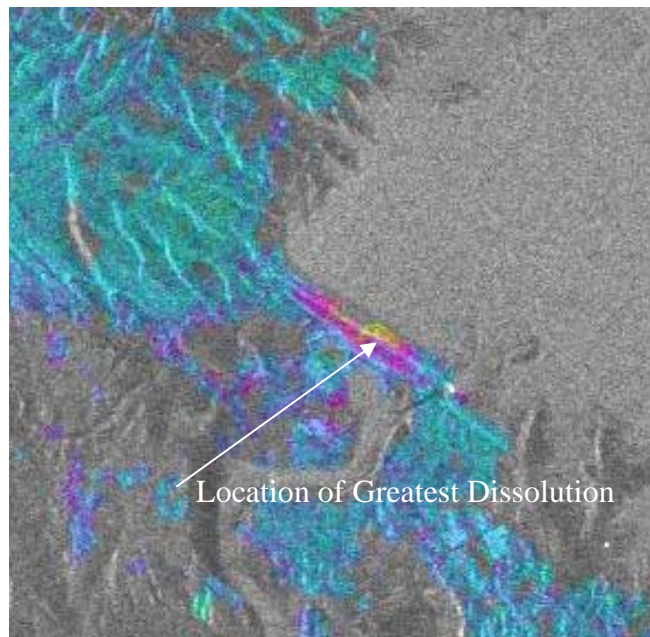
Figure 6.34. Interferogram stack of Mosul Dam Site using spectral filter with window size of 8, 20% coherence mask, multi-looked at 1 and 5 (Gomez, 2009).

6.6   *Lessons Learned*

Lessons learned from this study and derived from the results presented in Sections

6.2 through 6.5 include the following:

1.   For detecting localized deformation features, spatial resolution is the
       most important parameter. Larger spatial resolution reduces the ability
       to identify localized deformation features.

2.   Coherence is better maintained in mountainous areas using the spectral
       filter than the slope adaptive filter. However, coherence is better
       maintained around localized deformation features using the slope
       adaptive filter than the spectral filter.

3.   The cumulative deformation image obtained from enhanced spatial
       processing was the best for the Los Angles Red Line (urban), while the
       cumulative deformation image obtained from the spatial processing
       was the best for the Mosul Dam site (mountainous).   Different
       processing techniques are suitable for different applications.
       Traditional processing gives rapid full-scene coverage, while IPTA
       processing takes longer and does not provide full-scene coverage.
       Multiple baseline and IPTA processing provide estimates of
       deformation rate in addition to cumulative deformation while
       traditional, spatial and enhanced spatial provide only cumulative
       deformation estimates.

4.   The number of images used in an image stack may adversely affect the
       stack and prevent the ability to identify localized deformation features.

5.   The localized deformation features are not apparent in the image output from IPTA, but are apparent in the deformation time history for select points.

6.7   Recommendations for Processing

Recommendations developed from the lessons learned discussed in Section 6.6 are presented herein. These recommendations are applicable to all InSAR processing and focus on the processing techniques, when each technique is appropriate for use, and required modifications to the techniques for successful use.

The use of the enhanced spatial processing technique and the multiple-baseline processing technique is suggested for localized deformation features located in urban environments. Because the multiple-baseline processing technique uses the output from the enhanced spatial processing technique, a stacked interferogram and multiple individual time step interferograms are produced when both techniques are used. Using these combinations of images, localized deformation features can be identified in the stacked image, and then changes to the localized deformation feature with time can be monitored using the individual time step interferograms.

For sites in which the deformation is episodic, a moving stacking window (i.e. stack only the images which cross the time of construction) is suggested to capture the deformation at the location of interest. For the Los Angeles Red Line site, the stacking window was limited from one year before construction until one year after construction to prevent the lack of pre-construction deformation or the decay in post-construction deformation from affecting the results. The size of the window will depend upon the amount of data. If there is a limited amount of data over a short time span, the size of the

window should be limited to weeks or months before and after construction instead of one year as with the L.A. Red Line. Just as with stacking, when using the multiple-baseline processing technique, only the images that surround the time of construction should be used, since the images before and after the time of construction will be biased by lack of pre-construction deformation or the decay in post-construction deformation. For sites is which the deformation is monotonic, all of the images may be stacked (enhanced spatial) or used (multiple-baseline) as long as the rate of subsidence is constant. When the rate is not longer constant, only the images that surround the time span when the rate was constant shall be used, just as with the episodic deformation case described above. A moving window containing only small groups of images may be used if the dates of the construction are not known to determine when and where construction occurred.

Investigation into the effect of baseline dependence (master viewing geometry-slave) on the multiple-baseline approach will be useful in determining the cause of speckle in many of the multiple-baseline scenes. Developing a moving window stacking function will also enable rapid processing in order to produce the interferogram (enhanced spatial processing) or interferograms (multiple-baseline) with the most visible deformation feature.

The recommendations derived from this study are summarized as follows:

- The enhanced spatial and multiple-baseline processing techniques are suggested for urban areas. Deformation features for the Los Angeles Red Line are observable using the enhanced spatial and multiple-baseline

processing techniques. The features are not observable using the traditional, spatial and IPTA processing techniques.

- The spatial and enhanced spatial processing techniques are suggested for mountainous areas. Deformation features for the Mosul Dam site are observable using the spatial and enhanced spatial processing techniques. The features were not observable using the multiple-baseline processing technique because of portions of the scene containing null values. An interpolator can be used to fill the null values in order to generate an image, however, the robustness of the interpolation is questionable.

- A moving timeframe window is suggested for detection of an unknown feature to prevent averaging scenes containing little or no deformation with scenes containing large deformation. For episodic movements, the time span of images used in a stack affects the results of the stack. The time span is dependent upon the duration of the imagery coverage.

6.8   Summary

Combinations of multi-looking, filter type, filter size, coherence mask threshold, and image stacking parameters were investigated on the Los Angeles Red Line site to determine how varying these parameters affects the detection and characterization of localized deformation features associated with geotechnical engineering applications.

Results of these analyses indicate that increasing the multi-looking reduces the speckle of the image, but causes the image to lose sharpness or "smear" the localized deformation features. The slope adaptive filter allows for a smaller window than the spectral filter, allowing for more of the localized feature to be retained following

filtering. Increasing the filter size increases coherence using the spectral filter. Increasing the coherence mask threshold causes more of the scene to be masked, and may mask the feature that is subsiding. Images that do not surround an episodic event should not be used as these images may cause the localized deformation feature of interest becomes less visible.

Time-dependent processing techniques were also investigated on the Los Angeles Red Line Site to investigate the benefit of using temporal unwrapping or temporal filtering. The IPTA technique provides an image that displays the average differential interferometric phase rate, along with time series showing the deformation with time for selected individual points within the image. The multiple-baseline technique provides multiple images that display the cumulative differential interferometric phase relative to the initial scene. Subsidence caused by the construction of the Los Angeles Red Line is visibly discernable in the multiple-baseline images but is not discernable in the IPTA image. Whereas the deformation of selected points located above the Los Angeles Red Line is not discernable in the IPTA phase rate image, the deformation is discernable in the IPTA time series plot for each point. Investigating each individual point to determine if the point is subsiding is much more time consuming than determining if a point or area of points is subsiding by analyzing multiple cumulative differential interferogram images.

The spatial and enhanced spatial processing techniques produced images in which the Mosul Dam subsidence is observed. The location of the subsidence corresponds with the location of the historic river channel and highest grout take. Sinkholes located in the right abutment and downstream face are also detected using the enhanced spatial processing technique.

The ranking of processing techniques as determined from processing conducted on the Los Angeles Red Line (urban) site is: 1. enhanced spatial, 2. multiple-baseline, 3. spatial, 4. IPTA, and 5. traditional. The ranking of the processing techniques as determined from processing conducted on the Mosul Dam (non-urban) site is: 1. spatial, 2. enhanced spatial, and 3. multiple-baseline. Therefore, enhanced spatial processing is recommended for urban sites while spatial processing is recommended for non-urban sites.

Chapter 7: Summary, Conclusions and Recommendations for Future Work

The scope of work presented in this document was designed to address three main objectives related to the hypothesis:

1. Evaluate the effect of filtering, multi-looking, and masking of SAR data as applied to geotechnical engineering applications that often produce localized deformations (e.g. subway construction, monitoring of dams).

2. Evaluate five different methods used to determine ground deformations for Earth resource applications, as applied to geotechnical engineering applications.

3. Rank the five different methods, according to their effectiveness for use in geotechnical engineering applications.

The conclusions and recommendations derived from addressing these objectives are presented in this chapter.

In addition to providing discussion on obtaining the objectives, information about the satellites used to conduct this research, and how they were used, was presented in Chapter 2. The localized deformation movements associated with the Los Angeles Red Line and Mosul Dam sites was presented in Chapter 3, and data processing techniques and data used to conduct this research was presented in Chapters 4 and 5. The results obtained and recommendations regarding the processing techniques were presented in Chapter 6.

7.1   *Evaluations of Filtering, Multi-looking, Masking and Stacking of SAR Data*

Thirty-three variations of filtering (type and size), multi-looking and masking combinations were investigated, using Los Angeles Red Line Site imagery, to determine the advantages and disadvantages of variations to the processing parameters for geotechnical engineering applications. The effects of multi-looking, filter type, filter window size, and coherence mask threshold were evaluated. The amount and time span of images used in the stacking were also evaluated.

Results of the evaluations of the thirty-three combinations of filtering, multi-looking, masking, and stacking of SAR data as applied to geotechnical engineering applications are summarized below. Results of the processing techniques used on the specific site (L.A. Red Line and Mosul Dam) are discussed in Section 7.3:

- Increased multi-looking decreased spatial resolution (increased smearing) and increased radiometric resolution (decreased speckle).

- Increased multi-looking increased coherence.

- Increased filter size increased smearing.

- The slope adaptive filter allows for use of no coherence mask (all of the image can be unwrapped with no null data values), while the spectral filter requires a coherence mask (null data values are assigned to the portions of the image with coherence values below the threshold; only portions of the image with coherence values above the threshold can be unwrapped).

- Increased coherence mask threshold removed localized deformation feature visibility.

- The amount and quality of images used in a stack affect the results of the stacking. Fewer high quality (non-speckled) images surrounding the time span of the movement of the localized deformation feature allow for better detection of the localized deformation feature.

For scenes with low coherence (mountainous areas), increased multi-looking (2 and 10 looks) is required, while scenes with high coherence (cities) require decreased multi-looking (1 and 5 looks). Increasing the amount of multi-looking (for this study multi-looking was increased from 1 look in the range direction and 5 looks in the azimuth direction to 2 looks in the range direction and 10 looks in the azimuth direction) was found to reduce the spatial resolution causing the images to lose sharpness or smear localized deformation features. While the localized deformation features associated with subsidence of the Los Angeles Red Line are observable using both multi-looking combinations, the localized deformation feature associated with the L.A. Red Line appears to cover a larger surface area in images developed using 2 and 10 looks than in images developed using 1 and 5 looks. When a coherence mask is used along with increasing the amount of multi-looking, the image becomes more coherent. This increase in coherence allows more of the scene to be analyzed.

Better performance of the spectral filter occurred when large window sizes are used (32), as opposed to the slope adaptive filter in which no gain in performance was obtained with larger window sizes. A window size of 32 is recommended for the spectral filter while a window size of 2 is recommended for the slope adaptive filter. Increasing the filter window size was found to increase coherence in low coherence regions for the spectral filter; however, no change in coherence was observed with increasing filter

window size for the slope adaptive filter. For stacked interferograms using the same coherence mask threshold and the minimum filter size for each filter type (2 for slope adaptive and 8 for spectral), the spectral filter was found to produce more coherent images than the slope adaptive filter. However, the stacked interferogram obtained using the slope adaptive filter without a coherence mask (a stacked interferogram using the spectral filter cannot be produced without a coherence mask) was found to be more coherent than the stacked interferogram obtained using the slope adaptive filter with the minimal coherence mask.

Increasing the coherence mask threshold caused more of the scene to be masked. Whereas eliminating portions of the scene with low coherence may be necessary for proper unwrapping, deformation associated with localized features may appear to be incoherent and may be masked if the coherence threshold is set too high. Also, if the deformation feature is located within a low coherence region (e.g. the Santa Monica Mountains) the feature may also be masked. For the spectral filter, the coherence threshold was investigated between 10 and 50 percent. For the slope adaptive filter, the coherence threshold was investigated between 0 and 40 percent. For the Los Angeles Red Line Site, the lower threshold limits associated with each filter type prevented proper unwrapping in the mountainous areas (e.g. unwrapping errors in the mountains) but enabled detection of the localized subsidence associated with the L.A. Red Line. Higher threshold limits ensured proper unwrapping of the scene, but masked the subsidence associated with the L.A. Red Line.

Stacking also affects the detection of the localized subsidence associated with the Los Angeles Red Line. For the Los Angeles Red Line site, 207 interferograms with

baselines less than 125 meters were generated using the enhanced spatial processing technique. When results from all 207 interferograms are stacked, the deformation associated with the L.A. Red Line is not observable. Whereas, by stacking results from only the 27 interferograms generated between 1993 and 1995, the deformation at the location of interest is observable. Furthermore, if results from the 10 interferograms which span the dates of construction are used in the stack, the deformation at the location of interest is most observable. Therefore, the number of images used in a stack directly influences the output of the stack. The best results will be obtained using only the images that span the dates of construction and contain short baselines for stacking.

7.2   Evaluation of Traditional, Spatial, Enhanced Spatial, IPTA, and Multiple-Baseline Processing Techniques

In addition to the 33 different filtering (type and size), multi-looking and masking processing combinations (of which 3 of the 33; the traditional, spatial, and enhanced spatial processing techniques are included), the IPTA and multiple-baseline processing techniques were investigated. Traditional and spatial processing was conducted on a clip of the scene instead of the whole scene, as is typical for these processing techniques, for comparison purposes. The traditional and spatial processing smeared (traditional) and/or masked (spatial) the deformation associated with the L.A. Red Line; however, the output from enhanced spatial processing displayed the localized deformation feature well.

Results of the evaluation on the five SAR processing techniques as conducted on the Los Angeles Red Line site are summarized as:

- The traditional and spatial processing techniques smeared and/or masked the localized deformation feature associated with the L.A. Red Line subsidence.

- The localized deformation feature associated with the L.A. Red Line subsidence was observed in the images developed using the enhanced spatial and multiple-baseline processing techniques.

- The localized deformation feature associated with the Los Angeles Red Line was not observed using the images developed using IPTA processing technique. The feature was observed in the deformation time-history plots developed using the IPTA processing technique.

- Several of the images developed using the multiple-baseline processing technique were "speckled". This speckling is associated with the number of times an image is used and the way in which the image is used to make interferogram pairs with other images (baseline and redundancy dependence).

- The localized deformation feature associated with the L.A. Red Line subsidence is more apparent along Vermont Avenue (azimuth direction) than along Hollywood Boulevard (range direction).

- The large scale monotonic deformation feature associated with the Salt Lake Oil Field was observed in images developed using all processing techniques.

- The construction of the subway line is an episodic event. For this type of event, the amount and quality of images used in a stack affect the results of the stacking. Fewer high quality (non-speckled) images surrounding the time span of the movement of the feature of interest allow for better detection of the localized deformation feature.

The localized deformation associated with the L.A. Red Line is more pronounced along Vermont Avenue as compared with the feature along Hollywood Boulevard. Although the spatial resolution is multi-looked to form square 20 meter by 20 meter pixels as displayed in a multi-looked intensity image (MLI), the increased spatial resolution (4 meter pixel size) in the azimuth direction (north-south) in the single look complex (SLC) image is believed to contribute to the localized deformation feature being more visible in the azimuth direction (Vermont Avenue) as compared with the range direction (Hollywood Boulevard).

In addition to stacking of the interferograms developed using the traditional, spatial, and enhanced spatial processing techniques, the use of time-dependent processing (IPTA and multiple-baseline) also indicates that the localized deformation features obtained from episodic events are related to the time of construction of the L.A. Red Line. Using only interferograms associated with images surrounding the time of construction is suggested, as the feature begins to disappear when more interferograms that do not contain the deformation feature are used.

Results of the evaluation on the three SAR processing techniques as conducted on the Mosul Dam site are summarized as:

- The spatial processing techniques smeared and/or masked the localized deformation feature associated with subsidence of Mosul Dam. An interpolator was used to prevent null value data.
- The localized deformation feature associated with the subsidence of Mosul Dam was observed in the images developed using the spatial and enhanced spatial processing techniques.

- No images were developed using the multiple baseline processing technique because null value data in the enhanced spatial images prevented multiple-baseline processing. Therefore, the localized deformation feature associated with the subsidence of Mosul Dam was <u>not</u> observed using the multiple-baseline technique.

7.3   *Ranking of Processing Techniques for Geotechnical Engineering Applications*

The five processing techniques were ranked based on the advantages and disadvantages associated with each processing technique for the Los Angeles Red Line site. Factors including the amount of processing time required to produce a result, whether the localized deformation feature is detected using the processing technique, the spatial extent of the feature in the output, and whether a time-series can be produced were used to rank the processing techniques. Because the enhanced spatial processing technique has the most advantages of the traditional, spatial, and enhanced spatial processing techniques, the results from this processing technique were used as input into the multiple-baseline processing technique. The processing techniques are ranked in the following order: 1. enhanced spatial, 2. multiple-baseline, 3. spatial, 4. IPTA, and 5. traditional.

Although a 100 km by 100 km scene can be processed in days using the traditional and spatial techniques, the localized deformation feature is smeared and masked, and these techniques do not produce a time-series. The enhanced spatial processing technique was conducted on a 20 km by 20 km portion of the scene in a week or several weeks enabling detection of the localized deformation feature. The IPTA processing technique can take a month and was only conducted on a 10 km by 10 km

portion of the scene. However, unlike the enhanced spatial processing technique, the IPTA processing technique was conducted on a small fraction of the image, and is only capable of detecting the localized deformation feature by using a time series. The multiple-baseline procedure uses the output (interferograms displaying a fraction of the scene) from the enhanced spatial processing technique and is capable of producing time histories like IPTA. However, more of the scene is processed using the multiple-baseline approach, and the L.A. Red Line feature is more apparent in images produced using the multiple-baseline approach than in images produced using the IPTA processing approach. Because both the enhanced spatial and multiple-baseline processing techniques display the feature of interest, these processing techniques contain the most advantages. Following the testing of the various processing techniques, the spatial, enhanced spatial processing technique and multiple-baseline processing technique were used on the Mosul Dam Site.

The subsidence associated with movement of Mosul Dam was observed using the spatial and enhanced spatial processing techniques. The subsidence was not observed using the multiple-baseline processing technique. The spatial processing technique was ranked higher than the enhanced spatial processing technique because the spatial processing technique can be conducted faster than the enhanced spatial processing technique. Both the spatial and enhanced spatial processing technique ranked higher than the multiple-baseline technique because the subsidence was observed in images developed using the spatial and enhanced spatial processing techniques and not observed in images developed using the multiple-baseline technique. Therefore, the processing

techniques are ranked in the following order: 1. spatial, 2. enhanced spatial, and 3. multiple-baseline.

7.4   Recommendations for Future Work

As discussed in Chapter 2, satellites are now available with higher spatial and temporal resolution than the ERS-1, ERS-2, and ENVISAT satellites used for this study. The use of these higher resolution satellites (RADARSAT-2, TERRASAR-X, or COSMO-Sky-Meds) is recommended. These satellites were not used for this research because the processing focused on using historically archived data that was not available using the high resolution satellites. In addition to high resolution InSAR satellites, ground based interferometric radars should be used for detecting localized ground deformation features associated with geotechnical engineering applications.

Additional processing is recommended for the Los Angeles Red Line site, this processing includes:

- Investigating the effect of the baseline dependence, as obtained during initial resampling of the images into the master viewing geometry, of images on multiple-baseline processing as discussed previously in Section 6.3.2.

- Performing point domain multiple-baseline processing. This processing is similar to IPTA however multiple master scenes are used as opposed to only one master scene as used in IPTA. This processing will provide a more robust regression analysis of the data than IPTA.

- Evaluating the "statistically significant" localized deformation features produced using all processing techniques by comparing the subsidence estimate to the error estimate.

REFERENCES

Alaska SAR Facility Website, (viewed March 2009). "European Remote Sensing Satellite, ERS-1," http://www.asf.alaska.edu/content/reference/general/ERS1.pdf.

American Underground Construction Association (AUCA) Website, (Viewed February 2009), "Los Angeles Metro Red Line: Santa Monica Tunnels" http://www.auca.org/month/lametro.html.

BBC News Website, (viewed February 2009), "An Aerial View of Mosul Dam and Its Flood Plain," http://news.bbc.co.uk/2/shared/spl/hi/pop_ups/07/middle_east_enl_1193751804/html/1.stm.

BBC News Website, (viewed February 2009a), "Iraqi Dam at Risk of Collapse" http://news.bbc.co.uk/2/hi/middle_east/7069109.stm.

BBC News Website, (viewed February 2009c), "Mosul Dam Key Facts," http://news.bbc.co.uk/2/hi/middle_east/7070706.stm#infographic

Beaver, J. and Marra, M., (2006), "Using Coherent Target Monitoring for Detecting Subsidence Trends in Phoenix and London," PowerPoint presentation at IGARSS 2006, Denver, Colorado.

Bell, R., (viewed February 2009), "Hollywood Boulevard Sinkhole and Subsidence," http://www.prres.net/Papers/Bell_RE_Damages_Analytical_Tools_and_Their_Application_to_High_Profile_Case_Studies.pdf.

Burgmann, R., Rosen, P.A., and Fielding, E.J., (2000). "Synthetic Aperture Radar Interferometry to Measure Earth's Surface Topography and Its Deformation" Annual Review of Earth and Planetary Sciences, 28, 169-209.

Canadian Space Agency Website (viewed March 2009), "Components and Specification," http://www.asc-csa.gc.ca/eng/satellites/radarsat1/components.asp.

Carnec, C., Massonnet, D., King, C., (1996). Two Examples of the Use of SAR Interferometry and GPS Measurements. *Geophysical Research Letters* 23:3579-3582.

Charlwood, R.G., (2007). Robin G. Charlwood and Associates. Personal Communication.

Coffman, R.A., (2007). Application of Remote Sensing for Performance Monitoring of Dams. 27th Annual USSD Conference Poster Presentation. Philadelphia, Pennsylvania, March.

Constantini, M., (1998). "A Novel Phase Unwrapping Method Based on Network Programming," IEEE Transactions on Geoscience and Remote Sensing, Vol. 36, 3, pp. 813-821.

Cosmo-SkyMed Website, (viewed March 2009), "About Cosmo-SkyMed)", http://www.cosmo-skymed.it/en/index.htm.

Cotton, Shires, and Associates, Inc. Website, (viewed February 2009), "Tunnel Distress Investigation: Metropolitan Transit Authority Hollywood, California," http://www.cottonshires.com/company_news/pdfs/mta.pdf.

Daly, J.C.K., (viewed February 2009), "Analysis: Iraq's Pressing Water Needs," http://www.dbxexpo.com/story_detail.php?id=5373&language=&news_type=.

Delft Department of Earth Observation and Space Systems Website, (viewed March 2009). "ERS-1 and ERS-2 Mission Phases," http://www.deos.tudelft.nl/ers/phases/.

DESC-W Software Program (2009), Version 4.69.1 Documentation, ESA.

Earth Observation Satellites and Sensors for Risk Management Website, (viewed March 2009), "Sensor Details Cosmo-Skymed)," http://www.space-risks.com/SpaceData/index.php?id_page=8&Satellite_Name=COSMO-Skymed+(4X).

Elachi, C., and Van Zyl, J., (2006). Introduction to the Physics and Techniques of Remote Sensing. 2nd Edition. John Wiley & Sons, Inc., Hoboken, New Jersey.

Emerson, B., (2007). United Sates Army Corps of Engineers. Personal Communication.

Engineering News Record (ENR). (May 15, 1995). "L.A. Adverts Settlement in Another Tunnel Job" McGraw-Hill Inc. Vol. 234, No. 19, Pg. 15.

Engineering News Record (ENR). (November 3, 1997). "Milestone Los Angeles Subway Tunnel Hole Through" McGraw-Hill Inc. Vol. 239, No. 18, Pg. 5.

EO Sharing Earth Observation Resources Website, (viewed March 2009a), "SIR-A (Shuttle Imaging Radar)," http://directory.eoportal.org/get_announce.php?an_id=10000599.

EO Sharing Earth Observation Resources Website, (viewed March 2009b), "SIR-B," http://directory.eoportal.org/get_announce.php?an_id=10000600.

ERMapper (2009). Version 6.4 Documentation, ERDAS.

European Space Agency Website, (viewed March 2009a). "ERS Design," http://earth.esa.int/object/index.cfm?fobjectid=4221.

European Space Agency Website, (viewed March 2009b). "SAR Design SAR Image Mode," http://earth.esa.int/ers/eeo4.10075/eeo3.298.html.

European Space Agency Website, (viewed March 2009c). "Envisat Instruments," http://envisat.esa.int/object/index.cfm?fobjectid=3762.

European Space Agency Website, (viewed March 2009d). "Special Features of ASAR," http://envisat.esa.int/handbooks/asar/CNTR1-1-5.htm#eph.asar.ug.choos.specfeat.

European Space Agency Website, (viewed March 2009e). "ASAR-Envisat's Advanced Synthetic Aperture Radar," http://esapub.esrin.esa.it/bulletin/bullet102/Desnos102.pdf.

Federal Transit Authority (FTA) Website. (Viewed February 2009). "Existing FFGAs Fully Funded in the President's FY 2003 Budget Request: Los Angeles/MOS-3 Extensions of Metro Rail (North Hollywood)," http://www.fta.dot.gov/publications/reports/reports_to_congress/planning_enviro nment_3297.html.

Federal Transit Authority (FTA) Website. (Viewed February 2009). "MOS-3 Segments of Metro Rail," http://www.fta.dot.gov/publications/reports/planning_environment_2895.html#m osmetro.

Fielding, E.J., Blom, R.G., Evans, D.E. Burgman, R. (1997). Distinguishing Ground Subsidence Due to Subsurface Material Removal fom Vertical Tectonic Motions with SAR Interferometry. EOS Trans. AGU 78:141 (Abstr.).

Francis, P., (1999). Remote Sensing of Active Volcanoes. *Annual Review of Earth Planetary Science* 28:81-106.

Gabriel, A.K., Goldstein, R.M., and Zebker, H.A., (1989). Mapping Small Elevation Changes Over Large Areas – Differential Radar Interferometry. *J. Geophysical Research*. 94:9183-9191.

Galloway, D.L., Hudnut, K.W., Ingebritsen, S.E., Phillips, S.P., Peltzer, G. (1998). Detection of Aquifer System Compaction and Land Subsidence Using Interferometric Synthetic Radar, Antelope Valley, Mojave Desert, California, *Water Resources Research* 34:2573-2585.

GAMMA Remote Sensing Software (2008), December 4, 2008 Release Documentation, Gamma Remote Sensing.

GAMMA Remote Sensing. (August 2006), "Gamma ISP: Reference Manual, adf filter," Gumligen, Switzerland.

GAMMA Remote Sensing. (March 2008), "Documentation – Theory : SAR Processing Version 1.4.," Gumligen, Switzerland.

GAMMA Remote Sensing. (November 2007), "Documentation – Theory : Interferometric SAR Processing Version 1.0," Gumligen, Switzerland.

GAMMA Remote Sensing. (November 2008), "Documentation-User's Guide Differential Interferometry and Geocoding Software – DIFF&GEO Version 1.2 ," Gumligen, Switzerland.

Goldstein, R.M., Werner, C.L., (1998), "Radar Interferogram Filtering for Geophysical Applications," *Geophysical Research Letters*, 25(21), 4035-4038..

Gomez, F. (2009) MATLAB and GAMMA Shell Scripts. University of Missouri Geological Sciences, Columbia, MO. Obtained from Author via Personal Communication.

Hanssen, R.F. (2001) *Radar Interferometry: Data Interpretation and Error Analysis*. Kluwer Academic, Dordrecht; Boston.

Hatfield Consultants Website, (viewed March 2009), "TerraSAR-X", http://www.hatfieldgroup.com/services/gis_rs/pricelist/terrasar-x.aspx.

Japan Aerospace Exploration Agency Website, (viewed March 2009a), "Overview and Objectives," http://www.eorc.jaxa.jp/ALOS/en/about/about_index.htm.

Japan Aerospace Exploration Agency Website, (viewed March 2009b), "PALSAR," http://www.eorc.jaxa.jp/ALOS/en/about/palsar.htm.

Japan Aerospace Exploration Agency Website, (viewed March 2009c), "Japanese Earth Resources Satellite-1 (JERS-1)," http://www.eorc.jaxa.jp/JERS-1/en/index.html.

Jensen, John R. (2000). Remote Sensing of the Environment: An Earth Resource Perspective. Upper Saddle River, New Jersey. Prentice Hall. p. 544.

Jensen, John R. (2007) Geography 551: Principles of Remote Sensing Class Power Point Slides. University of South Carolina, Columbia, South Carolina. Obtained from Author Via-Personal Communication.

Kelley, J.R., Wakeley, L.D., Broadfoot, S.W., Pearson, M.L., McGrath, C.J., McGill, T.E., Jorgeson, J.D., and Talbot, C.A. (2007). Geologic Setting of Mosul Dam and Its Engineering Implications. ERDC TR-07-10. Vicksberg, MS: U.S. Army Research and Development Center.

Legarsky, J.J., Loehr, J.E., Davis, C.H., Rosenblad, B.L., Bloomfield, B., Hedrick, A.T., Coffman, R.A., Gomez, F. and Manjunath, D. (2007). Scatter Informatics using NASA JPL Polarimetric Airsar Imagery. American Geophysical Union Fall Meeting 2007. San Francisco, California, December.

Los Angeles Business Journal/entrepreneur.com, (viewed February 2009), "Receivership Urged for MTA," https://www.entrepreneur.com/trade/journals/article/18717152.html.

Los Angeles Times. "Timeline for the Red Line." June 18, 2000, in print edition A-26.

MacDonald, Dettwiler and Associated Ltd. Website, (viewed March 2009a), "Features and Benefits," http://www.radarsat2.info/about/features_benefits.asp.

MacDonald, Dettwiler and Associated Ltd. Website, (viewed March 2009b), "Radarsat-2 A New Era in Synthetic Aperture Radar," http://www.radarsat2.info/about/r2_brochure.pdf.

MacDonald, Dettwiler and Associated Ltd. Website, (viewed March 2009c), "Radarsat-2 In The News," http://www.radarsat2.info/outreach/innews/2007/12172007_gsi.asp.

MacKay, M.E., Rowland, S.K., Mouginis-Mark, P.J., Garbeil, H., (1998). Thick Lava Flows of Karisimbi Volcano, Rwanda: Insights SIR-C Interferometric Topography. *Bull. Volc.* 60:239-251.

Manjunath, D. (2008). "Point Target Interferometry as Applied to the Characterization of Localized Deformation Features," Ph.D. Dissertation, University of Missouri-Columbia.

Massonnet, D., Feigl, K., Rossi, M., Adragna, F., (1994). Radar Interferometric Mapping of Deformation in the Year After the Landers Earthquake. *Nature*. 369:227-230.

Massonnet, D., Holzer, T., Vadon, H. (1997). Land Subsidence Caused by the East Mesa Geothermal Field, California, Observed Using SAR Interferometry. *Geophysical Research Letters* 24:901-904.

Massonnet, D., Rossi, M., Carmona, C. Adragna, F. Peltzer, G., (1993). The Displacement Field of the Landers Earthquake Mapped by Radar Interferometry. *Nature*. 382:612-616.

MATLAB (2008), Version 7.7.0 (R2008b) Documentation, MathWorks.

Metropolitan Transit Authority (MTA). (July 1995). "That Sinking Feeling" *MTA Review*. pp. 3, 6, 11.

Metropolitan Transit Authority (MTA). (June 1995). "Subway Tunneling Reaches Santa Monica Mountains" *MTA Review*. 12-13.

Metropolitan Transit Authority (MTA). (March 1995). "Digging Resumes in Hollywood Boulevard Tunnel" *MTA Review*. pp. 11.

Middleton, W.D. (2002). Metropolitan Railways: Rapid Transit in America. Indiana University Press. Bloomington, Indiana, 288 pg.

Monsees, J. (2007). Parsons-Brinkerhoff. Personal Communication.

NASA Jet Propulsion Laboratory Website, (viewed March 2009a), "Mission," http://www2.jpl.nasa.gov/srtm/mission.htm.
NASA Jet Propulsion Laboratory Website, (viewed March 2009b), "From Spare Parts to New Mission," http://www2.jpl.nasa.gov/srtm/spareparts.html.

NASA Jet Propulsion Laboratory Website, (viewed March 2009c), "What is SIR-C/X-SAR?," http://southport.jpl.nasa.gov/desc/SIRCdesc.html.

NASA Jet Propulsion Laboratory Website, (viewed March 2009d), "Frequently Asked Questions," http://www2.jpl.nasa.gov/srtm/faq.html.

NASA Jet Propulsion Laboratory Website, (viewed March 2009e), "SIR-C Interferometry Coverage," http://southport.jpl.nasa.gov/scienceapps/interferometry/intmaps.html.

Office of Inspector General Website, (viewed February 2009), "Audit Report: Mega Project Review of Los Angeles Metro Rail Red Line Project," http://www.oig.dot.gov/StreamFile?file=/data/pdfdocs/tr1998154.pdf

Peltzer, G., Crampe, F., Hensley, S., (1998). Elastic stain accumulation along the Mojave Section of the San Andreas Fault, California, Observed with InSAR. *EOS Trans. AGU* 79:33 (Abstr.).

Pool, B. "Subway Sinks Talent agent's Career." Los Angeles Times. March 10, 2000, in print edition B-1.

Rackham, A. "Hollywood Business People Find Damage Growing; Subway Work is Suspended But Cracking, Sinkage Go On." Los Angeles Business Journal. December 12, 2000.

Reuters Website, (viewed December 2007), "Report Says US Contract Failed to Help Mosul Dam," http://uk.reuters.com/article/oilRpt/idUKN3019575320071030.

Richards, M. A. (2006) ECE6272:Fundamentals of Radar Signal Processing Class Power Point Slides. Georgia Tech. Atlanta, Georgia. Obtained from Author Via-Personal Communication.

Rosen, P.A., Werner, C.W., Hiramatsu, A., (1994) "Two-Dimensional Phase Unwrapping of SAR Interferograms by Change Connections Through Neural Trees, " Proceedings of IGARSS'94, Pasadena, 8-12 August.

Schmidt, D.A., and Bürgmann, R., (2003). Time dependent land uplift and subsidence in the Santa Clara valley, California, from a large InSAR data set. *J. Geophys. Res.*, v. 108, p.doi:10.1029/2002JB002267.

Stirbys, A.F., Radwanski, Z.R., Proctor, R.J., and Escandon, R.F. (1999). Los Angeles Metro Rail Project – Geologic and Geotechnical Design and Construction Constraints. *Engineering Geology*. 51(3), 203-224.

Suess, M., Riegger, S. Pitz, W., Werninghaus, R., (viewed March 2009), "Terrasar X-Design and Perfromance" http://www.tsi.enst.fr/~nicolas/ISAT2002/terrasarx.pdf.

Theriot, E.A., (viewed February 2009), "Reconstruction Assistance for Iraq's Eater Sector" http://www.waterforum.jp/jpn/iraq/doc/expert_meeting/plenary/3.pdf.

Wakeley, L.D., Kelly J.R., Talbot, C.A., Pearson, M.L., and Broadfoot, S.W. (2007). Geologic Conceptual Model of Mosul Dam. ERDC TR-07-6. Vicksberg, MS: U.S. Army Research and Development Center.

Water Power and Dam Construction, (viewed Jamuary 2008), "Leakage at Mosul Dam in North Iraq Has Engineers Worried and Recent Grouting Efforts have Not Been Executed Effectively, According to a US study." http://www.waterpowermagazine.com/storyprint.asp?sc=2048287.

Waxman, H. United States Representative Website, (viewed November 2009), "Metro Rail Letter," http://www.henrywaxman.house.gov/waxman/issues/issues_other_metro_rail_press_Pena_lett_9_19_94.htm.

Werner, C.L., Wegmuller, U., Strozzi, T. (2002) "Processing Strategies for Phase Unwrapping for Insar Applications" Technical Report. May 13, 2002. Bern, Switzerland.

Wright, A.G., (viewed February 2009), "Iraqi Dam Has Experts on Edge Until Inspection Eases Fears 05/05/2003," http://enr.construction.com/news/Front2003/archives/030505.asp.

APPENDIX A: COMPUTER CODE USED FOR PROCESSING

All of the computer code used for InSAR processing on the Los Angeles Red Line Site and the Mosul Dam site are displayed in this Appendix. This code includes MATLAB code, and Linux code (shell scripts and command line). The original code programs as developed by Dr. Franscisco Gomez are modified by researchers at the University of Missouri on a site specific basis. Dr. Gomez's code utilizes built in functions within the MATLAB and GAMMA Remote Sensing software programs.

Program:	ers_MSP_setup.sh
Site:	Note: this script was developed after processing of both sites, but can be used for future sites (ERS platform)
Use:	Linux shell script to process multiple scenes very quickly
Programmed By:	Dr. Francisco Gomez
Comments:	This shell script creates a command line files to create level 1 data from level 0 data (for all scenes).
Directory Output:	-
Final output:	MSP_commands.txt

Directory in Which Processing was Conducted: -

```bash
#!/bin/bash
#
# ers_MSP_setup.sh
#
# This script prepares raw ERS SAR data for processing and focusing into
# Single-Look Complex imagery.  Raw data (CEOS) are stored in directories
# named with 'e1' or 'e2' followed by a five-digit orbit (e.g., e112345).
# The 7-character scene names are individually listed (one per line) in the input file.
#
# User inputs
if [ $# -lt 2 ]; then
echo "USAGE ers_MSP_setup <raw data directory> <SCENE list>"
exit
fi

#
echo $REFDIR
REFDIR=$1
INFILE=$2
#

if [ -e $REFDIR ]; then
while read SCENE
do
echo $SCENE
ORBIT=`echo $SCENE | cut -c 3-7`
SAT=`echo $SCENE | cut -c 1-2`

#if [ ! -e $REFDIR/$SCENE/dat_01.001 ]; then echo "$ORBIT DAT and/or LEA file not
present."
if [ ! -e $REFDIR/$SCENE/DAT_01.001 ]; then echo "$ORBIT DAT and/or LEA file
not present."
else
if [ ! -e $SCENE ]; then mkdir $SCENE; fi
cd $SCENE
```

```
# Set basic variables
RAWDIR1=$REFDIR'/'$SCENE
ERS=`echo $SAT | sed -e 's/e/ERS/'`

# Generate Commands
echo "# MSP Commands for $SCENE" > MSP_commands.txt
echo
#if [ -e $REFDIR/$SCENE/dat_01.001 ]; then
#echo "ln -s $RAWDIR1/dat_01.001 "$ORBIT".raw"  >> MSP_commands.txt
#echo "ln -s $RAWDIR1/lea_01.001 "$ORBIT".ldr" >> MSP_commands.txt
#else
echo "ln -s $RAWDIR1/DAT_01.001 "$ORBIT".raw"  >> MSP_commands.txt
echo "ln -s $RAWDIR1/LEA_01.001 "$ORBIT".ldr" >> MSP_commands.txt
#fi
echo "cp /progs/gamma/MSP/sensors/$ERS* ." >> MSP_commands.txt
echo >> MSP_commands.txt
echo "ERS_proc_ESA "$ORBIT".ldr p"$ORBIT".slc.par <
/progs/gamma/slc_par_info_ESA" >> MSP_commands.txt
echo >> MSP_commands.txt
echo "DELFT_proc2 p"$ORBIT".slc.par /atlas/data/ers/PRC/delft/"$ERS "7 10" >>
MSP_commands.txt
echo >> MSP_commands.txt
echo "ERS_fix ESA/ESRIN "$ERS"_ESA.par p$ORBIT.slc.par 0 "$ORBIT".raw
$ORBIT.fix" >> MSP_commands.txt
echo >> MSP_commands.txt
echo "ERS_PROC "$ERS"_ESA.par $ORBIT 2 10" >> MSP_commands.txt
echo >> MSP_commands.txt
echo "ln -s "$ERS"_ESA.par ERS.par"
echo >> MSP_commands.txt
cd ..
fi
done < $INFILE
fi
```

Program:	ers_MSP_batch.sh
Site:	Note: this script was developed after processing of both sites, but can be used for future sites (ERS platform)
Use:	Linux shell script to process multiple scenes very quickly
Programmed By:	Dr. Francisco Gomez
Comments:	This shell script runs the MSP_commands.txt files created using ers_MSP_setup.sh.
Directory Output:	-
Final output:	MSP_commands.txt

Directory in Which Processing was Conducted: /sahara/insar/socal2/

```
#!/bin/bash
#
# This script is executed in a directory containing the directories that have been setup
# for processing RAW ERS SAR data (using 'ers_MSP_setup').  It simply looks in all
# subdirectories with 7-character names (i.e., 'e1' or 'e2' followed by the orbit),
# and if the file# 'MSP_commands.txt' exists, it executes it to process the data.
# Scenes to process are listed in an input file that is specified by the user.
# If the SLC exists, it is not reprocessed.
#

# User inputs
if [ $# -lt 1 ]; then
echo "USAGE ers_MSP_batch <scene list>"
exit
fi

INFILE=$1
ORBIT=`echo $SCENE | cut -c 1-7`
SAT=`echo $SCENE | cut -c 1-2`

while read SCENE
do
if [ -e $SCENE ]; then
cd $SCENE
echo $SCENE
if [ ! -e $ORBIT.slc ]; then
sh MSP_commands.txt
else
echo $ORBIT".slc already created."
fi
cd ..
else
echo $ORBIT" directory not available"
fi
done < $INFILE
```

Program:	ev_MSP_setup.sh
Site:	Msoul Dam Site
Use:	Linux shell script to process multiple scenes very quickly
Programmed By:	Dr. Francisco Gomez
Comments:	This shell script creates a command line files to create level 1 data from level 0 data (for all scenes).
Directory Output:	-
Final output:	MSP_commands.txt

Directory in Which Processing was Conducted: /cgi2/data/slc/envisat/2042/0729

```bash
#!/bin/bash
#
# ev_MSP_setup.sh
#
# This script prepares raw Envisat ASAR data for processing and focussing into
# Single-Look Complex imagery.  Raw data (N1 files) are stored in a single directory,
# and the N1 files to process are listed (one per line) in the input file.
#
# User inputs
if [ $# -lt 2 ]; then
echo "USAGE ev_MSP_setup <raw data directory> <N1 list>"
exit
fi

#
REFDIR=$1
INFILE=$2
#
# Specify directory containing Envisat auxilliary files
AUXDIR=/atlas/data/envisat/aux

if [ -e $REFDIR ]; then
while read N1
do
echo $N1
ORBIT=`echo $N1 | cut -c 50-54`
DATE=`echo $N1 | cut -c 15-22`
echo $ORBIT" "$DATE
if [ ! -e $REFDIR/$N1 ]; then echo "$ORBIT N1 file not present."
else
if [ ! -e $ORBIT ]; then mkdir $ORBIT; fi
cd $ORBIT

echo "# MSP processing commands for $ORBIT" > MSP_commands.txt
```

```
if [ $DATE -ge 20020815 ]; then
INS='ASA_INS_AXVIEC20031212_122530_20020815_131000_20021017_162400'; fi
if [ $DATE -ge 20021017 ]; then
INS='ASA_INS_AXVIEC20031212_105841_20021017_162400_20021030_110000'; fi
if [ $DATE -ge 20021030 ]; then
INS='ASA_INS_AXVIEC20031209_113259_20021030_110000_20030211_000000'; fi
if [ $DATE -ge 20030211 ]; then
INS='ASA_INS_AXVIEC20061220_105425_20030211_000000_20071231_000000'; fi
if [ $DATE -ge 20070307 ]; then
INS='ASA_INS_AXVIEC20071218_083603_20070307_060000_20081231_000000'; fi

if [ $DATE -ge 20020413 ]; then
XCA='ASA_XCA_AXVIEC20070130_105508_20020413_000000_20030211_000000';
fi
if [ $DATE -ge 20030211 ]; then
XCA='ASA_XCA_AXVIEC20070130_110635_20030211_000000_20030601_000000';
fi
if [ $DATE -ge 20030601 ]; then
XCA='ASA_XCA_AXVIEC20070130_111029_20030601_000000_20030804_000000';
fi
if [ $DATE -ge 20030804 ]; then
XCA='ASA_XCA_AXVIEC20070130_111245_20030804_000000_20040412_000000';
fi
if [ $DATE -ge 20040412 ]; then
XCA='ASA_XCA_AXVIEC20070130_111449_20040412_000000_20050101_000000';
fi
if [ $DATE -ge 20050101 ]; then
XCA='ASA_XCA_AXVIEC20070130_111710_20050101_000000_20050914_000000';
fi
if [ $DATE -ge 20050916 ]; then
XCA='ASA_XCA_AXVIEC20070215_184408_20050916_195733_20070204_165113';
fi
if [ $DATE -ge 20070204 ]; then
XCA='ASA_XCA_AXVIEC20071218_082742_20070204_165113_20081231_000000';
fi

echo "ln -s -f $REFDIR/$N1 $ORBIT.N1" >> MSP_commands.txt
echo "ln -s -f $AUXDIR/$XCA xca" >> MSP_commands.txt
echo "ln -s -f $AUXDIR/$INS ins" >> MSP_commands.txt
echo >> MSP_commands.txt
echo "ASAR_XCA xca is2.ant IS2 VV" >> MSP_commands.txt
echo "ASAR_IM_proc $ORBIT.N1 ins $ORBIT.is2.par p$ORBIT.slc.par $ORBIT.raw
is2.ant" >> MSP_commands.txt
echo "DELFT_proc2 p$ORBIT.slc.par /atlas/data/envisat/PRC/delft 10 10" >>
MSP_commands.txt
echo >> MSP_commands.txt
```

```
echo "azsp_IQ $ORBIT.is2.par p$ORBIT.slc.par $ORBIT.raw $ORBIT.azsp | tee
azsp.out " >> MSP_commands.txt
echo >> MSP_commands.txt
echo "pre_rc $ORBIT.is2.par p$ORBIT.slc.par $ORBIT.raw $ORBIT.rc | tee pre_rc.out"
>> MSP_commands.txt
echo >> MSP_commands.txt
echo "autof $ORBIT.is2.par p$ORBIT.slc.par $ORBIT.rc $ORBIT.autof 5.0 - 2048 5000
1024 1 | tee autof1.out" >> MSP_commands.txt
echo "autof $ORBIT.is2.par p$ORBIT.slc.par $ORBIT.rc $ORBIT.autof 5.0 - 2048 5000
1024 1 | tee autof2.out" >> MSP_commands.txt
echo >> MSP_commands.txt
echo "az_proc $ORBIT.is2.par p$ORBIT.slc.par $ORBIT.rc $ORBIT.slc - 1 | tee
az_proc.out" >> MSP_commands.txt
echo >> MSP_commands.txt
echo "multi_SLC p$ORBIT.slc.par p$ORBIT.mli.par $ORBIT.slc $ORBIT.mli 2 10" >>
MSP_commands.txt
echo >> MSP_commands.txt
echo "MLI_RAS $ORBIT" >> MSP_commands.txt
echo
echo "rm $ORBIT.rc" >> MSP_commands.txt
echo "rm $ORBIT.raw" >> MSP_commands.txt
cd ..
fi
done < $INFILE

fi
```

Program:	ev_MSP_batch.sh
Site:	Mosul Dam Site
Use:	Linux shell script to process multiple scenes very quickly
Programmed By:	Dr. Francisco Gomez
Comments:	This shell script runs the command line files created using ev_MSP_setup.sh.
Directory Output:	-
Final output:	.slc, p.slc.par, files

Directory in Which Processing was Conducted: /cgi2/data/slc/envisat/2042/0729

```
#!/bin/bash
#
# This script is executed in a directory containing the directories that have been setup
# for processing RAW Envisat ASAR data (using 'ev_MSP_setup').  It simply looks in all
# subdirectories named with 5-digit numbers (i.e. ,the orbit ids), and if the file
# 'MSP_commands.txt' exists, it executes it to process the data.  Orbits to process
# are listed in an input file that is specified by the user.  If the SLC exists, it
# is not reprocessed.
#

# User inputs
if [ $# -lt 1 ]; then
echo "USAGE ev_MSP_batch <orbit list>"
exit
fi

INFILE=$1

while read ORBIT
do
if [ -e $ORBIT ]; then
cd $ORBIT
echo $ORBIT
if [ ! -e $ORBIT.slc ]; then
sh MSP_commands.txt
else
echo $ORBIT".slc already created."
fi
cd ..
else
echo $ORBIT" directory not available"
fi
done < $INFILE
```

Program:	MSP_commands.txt
Site:	Mosul Dam Site
Use:	Linux shell script to process multiple scenes very quickly
Programmed By:	Dr. Francisco Gomez
Comments:	This is the command file created using the ev_MSP_setup.sh shell script. The commands contained in this command file are run using the ev_MSP_batch.sh shell script.
Directory Output:	-
Final output:	.slc, p.slc.par, files

Directory in Which Processing was Conducted: /cgi2/data/slc/envisat/2042/0729

```
# MSP processing commands for 06108
ln -s -f
/cgi/data/envisat/sort/asa_im__0cnpde20030501_185406_000000172016_00042_06108_
0573.n1 06108.N1
ln -s -f
/atlas/data/envisat/aux/ASA_XCA_AXVIEC20070130_110635_20030211_000000_200
30601_000000 xca
ln -s -f
/atlas/data/envisat/aux/ASA_INS_AXVIEC20061220_105425_20030211_000000_2007
1231_000000 ins

ASAR_XCA xca is2.ant IS2 VV
ASAR_IM_proc 06108.N1 ins 06108.is2.par p06108.slc.par 06108.raw is2.ant
DELFT_proc2 p06108.slc.par /atlas/data/envisat/PRC/delft 10 10

azsp_IQ 06108.is2.par p06108.slc.par 06108.raw 06108.azsp | tee azsp.out

pre_rc 06108.is2.par p06108.slc.par 06108.raw 06108.rc | tee pre_rc.out

autof 06108.is2.par p06108.slc.par 06108.rc 06108.autof 5.0 - 2048 5000 1024 1 | tee
autof1.out
autof 06108.is2.par p06108.slc.par 06108.rc 06108.autof 5.0 - 2048 5000 1024 1 | tee
autof2.out

az_proc 06108.is2.par p06108.slc.par 06108.rc 06108.slc - 1 | tee az_proc.out

multi_SLC p06108.slc.par p06108.mli.par 06108.slc 06108.mli 2 10

MLI_RAS 06108
rm 06108.rc
rm 06108.raw
```

Program: ISP_prep.sh
Site: Mosul Dam Site
Use: Linux shell script to process multiple scenes very quickly
Programmed By: Dr. Francisco Gomez
Comments: This shell script creates a command file which will create symbolic
                    links to the .slc files located in /cgi2/data/slc/envisat/2042/0729,
                    and conduct the par_MSP command which creates slc.par files.
Directory Output: /rslc
Final output: ISP_prep.txt command file
Directory in Which Processing was Conducted: /cgi1/insar/mosul/rslc

SLCDIR='/cgi1/insar/mosul/slc'

```
# Create symbolic links and MSP parameter files for ENVISAT
for DIREC in $SLCDIR/[0-9][0-9][0-9][0-9][0-9]
do
ORBIT=`echo $DIREC | sed -e 's/^\/.*slc\///'`
if [ -e $SLCDIR/$ORBIT/$ORBIT.slc ]; then
echo "ln -s $DIREC/"$ORBIT".slc "$ORBIT".slc"
echo "par_MSP $DIREC/"$ORBIT".is2.par $DIREC/p"$ORBIT".slc.par "$ORBIT".par"
fi
done

echo
echo "###################"
echo
```

Program: ISP_prep.txt
Site: Mosul Dam Site
Use: Linux shell script to process multiple scenes very quickly
Programmed By: Dr. Francisco Gomez
Comments: This is the command file created using the ISP_prep.sh. When this
                        text file is run as a shell script, the .slc files located in
                        /cgi2/data/slc/envisat/2042/0729 are symbolic linked, and
                        par_MSP command is conducted which creates slc.par files.
Directory Output: /rslc
Final output: .symbolic links, and .slc.par files
Directory in Which Processing was Conducted: /cgi1/insar/mosul/rslc

ln -s /cgi1/insar/mosul/slc/05607/05607.slc 05607.slc
par_MSP /cgi1/insar/mosul/slc/05607/05607.is2.
/cgi1/insar/mosul/slc/05607/p05607.slc.par 05607.par
ln -s /cgi1/insar/mosul/slc/06108/06108.slc 06108.slc
par_MSP /cgi1/insar/mosul/slc/06108/06108.is2.par
/cgi1/insar/mosul/slc/06108/p06108.slc.par 06108.par
ln -s /cgi1/insar/mosul/slc/12120/12120.slc 12120.slc
par_MSP /cgi1/insar/mosul/slc/12120/12120.is2.par
/cgi1/insar/mosul/slc/12120/p12120.slc.par 12120.par
ln -s /cgi1/insar/mosul/slc/12621/12621.slc 12621.slc
par_MSP /cgi1/insar/mosul/slc/12621/12621.is2.par
/cgi1/insar/mosul/slc/12621/p12621.slc.par 12621.par
ln -s /cgi1/insar/mosul/slc/13122/13122.slc 13122.slc
par_MSP /cgi1/insar/mosul/slc/13122/13122.is2.par
/cgi1/insar/mosul/slc/13122/p13122.slc.par 13122.par
ln -s /cgi1/insar/mosul/slc/13623/13623.slc 13623.slc
par_MSP /cgi1/insar/mosul/slc/13623/13623.is2.par
/cgi1/insar/mosul/slc/13623/p13623.slc.par 13623.par
ln -s /cgi1/insar/mosul/slc/14625/14625.slc 14625.slc
par_MSP /cgi1/insar/mosul/slc/14625/14625.is2.par
/cgi1/insar/mosul/slc/14625/p14625.slc.par 14625.par
ln -s /cgi1/insar/mosul/slc/15126/15126.slc 15126.slc
par_MSP /cgi1/insar/mosul/slc/15126/15126.is2.par
/cgi1/insar/mosul/slc/15126/p15126.slc.par 15126.par
ln -s /cgi1/insar/mosul/slc/16629/16629.slc 16629.slc
par_MSP /cgi1/insar/mosul/slc/16629/16629.is2.par
/cgi1/insar/mosul/slc/16629/p16629.slc.par 16629.par
ln -s /cgi1/insar/mosul/slc/17631/17631.slc 17631.slc
par_MSP /cgi1/insar/mosul/slc/17631/17631.is2.par
/cgi1/insar/mosul/slc/17631/p17631.slc.par 17631.par
ln -s /cgi1/insar/mosul/slc/19134/19134.slc 19134.slc
par_MSP /cgi1/insar/mosul/slc/19134/19134.is2.par
/cgi1/insar/mosul/slc/19134/p19134.slc.par 19134.par
ln -s /cgi1/insar/mosul/slc/19635/19635.slc 19635.slc

```
par_MSP /cgi1/insar/mosul/slc/19635/19635.is2.par
/cgi1/insar/mosul/slc/19635/p19635.slc.par 19635.par
ln -s /cgi1/insar/mosul/slc/22140/22140.slc 22140.slc
par_MSP /cgi1/insar/mosul/slc/22140/22140.is2.par
/cgi1/insar/mosul/slc/22140/p22140.slc.par 22140.par
ln -s /cgi1/insar/mosul/slc/24144/24144.slc 24144.slc
par_MSP /cgi1/insar/mosul/slc/24144/24144.is2.par
/cgi1/insar/mosul/slc/24144/p24144.slc.par 24144.par
ln -s /cgi1/insar/mosul/slc/25146/25146.slc 25146.slc
par_MSP /cgi1/insar/mosul/slc/25146/25146.is2.par
/cgi1/insar/mosul/slc/25146/p25146.slc.par 25146.par
ln -s /cgi1/insar/mosul/slc/26649/26649.slc 26649.slc
par_MSP /cgi1/insar/mosul/slc/26649/26649.is2.par
/cgi1/insar/mosul/slc/26649/p26649.slc.par 26649.par

###################
```

Program:	ISP_initoff.sh
Site:	Mosul Dam Site
Use:	Linux shell script to process multiple scenes very quickly
Programmed By:	Dr. Francisco Gomez
Comments:	This shell script creates a command file which will create .off files and generate initial offsets within these files.
Directory Output:	/rslc
Final output:	ISP_initoff.txt command file

Directory in Which Processing was Conducted: /cgi1/insar/mosul/rslc

```
if [ $# -lt 1 ] ; then
echo "Which scene is the master?"
echo
echo "USAGE:  ISP_initoff <master>"
exit
fi

if [ -e $1.slc ] ; then
MASTER=$1
else
echo "Invalid master scene."
exit
fi

#MASTER=e120897

# Create offset/ISP parameter files and initial offset estimates

for PARFILE in *.par
do
SCENE=`echo $PARFILE | sed -e 's/.par$//'`
if [ -e $MASTER"_"$SCENE.off ]; then
echo
else
if [ $SCENE != $MASTER ] ; then
echo "create_offset $MASTER.par $SCENE.par "$MASTER"_"$SCENE".off <
off_info"
echo "init_offset_orbit $MASTER.par $SCENE.par "$MASTER"_"$SCENE".off 2500
10000 | tee "$MASTER"_"$SCENE".out"
#echo "init_offset $MASTER.slc $SCENE.slc $MASTER.par $SCENE.par
"$MASTER"_"$SCENE".off 2 10 2500 10000 0 0 | tee "$MASTER"_"$SCENE".out"
echo "init_offset $MASTER.slc $SCENE.slc $MASTER.par $SCENE.par
"$MASTER"_"$SCENE".off 1 1 2500 10000 | tee -a "$MASTER"_"$SCENE".out"
echo
fi
fi
```

```
done
echo
echo "#####"
echo
```

Program: ISP_initoff.txt
Site: Mosul Dam Site
Use: Linux shell script to process multiple scenes very quickly
Programmed By: Dr. Francisco Gomez
Comments: This is the command file created using the ISP_initoff.sh. When
                     this text file is run as a shell script, .off files are created and initial
                     offsets are placed within those files.
Directory Output: /rslc
Final output: .off files
Directory in Which Processing was Conducted: /cgi1/insar/mosul/rslc

create_offset 24144.par 05607.par 24144_05607.off < off_info
init_offset_orbit 24144.par 05607.par 24144_05607.off 2500 10000 | tee
24144_05607.out
init_offset 24144.slc 05607.slc 24144.par 05607.par 24144_05607.off 1 1 2500 10000 |
tee -a 24144_05607.out

create_offset 24144.par 06108.par 24144_06108.off < off_info
init_offset_orbit 24144.par 06108.par 24144_06108.off 2500 10000 | tee
24144_06108.out
init_offset 24144.slc 06108.slc 24144.par 06108.par 24144_06108.off 1 1 2500 10000 |
tee -a 24144_06108.out

create_offset 24144.par 12120.par 24144_12120.off < off_info
init_offset_orbit 24144.par 12120.par 24144_12120.off 2500 10000 | tee
24144_12120.out
init_offset 24144.slc 12120.slc 24144.par 12120.par 24144_12120.off 1 1 2500 10000 |
tee -a 24144_12120.out

create_offset 24144.par 12621.par 24144_12621.off < off_info
init_offset_orbit 24144.par 12621.par 24144_12621.off 2500 10000 | tee
24144_12621.out
init_offset 24144.slc 12621.slc 24144.par 12621.par 24144_12621.off 1 1 2500 10000 |
tee -a 24144_12621.out

create_offset 24144.par 13122.par 24144_13122.off < off_info
init_offset_orbit 24144.par 13122.par 24144_13122.off 2500 10000 | tee
24144_13122.out
init_offset 24144.slc 13122.slc 24144.par 13122.par 24144_13122.off 1 1 2500 10000 |
tee -a 24144_13122.out

create_offset 24144.par 13623.par 24144_13623.off < off_info
init_offset_orbit 24144.par 13623.par 24144_13623.off 2500 10000 | tee
24144_13623.out
init_offset 24144.slc 13623.slc 24144.par 13623.par 24144_13623.off 1 1 2500 10000 |
tee -a 24144_13623.out

create_offset 24144.par 14625.par 24144_14625.off < off_info
init_offset_orbit 24144.par 14625.par 24144_14625.off 2500 10000 | tee
24144_14625.out
init_offset 24144.slc 14625.slc 24144.par 14625.par 24144_14625.off 1 1 2500 10000 |
tee -a 24144_14625.out

create_offset 24144.par 15126.par 24144_15126.off < off_info
init_offset_orbit 24144.par 15126.par 24144_15126.off 2500 10000 | tee
24144_15126.out
init_offset 24144.slc 15126.slc 24144.par 15126.par 24144_15126.off 1 1 2500 10000 |
tee -a 24144_15126.out

create_offset 24144.par 16629.par 24144_16629.off < off_info
init_offset_orbit 24144.par 16629.par 24144_16629.off 2500 10000 | tee
24144_16629.out
init_offset 24144.slc 16629.slc 24144.par 16629.par 24144_16629.off 1 1 2500 10000 |
tee -a 24144_16629.out

create_offset 24144.par 17631.par 24144_17631.off < off_info
init_offset_orbit 24144.par 17631.par 24144_17631.off 2500 10000 | tee
24144_17631.out
init_offset 24144.slc 17631.slc 24144.par 17631.par 24144_17631.off 1 1 2500 10000 |
tee -a 24144_17631.out

create_offset 24144.par 19134.par 24144_19134.off < off_info
init_offset_orbit 24144.par 19134.par 24144_19134.off 2500 10000 | tee
24144_19134.out
init_offset 24144.slc 19134.slc 24144.par 19134.par 24144_19134.off 1 1 2500 10000 |
tee -a 24144_19134.out

create_offset 24144.par 19635.par 24144_19635.off < off_info
init_offset_orbit 24144.par 19635.par 24144_19635.off 2500 10000 | tee
24144_19635.out
init_offset 24144.slc 19635.slc 24144.par 19635.par 24144_19635.off 1 1 2500 10000 |
tee -a 24144_19635.out

create_offset 24144.par 22140.par 24144_22140.off < off_info
init_offset_orbit 24144.par 22140.par 24144_22140.off 2500 10000 | tee
24144_22140.out
init_offset 24144.slc 22140.slc 24144.par 22140.par 24144_22140.off 1 1 2500 10000 |
tee -a 24144_22140.out

create_offset 24144.par 25146.par 24144_25146.off < off_info
init_offset_orbit 24144.par 25146.par 24144_25146.off 2500 10000 | tee
24144_25146.out

init_offset 24144.slc 25146.slc 24144.par 25146.par 24144_25146.off 1 1 2500 10000 | tee -a 24144_25146.out

create_offset 24144.par 26649.par 24144_26649.off < off_info
init_offset_orbit 24144.par 26649.par 24144_26649.off 2500 10000 | tee 24144_26649.out
init_offset 24144.slc 26649.slc 24144.par 26649.par 24144_26649.off 1 1 2500 10000 | tee -a 24144_26649.out

#####

Program:	ISP_offsets.sh
Site:	Mosul Dam Site
Use:	Linux shell script to process multiple scenes very quickly
Programmed By:	Dr. Francisco Gomez
Comments:	This shell script creates a command file which will update .off files, generate .offs files and .coffs and .snr files and generate initial offsets within these files.
Directory Output:	/rslc
Final output:	ISP_offsets.txt command file

Directory in Which Processing was Conducted: /cgi1/insar/mosul/rslc

MASTER=24144

Calculate offsets to register all slaves to the master


```
for OFFFILE in *.off
do
ROOTNAME=`echo $OFFFILE | sed -e 's/.off$//'`
SLAVE=`echo $ROOTNAME | sed -e 's/'$MASTER'_//'`
if [ -e $SLAVE.rslc ]; then echo "#####"
else
echo "offset_pwr $MASTER.slc $SLAVE.slc $MASTER.par $SLAVE.par
$ROOTNAME.off $ROOTNAME.offs $ROOTNAME.snr 100 250 - 2 50 60 6.0 | tee -a
$ROOTNAME.txt"
fi
done
```

```
echo "#################################"
```
Estimate offset polynomials

```
for OFFFILE in *.off
do
ROOTNAME=`echo $OFFFILE | sed -e 's/.off$//'`
SLAVE=`echo $ROOTNAME | sed -e 's/'$MASTER'_//'`
if [ -e $SLAVE.rslc ]; then echo "#####"
else
echo "offset_fit $ROOTNAME.offs $ROOTNAME.snr $ROOTNAME.off
$ROOTNAME.coffs - 6.0 4 1"
fi
done
```

```
echo "#################################"
```
Resample Slave SLCs to Master geometry

```
for OFFFILE in *.off
do
```

```
ROOTNAME=`echo $OFFFILE | sed -e 's/.off$//'`
SLAVE=`echo $ROOTNAME | sed -e 's/'$MASTER'_//'`
if [ -e $SLAVE.rslc ]; then echo "#####"
else
echo "SLC_interp $SLAVE.slc $MASTER.par $SLAVE.par $ROOTNAME.off
$SLAVE.rslc $SLAVE.rpar | tee -a $ROOTNAME.txt"
fi
done
echo
echo "#################################"
echo
```

Program:	ISP_offsets.txt
Site:	Mosul Dam Site
Use:	Linux shell script to process multiple scenes very quickly
Programmed By:	Dr. Francisco Gomez
Comments:	This is the command file created using the ISP_initoff.sh. When this text file is run as a shell script, .off files are updated, .offs, .coffs, .snr, .rslc, .rpar files are created.
Directory Output:	/rslc
Final output:	.off, .offs, .coffs, .snr and .rslc and .rpar files

Directory in Which Processing was Conducted: /cgi1/insar/mosul/rslc

offset_pwr 24144.slc 05607.slc 24144.par 05607.par 24144_05607.off 24144_05607.offs
24144_05607.snr 100 250 - 2 50 60 6.0 | tee -a 24144_05607.txt
offset_pwr 24144.slc 06108.slc 24144.par 06108.par 24144_06108.off 24144_06108.offs
24144_06108.snr 100 250 - 2 50 60 6.0 | tee -a 24144_06108.txt
offset_pwr 24144.slc 12120.slc 24144.par 12120.par 24144_12120.off 24144_12120.offs
24144_12120.snr 100 250 - 2 50 60 6.0 | tee -a 24144_12120.txt
offset_pwr 24144.slc 12621.slc 24144.par 12621.par 24144_12621.off 24144_12621.offs
24144_12621.snr 100 250 - 2 50 60 6.0 | tee -a 24144_12621.txt
offset_pwr 24144.slc 13122.slc 24144.par 13122.par 24144_13122.off 24144_13122.offs
24144_13122.snr 100 250 - 2 50 60 6.0 | tee -a 24144_13122.txt
offset_pwr 24144.slc 13623.slc 24144.par 13623.par 24144_13623.off 24144_13623.offs
24144_13623.snr 100 250 - 2 50 60 6.0 | tee -a 24144_13623.txt
offset_pwr 24144.slc 14625.slc 24144.par 14625.par 24144_14625.off 24144_14625.offs
24144_14625.snr 100 250 - 2 50 60 6.0 | tee -a 24144_14625.txt
offset_pwr 24144.slc 15126.slc 24144.par 15126.par 24144_15126.off 24144_15126.offs
24144_15126.snr 100 250 - 2 50 60 6.0 | tee -a 24144_15126.txt
offset_pwr 24144.slc 16629.slc 24144.par 16629.par 24144_16629.off 24144_16629.offs
24144_16629.snr 100 250 - 2 50 60 6.0 | tee -a 24144_16629.txt
offset_pwr 24144.slc 17631.slc 24144.par 17631.par 24144_17631.off 24144_17631.offs
24144_17631.snr 100 250 - 2 50 60 6.0 | tee -a 24144_17631.txt
offset_pwr 24144.slc 19134.slc 24144.par 19134.par 24144_19134.off 24144_19134.offs
24144_19134.snr 100 250 - 2 50 60 6.0 | tee -a 24144_19134.txt
offset_pwr 24144.slc 19635.slc 24144.par 19635.par 24144_19635.off 24144_19635.offs
24144_19635.snr 100 250 - 2 50 60 6.0 | tee -a 24144_19635.txt
offset_pwr 24144.slc 22140.slc 24144.par 22140.par 24144_22140.off 24144_22140.offs
24144_22140.snr 100 250 - 2 50 60 6.0 | tee -a 24144_22140.txt
offset_pwr 24144.slc 25146.slc 24144.par 25146.par 24144_25146.off 24144_25146.offs
24144_25146.snr 100 250 - 2 50 60 6.0 | tee -a 24144_25146.txt
offset_pwr 24144.slc 26649.slc 24144.par 26649.par 24144_26649.off 24144_26649.offs
24144_26649.snr 100 250 - 2 50 60 6.0 | tee -a 24144_26649.txt
###################################
offset_fit 24144_05607.offs 24144_05607.snr 24144_05607.off 24144_05607.coffs - 6.0
4 1
offset_fit 24144_06108.offs 24144_06108.snr 24144_06108.off 24144_06108.coffs - 6.0
4 1

offset_fit 24144_12120.offs 24144_12120.snr 24144_12120.off 24144_12120.coffs - 6.0 4 1

offset_fit 24144_12621.offs 24144_12621.snr 24144_12621.off 24144_12621.coffs - 6.0 4 1

offset_fit 24144_13122.offs 24144_13122.snr 24144_13122.off 24144_13122.coffs - 6.0 4 1

offset_fit 24144_13623.offs 24144_13623.snr 24144_13623.off 24144_13623.coffs - 6.0 4 1

offset_fit 24144_14625.offs 24144_14625.snr 24144_14625.off 24144_14625.coffs - 6.0 4 1

offset_fit 24144_15126.offs 24144_15126.snr 24144_15126.off 24144_15126.coffs - 6.0 4 1

offset_fit 24144_16629.offs 24144_16629.snr 24144_16629.off 24144_16629.coffs - 6.0 4 1

offset_fit 24144_17631.offs 24144_17631.snr 24144_17631.off 24144_17631.coffs - 6.0 4 1

offset_fit 24144_19134.offs 24144_19134.snr 24144_19134.off 24144_19134.coffs - 6.0 4 1

offset_fit 24144_19635.offs 24144_19635.snr 24144_19635.off 24144_19635.coffs - 6.0 4 1

offset_fit 24144_22140.offs 24144_22140.snr 24144_22140.off 24144_22140.coffs - 6.0 4 1

offset_fit 24144_25146.offs 24144_25146.snr 24144_25146.off 24144_25146.coffs - 6.0 4 1

offset_fit 24144_26649.offs 24144_26649.snr 24144_26649.off 24144_26649.coffs - 6.0 4 1

####################################
SLC_interp 05607.slc 24144.par 05607.par 24144_05607.off 05607.rslc 05607.rpar | tee - a 24144_05607.txt
SLC_interp 06108.slc 24144.par 06108.par 24144_06108.off 06108.rslc 06108.rpar | tee - a 24144_06108.txt
SLC_interp 12120.slc 24144.par 12120.par 24144_12120.off 12120.rslc 12120.rpar | tee - a 24144_12120.txt
SLC_interp 12621.slc 24144.par 12621.par 24144_12621.off 12621.rslc 12621.rpar | tee - a 24144_12621.txt
SLC_interp 13122.slc 24144.par 13122.par 24144_13122.off 13122.rslc 13122.rpar | tee - a 24144_13122.txt
SLC_interp 13623.slc 24144.par 13623.par 24144_13623.off 13623.rslc 13623.rpar | tee - a 24144_13623.txt
SLC_interp 14625.slc 24144.par 14625.par 24144_14625.off 14625.rslc 14625.rpar | tee - a 24144_14625.txt
SLC_interp 15126.slc 24144.par 15126.par 24144_15126.off 15126.rslc 15126.rpar | tee - a 24144_15126.txt
SLC_interp 16629.slc 24144.par 16629.par 24144_16629.off 16629.rslc 16629.rpar | tee - a 24144_16629.txt

SLC_interp 17631.slc 24144.par 17631.par 24144_17631.off 17631.rslc 17631.rpar | tee -a 24144_17631.txt
SLC_interp 19134.slc 24144.par 19134.par 24144_19134.off 19134.rslc 19134.rpar | tee -a 24144_19134.txt
SLC_interp 19635.slc 24144.par 19635.par 24144_19635.off 19635.rslc 19635.rpar | tee -a 24144_19635.txt
SLC_interp 22140.slc 24144.par 22140.par 24144_22140.off 22140.rslc 22140.rpar | tee -a 24144_22140.txt
SLC_interp 25146.slc 24144.par 25146.par 24144_25146.off 25146.rslc 25146.rpar | tee -a 24144_25146.txt
SLC_interp 26649.slc 24144.par 26649.par 24144_26649.off 26649.rslc 26649.rpar | tee -a 24144_26649.txt

####################################

Program: rslc_work.txt
Site: Los Angeles Red Line
Use: Linux shell script to process multiple scenes very quickly
Programmed By: Richard Coffman
Comments: This shell script creates a command file which will clip the .rslc
                      files and create clipped .rslc files and .rpar files.
Directory Output: /rslc1
Final output: rslc_clip.txt command file
Directory in Which Processing was Conducted: /sahara/insar/socal2/rslc1

```
rm rslc_clip.txt
for FILE in ../rslc/*.rpar
do
SCENE=`echo $FILE | sed -e 's/.rpar$//' | sed -e 's/^..\/rslc\///'`
printf "SLC_copy ../rslc/$SCENE.rslc ../rslc/$SCENE.rpar $SCENE.rslc $SCENE.rpar -
- 1000 1000 0 5000\n" | tee -a rslc_clip.txt
done
```

Program: rslc_clip.txt
Site: Los Angeles Red Line
Use: Linux shell script to process multiple scenes very quickly
Programmed By: Richard Coffman
Comments: This shell script runs the command file which was created using rslc_work.txt and will create clipped .rslc files and .rpar files.
Directory Output: /rslc1
Final output: .rslc and .rpar files
Directory in Which Processing was Conducted: /sahara/insar/socal2/rslc1

SLC_copy ../rslc/e104595.rslc ../rslc/e104595.rpar e104595.rslc e104595.rpar - - 1000 1000 0 5000
SLC_copy ../rslc/e106098.rslc ../rslc/e106098.rpar e106098.rslc e106098.rpar - - 1000 1000 0 5000
SLC_copy ../rslc/e106599.rslc ../rslc/e106599.rpar e106599.rslc e106599.rpar - - 1000 1000 0 5000
SLC_copy ../rslc/e107100.rslc ../rslc/e107100.rpar e107100.rslc e107100.rpar - - 1000 1000 0 5000
SLC_copy ../rslc/e107601.rslc ../rslc/e107601.rpar e107601.rslc e107601.rpar - - 1000 1000 0 5000
SLC_copy ../rslc/e111108.rslc ../rslc/e111108.rpar e111108.rslc e111108.rpar - - 1000 1000 0 5000
SLC_copy ../rslc/e111609.rslc ../rslc/e111609.rpar e111609.rslc e111609.rpar - - 1000 1000 0 5000
SLC_copy ../rslc/e112110.rslc ../rslc/e112110.rpar e112110.rslc e112110.rpar - - 1000 1000 0 5000
SLC_copy ../rslc/e119468.rslc ../rslc/e119468.rpar e119468.rslc e119468.rpar - - 1000 1000 0 5000
SLC_copy ../rslc/e119969.rslc ../rslc/e119969.rpar e119969.rslc e119969.rpar - - 1000 1000 0 5000
SLC_copy ../rslc/e120470.rslc ../rslc/e120470.rpar e120470.rslc e120470.rpar - - 1000 1000 0 5000
SLC_copy ../rslc/e120971.rslc ../rslc/e120971.rpar e120971.rslc e120971.rpar - - 1000 1000 0 5000
SLC_copy ../rslc/e121472.rslc ../rslc/e121472.rpar e121472.rslc e121472.rpar - - 1000 1000 0 5000
SLC_copy ../rslc/e121973.rslc ../rslc/e121973.rpar e121973.rslc e121973.rpar - - 1000 1000 0 5000
SLC_copy ../rslc/e122474.rslc ../rslc/e122474.rpar e122474.rslc e122474.rpar - - 1000 1000 0 5000
SLC_copy ../rslc/e122975.rslc ../rslc/e122975.rpar e122975.rslc e122975.rpar - - 1000 1000 0 5000
SLC_copy ../rslc/e123476.rslc ../rslc/e123476.rpar e123476.rslc e123476.rpar - - 1000 1000 0 5000
SLC_copy ../rslc/e123977.rslc ../rslc/e123977.rpar e123977.rslc e123977.rpar - - 1000 1000 0 5000

SLC_copy ../rslc/e124979.rslc ../rslc/e124979.rpar e124979.rslc e124979.rpar - - 1000 1000 0 5000

SLC_copy ../rslc/e125480.rslc ../rslc/e125480.rpar e125480.rslc e125480.rpar - - 1000 1000 0 5000

SLC_copy ../rslc/e202801.rslc ../rslc/e202801.rpar e202801.rslc e202801.rpar - - 1000 1000 0 5000

SLC_copy ../rslc/e203302.rslc ../rslc/e203302.rpar e203302.rslc e203302.rpar - - 1000 1000 0 5000

SLC_copy ../rslc/e203803.rslc ../rslc/e203803.rpar e203803.rslc e203803.rpar - - 1000 1000 0 5000

SLC_copy ../rslc/e204304.rslc ../rslc/e204304.rpar e204304.rslc e204304.rpar - - 1000 1000 0 5000

SLC_copy ../rslc/e206308.rslc ../rslc/e206308.rpar e206308.rslc e206308.rpar - - 1000 1000 0 5000

SLC_copy ../rslc/e207310.rslc ../rslc/e207310.rpar e207310.rslc e207310.rpar - - 1000 1000 0 5000

SLC_copy ../rslc/e207811.rslc ../rslc/e207811.rpar e207811.rslc e207811.rpar - - 1000 1000 0 5000

SLC_copy ../rslc/e208312.rslc ../rslc/e208312.rpar e208312.rslc e208312.rpar - - 1000 1000 0 5000

SLC_copy ../rslc/e208813.rslc ../rslc/e208813.rpar e208813.rslc e208813.rpar - - 1000 1000 0 5000

SLC_copy ../rslc/e209815.rslc ../rslc/e209815.rpar e209815.rslc e209815.rpar - - 1000 1000 0 5000

SLC_copy ../rslc/e210316.rslc ../rslc/e210316.rpar e210316.rslc e210316.rpar - - 1000 1000 0 5000

SLC_copy ../rslc/e210817.rslc ../rslc/e210817.rpar e210817.rslc e210817.rpar - - 1000 1000 0 5000

SLC_copy ../rslc/e211318.rslc ../rslc/e211318.rpar e211318.rslc e211318.rpar - - 1000 1000 0 5000

SLC_copy ../rslc/e211819.rslc ../rslc/e211819.rpar e211819.rslc e211819.rpar - - 1000 1000 0 5000

SLC_copy ../rslc/e213322.rslc ../rslc/e213322.rpar e213322.rslc e213322.rpar - - 1000 1000 0 5000

SLC_copy ../rslc/e213823.rslc ../rslc/e213823.rpar e213823.rslc e213823.rpar - - 1000 1000 0 5000

SLC_copy ../rslc/e214324.rslc ../rslc/e214324.rpar e214324.rslc e214324.rpar - - 1000 1000 0 5000

SLC_copy ../rslc/e214825.rslc ../rslc/e214825.rpar e214825.rslc e214825.rpar - - 1000 1000 0 5000

SLC_copy ../rslc/e217330.rslc ../rslc/e217330.rpar e217330.rslc e217330.rpar - - 1000 1000 0 5000

SLC_copy ../rslc/e217831.rslc ../rslc/e217831.rpar e217831.rslc e217831.rpar - - 1000 1000 0 5000

SLC_copy ../rslc/e218332.rslc ../rslc/e218332.rpar e218332.rslc e218332.rpar - - 1000 1000 0 5000

SLC_copy ../rslc/e218833.rslc ../rslc/e218833.rpar e218833.rslc e218833.rpar - - 1000 1000 0 5000

SLC_copy ../rslc/e219334.rslc ../rslc/e219334.rpar e219334.rslc e219334.rpar - - 1000 1000 0 5000

SLC_copy ../rslc/e219835.rslc ../rslc/e219835.rpar e219835.rslc e219835.rpar - - 1000 1000 0 5000

SLC_copy ../rslc/e220336.rslc ../rslc/e220336.rpar e220336.rslc e220336.rpar - - 1000 1000 0 5000

SLC_copy ../rslc/e222340.rslc ../rslc/e222340.rpar e222340.rslc e222340.rpar - - 1000 1000 0 5000

SLC_copy ../rslc/e223342.rslc ../rslc/e223342.rpar e223342.rslc e223342.rpar - - 1000 1000 0 5000

SLC_copy ../rslc/e224344.rslc ../rslc/e224344.rpar e224344.rslc e224344.rpar - - 1000 1000 0 5000

SLC_copy ../rslc/e226348.rslc ../rslc/e226348.rpar e226348.rslc e226348.rpar - - 1000 1000 0 5000

SLC_copy ../rslc/e226849.rslc ../rslc/e226849.rpar e226849.rslc e226849.rpar - - 1000 1000 0 5000

SLC_copy ../rslc/e227851.rslc ../rslc/e227851.rpar e227851.rslc e227851.rpar - - 1000 1000 0 5000

SLC_copy ../rslc/e229354.rslc ../rslc/e229354.rpar e229354.rslc e229354.rpar - - 1000 1000 0 5000

Program:	geocoding_commands.txt
Site:	Los Angeles Red Line
Use:	Linux shell script to process multiple scenes very quickly
Programmed By:	Richard Coffman
Comments:	This shell script creates hgt_map and geo_par files using the .ers and .msb files created from ERMapper.
Directory Output:	/GEO
Final output:	hgt_map and geo_par

Directory in Which Processing was Conducted: /sahara/insar/socal2/GEO

cd ../GEO

Create symbolic links to SLC parameter file (master only), OFF/ISP parameter file, and a power image

ln -s ../rslc1/e122975.rpar
ln -s ../rslc1/e122975_e106098.off
ln -s ../rslc1/e122975_e106098.pwr1

Generate initial Geocoding Lookup Table

create_dem_par la_redline_nutm11.dem_par e122975.rpar

gc_map e122975.rpar e122975_e106098.off la_redline_nutm11.dem_par
la_redline_nutm11.msb 442.dem_par 442.dem 442.map2rdc 1.5 1.5 442.sim_sar - - - - - -

| DEM width: | 1250 |
| DEM nlines: | 1231 |

Transform simulated SAR (sim_sar) power image from map to radar coordinates

geocode 442.map2rdc 442.sim_sar 1250 442.sim_sar.rdc 1000
raspwr 442.sim_sar.rdc 1000
gimp 442.sim_sar.rdc.ras

Create DIFF_PAR parameter file for co-registration of sim_sar image with a real power image

create_diff_par e122975_e106098.off - e122975_e106098.geo_par 0

Estimate offsets between sim_sar and real power image for fine registration

init_offsetm e122975_e106098.pwr1 442.sim_sar.rdc e122975_e106098.geo_par 1 1

offset_pwrm e122975_e106098.pwr1 442.sim_sar.rdc e122975_e106098.geo_par
e122975_e106098.doffs e122975_e106098.dsnr 75 75 - - 50 50

offset_fitm e122975_e106098.doffs e122975_e106098.dsnr e122975_e106098.geo_par e122975_e106098.dcoffs - 6.0 4 1

Apply offset polynomial to refine Geocoding Lookup Table

gc_map_fine 442.map2rdc 1250 e122975_e106098.geo_par 442.MAP2RDC 0

Now you can use the ACCURATE Geocoding Lookup Table

geocode 442.MAP2RDC 442.dem 1250 442.hgt_map 1000
raspwr 442.hgt_map 1000
gimp 442.hgt_map.ras

###########
Geocoding is now complete. We have an accurate Geocoding Look-up Table, and we have a DEM transformed into the radar coordinates of the MASTER image.
###########

Program: ERMAPPER
Site: Vancouver
Use: Preparation of DEM data
Programmed By: Richard Coffman
Comments: This shell script creates an .ers digital elevation model to be used
                    in geocoding.
Directory Output: STEREO
Final output: .ers
Directory in Which Processing was Conducted: STEREO

Geocoding May. 7, 2009 Vancouver

SARPIX_COORD 042908.slc.par - -

WGS84 COORDINATES

	IAZ PIX	JRPIX	LAT	LONG
1	0	0	39.5038611	127.2937188
2	0	1930	39.5970400	127.9610860
3	2489	0	40.4091498	127.0740043
4	2489	1930	40.5021806	127.7506037

Go to stereo

F://DEM/srtm.V2/EURASIA

STRM REFERENCE BY BOTTOM LEFT OF SQUARE
GAMMA REFERENCE BY TOP LEFT OF SQUARE

N=+
S= -
E= +
W= -

49.3463090   49.399362

```
-123.321700                    -122.8943706
┌─────────────────────────────┐
│                             │
│                             │
│                             │
│                             │
│                             │
│                             │
│                             │
│                             │
└─────────────────────────────┘
48.9447992                     48.9982660
-123.3321700                   -122.7796121
```

50, -124   50, -123   50, -122

```
┌─────────────────┬─────────────────┐
│                 │                 │
│                 │                 │
│          ┌∙∙∙∙┐│                 │
49, -124 ──┼─────∙────∙────────────── 49, -122
│          │∙    │   ∙            │
│          └∙∙∙∙∙┘                 │
│                 │                 │
└─────────────────┴─────────────────┘
```
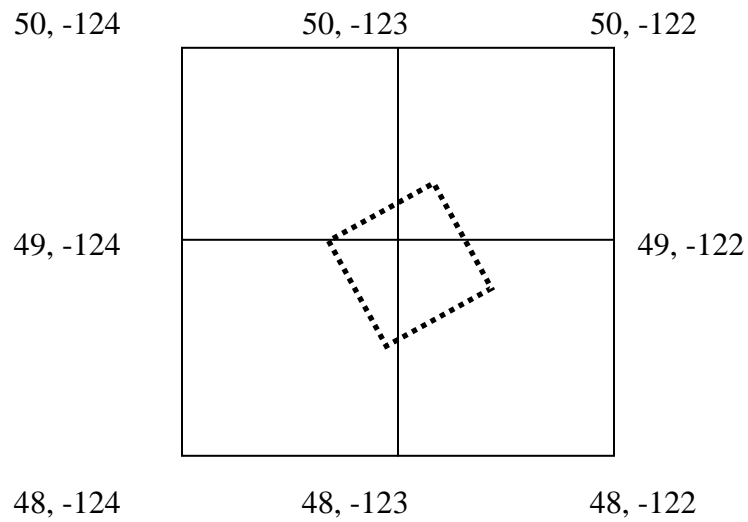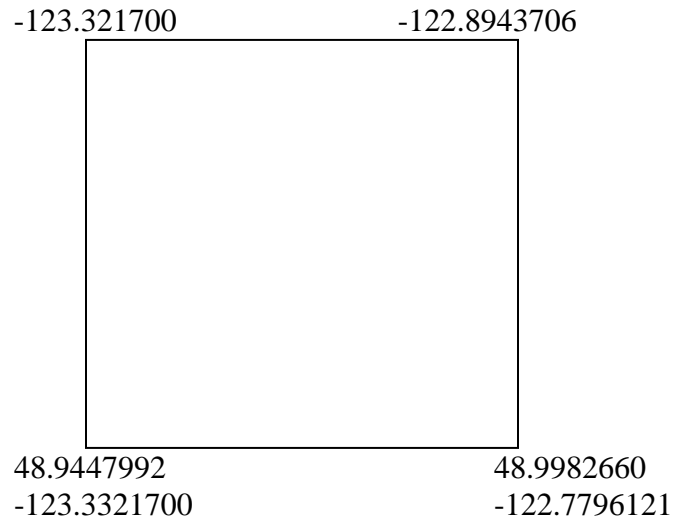
48, -124   48, -123   48, -122

Need 4 Scenes:
48, -124
48. -123
49, -124
49, -123

 Copy & paste then extract
Open for ER Mapper
In the third toolbar white three layer
Create .ERS From .HGT

Two Green Buttons-Edit Algorithm
        -Edit
        -Add Raster Layer

244

-Pseudo
-Assign .HGT ERS Files to Each Layer
-Apply To This Layer Only

File
Save As
Vancouver.ALL

File
Save As
Vancouver.ERS -Raster Data

Use Defaults
Except for: Unassigned 8-bit integer->16 bit
Pixel width = 0.000833333

How to convert from Cartesian to ellipsoid coordinates

Use chart on wall
UTM Zone 52

Processes

Start Geocoding Wizard
1) Input File Created in Previous Step Vancouver.ERS
   Map to Map Reprojection
2) Projection- UTM Datum-WGS84
   -NUTM 52
3) Rectify
   -Output Vancouver_nutm52
   -Cell Size = 80, 80
   - Resampling – Cubic Convolution
   -Start Rectification & Save File

   Secure FX FTP the following files to cgi1 – Binary
   Vancouver_nutm52
   Vancouver_nutm52.ers

   To CGI1-

   Swap_bytes on the file on cgi1 raid
   LSB to MSB Option 2

   Swap_bytes Vancouver_nutm52 Singhung_nutm52.msb2

   Creating dem_par file use the following inputs

UTM
WSG84
52
Default
Vancouver
Integer*2
Default 0.000
Default 1.00000
1637 – From Vancouver_nutm52.ers (# of Cells per line, DEM Width)
2347- (DEM Length)
-80 80 -posting

Program: itab creation flow
Site: Los Angeles Red Line
Use: Linux shell script to process multiple scenes very quickly
Programmed By: Richard Coffman
Comments: This shell script creates an itab file, it also displays a histogram of how often an image is used, and another image displaying which pairs are used.
Directory Output: /15initial/
Final output: itab
Directory in Which Processing was Conducted: /cgi1/insar/socal/15initial/

#To make itab file use the following matlab commands
#Copy the base.socal2 file over from /betic/insar/baseline_calc
#Delete the scenes which are not possessed. Also, reorganize with time, not platform.
#Rename it as base.timeorder

matlab #Opens the Matlab program

#Run the following commands in matlab
load base.timeorder
bperp_plot(base(:,4),base(:,3),base(:,5),125,1992,2001)
itab_bptime(base(:,5),base(:,4),125,10000)
load itab
itab_hist(itab)

Program: bperp_plot.m
Site: Los Angeles Red Line
Use: Linux shell script to process multiple scenes very quickly
Programmed By: Dr. Francisco Gomez
Comments: This shell script creates an image displaying which pairs are
                  created using the baseline file created using ers_bperp.
Directory Output: /15initial/
Final output: image
Directory in Which Processing was Conducted: /cgi1/insar/socal/15initial/

```
function bperp_plot(datein,orbits,baseraw,bmax,year1,year2)
% USAGE:  bperp_plot(dates,orbits,baselines,bmax,year min, year max)
% Plots baseline vs. dates of two SAR acquisitions.
%

%
daysinyear = 365.2430;
%bmax = 100;

X = size(datein);
dateraw = num2str(datein);
for i = 1:X(1)
temp = [dateraw(i,1:4) '/' dateraw(i,5:6) '/' dateraw(i,7:8)];

dates(i,:) = temp;
end

numdates = datenum(dates);
clear baseout
clear plotout
count = 0;
for i = 2:X(1)
   % i - 1 is the master
   for j = i:X(1)
      % j is the slave
      bp = baseraw(i-1) - baseraw(j);
      if abs(bp) <= bmax
         temp = [orbits(i-1) orbits(j) ceil(bp) numdates(i-1) numdates(j) abs(numdates(i-
1)-numdates(j))];
         count = count +1;
         baseout(count,:) = temp;
         plotout(count).data = [numdates(i-1) abs(bp);numdates(j) abs(bp)];
      end
   end
end
```

248

```
Y = size(baseout);
figure
hold on
for i = 1:Y(1)
    plot(plotout(i).data(:,1),plotout(i).data(:,2),'b-
',plotout(i).data(:,1),plotout(i).data(:,2),'bo')
end
datetick('x',10)
axis([datenum(year1*daysinyear) datenum(year2*daysinyear) 0 bmax])
set(gca,'XTick',datenum(year1*daysinyear):daysinyear:datenum(year2*daysinyear))
set(gca,'XTickLabel',{year1:1:year2})
grid on
hold off
count
```

Program: itab_bptime.m
Site: Los Angeles Red Line
Use: Linux shell script to process multiple scenes very quickly
Programmed By: Dr. Francisco Gomez
Comments: This shell script creates an itab file created using ers_bperp.
Directory Output: /15initial/
Final output: itab
Directory in Which Processing was Conducted: /cgi1/insar/socal/15initial/

```
function [v w]=itab_bptime(baseraw,dates,bmax,tmax)
% USAGE:  itab_bperp(baselines,dates,bmax,tmax)
% make IPTA itab file for all combinations with baselines less than bmax
% and time spans (in days) less than tmax
% This also saves the itab to the file name "itab".

%
%bmax = 100;
X = size(baseraw);

dateraw = num2str(dates);

for i = 1:X(1)
temp = [dateraw(i,1:4) '/' dateraw(i,5:6) '/' dateraw(i,7:8)];
datestemp(i,:) = temp;
end

numdates = datenum(datestemp);
clear i

clear itab
count = 0;
for i = 2:X(1)
   % i - 1 is the master
   for j = i:X(1)
      % j is the slave
      bp = baseraw(i-1) - baseraw(j);
      daydif = numdates(j) - numdates(i-1);
      if abs(bp) <= bmax & (i - 1) ~= j & abs(daydif) <= tmax
         count = count +1;
         itab(count,:) = [ i-1 j count 1];
         outlist(count,:) = [count dates(i-1) dates(j) daydif bp];
      end
   end
end

v=itab;
```

```
w = outlist;
dlmwrite('itab',itab,' ')
dlmwrite('itab_info',outlist,'delimiter',' ','precision',8)
```

Program: itab_hist.m
Site: Los Angeles Red Line
Use: Linux shell script to process multiple scenes very quickly
Programmed By: Dr. Francisco Gomez
Comments: This shell script creates a histogram using the itab file created
                        using itab_bptime.
Directory Output: /15initial/
Final output: histogram image
Directory in Which Processing was Conducted: /cgi1/insar/socal/15initial/

function itab_hist(itab)

% USAGE: itab_hist(itab,output eps)
% Plots histograms of scene usage based on an itab file.
% Can be modified to print the histogram to an EPS file, too.
%

%
Y = size(itab);

clear itabtemp
itabtemp(:,1:2)=itab(:,1:2);
itabtemp2=[itabtemp(:,1);itabtemp(:,2)];
hist(itabtemp2,[min(min(itab(:,1:2))):max(max(itab(:,1:2)))])
grid minor
set(gca,'XTick',0:5:max(max(itab(:,1:2))))
set(gca,'XTickLabel',{0:5:max(max(itab(:,1:2)))})
%print -depsc outfile

Program:	PROCESS_ALL2.sh
Site:	Los Angeles Red Line
Use:	Linux shell script to process multiple scenes very quickly
Programmed By:	Dr. Francisco Gomez (modifications by Richard Coffman)
Comments:	This shell script calls other shell scripts (ex. CREATE_OFF, OFFSET, etc.). The other shell scripts call GAMMA Remote Sensing Software scripts (ex. create_offset, offset_pwr, offset_fit, etc.).Each of the scripts are presented sequentially as they are referred to here in this program.
Final output:	44 unwrapped differential interferograms
	Multi-looking: 1 look in the range, 5 looks in the azimuth
	Filtering: Slope Adaptive Filter
	Filter Window Size:
	Coherence Threshold Mask: 0

Directory in Which Processing was Conducted: /cgi1/insar/socal/15initial/

```
# Master script syntax
#CREATE_OFF <itab> <slc tab> <rn looks> <az looks> <rn samples> <az samples> <rn
window> <az window> <snr thresh>
#OFFSET_CALC <itab> <slc tab>
#INTERF <itab> <slc tab>
#BASEFLAT <itab> <slc tab> <hgt map> <diff/geo par>
#FILTER <itab> <slc tab> <filter flag: 0=adf, 1=adapt_filt>
#UNWRAP <itab> <slc tab> <cc thresh>
#BASEREFINE <itab> <slc tab> <hgt map> <diff/geo par>
#REUNWRAP <itab> <slc tab> <filter flag: 0=adf, 1=adapt_filt> <filter size> <cc
thresh>


translate_itab itab RSLC_tab
CREATE_OFF itab RSLC_tab 20 50 100 200 6
OFFSET_CALC itab RSLC_tab
INTERF itab RSLC_tab 1 5
#copy over the height map and geo_par from LA work on /sahara/insar/socal2/INT-paco
ln -s ../reprocess/hgt_map
ln -s ../reprocess/geo_par
BASEFLAT itab RSLC_tab hgt_map geo_par
mk_mli_all RSLC_tab mli 1 5
FILTER itab RSLC_tab 0 8
RASMPH itab RSLC_tab SM_NOTOPO SMRAS sm_notopo
UNWRAPPER itab RSLC_tab 50
BASEREFINE itab RSLC_tab hgt_map geo_par 50 100
RASRMG itab RSLC_tab UNW UNWRAS unw_dif 1 0.2


#The following commands are now run using the reunwrap_commands.txt file
#REUNWRAP itab RSLC_tab geo_par 1 2 0
#RASRMG itab RSLC_tab UNW UNWRAS unw_dif2 1 0.2
```

253

Program: translate_itab
Site: Los Angeles Red Line
Use: Linux shell script to process multiple scenes very quickly
Programmed By: Dr. Francisco Gomez
Comments: This shell script uses the previously created itab and RSLC_tab to
                    calculate an ISP.input file with the master-slave combinations.
Final output: ISP.input
Directory in Which Processing was Conducted: /cgi1/insar/socal/15initial/

```bash
#!/bin/bash
#
# Right now, this simply writes the master and slave pairs to a text file.  However,
# manipulating this to execute Gamma programs is fairly straightforward from here.
# The trick will be to keep things organized ...
#
# User inputs
if [ $# -lt 2 ]; then
echo "translate_itab <itab> <slc tab>"
exit
fi


#
ITAB=$1
SLCTAB=$2
OUTFILE='ISP.input'

if [ -e $OUTFILE ]; then /bin/rm $OUTFILE; fi
touch $OUTFILE

while read LINE
do

ID1=`echo $LINE | awk '{print $1}'`
ID2=`echo $LINE | awk '{print $2}'`
INTID=`echo $LINE | awk '{print $3}'`
FLAG=`echo $LINE | awk '{print $4}'`

X=1
while read TEMP
do
if [ $X = $ID1 ]; then
MASTER=`echo $TEMP | awk '{print $1}' | sed -e "s/^.*\///" | sed -e "s/\.rslc//"`
SLC1=`echo $TEMP | awk '{print $1}'`
PAR1=`echo $TEMP | awk '{print $2}'`
fi
X=`expr $X + 1`
```

254

```
done < $SLCTAB

X=1
while read TEMP
do
if [ $X = $ID2 ]; then
SLAVE=`echo $TEMP | awk '{print $1}' | sed -e "s/^.*\///" | sed -e "s/\.rslc//"`
SLC2=`echo $TEMP | awk '{print $1}'`
PAR2=`echo $TEMP | awk '{print $2}'`
fi
X=`expr $X + 1`
done < $SLCTAB

if [ $INTID -lt 10 ]; then INTID=0$INTID;fi
if [ $INTID -lt 100 ]; then INTID=0$INTID;fi

echo $INTID" "$MASTER" "$SLAVE" "$SLC1" "$SLC2" "$PAR1" "$PAR2" "$FLAG
                    >> $OUTFILE
#echo $INTID
done < $ITAB

# Maybe it will be better to write the SLC and PAR file names, as well as the
# root orbit names to the output file.  Remember that the SLCs and PAR files
# will require relative path names -- the directory will be messy with all
# of the symbolic links.  This output file can then be read by the scripts that
# execute the actual commands, rather than cycling through this mess with the
# ITAB and SLC_TAB files repeatedly.
```

File: ISP.input
File obtained from: translate_itab
Site: Los Angeles Red Line
Comments: 207 interferometric pairs (Note the 1 at the end of each line is a marker to
determine if that interferogram pair will be used 1=yes, 0=no)

001 e104595 e107100 rslc1/e104595.rslc rslc1/e107100.rslc rslc1/e104595.rpar
rslc1/e107100.rpar 1
002 e104595 e112110 rslc1/e104595.rslc rslc1/e112110.rslc rslc1/e104595.rpar
rslc1/e112110.rpar 1
003 e104595 e120971 rslc1/e104595.rslc rslc1/e120971.rslc rslc1/e104595.rpar
rslc1/e120971.rpar 1
004 e104595 e121973 rslc1/e104595.rslc rslc1/e121973.rslc rslc1/e104595.rpar
rslc1/e121973.rpar 1
005 e104595 e122975 rslc1/e104595.rslc rslc1/e122975.rslc rslc1/e104595.rpar
rslc1/e122975.rpar 1
006 e104595 e123476 rslc1/e104595.rslc rslc1/e123476.rslc rslc1/e104595.rpar
rslc1/e123476.rpar 1
007 e104595 e206308 rslc1/e104595.rslc rslc1/e206308.rslc rslc1/e104595.rpar
rslc1/e206308.rpar 1
008 e106098 e202801 rslc1/e106098.rslc rslc1/e202801.rslc rslc1/e106098.rpar
rslc1/e202801.rpar 1
009 e106098 e123977 rslc1/e106098.rslc rslc1/e123977.rslc rslc1/e106098.rpar
rslc1/e123977.rpar 1
010 e106098 e204304 rslc1/e106098.rslc rslc1/e204304.rslc rslc1/e106098.rpar
rslc1/e204304.rpar 1
011 e106098 e210316 rslc1/e106098.rslc rslc1/e210316.rslc rslc1/e106098.rpar
rslc1/e210316.rpar 1
012 e106098 e224344 rslc1/e106098.rslc rslc1/e224344.rslc rslc1/e106098.rpar
rslc1/e224344.rpar 1
013 e106599 e119468 rslc1/e106599.rslc rslc1/e119468.rslc rslc1/e106599.rpar
rslc1/e119468.rpar 1
014 e106599 e120470 rslc1/e106599.rslc rslc1/e120470.rslc rslc1/e106599.rpar
rslc1/e120470.rpar 1
015 e106599 e207310 rslc1/e106599.rslc rslc1/e207310.rslc rslc1/e106599.rpar
rslc1/e207310.rpar 1
016 e106599 e208813 rslc1/e106599.rslc rslc1/e208813.rslc rslc1/e106599.rpar
rslc1/e208813.rpar 1
017 e106599 e211318 rslc1/e106599.rslc rslc1/e211318.rslc rslc1/e106599.rpar
rslc1/e211318.rpar 1
018 e106599 e214324 rslc1/e106599.rslc rslc1/e214324.rslc rslc1/e106599.rpar
rslc1/e214324.rpar 1
019 e106599 e218833 rslc1/e106599.rslc rslc1/e218833.rslc rslc1/e106599.rpar
rslc1/e218833.rpar 1
020 e106599 e220336 rslc1/e106599.rslc rslc1/e220336.rslc rslc1/e106599.rpar
rslc1/e220336.rpar 1

021 e106599 e226849 rslc1/e106599.rslc rslc1/e226849.rslc rslc1/e106599.rpar
        rslc1/e226849.rpar 1
022 e106599 e227851 rslc1/e106599.rslc rslc1/e227851.rslc rslc1/e106599.rpar
        rslc1/e227851.rpar 1
023 e106599 e229354 rslc1/e106599.rslc rslc1/e229354.rslc rslc1/e106599.rpar
        rslc1/e229354.rpar 1
024 e107100 e112110 rslc1/e107100.rslc rslc1/e112110.rslc rslc1/e107100.rpar
        rslc1/e112110.rpar 1
025 e107100 e121973 rslc1/e107100.rslc rslc1/e121973.rslc rslc1/e107100.rpar
        rslc1/e121973.rpar 1
026 e107100 e122975 rslc1/e107100.rslc rslc1/e122975.rslc rslc1/e107100.rpar
        rslc1/e122975.rpar 1
027 e107100 e206308 rslc1/e107100.rslc rslc1/e206308.rslc rslc1/e107100.rpar
        rslc1/e206308.rpar 1
028 e107100 e207811 rslc1/e107100.rslc rslc1/e207811.rslc rslc1/e107100.rpar
        rslc1/e207811.rpar 1
029 e107100 e222340 rslc1/e107100.rslc rslc1/e222340.rslc rslc1/e107100.rpar
        rslc1/e222340.rpar 1
030 e107601 e111108 rslc1/e107601.rslc rslc1/e111108.rslc rslc1/e107601.rpar
        rslc1/e111108.rpar 1
031 e107601 e125480 rslc1/e107601.rslc rslc1/e125480.rslc rslc1/e107601.rpar
        rslc1/e125480.rpar 1
032 e107601 e214825 rslc1/e107601.rslc rslc1/e214825.rslc rslc1/e107601.rpar
        rslc1/e214825.rpar 1
033 e107601 e218332 rslc1/e107601.rslc rslc1/e218332.rslc rslc1/e107601.rpar
        rslc1/e218332.rpar 1
034 e107601 e219835 rslc1/e107601.rslc rslc1/e219835.rslc rslc1/e107601.rpar
        rslc1/e219835.rpar 1
035 e107601 e223342 rslc1/e107601.rslc rslc1/e223342.rslc rslc1/e107601.rpar
        rslc1/e223342.rpar 1
036 e111108 e119468 rslc1/e111108.rslc rslc1/e119468.rslc rslc1/e111108.rpar
        rslc1/e119468.rpar 1
037 e111108 e125480 rslc1/e111108.rslc rslc1/e125480.rslc rslc1/e111108.rpar
        rslc1/e125480.rpar 1
038 e111108 e214324 rslc1/e111108.rslc rslc1/e214324.rslc rslc1/e111108.rpar
        rslc1/e214324.rpar 1
039 e111108 e214825 rslc1/e111108.rslc rslc1/e214825.rslc rslc1/e111108.rpar
        rslc1/e214825.rpar 1
040 e111108 e218332 rslc1/e111108.rslc rslc1/e218332.rslc rslc1/e111108.rpar
        rslc1/e218332.rpar 1
041 e111108 e219835 rslc1/e111108.rslc rslc1/e219835.rslc rslc1/e111108.rpar
        rslc1/e219835.rpar 1
042 e111108 e223342 rslc1/e111108.rslc rslc1/e223342.rslc rslc1/e111108.rpar
        rslc1/e223342.rpar 1
043 e111108 e226849 rslc1/e111108.rslc rslc1/e226849.rslc rslc1/e111108.rpar
        rslc1/e226849.rpar 1

044 e111609 e120470 rslc1/e111609.rslc rslc1/e120470.rslc rslc1/e111609.rpar
        rslc1/e120470.rpar 1
045 e111609 e120971 rslc1/e111609.rslc rslc1/e120971.rslc rslc1/e111609.rpar
        rslc1/e120971.rpar 1
046 e111609 e121472 rslc1/e111609.rslc rslc1/e121472.rslc rslc1/e111609.rpar
        rslc1/e121472.rpar 1
047 e111609 e203302 rslc1/e111609.rslc rslc1/e203302.rslc rslc1/e111609.rpar
        rslc1/e203302.rpar 1
048 e111609 e203803 rslc1/e111609.rslc rslc1/e203803.rslc rslc1/e111609.rpar
        rslc1/e203803.rpar 1
049 e111609 e208813 rslc1/e111609.rslc rslc1/e208813.rslc rslc1/e111609.rpar
        rslc1/e208813.rpar 1
050 e111609 e209815 rslc1/e111609.rslc rslc1/e209815.rslc rslc1/e111609.rpar
        rslc1/e209815.rpar 1
051 e111609 e210817 rslc1/e111609.rslc rslc1/e210817.rslc rslc1/e111609.rpar
        rslc1/e210817.rpar 1
052 e111609 e211318 rslc1/e111609.rslc rslc1/e211318.rslc rslc1/e111609.rpar
        rslc1/e211318.rpar 1
053 e111609 e211819 rslc1/e111609.rslc rslc1/e211819.rslc rslc1/e111609.rpar
        rslc1/e211819.rpar 1
054 e111609 e217330 rslc1/e111609.rslc rslc1/e217330.rslc rslc1/e111609.rpar
        rslc1/e217330.rpar 1
055 e111609 e218833 rslc1/e111609.rslc rslc1/e218833.rslc rslc1/e111609.rpar
        rslc1/e218833.rpar 1
056 e111609 e220336 rslc1/e111609.rslc rslc1/e220336.rslc rslc1/e111609.rpar
        rslc1/e220336.rpar 1
057 e111609 e226348 rslc1/e111609.rslc rslc1/e226348.rslc rslc1/e111609.rpar
        rslc1/e226348.rpar 1
058 e111609 e227851 rslc1/e111609.rslc rslc1/e227851.rslc rslc1/e111609.rpar
        rslc1/e227851.rpar 1
059 e111609 e229354 rslc1/e111609.rslc rslc1/e229354.rslc rslc1/e111609.rpar
        rslc1/e229354.rpar 1
060 e112110 e120971 rslc1/e112110.rslc rslc1/e120971.rslc rslc1/e112110.rpar
        rslc1/e120971.rpar 1
061 e112110 e121973 rslc1/e112110.rslc rslc1/e121973.rslc rslc1/e112110.rpar
        rslc1/e121973.rpar 1
062 e112110 e122975 rslc1/e112110.rslc rslc1/e122975.rslc rslc1/e112110.rpar
        rslc1/e122975.rpar 1
063 e112110 e123476 rslc1/e112110.rslc rslc1/e123476.rslc rslc1/e112110.rpar
        rslc1/e123476.rpar 1
064 e119468 e125480 rslc1/e119468.rslc rslc1/e125480.rslc rslc1/e119468.rpar
        rslc1/e125480.rpar 1
065 e119468 e207310 rslc1/e119468.rslc rslc1/e207310.rslc rslc1/e119468.rpar
        rslc1/e207310.rpar 1
066 e119468 e214324 rslc1/e119468.rslc rslc1/e214324.rslc rslc1/e119468.rpar
        rslc1/e214324.rpar 1

067 e119468 e214825 rslc1/e119468.rslc rslc1/e214825.rslc rslc1/e119468.rpar
        rslc1/e214825.rpar 1
068 e119468 e218833 rslc1/e119468.rslc rslc1/e218833.rslc rslc1/e119468.rpar
        rslc1/e218833.rpar 1
069 e119468 e226849 rslc1/e119468.rslc rslc1/e226849.rslc rslc1/e119468.rpar
        rslc1/e226849.rpar 1
070 e119468 e227851 rslc1/e119468.rslc rslc1/e227851.rslc rslc1/e119468.rpar
        rslc1/e227851.rpar 1
071 e119468 e229354 rslc1/e119468.rslc rslc1/e229354.rslc rslc1/e119468.rpar
        rslc1/e229354.rpar 1
072 e120470 e121472 rslc1/e120470.rslc rslc1/e121472.rslc rslc1/e120470.rpar
        rslc1/e121472.rpar 1
073 e120470 e207310 rslc1/e120470.rslc rslc1/e207310.rslc rslc1/e120470.rpar
        rslc1/e207310.rpar 1
074 e120470 e208813 rslc1/e120470.rslc rslc1/e208813.rslc rslc1/e120470.rpar
        rslc1/e208813.rpar 1
075 e120470 e209815 rslc1/e120470.rslc rslc1/e209815.rslc rslc1/e120470.rpar
        rslc1/e209815.rpar 1
076 e120470 e211318 rslc1/e120470.rslc rslc1/e211318.rslc rslc1/e120470.rpar
        rslc1/e211318.rpar 1
077 e120470 e218833 rslc1/e120470.rslc rslc1/e218833.rslc rslc1/e120470.rpar
        rslc1/e218833.rpar 1
078 e120470 e220336 rslc1/e120470.rslc rslc1/e220336.rslc rslc1/e120470.rpar
        rslc1/e220336.rpar 1
079 e120470 e226348 rslc1/e120470.rslc rslc1/e226348.rslc rslc1/e120470.rpar
        rslc1/e226348.rpar 1
080 e120470 e227851 rslc1/e120470.rslc rslc1/e227851.rslc rslc1/e120470.rpar
        rslc1/e227851.rpar 1
081 e120470 e229354 rslc1/e120470.rslc rslc1/e229354.rslc rslc1/e120470.rpar
        rslc1/e229354.rpar 1
082 e120971 e121472 rslc1/e120971.rslc rslc1/e121472.rslc rslc1/e120971.rpar
        rslc1/e121472.rpar 1
083 e120971 e121973 rslc1/e120971.rslc rslc1/e121973.rslc rslc1/e120971.rpar
        rslc1/e121973.rpar 1
084 e120971 e122975 rslc1/e120971.rslc rslc1/e122975.rslc rslc1/e120971.rpar
        rslc1/e122975.rpar 1
085 e120971 e203302 rslc1/e120971.rslc rslc1/e203302.rslc rslc1/e120971.rpar
        rslc1/e203302.rpar 1
086 e120971 e123476 rslc1/e120971.rslc rslc1/e123476.rslc rslc1/e120971.rpar
        rslc1/e123476.rpar 1
087 e120971 e203803 rslc1/e120971.rslc rslc1/e203803.rslc rslc1/e120971.rpar
        rslc1/e203803.rpar 1
088 e120971 e209815 rslc1/e120971.rslc rslc1/e209815.rslc rslc1/e120971.rpar
        rslc1/e209815.rpar 1
089 e120971 e210817 rslc1/e120971.rslc rslc1/e210817.rslc rslc1/e120971.rpar
        rslc1/e210817.rpar 1

090 e120971 e211819 rslc1/e120971.rslc rslc1/e211819.rslc rslc1/e120971.rpar
        rslc1/e211819.rpar 1
091 e120971 e217330 rslc1/e120971.rslc rslc1/e217330.rslc rslc1/e120971.rpar
        rslc1/e217330.rpar 1
092 e121472 e203302 rslc1/e121472.rslc rslc1/e203302.rslc rslc1/e121472.rpar
        rslc1/e203302.rpar 1
093 e121472 e203803 rslc1/e121472.rslc rslc1/e203803.rslc rslc1/e121472.rpar
        rslc1/e203803.rpar 1
094 e121472 e208813 rslc1/e121472.rslc rslc1/e208813.rslc rslc1/e121472.rpar
        rslc1/e208813.rpar 1
095 e121472 e209815 rslc1/e121472.rslc rslc1/e209815.rslc rslc1/e121472.rpar
        rslc1/e209815.rpar 1
096 e121472 e210817 rslc1/e121472.rslc rslc1/e210817.rslc rslc1/e121472.rpar
        rslc1/e210817.rpar 1
097 e121472 e211318 rslc1/e121472.rslc rslc1/e211318.rslc rslc1/e121472.rpar
        rslc1/e211318.rpar 1
098 e121472 e211819 rslc1/e121472.rslc rslc1/e211819.rslc rslc1/e121472.rpar
        rslc1/e211819.rpar 1
099 e121472 e217330 rslc1/e121472.rslc rslc1/e217330.rslc rslc1/e121472.rpar
        rslc1/e217330.rpar 1
100 e121472 e218833 rslc1/e121472.rslc rslc1/e218833.rslc rslc1/e121472.rpar
        rslc1/e218833.rpar 1
101 e121472 e220336 rslc1/e121472.rslc rslc1/e220336.rslc rslc1/e121472.rpar
        rslc1/e220336.rpar 1
102 e121472 e226348 rslc1/e121472.rslc rslc1/e226348.rslc rslc1/e121472.rpar
        rslc1/e226348.rpar 1
103 e121472 e227851 rslc1/e121472.rslc rslc1/e227851.rslc rslc1/e121472.rpar
        rslc1/e227851.rpar 1
104 e121472 e229354 rslc1/e121472.rslc rslc1/e229354.rslc rslc1/e121472.rpar
        rslc1/e229354.rpar 1
105 e121973 e122975 rslc1/e121973.rslc rslc1/e122975.rslc rslc1/e121973.rpar
        rslc1/e122975.rpar 1
106 e121973 e123476 rslc1/e121973.rslc rslc1/e123476.rslc rslc1/e121973.rpar
        rslc1/e123476.rpar 1
107 e121973 e206308 rslc1/e121973.rslc rslc1/e206308.rslc rslc1/e121973.rpar
        rslc1/e206308.rpar 1
108 e202801 e123977 rslc1/e202801.rslc rslc1/e123977.rslc rslc1/e202801.rpar
        rslc1/e123977.rpar 1
109 e202801 e204304 rslc1/e202801.rslc rslc1/e204304.rslc rslc1/e202801.rpar
        rslc1/e204304.rpar 1
110 e202801 e210316 rslc1/e202801.rslc rslc1/e210316.rslc rslc1/e202801.rpar
        rslc1/e210316.rpar 1
111 e122975 e123476 rslc1/e122975.rslc rslc1/e123476.rslc rslc1/e122975.rpar
        rslc1/e123476.rpar 1
112 e122975 e206308 rslc1/e122975.rslc rslc1/e206308.rslc rslc1/e122975.rpar
        rslc1/e206308.rpar 1

113 e203302 e123476 rslc1/e203302.rslc rslc1/e123476.rslc rslc1/e203302.rpar
    rslc1/e123476.rpar 1
114 e203302 e203803 rslc1/e203302.rslc rslc1/e203803.rslc rslc1/e203302.rpar
    rslc1/e203803.rpar 1
115 e203302 e209815 rslc1/e203302.rslc rslc1/e209815.rslc rslc1/e203302.rpar
    rslc1/e209815.rpar 1
116 e203302 e210817 rslc1/e203302.rslc rslc1/e210817.rslc rslc1/e203302.rpar
    rslc1/e210817.rpar 1
117 e203302 e211318 rslc1/e203302.rslc rslc1/e211318.rslc rslc1/e203302.rpar
    rslc1/e211318.rpar 1
118 e203302 e211819 rslc1/e203302.rslc rslc1/e211819.rslc rslc1/e203302.rpar
    rslc1/e211819.rpar 1
119 e203302 e217330 rslc1/e203302.rslc rslc1/e217330.rslc rslc1/e203302.rpar
    rslc1/e217330.rpar 1
120 e203302 e220336 rslc1/e203302.rslc rslc1/e220336.rslc rslc1/e203302.rpar
    rslc1/e220336.rpar 1
121 e203302 e226348 rslc1/e203302.rslc rslc1/e226348.rslc rslc1/e203302.rpar
    rslc1/e226348.rpar 1
122 e123476 e203803 rslc1/e123476.rslc rslc1/e203803.rslc rslc1/e123476.rpar
    rslc1/e203803.rpar 1
123 e123476 e211819 rslc1/e123476.rslc rslc1/e211819.rslc rslc1/e123476.rpar
    rslc1/e211819.rpar 1
124 e123476 e217330 rslc1/e123476.rslc rslc1/e217330.rslc rslc1/e123476.rpar
    rslc1/e217330.rpar 1
125 e203803 e209815 rslc1/e203803.rslc rslc1/e209815.rslc rslc1/e203803.rpar
    rslc1/e209815.rpar 1
126 e203803 e210817 rslc1/e203803.rslc rslc1/e210817.rslc rslc1/e203803.rpar
    rslc1/e210817.rpar 1
127 e203803 e211318 rslc1/e203803.rslc rslc1/e211318.rslc rslc1/e203803.rpar
    rslc1/e211318.rpar 1
128 e203803 e211819 rslc1/e203803.rslc rslc1/e211819.rslc rslc1/e203803.rpar
    rslc1/e211819.rpar 1
129 e203803 e217330 rslc1/e203803.rslc rslc1/e217330.rslc rslc1/e203803.rpar
    rslc1/e217330.rpar 1
130 e203803 e220336 rslc1/e203803.rslc rslc1/e220336.rslc rslc1/e203803.rpar
    rslc1/e220336.rpar 1
131 e203803 e226348 rslc1/e203803.rslc rslc1/e226348.rslc rslc1/e203803.rpar
    rslc1/e226348.rpar 1
132 e123977 e204304 rslc1/e123977.rslc rslc1/e204304.rslc rslc1/e123977.rpar
    rslc1/e204304.rpar 1
133 e123977 e210316 rslc1/e123977.rslc rslc1/e210316.rslc rslc1/e123977.rpar
    rslc1/e210316.rpar 1
134 e204304 e210316 rslc1/e204304.rslc rslc1/e210316.rslc rslc1/e204304.rpar
    rslc1/e210316.rpar 1
135 e125480 e214324 rslc1/e125480.rslc rslc1/e214324.rslc rslc1/e125480.rpar
    rslc1/e214324.rpar 1

136 e125480 e214825 rslc1/e125480.rslc rslc1/e214825.rslc rslc1/e125480.rpar
        rslc1/e214825.rpar 1
137 e125480 e218332 rslc1/e125480.rslc rslc1/e218332.rslc rslc1/e125480.rpar
        rslc1/e218332.rpar 1
138 e125480 e219835 rslc1/e125480.rslc rslc1/e219835.rslc rslc1/e125480.rpar
        rslc1/e219835.rpar 1
139 e125480 e223342 rslc1/e125480.rslc rslc1/e223342.rslc rslc1/e125480.rpar
        rslc1/e223342.rpar 1
140 e206308 e207811 rslc1/e206308.rslc rslc1/e207811.rslc rslc1/e206308.rpar
        rslc1/e207811.rpar 1
141 e206308 e222340 rslc1/e206308.rslc rslc1/e222340.rslc rslc1/e206308.rpar
        rslc1/e222340.rpar 1
142 e207310 e208813 rslc1/e207310.rslc rslc1/e208813.rslc rslc1/e207310.rpar
        rslc1/e208813.rpar 1
143 e207310 e211318 rslc1/e207310.rslc rslc1/e211318.rslc rslc1/e207310.rpar
        rslc1/e211318.rpar 1
144 e207310 e214324 rslc1/e207310.rslc rslc1/e214324.rslc rslc1/e207310.rpar
        rslc1/e214324.rpar 1
145 e207310 e218833 rslc1/e207310.rslc rslc1/e218833.rslc rslc1/e207310.rpar
        rslc1/e218833.rpar 1
146 e207310 e220336 rslc1/e207310.rslc rslc1/e220336.rslc rslc1/e207310.rpar
        rslc1/e220336.rpar 1
147 e207310 e226849 rslc1/e207310.rslc rslc1/e226849.rslc rslc1/e207310.rpar
        rslc1/e226849.rpar 1
148 e207310 e227851 rslc1/e207310.rslc rslc1/e227851.rslc rslc1/e207310.rpar
        rslc1/e227851.rpar 1
149 e207310 e229354 rslc1/e207310.rslc rslc1/e229354.rslc rslc1/e207310.rpar
        rslc1/e229354.rpar 1
150 e207811 e222340 rslc1/e207811.rslc rslc1/e222340.rslc rslc1/e207811.rpar
        rslc1/e222340.rpar 1
151 e207811 e224344 rslc1/e207811.rslc rslc1/e224344.rslc rslc1/e207811.rpar
        rslc1/e224344.rpar 1
152 e208813 e209815 rslc1/e208813.rslc rslc1/e209815.rslc rslc1/e208813.rpar
        rslc1/e209815.rpar 1
153 e208813 e211318 rslc1/e208813.rslc rslc1/e211318.rslc rslc1/e208813.rpar
        rslc1/e211318.rpar 1
154 e208813 e218833 rslc1/e208813.rslc rslc1/e218833.rslc rslc1/e208813.rpar
        rslc1/e218833.rpar 1
155 e208813 e220336 rslc1/e208813.rslc rslc1/e220336.rslc rslc1/e208813.rpar
        rslc1/e220336.rpar 1
156 e208813 e226348 rslc1/e208813.rslc rslc1/e226348.rslc rslc1/e208813.rpar
        rslc1/e226348.rpar 1
157 e208813 e227851 rslc1/e208813.rslc rslc1/e227851.rslc rslc1/e208813.rpar
        rslc1/e227851.rpar 1
158 e208813 e229354 rslc1/e208813.rslc rslc1/e229354.rslc rslc1/e208813.rpar
        rslc1/e229354.rpar 1

159 e209815 e210817 rslc1/e209815.rslc rslc1/e210817.rslc rslc1/e209815.rpar
        rslc1/e210817.rpar 1
160 e209815 e211318 rslc1/e209815.rslc rslc1/e211318.rslc rslc1/e209815.rpar
        rslc1/e211318.rpar 1
161 e209815 e211819 rslc1/e209815.rslc rslc1/e211819.rslc rslc1/e209815.rpar
        rslc1/e211819.rpar 1
162 e209815 e217330 rslc1/e209815.rslc rslc1/e217330.rslc rslc1/e209815.rpar
        rslc1/e217330.rpar 1
163 e209815 e220336 rslc1/e209815.rslc rslc1/e220336.rslc rslc1/e209815.rpar
        rslc1/e220336.rpar 1
164 e209815 e226348 rslc1/e209815.rslc rslc1/e226348.rslc rslc1/e209815.rpar
        rslc1/e226348.rpar 1
165 e209815 e229354 rslc1/e209815.rslc rslc1/e229354.rslc rslc1/e209815.rpar
        rslc1/e229354.rpar 1
166 e210817 e211318 rslc1/e210817.rslc rslc1/e211318.rslc rslc1/e210817.rpar
        rslc1/e211318.rpar 1
167 e210817 e211819 rslc1/e210817.rslc rslc1/e211819.rslc rslc1/e210817.rpar
        rslc1/e211819.rpar 1
168 e210817 e217330 rslc1/e210817.rslc rslc1/e217330.rslc rslc1/e210817.rpar
        rslc1/e217330.rpar 1
169 e210817 e220336 rslc1/e210817.rslc rslc1/e220336.rslc rslc1/e210817.rpar
        rslc1/e220336.rpar 1
170 e210817 e226348 rslc1/e210817.rslc rslc1/e226348.rslc rslc1/e210817.rpar
        rslc1/e226348.rpar 1
171 e211318 e211819 rslc1/e211318.rslc rslc1/e211819.rslc rslc1/e211318.rpar
        rslc1/e211819.rpar 1
172 e211318 e217330 rslc1/e211318.rslc rslc1/e217330.rslc rslc1/e211318.rpar
        rslc1/e217330.rpar 1
173 e211318 e218833 rslc1/e211318.rslc rslc1/e218833.rslc rslc1/e211318.rpar
        rslc1/e218833.rpar 1
174 e211318 e220336 rslc1/e211318.rslc rslc1/e220336.rslc rslc1/e211318.rpar
        rslc1/e220336.rpar 1
175 e211318 e226348 rslc1/e211318.rslc rslc1/e226348.rslc rslc1/e211318.rpar
        rslc1/e226348.rpar 1
176 e211318 e227851 rslc1/e211318.rslc rslc1/e227851.rslc rslc1/e211318.rpar
        rslc1/e227851.rpar 1
177 e211318 e229354 rslc1/e211318.rslc rslc1/e229354.rslc rslc1/e211318.rpar
        rslc1/e229354.rpar 1
178 e211819 e217330 rslc1/e211819.rslc rslc1/e217330.rslc rslc1/e211819.rpar
        rslc1/e217330.rpar 1
179 e211819 e220336 rslc1/e211819.rslc rslc1/e220336.rslc rslc1/e211819.rpar
        rslc1/e220336.rpar 1
180 e211819 e226348 rslc1/e211819.rslc rslc1/e226348.rslc rslc1/e211819.rpar
        rslc1/e226348.rpar 1
181 e214324 e214825 rslc1/e214324.rslc rslc1/e214825.rslc rslc1/e214324.rpar
        rslc1/e214825.rpar 1

182 e214324 e218833 rslc1/e214324.rslc rslc1/e218833.rslc rslc1/e214324.rpar
        rslc1/e218833.rpar 1
183 e214324 e226849 rslc1/e214324.rslc rslc1/e226849.rslc rslc1/e214324.rpar
        rslc1/e226849.rpar 1
184 e214324 e227851 rslc1/e214324.rslc rslc1/e227851.rslc rslc1/e214324.rpar
        rslc1/e227851.rpar 1
185 e214825 e218332 rslc1/e214825.rslc rslc1/e218332.rslc rslc1/e214825.rpar
        rslc1/e218332.rpar 1
186 e214825 e219835 rslc1/e214825.rslc rslc1/e219835.rslc rslc1/e214825.rpar
        rslc1/e219835.rpar 1
187 e214825 e223342 rslc1/e214825.rslc rslc1/e223342.rslc rslc1/e214825.rpar
        rslc1/e223342.rpar 1
188 e214825 e226849 rslc1/e214825.rslc rslc1/e226849.rslc rslc1/e214825.rpar
        rslc1/e226849.rpar 1
189 e217330 e220336 rslc1/e217330.rslc rslc1/e220336.rslc rslc1/e217330.rpar
        rslc1/e220336.rpar 1
190 e217330 e226348 rslc1/e217330.rslc rslc1/e226348.rslc rslc1/e217330.rpar
        rslc1/e226348.rpar 1
191 e218332 e219835 rslc1/e218332.rslc rslc1/e219835.rslc rslc1/e218332.rpar
        rslc1/e219835.rpar 1
192 e218332 e223342 rslc1/e218332.rslc rslc1/e223342.rslc rslc1/e218332.rpar
        rslc1/e223342.rpar 1
193 e218833 e220336 rslc1/e218833.rslc rslc1/e220336.rslc rslc1/e218833.rpar
        rslc1/e220336.rpar 1
194 e218833 e226348 rslc1/e218833.rslc rslc1/e226348.rslc rslc1/e218833.rpar
        rslc1/e226348.rpar 1
195 e218833 e226849 rslc1/e218833.rslc rslc1/e226849.rslc rslc1/e218833.rpar
        rslc1/e226849.rpar 1
196 e218833 e227851 rslc1/e218833.rslc rslc1/e227851.rslc rslc1/e218833.rpar
        rslc1/e227851.rpar 1
197 e218833 e229354 rslc1/e218833.rslc rslc1/e229354.rslc rslc1/e218833.rpar
        rslc1/e229354.rpar 1
198 e219835 e223342 rslc1/e219835.rslc rslc1/e223342.rslc rslc1/e219835.rpar
        rslc1/e223342.rpar 1
199 e220336 e226348 rslc1/e220336.rslc rslc1/e226348.rslc rslc1/e220336.rpar
        rslc1/e226348.rpar 1
200 e220336 e227851 rslc1/e220336.rslc rslc1/e227851.rslc rslc1/e220336.rpar
        rslc1/e227851.rpar 1
201 e220336 e229354 rslc1/e220336.rslc rslc1/e229354.rslc rslc1/e220336.rpar
        rslc1/e229354.rpar 1
202 e222340 e224344 rslc1/e222340.rslc rslc1/e224344.rslc rslc1/e222340.rpar
        rslc1/e224344.rpar 1
203 e226348 e227851 rslc1/e226348.rslc rslc1/e227851.rslc rslc1/e226348.rpar
        rslc1/e227851.rpar 1
204 e226348 e229354 rslc1/e226348.rslc rslc1/e229354.rslc rslc1/e226348.rpar
        rslc1/e229354.rpar 1

205 e226849 e227851 rslc1/e226849.rslc rslc1/e227851.rslc rslc1/e226849.rpar
        rslc1/e227851.rpar 1
206 e226849 e229354 rslc1/e226849.rslc rslc1/e229354.rslc rslc1/e226849.rpar
        rslc1/e229354.rpar 1
207 e227851 e229354 rslc1/e227851.rslc rslc1/e229354.rslc rslc1/e227851.rpar
        rslc1/e229354.rpar 1

Program: CREATE_OFF
Site: Los Angeles Red Line
Use: Linux shell script to process multiple scenes very quickly
Programmed By: Dr. Francisco Gomez
Comments: This shell script uses the previously created ISP.input, itab, and RSLC_tab files to create a file for the offset estimates to be saved in. Note: the OFF.input file is a placeholder file which contains the number of range samples (20) and number of azimuth samples (50) on the third line, the range window (100) and azimuth window (200) on the fourth line, and the signal to noise threshold on the fifth line (6).
Directory Output: COMMANDS/ and OFF/
Final output: .off files within the OFF/ folder (one file for each interferogram pair)
                 .commands files within the COMMANDS/ folder (one file for each interferogram pair)
Directory in Which Processing was Conducted: /cgi1/insar/socal/15initial/

```bash
#!/bin/bash
#
# Create OFF files
#
# User inputs
if [ $# -lt 7 ]; then
echo "CREATE_OFF <itab> <slc tab> <rn samples> <az samples> <rn window> <az
      window> <snr thresh>"
exit
fi
ITAB=$1
SLCTAB=$2
NR=$3
NAZ=$4
WINR=$5
WINAZ=$6
SNR=$7

INFILE='ISP.input'
#NR=20
#NAZ=40
#WINR=64
#WINAZ=100
#SNR=6

if [ ! -e COMMANDS ]; then mkdir COMMANDS; fi
if [ ! -e OFF ]; then mkdir OFF; fi
```

```
if [ ! -e $INFILE ]; then translate_itab $ITAB $SLCTAB; fi
if [ -e OFF.input ]; then /bin/rm OFF.input; fi

touch OFF.input
echo >> OFF.input
echo >> OFF.input
echo $NR" "$NAZ >> OFF.input
echo $WINR" "$WINAZ >> OFF.input
echo $SNR >> OFF.input
echo >> OFF.input
echo >> OFF.input

while read LINE
do
INTID=`echo $LINE | awk '{print $1}'`
MASTER=`echo $LINE | awk '{print $2}'`
SLAVE=`echo $LINE | awk '{print $3}'`
SLC1=`echo $LINE | awk '{print $4}'`
SLC2=`echo $LINE | awk '{print $5}'`
PAR1=`echo $LINE | awk '{print $6}'`
PAR2=`echo $LINE | awk '{print $7}'`
FLAG=`echo $LINE | awk '{print $8}'`

if [ ! -e COMMANDS/$INTID.commands ]; then touch
        COMMANDS/$INTID.commands; fi

if [ $FLAG = "1" ]; then

echo "create_offset $PAR1 $PAR2 OFF/$INTID.off 1 $RLKS $AZLKS < OFF.input"
        >> COMMANDS/$INTID.commands
echo >> COMMANDS/$INTID.commands
create_offset $PAR1 $PAR2 OFF/$INTID.off 1 $RLKS $AZLKS < OFF.input

fi

done < $INFILE

#Example Output located in the COMMANDS/#.commands file
#create_offset rslc1/e104595.rpar rslc1/e107100.rpar OFF/001.off 1   < OFF.input
```

Program: OFFSET_CALC
Site: Los Angeles Red Line
Use: Linux shell script to process multiple scenes very quickly
Programmed By: Dr. Francisco Gomez
Comments: This shell script uses the previously created ISP.input, itab,
                      RSLC_tab and .off files to place offset estimates into the .off files.
Directory Output: COMMANDS/, OFF/, OFFSET/
Final output: modifies .off files within the OFF/ folder (for each interferogram
                      pair)
                      updates .command files within the COMMANDS/ folder (for each
                      interferogram pair)
                      .snr, .out, and .offset files within the OFFSET/ folder (one for each
                      interferogram pair)
Directory in Which Processing was Conducted: /cgi1/insar/socal/15initial/

```bash
#!/bin/bash
#
# Estimate offsets and the resampling polynomial
#
# User inputs
if [ $# -lt 2 ]; then
echo "OFFSET_CALC <itab> <slc tab>"
exit
fi

ITAB=$1
SLCTAB=$2

INFILE='ISP.input'

if [ ! -e COMMANDS ]; then mkdir COMMANDS; fi
if [ ! -e OFFSET ]; then mkdir OFFSET; fi
if [ ! -e $INFILE ]; then translate_itab $ITAB $SLCTAB; fi

while read LINE
do
INTID=`echo $LINE | awk '{print $1}'`
MASTER=`echo $LINE | awk '{print $2}'`
SLAVE=`echo $LINE | awk '{print $3}'`
SLC1=`echo $LINE | awk '{print $4}'`
SLC2=`echo $LINE | awk '{print $5}'`
PAR1=`echo $LINE | awk '{print $6}'`
PAR2=`echo $LINE | awk '{print $7}'`
FLAG=`echo $LINE | awk '{print $8}'`
```

```
if [ ! -e COMMANDS/$INTID.commands ]; then touch
      COMMANDS/$INTID.commands; fi

if [ $FLAG = "1" ]; then

echo $INTID": "$MASTER"-"$SLAVE":  Calculating Offset"

# For now, assume init_offset is not necessary, as the SLCs have already been
      coregistered once.
#echo "init_offset $SLC1 $SLC2 $PAR1 $PAR2 OFF/$INTID.off 1 1" >>
      COMMANDS/$INTID.commands
#echo >> COMMANDS/$INTID.commands
#init_offset $SLC1 $SLC2 $PAR1 $PAR2 OFF/$INTID.off 1 1

echo "offset_pwr $SLC1 $SLC2 $PAR1 $PAR2 OFF/$INTID.off
      OFFSET/$INTID.offset OFFSET/$INTID.snr > OFFSET/$INTID.out" >>
      COMMANDS/$INTID.commands
echo >> COMMANDS/$INTID.commands
offset_pwr $SLC1 $SLC2 $PAR1 $PAR2 OFF/$INTID.off OFFSET/$INTID.offset
      OFFSET/$INTID.snr > OFFSET/$INTID.out

echo "offset_fit OFFSET/$INTID.offset OFFSET/$INTID.snr OFF/$INTID.off >>
      OFFSET/$INTID.out" >> COMMANDS/$INTID.commands
echo >> COMMANDS/$INTID.commands
offset_fit OFFSET/$INTID.offset OFFSET/$INTID.snr OFF/$INTID.off >>
      OFFSET/$INTID.out

fi

done < $INFILE


#Example Output located in the COMMANDS/#.commands file
#offset_pwr rslc1/e104595.rslc rslc1/e107100.rslc rslc1/e104595.rpar rslc1/e107100.rpar
OFF/001.off OFFSET/001.offset OFFSET/001.snr > OFFSET/001.out

#offset_fit OFFSET/001.offset OFFSET/001.snr OFF/001.off >> OFFSET/001.out
```

Program: INTERF
Site: Los Angeles Red Line
Use: Linux shell script to process multiple scenes very quickly
Programmed By: Dr. Francisco Gomez
Comments: This shell script uses the previously created ISP.input, itab, and
                          RSLC_tab files to create unflattened wrapped interferograms.
Directory Output: COMMANDS/, INT/
Final output: updates .command files within the COMMANDS/ folder (for each
                          interferogram pair)
                          .int files within the INT/ folders (one for each interferogram pair)
Directory in Which Processing was Conducted: /cgi1/insar/socal/15initial/

```bash
#!/bin/bash
#
# Create interferograms
#
# User inputs
if [ $# -lt 2 ]; then
echo "INTERF <itab> <slc tab> <range looks> <azimuth looks>"
exit
fi

ITAB=$1
SLCTAB=$2
RLKS=$3
AZLKS=$4
#RLKS=1
#AZLKS=5

INFILE='ISP.input'

if [ ! -e COMMANDS ]; then mkdir COMMANDS; fi
if [ ! -e INT ]; then mkdir INT; fi
if [ ! -e $INFILE ]; then translate_itab $ITAB $SLCTAB; fi

while read LINE
do
INTID=`echo $LINE | awk '{print $1}'`
MASTER=`echo $LINE | awk '{print $2}'`
SLAVE=`echo $LINE | awk '{print $3}'`
SLC1=`echo $LINE | awk '{print $4}'`
SLC2=`echo $LINE | awk '{print $5}'`
PAR1=`echo $LINE | awk '{print $6}'`
PAR2=`echo $LINE | awk '{print $7}'`
FLAG=`echo $LINE | awk '{print $8}'`
```

```
if [ ! -e COMMANDS/$INTID.commands ]; then touch
COMMANDS/$INTID.commands; fi

if [ $FLAG = "1" ]; then

echo $INTID": "$MASTER"-"$SLAVE":  Interferring"

# Trying to avoid making lots of power images ... hopefully this works
echo "interf_SLC $SLC1 $SLC2 $PAR1 $PAR2 OFF/$INTID.off - - INT/$INTID.int
     $RLKS $AZLKS > INT/$INTID.out " >> COMMANDS/$INTID.commands
echo >> COMMANDS/$INTID.commands
interf_SLC $SLC1 $SLC2 $PAR1 $PAR2 OFF/$INTID.off - - INT/$INTID.int $RLKS
       $AZLKS > INT/$INTID.out

fi

done < $INFILE


#Example Output located in the COMMANDS/#.commands file
interf_SLC rslc1/e104595.rslc rslc1/e107100.rslc rslc1/e104595.rpar rslc1/e107100.rpar
OFF/001.off - - INT/001.int 1 5 > INT/001.out
```

Program: BASEFLAT
Site: Los Angeles Red Line
Use: Linux shell script to process multiple scenes very quickly
Programmed By: Dr. Francisco Gomez
Comments: This shell script uses the previously created ISP.input, itab,
                    RSLC_tab, hgt_map, and geo_par files to estimate baselines and
                    create flattened wrapped interferograms.
Directory Output: COMMANDS/, BASE/, SIM/, INT/
Final output: updates .command files within the COMMANDS/ folder (for each
                    interferogram pair)
                    .base files within the BASE/ folder (for each interferogram pair)
                    .sim_unw files within the SIM/ folder (for each interferogram pair)
                    .int_notopo files within the INT/ folder (for each interferogram
                    pair)
Directory in Which Processing was Conducted: /cgi1/insar/socal/15initial/


```bash
#!/bin/bash
#
# Estimate baseline, flatten, and filter
#
# User inputs
if [ $# -lt 2 ]; then
echo "BASEFLAT <itab> <slc tab> <hgt map> <diff/geo par>"
exit
fi

ITAB=$1
SLCTAB=$2
HGT=$3
GEOPAR=$4
#HGT='hgt_map'
#GEOPAR='geo_par'
INFILE='ISP.input'

if [ ! -e COMMANDS ]; then mkdir COMMANDS; fi
if [ ! -e BASE ]; then mkdir BASE; fi
if [ ! -e SIM ]; then mkdir SIM; fi
if [ ! -e $INFILE ]; then translate_itab $ITAB $SLCTAB; fi

while read LINE
do
INTID=`echo $LINE | awk '{print $1}'`
MASTER=`echo $LINE | awk '{print $2}'`
SLAVE=`echo $LINE | awk '{print $3}'`
SLC1=`echo $LINE | awk '{print $4}'`
SLC2=`echo $LINE | awk '{print $5}'`
```

272

```
PAR1=`echo $LINE | awk '{print $6}'`
PAR2=`echo $LINE | awk '{print $7}'`
FLAG=`echo $LINE | awk '{print $8}'`

if [ ! -e COMMANDS/$INTID.commands ]; then touch
COMMANDS/$INTID.commands; fi

if [ $FLAG = "1" ]; then

echo $INTID": "$MASTER"-"$SLAVE":  Flattening"

# Estimate baseline using orbits
echo "base_init $PAR1 $PAR2 OFF/$INTID.off INT/$INTID.int BASE/$INTID.base 0
      > BASE/$INTID.baseout" >> COMMANDS/$INTID.commands
echo >> COMMANDS/$INTID.commands
base_init $PAR1 $PAR2 OFF/$INTID.off INT/$INTID.int BASE/$INTID.base 0 >
      BASE/$INTID.baseout

echo "phase_sim $PAR1 OFF/$INTID.off BASE/$INTID.base $HGT
      SIM/$INTID.sim_unw 0 0 > SIM/$INTID.simout" >>
      COMMANDS/$INTID.commands
echo >> COMMANDS/$INTID.commands
phase_sim $PAR1 OFF/$INTID.off BASE/$INTID.base $HGT SIM/$INTID.sim_unw 0
      0 > SIM/$INTID.simout

echo "sub_phase INT/$INTID.int SIM/$INTID.sim_unw $GEOPAR
      INT/$INTID.int_notopo 1 0 > temp.out" >> COMMANDS/$INTID.commands
echo >> COMMANDS/$INTID.commands
sub_phase INT/$INTID.int SIM/$INTID.sim_unw $GEOPAR INT/$INTID.int_notopo 1
      0 > temp.out

fi

done < $INFILE


#Example Output located in the COMMANDS/#.commands file
#base_init rslc1/e104595.rpar rslc1/e107100.rpar OFF/001.off INT/001.int
      BASE/001.base 0 > BASE/001.baseout
#phase_sim rslc1/e104595.rpar OFF/001.off BASE/001.base hgt_map SIM/001.sim_unw
      0 0 > SIM/001.simout
#sub_phase INT/001.int SIM/001.sim_unw geo_par INT/001.int_notopo 1 0 > temp.out
```

Program: mk_mli_all
Site: Los Angeles Red Line
Use: Linux shell script to process multiple scenes very quickly
Programmed By: GAMMA Remote Sensing
Comments: This shell script uses the previously created RSLC_tab, to create
                     multi-looked intensity images.
Directory Output: mli/
Final output: updates .command files within the COMMANDS/ folder (for each
                     interferogram pair)
                     .mli files within the mli/ folder (for each RSLC image)
Directory in Which Processing was Conducted: /cgi1/insar/socal/15initial/

Syntax: mk_mli_all <SLC_tab> <MLI_dir> <rlks> <azlks> [sflag] [scale] [exp] [exp2

Example: mk_mli_all RSLC_tab mli 1 5

Program: FILTER
Site: Los Angeles Red Line
Use: Linux shell script to process multiple scenes very quickly
Programmed By: Dr. Francisco Gomez
Comments: This shell script uses the previously created ISP.input, itab,
                      .int_notopo files to create flattened, filtered, wrapped
                      interferograms, and to generate coherence masks.
Directory Output: COMMANDS/, SM_NOTOPO/
Final output: updates .command files within the COMMANDS/ folder (for each
                      interferogram pair)
                      .sm_notopo files within the SM_NOTOPO/ folder (for each
                      interferogram pair)
                      .cc files within the SM_NOTOPO/ folder (for each interferogram
                      pair)
Directory in Which Processing was Conducted: /cgi1/insar/socal/15initial/

```bash
#!/bin/bash
#
# Filter (flag=0 --> adf; flag=1 --> adapt_filt)
#
# User inputs
if [ $# -lt 3 ]; then
echo "FILTER <itab> <slc tab> <filter flag: 0=adf, 1=adapt_filt> <filter size>"
exit
fi

ITAB=$1
SLCTAB=$2
FILTFLAG=$3
FILTSIZE=$4
#FILTFLAG=0
INFILE='ISP.input'

if [ ! -e COMMANDS ]; then mkdir COMMANDS; fi
if [ ! -e SM_NOTOPO ]; then mkdir SM_NOTOPO; fi
if [ ! -e $INFILE ]; then translate_itab $ITAB $SLCTAB; fi

while read LINE
do
INTID=`echo $LINE | awk '{print $1}'`
MASTER=`echo $LINE | awk '{print $2}'`
SLAVE=`echo $LINE | awk '{print $3}'`
SLC1=`echo $LINE | awk '{print $4}'`
SLC2=`echo $LINE | awk '{print $5}'`
PAR1=`echo $LINE | awk '{print $6}'`
PAR2=`echo $LINE | awk '{print $7}'`
FLAG=`echo $LINE | awk '{print $8}'`
```

```
WIDTH=`grep interferogram_width OFF/$INTID.off | awk '{print $2}'`

if [ ! -e COMMANDS/$INTID.commands ]; then touch
        COMMANDS/$INTID.commands; fi

if [ $FLAG = "1" ]; then

echo $INTID": "$MASTER"-"$SLAVE":  Filtering"

if [ $FILTFLAG != 1 ]; then
echo "adf INT/$INTID.int_notopo SM_NOTOPO/$INTID.sm_notopo
        SM_NOTOPO/$INTID.cc $WIDTH 0.5 "$FILTSIZE" - - - - 0.25" >>
        COMMANDS/$INTID.commands
echo >> COMMANDS/$INTID.commands
adf INT/$INTID.int_notopo SM_NOTOPO/$INTID.sm_notopo
        SM_NOTOPO/$INTID.cc $WIDTH 0.5 $FILTSIZE - - - - 0.25 > temp.out
else
echo "adapt_filt INT/$INTID.int_notopo SM_NOTOPO/$INTID.sm_notopo $WIDTH
        0.25  $FILTSIZE" >> COMMANDS/$INTID.commands
echo >> COMMANDS/$INTID.commands
adapt_filt INT/$INTID.int_notopo SM_NOTOPO/$INTID.sm_notopo $WIDTH 0.25
        $FILTSIZE > SM_NOTOPO/$INTIT.adapt_filt.out
echo "cc_wave INT/$INTID.int_notopo mli/$MASTER.rmli mli/$SLAVE.rmli
        SM_NOTOPO/$INTID.cc $WIDTH" >> COMMANDS/$INTID.commands
echo >> COMMANDS/$INTID.commands
cc_wave INT/$INTID.int_notopo mli/$MASTER.rmli mli/$SLAVE.rmli
        SM_NOTOPO/$INTID.cc $WIDTH > temp.out
fi

fi

done < $INFILE

#Example Output located in the COMMANDS/#.commands file
#adf INT/001.int_notopo SM_NOTOPO/001.sm_notopo SM_NOTOPO/001.cc 1000 0.5
        8 - - - - 0.25
```

Program: RASMPH
Site: Los Angeles Red Line
Use: Linux shell script to process multiple scenes very quickly
Programmed By: Dr. Francisco Gomez
Comments: This shell script uses the previously created ISP.input, itab,
       RSLC_tab, and .sm_notopo files to create raster images of the
       flattened, filtered, wrapped interferograms
Directory Output: SM_NOTOPO/
Final output: .sm_notopo.ras files within the SM_NOTOPO/ folder (for each
       interferogram pair)
Directory in Which Processing was Conducted: /cgi1/insar/socal/15initial/

```
#!/bin/bash
#
# Create raster images from wrapped phase and power images
#
# User inputs
if [ $# -lt 5 ]; then
echo "RAS_MPH <itab> <slc tab> <in dir> <out dir> <suffix>"
exit
fi

ITAB=$1
SLCTAB=$2
INDIR=$3
OUTDIR=$4
SUFFIX=$5
INFILE='ISP.input'

if [ ! -e COMMANDS ]; then mkdir COMMANDS; fi
if [ ! -e $OUTDIR ]; then mkdir $OUTDIR; fi
if [ ! -e $INFILE ]; then ./translate_itab itab RSLC_tab; fi

while read LINE
do
INTID=`echo $LINE | awk '{print $1}'`
MASTER=`echo $LINE | awk '{print $2}'`
SLAVE=`echo $LINE | awk '{print $3}'`
SLC1=`echo $LINE | awk '{print $4}'`
SLC2=`echo $LINE | awk '{print $5}'`
PAR1=`echo $LINE | awk '{print $6}'`
PAR2=`echo $LINE | awk '{print $7}'`

WIDTH=`grep interferogram_width OFF/$INTID.off | awk '{print $2}'`
```

```
if [ ! -e COMMANDS/$INTID.commands ]; then touch
COMMANDS/$INTID.commands; fi

echo $INTID": "$MASTER"-"$SLAVE

if [ -e $INDIR/$INTID.$SUFFIX ]; then
rasmph $INDIR/$INTID.$SUFFIX $WIDTH - - - - - - - $OUTDIR/$INTID.$SUFFIX.ras
fi

done < $INFILE

#Example:
#rasmph SM_NOTOPO/001.sm_notopo 1000 - - - - - - - SMRAS/001.sm_notopo.ras
```

Program:	UNWRAPPER
Site:	Los Angeles Red Line
Use:	Linux shell script to process multiple scenes very quickly
Programmed By:	Dr. Francisco Gomez
Comments:	This shell script uses the previously created ISP.input, itab, RSLC_tab, .sm_notopo, .cc, .rmli, and .cc_mask.ras files to create raster images of coherence masks and unwrapped, flattened interferograms
Directory Output:	COMMANDS/, UNW/
Final output:	.cc_mask.ras files within the UNW/ folder (for each interferogram pair)
	.unw files within the UNW/ folder (for each interferogram pair)

Directory in Which Processing was Conducted: /cgi1/insar/socal/15initial/

```bash
#!/bin/bash
#
# Unwrap
#
# User inputs
if [ $# -lt 2 ]; then
echo "UNWRAPPER <itab> <slc tab> <cc thresh>"
exit
fi

ITAB=$1
SLCTAB=$2
CCTHRESH=$3
#CCTHRESH=50
INFILE='ISP.input'

if [ ! -e COMMANDS ]; then mkdir COMMANDS; fi
if [ ! -e UNW ]; then mkdir UNW; fi
if [ ! -e $INFILE ]; then translate_itab $ITAB $SLCTAB; fi

while read LINE
do
INTID=`echo $LINE | awk '{print $1}'`
MASTER=`echo $LINE | awk '{print $2}'`
SLAVE=`echo $LINE | awk '{print $3}'`
SLC1=`echo $LINE | awk '{print $4}'`
SLC2=`echo $LINE | awk '{print $5}'`
PAR1=`echo $LINE | awk '{print $6}'`
PAR2=`echo $LINE | awk '{print $7}'`
FLAG=`echo $LINE | awk '{print $8}'`

WIDTH=`grep interferogram_width OFF/$INTID.off | awk '{print $2}'`
```

```
if [ ! -e COMMANDS/$INTID.commands ]; then touch
COMMANDS/$INTID.commands; fi

if [ $FLAG = "1" ]; then

echo $INTID": "$MASTER"-"$SLAVE":  Unwrapping"

echo "rascc_mask SM_NOTOPO/$INTID.cc mli/$MASTER.rmli $WIDTH - - - - -
0.$CCTHRESH - - - - - UNW/$INTID.cc_mask.$CCTHRESH.ras" >>
COMMANDS/$INTID.commands
echo >> COMMANDS/$INTID.commands
rascc_mask SM_NOTOPO/$INTID.cc mli/$MASTER.rmli $WIDTH - - - - -
0.$CCTHRESH - - - - - UNW/$INTID.cc_mask.$CCTHRESH.ras > temp.out

echo "mcf SM_NOTOPO/$INTID.sm_notopo SM_NOTOPO/$INTID.cc
UNW/$INTID.cc_mask.$CCTHRESH.ras UNW/$INTID.unw $WIDTH 0 - - - - 1 1 - - -
0" >> COMMANDS/$INTID.commands
echo >> COMMANDS/$INTID.commands
mcf SM_NOTOPO/$INTID.sm_notopo SM_NOTOPO/$INTID.cc
UNW/$INTID.cc_mask.$CCTHRESH.ras UNW/$INTID.unw $WIDTH 0 - - - - 1 1 - - -
0 > temp.out

fi

done < $INFILE

#Example Output located in the COMMANDS/#.commands file
#rascc_mask SM_NOTOPO/001.cc mli/e104595.rmli 1000 - - - - - 0.50 - - - - -
UNW/001.cc_mask.50.ras

#mcf SM_NOTOPO/001.sm_notopo SM_NOTOPO/001.cc UNW/001.cc_mask.50.ras
UNW/001.unw 1000 0 - - - - 1 1 - - - 0
```

Program:	BASEREFINE
Site:	Los Angeles Red Line
Use:	Linux shell script to process multiple scenes very quickly
Programmed By:	Dr. Francisco Gomez
Comments:	This shell script uses the previously created ISP.input, itab, RSLC_tab, hgt_map, and geo_par files to add simulated phase to the unwrapped, flattened interferograms, extract ground control points, and the phase of ground control points, refine the baselines using the ground control point phase values, resimulate the topographic phase, and subtract the resimulated topographic phase to create unwrapped, flattened differential interferograms
Directory Output:	COMMANDS/, UNW/, GCP/, BASE/, SIM/,
Final output:	.unw_noflat files within the UNW/ folder (for each interferogram pair)
	.gcp files within the GCP/ folder (for each interferogram pair)
	updated .off files within the OFF/ folder (for each interferogram pair)
	.updated .base files within the BASE/ folder for each interferogram pair)
	.sim_unw2 files within the SIM/folder (for each interferogram pair)
	.unw_dif files within the UNW/ folder (for each interferogram pair)

Directory in Which Processing was Conducted: /cgi1/insar/socal/15initial/

```bash
#!/bin/bash
#
# Refine baseline and re-flatten
#
# User inputs
if [ $# -lt 6 ]; then
echo "BASEREFINE <itab> <slc tab> <hgt map> <diff/geo par> <rn samples> <az
samples>"
exit
fi

ITAB=$1
SLCTAB=$2
HGT=$3
GEOPAR=$4
NR=$5
NAZ=$6
#HGT='hgt_map'
#GEOPAR='geo_par'
INFILE='ISP.input'
```

```
if [ ! -e COMMANDS ]; then mkdir COMMANDS; fi
if [ ! -e GCP ]; then mkdir GCP; fi
if [ ! -e BASE ]; then mkdir BASE; fi
if [ ! -e SIM ]; then mkdir SIM; fi
if [ ! -e $INFILE ]; then translate_itab $ITAB $SLCTAB; fi

while read LINE
do
INTID=`echo $LINE | awk '{print $1}'`
MASTER=`echo $LINE | awk '{print $2}'`
SLAVE=`echo $LINE | awk '{print $3}'`
SLC1=`echo $LINE | awk '{print $4}'`
SLC2=`echo $LINE | awk '{print $5}'`
PAR1=`echo $LINE | awk '{print $6}'`
PAR2=`echo $LINE | awk '{print $7}'`
FLAG=`echo $LINE | awk '{print $8}'`

if [ ! -e COMMANDS/$INTID.commands ]; then touch
COMMANDS/$INTID.commands; fi

if [ $FLAG = "1" ]; then

echo $INTID": "$MASTER"-"$SLAVE":  Re-flattening"

echo "sub_phase UNW/$INTID.unw SIM/$INTID.sim_unw $GEOPAR
UNW/$INTID.unw_noflat 0 1" >> COMMANDS/$INTID.commands
echo >> COMMANDS/$INTID.commands
sub_phase UNW/$INTID.unw SIM/$INTID.sim_unw $GEOPAR
UNW/$INTID.unw_noflat 0 1 > temp.out

echo "extract_gcp $HGT OFF/$INTID.off GCP/$INTID.gcp $NR $NAZ" >>
COMMANDS/$INTID.commands
echo >> COMMANDS/$INTID.commands
extract_gcp $HGT OFF/$INTID.off GCP/$INTID.gcp $NR $NAZ > temp.out

echo "gcp_phase UNW/$INTID.unw_noflat OFF/$INTID.off GCP/$INTID.gcp
GCP/$INTID.gcp_data 3" >> COMMANDS/$INTID.commands
echo >> COMMANDS/$INTID.commands
gcp_phase UNW/$INTID.unw_noflat OFF/$INTID.off GCP/$INTID.gcp
GCP/$INTID.gcp_data 3 > temp.out

echo "base_ls $PAR1 OFF/$INTID.off GCP/$INTID.gcp_data BASE/$INTID.base 0 1 1
1 1 5" >> COMMANDS/$INTID.commands
echo >> COMMANDS/$INTID.commands
base_ls $PAR1 OFF/$INTID.off GCP/$INTID.gcp_data BASE/$INTID.base 0 1 1 1 1 5
> BASE/$INTID.basels_out
```

```
echo "phase_sim $PAR1 OFF/$INTID.off BASE/$INTID.base $HGT
SIM/$INTID.sim_unw2 0 1" >> COMMANDS/$INTID.commands
echo >> COMMANDS/$INTID.commands
phase_sim $PAR1 OFF/$INTID.off BASE/$INTID.base $HGT SIM/$INTID.sim_unw2
0 1 > SIM/$INTID.simout2

echo "sub_phase UNW/$INTID.unw_noflat SIM/$INTID.sim_unw2 $GEOPAR
UNW/$INTID.unw_dif 0 0" >> COMMANDS/$INTID.commands
echo >> COMMANDS/$INTID.commands
sub_phase UNW/$INTID.unw_noflat SIM/$INTID.sim_unw2 $GEOPAR
UNW/$INTID.unw_dif 0 0 > temp.out

fi

done < $INFILE

#Example Output located in the COMMANDS/#.commands file
#sub_phase UNW/001.unw SIM/001.sim_unw geo_par UNW/001.unw_noflat 0 1

#extract_gcp hgt_map OFF/001.off GCP/001.gcp 50 100

#gcp_phase UNW/001.unw_noflat OFF/001.off GCP/001.gcp GCP/001.gcp_data 3

#base_ls rslc1/e104595.rpar OFF/001.off GCP/001.gcp_data BASE/001.base 0 1 1 1 1 5

#phase_sim rslc1/e104595.rpar OFF/001.off BASE/001.base hgt_map
SIM/001.sim_unw2 0 1

#sub_phase UNW/001.unw_noflat SIM/001.sim_unw2 geo_par UNW/001.unw_dif 0 0
```

Program: RASRMG
Site: Los Angeles Red Line
Use: Linux shell script to process multiple scenes very quickly
Programmed By: Dr. Francisco Gomez
Comments: This shell script uses the previously created ISP.input, itab,
                 RSLC_tab, and .unw_dif files to create raster images of the
                 flattened, filtered, unwrapped differential interferograms
Directory Output: UNWRAS/
Final output: .unw_dif.ras files within the UNWRAS/ folder (for each
                 interferogram pair)
Directory in Which Processing was Conducted: /cgi1/insar/socal/15initial/

```bash
#!/bin/bash
#
# Create raster images from unwrapped phase and power images
#
# User inputs
if [ $# -lt 6 ]; then
echo "RAS_RMG <itab> <slc tab> <in dir> <out dir> <suffix> <phase scale> <cc
thresh>"
exit
fi

ITAB=$1
SLCTAB=$2
INDIR=$3
OUTDIR=$4
SUFFIX=$5
PHSCALE=$6
CCTHRESH=$7
INFILE='ISP.input'

if [ ! -e COMMANDS ]; then mkdir COMMANDS; fi
if [ ! -e $OUTDIR ]; then mkdir $OUTDIR; fi
if [ ! -e $INFILE ]; then ./translate_itab itab RSLC_tab; fi

while read LINE
do
INTID=`echo $LINE | awk '{print $1}'`
MASTER=`echo $LINE | awk '{print $2}'`
SLAVE=`echo $LINE | awk '{print $3}'`
SLC1=`echo $LINE | awk '{print $4}'`
SLC2=`echo $LINE | awk '{print $5}'`
PAR1=`echo $LINE | awk '{print $6}'`
PAR2=`echo $LINE | awk '{print $7}'`
```

```
WIDTH=`grep interferogram_width OFF/$INTID.off | awk '{print $2}'`

if [ ! -e COMMANDS/$INTID.commands ]; then touch
COMMANDS/$INTID.commands; fi

echo $INTID": "$MASTER"-"$SLAVE

if [ -e $INDIR/$INTID.$SUFFIX ]; then
rasrmg $INDIR/$INTID.$SUFFIX mli/$MASTER.rmli $WIDTH - - - - - $PHSCALE - -
- - $OUTDIR/$INTID.$SUFFIX.ras SM_NOTOPO/$INTID.cc - $CCTHRESH
fi

done < $INFILE

#Example:
#rasrmg UNW/001.unw_dif mli/e104595.rmli 1000 - - - - - 1 - - - -
UNWRAS/001.unw_dif.ras SM_NOTOPO/001.cc - 0.2
```

Program:	reunwrap_commands.txt
Site:	Los Angeles Red Line
Use:	Linux shell script to process multiple scenes very quickly
Programmed By:	Richard Coffman
Comments:	This shell script creates folders to do varying versions of filter, filter size, and coherence mask by using the previously created ISP.input, itab, RSLC_tab, hgt_map, geo_par, .off, .int, .sim_unw2, and .mli files to subtract the simulated unwrapped phase to flatten the interferograms, filter the interferogram, and creates a coherence mask, then unwrap the flattened interferograms to produce flattened, unwrapped, differential interferograms
Directory Output:	COMMANDS/, INT/, SM_NOTOPO/, UNW/
Final output:	.int_notopo2 files within the INT/ folder (for each interferogram pair)
	.sm_notopo2 files within the SM_NOTOPO/ folder (for each interferogram pair)
	.cc2 within fiels the SM_NOTOPO/ folder (for each interferogram pair)
	.cc_mask.ras files within the UNW/ folder (for each interferogram pair)
	.unw_dif files within the UNW/ folder (for each interferogram pair)

Directory in Which Processing was Conducted: /cgi1/insar/socal/12015/

#This processing code is to be used to conducted processing in folders of type 12015
#First number = flag for type of filter (0=adf, 1=slope adaptive)
#Second number = filter size (8, 16, 32 for adf), (2,4,8 for slope adaptive)
#Third number = coherence threshold (as percentage) (0, 20, 50, etc.) (eg. 0,2,5)
#Fourth number = number of looks in the range direction (1, 2)
#Fifth number = number of looks in the azimuth direction (5, 10)

mkdir 12015
cd 12015
#Copy the following files from /cgi1/insar/socal/15initial into the new folder 12015
cp /cgi1/insar/socal/15initial/reunwrap_commands.txt .
cp -r /cgi1/insar/socal/15initial/OFF .
cp -r /cgi1/insar/socal/15initial/COMMANDS .
cp /cgi1/insar/socal/15initial/itab .
cp /cgi1/insar/socal/15initial/RSLC_tab .
ln -s ../reprocess/hgt_map
ln -s ../reprocess/geo_par

mkdir mli
cd mli
cp /cgi1/insar/socal/15initial/symbolic_links_mli.sh .
sh symbolic_links_mli.sh

cp /cgi1/insar/socal/15initial/symbolic_links_mli.par.sh .
sh symbolic_links_mli.par.sh
ln -s /cgi1/insar/socal/15initial/mli/rmli_1_5.ave
ln -s /cgi1/insar/socal/15initial/mli/rmli_1_5.ave.ras
cd ../

mkdir INT
cd INT
cp /cgi1/insar/socal/15initial/symbolic_links_int.sh .
sh symbolic_links_int.sh
cd ../

mkdir SIM
cd SIM
cp /cgi1/insar/socal/15initial/symbolic_links_sim.sh .
sh symbolic_links_sim.sh
cd ../

mkdir SM_NOTOPO
mkdir UNW
mkdir UNWRAS
ln -s /cgi1/insar/socal/15initial/ISP.input

REUNWRAP itab RSLC_tab geo_par 1 2 0

#In the SM_NOTOPO directory run the following
cd SM_NOTOPO
cp /cgi1/insar/socal/15initial/SM_NOTOPO/shell.sh .
sh shell.sh
gedit shell.txt
#Find and replace cc/1 with cc and save the file
sh shell.txt
cd ../pwd

RASRMG itab RSLC_tab UNW UNWRAS unw_dif2 1 0.2

#Now STACK or do mb, or both
mkdir STACK
cd STACK
#Note diff_tab_eq_weight1 contains all of the pairs before 1/1996
cp /cgi1/insar/socal/15initial/STACK/diff_tab_eq_weight1 .
gedit diff_tab_eq_weight1
#Find and replace _dif with _dif2
#Save diff_tab_eq_weight1
cp /cgi1/insar/socal/15initial/STACK/stacking_commands_1.txt .

#Note: diff_tab_eq_weight2 contains all of the pairs before 1/1996 which cross the time of construction i.e. the first SLC is <5 and the second SLC is >6
cp /cgi1/insar/socal/15initial/STACK/diff_tab_eq_weight2 .
gedit diff_tab_eq_weight2
#Find and replace _dif with _dif2
#Save diff_tab_eq_weight2
cp /cgi1/insar/socal/15initial/STACK/stacking_commands_2.txt .
#Run the first three commands (stacking, rasrmg, gimp) from the stacking_commands files
cd ../

mkdir mb
cd mb
cp /cgi1/insar/socal/15initial/mb/mb_commands.txt .
gedit mb_commands.txt
#run the commands in mb_commands.txt

#Example Output located in the COMMANDS/#.commands file
#sub_phase INT/001.int SIM/001.sim_unw2 geo_par INT/001.int_notopo2 1 0 > temp.out

#adapt_filt INT/001.int_notopo2 SM_NOTOPO/001.sm_notopo2 1000 0.25 2

#cc_wave INT/001.int_notopo2 mli/e104595.rmli mli/e107100.rmli SM_NOTOPO/001.cc2 1000

#rascc_mask SM_NOTOPO/001.cc2 mli/e104595.rmli 1000 - - - - - 0.0 - - - - - UNW/001.cc_mask.0.ras

#mcf SM_NOTOPO/001.sm_notopo2 SM_NOTOPO/001.cc2 UNW/001.cc_mask.0.ras UNW/001.unw_dif2 1000 0 - - - - 1 1 - - - 0

Program:	REUNWRAP
Site:	Los Angeles Red Line
Use:	Linux shell script to process multiple scenes very quickly
Programmed By:	Dr. Francisco Gomez
Comments:	This shell script uses the previously created ISP.input, itab, RSLC_tab, hgt_map, geo_par, .off, .int, .sim_unw2, and .mli files to subtract the simulated unwrapped phase to flatten the interferograms, filter the interferogram, and creates a coherence mask, then unwrap the flattened interferograms to produce flattened, unwrapped, differential interferograms
Directory Output:	COMMANDS/, INT/, SM_NOTOPO/, UNW/
Final output:	.int_notopo2 files within the INT/ folder (for each interferogram pair)
	.sm_notopo2 files within the SM_NOTOPO/ folder (for each interferogram pair)
	.cc2 within fiels the SM_NOTOPO/ folder (for each interferogram pair)
	.cc_mask.ras files within the UNW/ folder (for each interferogram pair)
	.unw_dif files within the UNW/ folder (for each interferogram pair)

Directory in Which Processing was Conducted: /cgi1/insar/socal/12015/

```
#!/bin/bash
#
# Use precision baseline and re-run: flatten, filter, unwrap.
# This assumes you have already run BASEREFINE and generated the *.sim_unw2 files.
#
# User inputs
if [ $# -lt 5 ]; then
echo "REUNWRAP <itab> <slc tab> <diff/geo par> <filter flag: 0=adf, 1=adapt_filt>
<filter size> <cc thresh>"
exit
fi

ITAB=$1
SLCTAB=$2
GEOPAR=$3
FILTFLAG=$4
FILTSIZE=$5
CCTHRESH=$6
#FILTFLAG=0
INFILE='ISP.input'

if [ ! -e COMMANDS ]; then mkdir COMMANDS; fi
if [ ! -e SM_NOTOPO ]; then mkdir SM_NOTOPO; fi
```

```
if [ ! -e $INFILE ]; then translate_itab $ITAB $SLCTAB; fi


#
### FLATTEN
#

while read LINE
do
INTID=`echo $LINE | awk '{print $1}'`
MASTER=`echo $LINE | awk '{print $2}'`
SLAVE=`echo $LINE | awk '{print $3}'`
SLC1=`echo $LINE | awk '{print $4}'`
SLC2=`echo $LINE | awk '{print $5}'`
PAR1=`echo $LINE | awk '{print $6}'`
PAR2=`echo $LINE | awk '{print $7}'`
FLAG=`echo $LINE | awk '{print $8}'`

if [ ! -e COMMANDS/$INTID.commands ]; then touch
COMMANDS/$INTID.commands; fi

if [ $FLAG = "1" ]; then

echo $INTID": "$MASTER"-"$SLAVE": Flattening"

echo "sub_phase INT/$INTID.int SIM/$INTID.sim_unw2 $GEOPAR
INT/$INTID.int_notopo2 1 0 > temp.out" >> COMMANDS/$INTID.commands
echo >> COMMANDS/$INTID.commands
sub_phase INT/$INTID.int SIM/$INTID.sim_unw2 $GEOPAR
INT/$INTID.int_notopo2 1 0 > temp.out

fi

done < $INFILE

#
### FILTER
#

while read LINE
do
INTID=`echo $LINE | awk '{print $1}'`
MASTER=`echo $LINE | awk '{print $2}'`
SLAVE=`echo $LINE | awk '{print $3}'`
SLC1=`echo $LINE | awk '{print $4}'`
SLC2=`echo $LINE | awk '{print $5}'`
```

```
PAR1=`echo $LINE | awk '{print $6}'`
PAR2=`echo $LINE | awk '{print $7}'`

WIDTH=`grep interferogram_width OFF/$INTID.off | awk '{print $2}'`

if [ ! -e COMMANDS/$INTID.commands ]; then touch
COMMANDS/$INTID.commands; fi

if [ $FLAG = "1" ]; then

echo $INTID": "$MASTER"-"$SLAVE": Filtering"

if [ $FILTFLAG != 1 ]; then
echo "adf INT/$INTID.int_notopo2 SM_NOTOPO/$INTID.sm_notopo2
SM_NOTOPO/$INTID.cc2 $WIDTH 0.5 "$FILTSIZE" - - - - 0.25" >>
COMMANDS/$INTID.commands
echo >> COMMANDS/$INTID.commands
adf INT/$INTID.int_notopo2 SM_NOTOPO/$INTID.sm_notopo2
SM_NOTOPO/$INTID.cc2 $WIDTH 0.5 $FILTSIZE - - - - 0.25 > temp.out
else
echo "adapt_filt INT/$INTID.int_notopo2 SM_NOTOPO/$INTID.sm_notopo2 $WIDTH
0.25  $FILTSIZE" >> COMMANDS/$INTID.commands
echo >> COMMANDS/$INTID.commands
adapt_filt INT/$INTID.int_notopo2 SM_NOTOPO/$INTID.sm_notopo2 $WIDTH 0.25
$FILTSIZE > SM_NOTOPO/$INTIT.adapt_filt.out
echo "cc_wave INT/$INTID.int_notopo2 mli/$MASTER.rmli mli/$SLAVE.rmli
SM_NOTOPO/$INTID.cc2 $WIDTH" >> COMMANDS/$INTID.commands
echo >> COMMANDS/$INTID.commands
cc_wave INT/$INTID.int_notopo2 mli/$MASTER.rmli mli/$SLAVE.rmli
SM_NOTOPO/$INTID.cc2 $WIDTH > temp.out
fi

fi

done < $INFILE

#
### UNWRAP
#

while read LINE
do
INTID=`echo $LINE | awk '{print $1}'`
MASTER=`echo $LINE | awk '{print $2}'`
SLAVE=`echo $LINE | awk '{print $3}'`
SLC1=`echo $LINE | awk '{print $4}'`
```

```
SLC2=`echo $LINE | awk '{print $5}'`
PAR1=`echo $LINE | awk '{print $6}'`
PAR2=`echo $LINE | awk '{print $7}'`

WIDTH=`grep interferogram_width OFF/$INTID.off | awk '{print $2}'`

if [ ! -e COMMANDS/$INTID.commands ]; then touch
COMMANDS/$INTID.commands; fi

if [ $FLAG = "1" ]; then

echo $INTID": "$MASTER"-"$SLAVE": Unwrapping"

echo "rascc_mask SM_NOTOPO/$INTID.cc2 mli/$MASTER.rmli $WIDTH - - - - -
0.$CCTHRESH - - - - - UNW/$INTID.cc_mask.$CCTHRESH.ras" >>
COMMANDS/$INTID.commands
echo >> COMMANDS/$INTID.commands
rascc_mask SM_NOTOPO/$INTID.cc2 mli/$MASTER.rmli $WIDTH - - - - -
0.$CCTHRESH - - - - - UNW/$INTID.cc_mask.$CCTHRESH.ras > temp.out

echo "mcf SM_NOTOPO/$INTID.sm_notopo2 SM_NOTOPO/$INTID.cc2
UNW/$INTID.cc_mask.$CCTHRESH.ras UNW/$INTID.unw_dif2 $WIDTH 0 - - - - 1 1
- - - 0" >> COMMANDS/$INTID.commands
echo >> COMMANDS/$INTID.commands
mcf SM_NOTOPO/$INTID.sm_notopo2 SM_NOTOPO/$INTID.cc2
UNW/$INTID.cc_mask.$CCTHRESH.ras UNW/$INTID.unw_dif2 $WIDTH 0 - - - - 1 1
- - - 0 > temp.out

fi

done < $INFILE
```
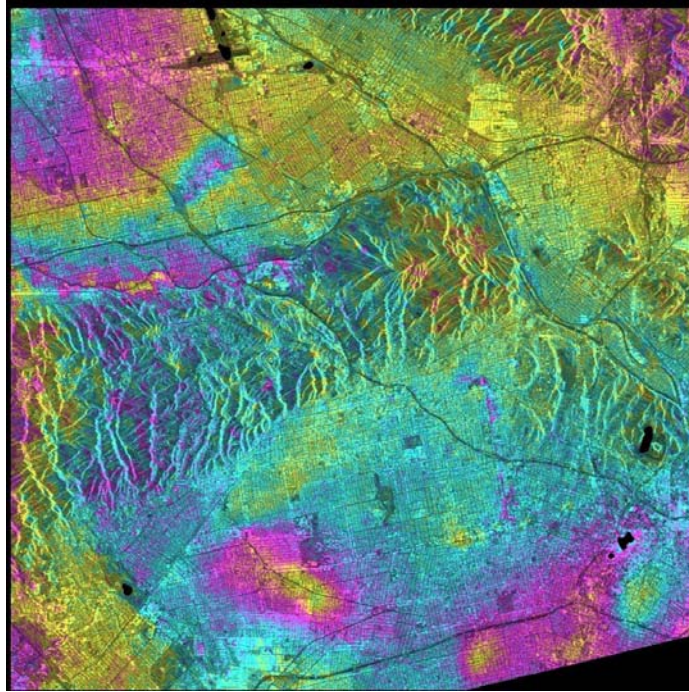
Figure B. 1. Slope Adaptive Filter, Window Size 2, 0% Coherence Mask, 1 and 5 Multi-looking.
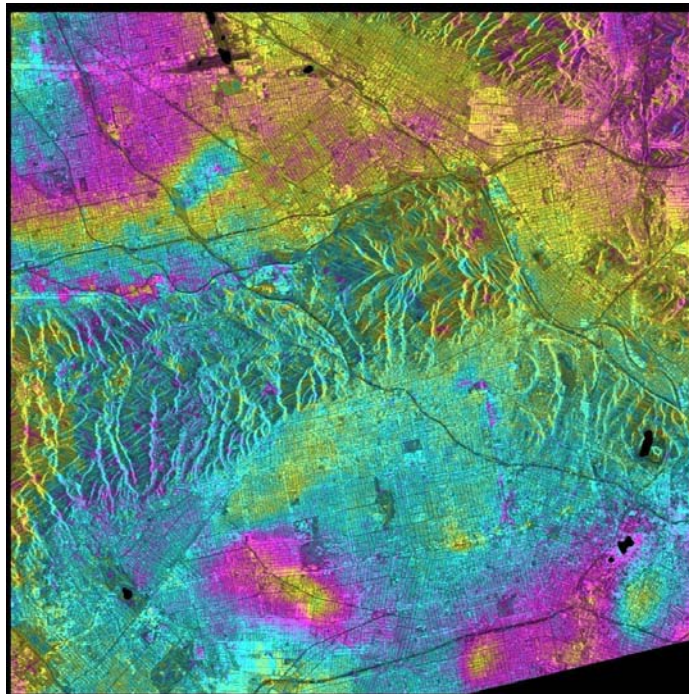
Figure B. 2. Slope Adaptive Filter, Window Size 4, 0% Coherence Mask, 1 and 5 Multi-looking.
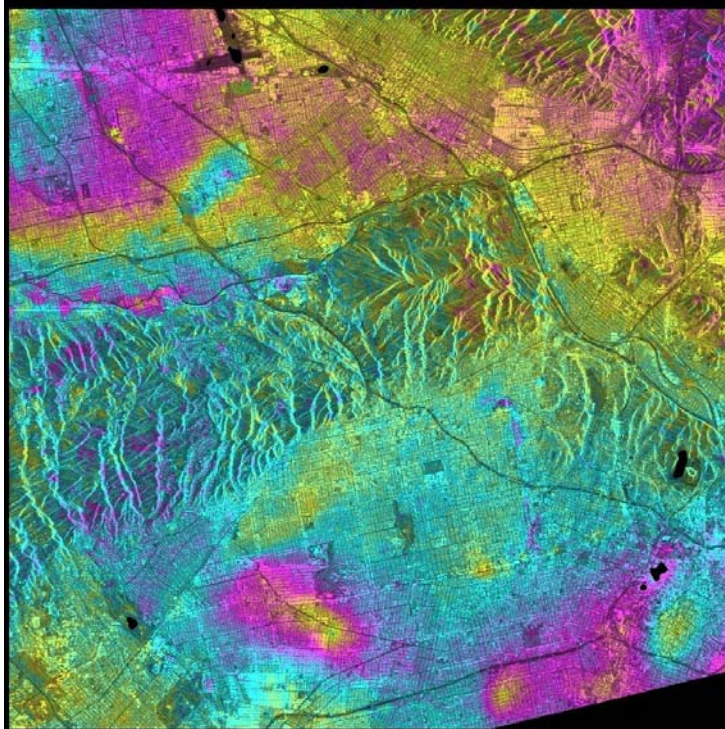
Figure B. 3. Slope Adaptive Filter, Window Size 8, 0% Coherence Mask, 1 and 5 Multi-looking.
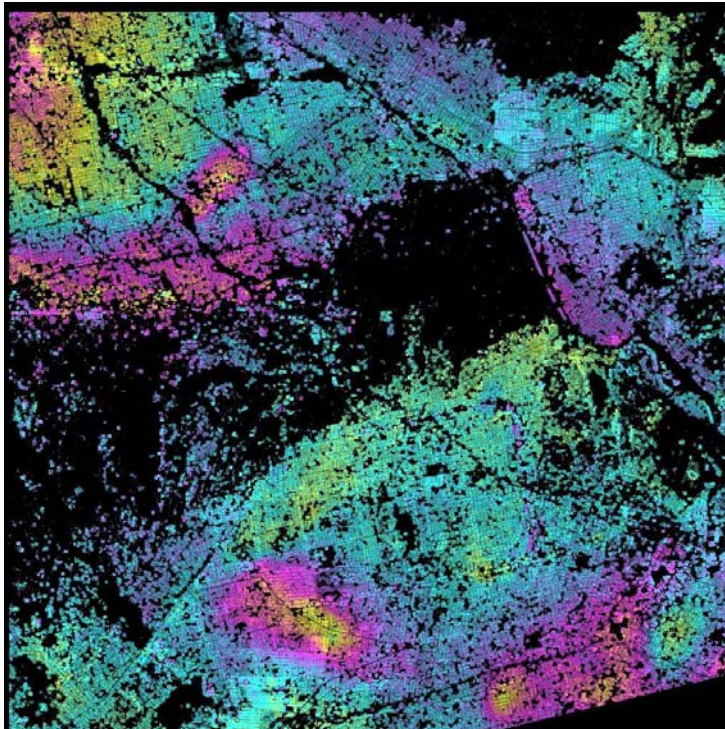
Figure B. 4. Slope Adaptive Filter, Window Size 2, 20% Coherence Mask, 1 and 5 Multi-looking.
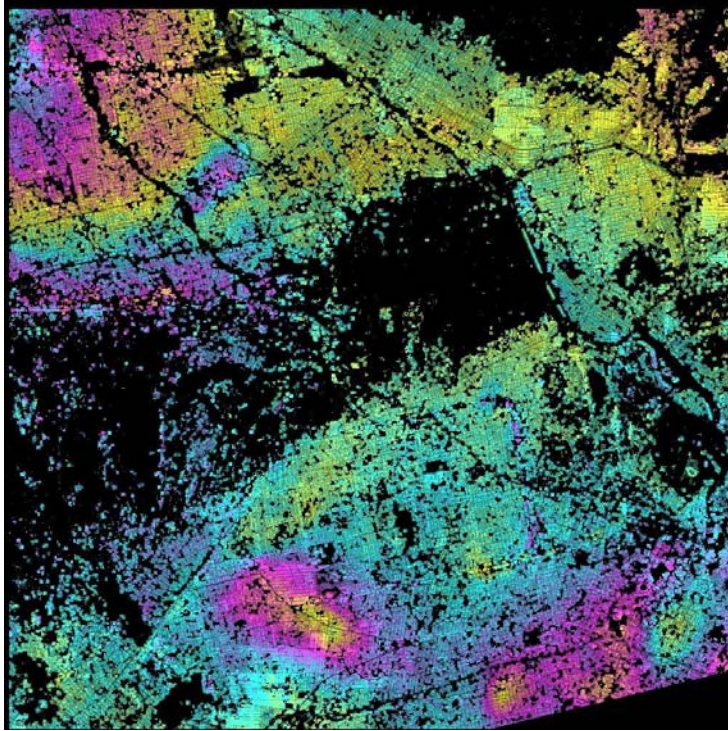
Figure B. 5. Slope Adaptive Filter, Window Size 4, 20% Coherence Mask, 1 and 5 Multi-looking.
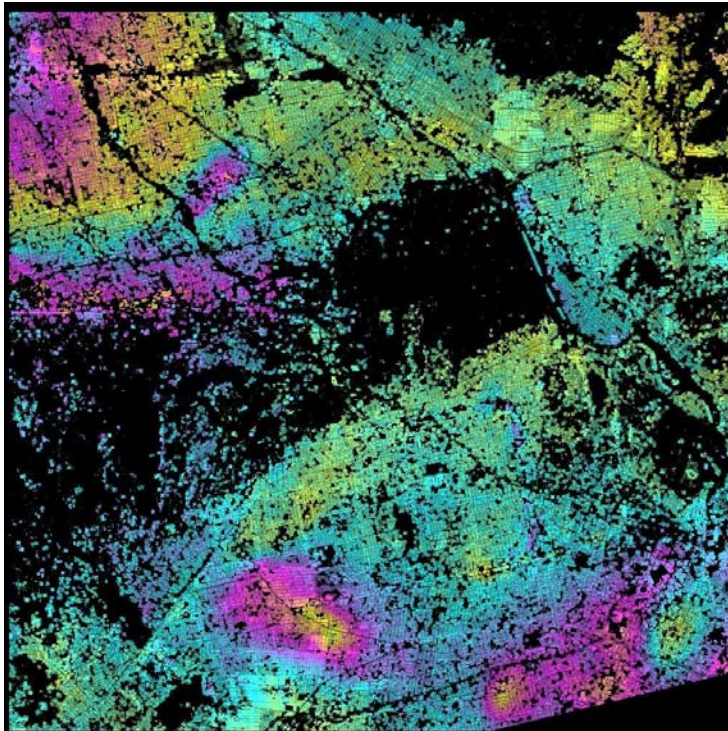
Figure B. 6. Slope Adaptive Filter, Window Size 8, 20% Coherence Mask, 1 and 5 Multi-looking.
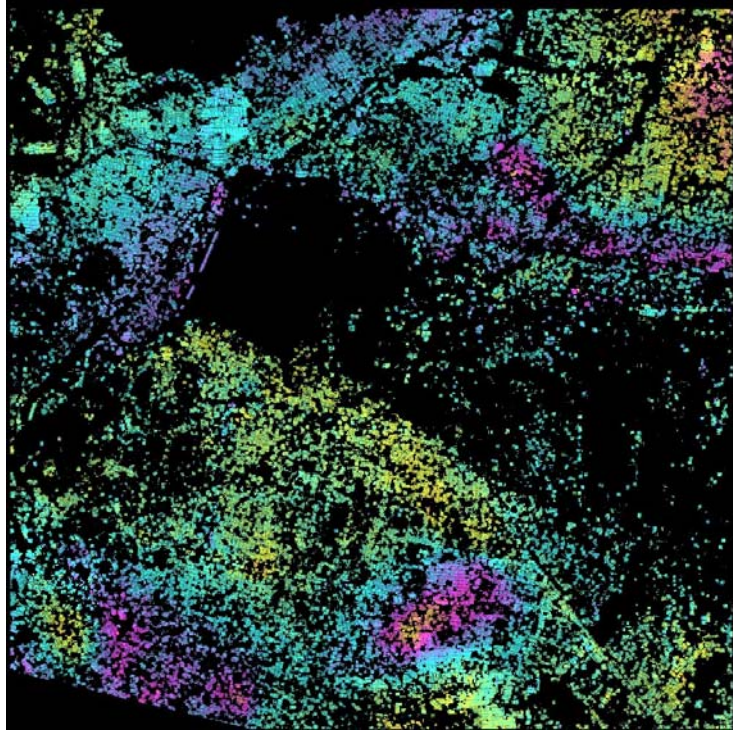
Figure B. 7. Slope Adaptive Filter, Window Size 2, 30% Coherence Mask, 1 and 5 Multi-looking.
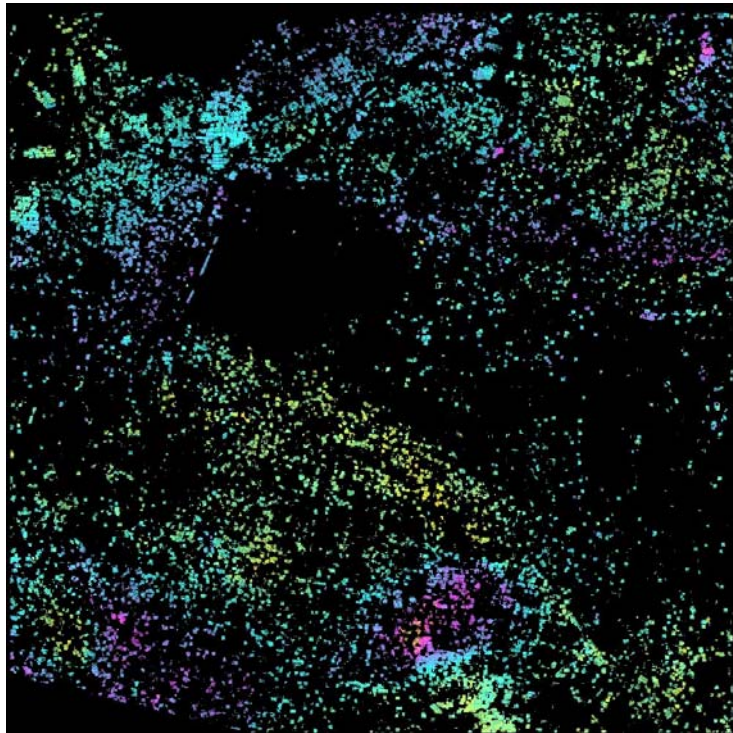
Figure B. 8. Slope Adaptive Filter, Window Size 2, 40% Coherence Mask, 1 and 5 Multi-looking.
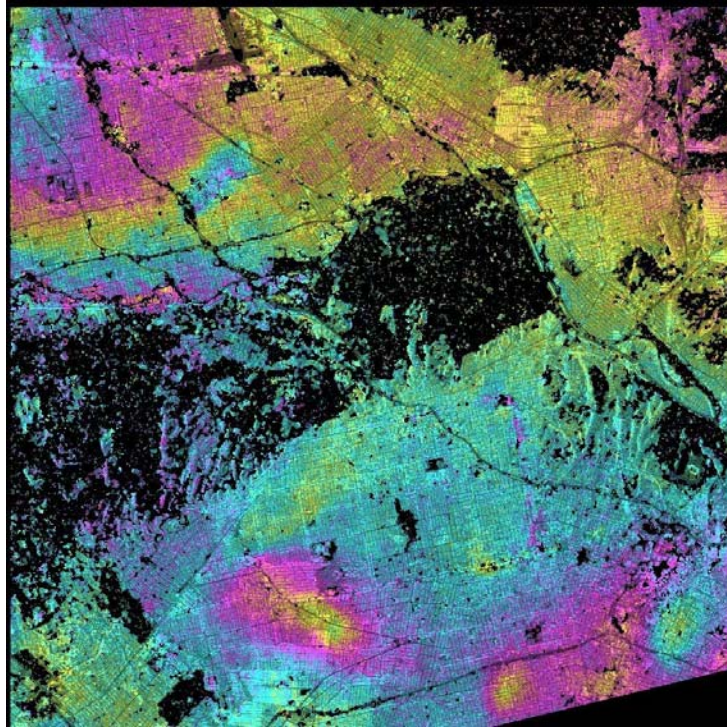
Figure B. 9. Spectral Filter, Window Size 8, 20% Coherence Mask, 1 and 5 Multi-looking.
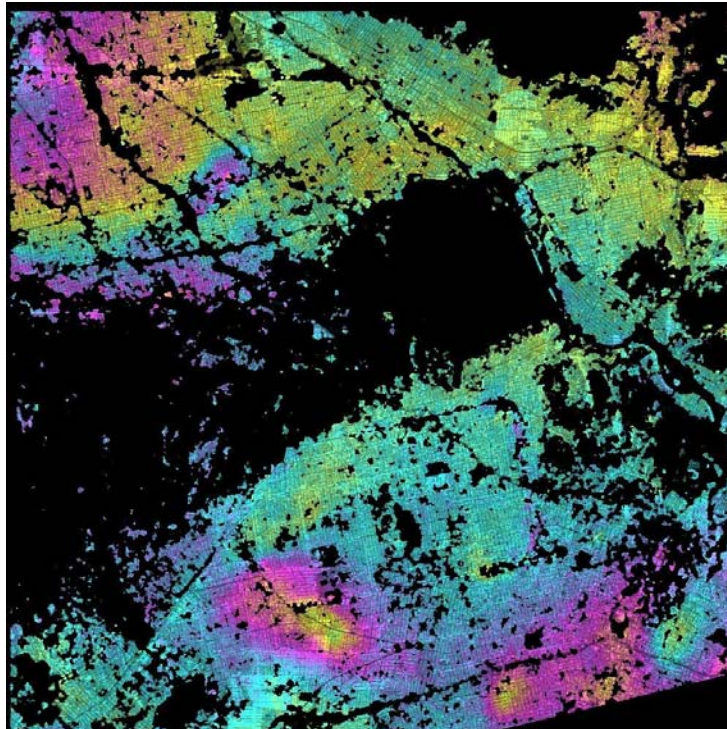
Figure B. 10. Spectral Filter, Window Size 16, 20% Coherence Mask, 1 and 5 Multi-looking.
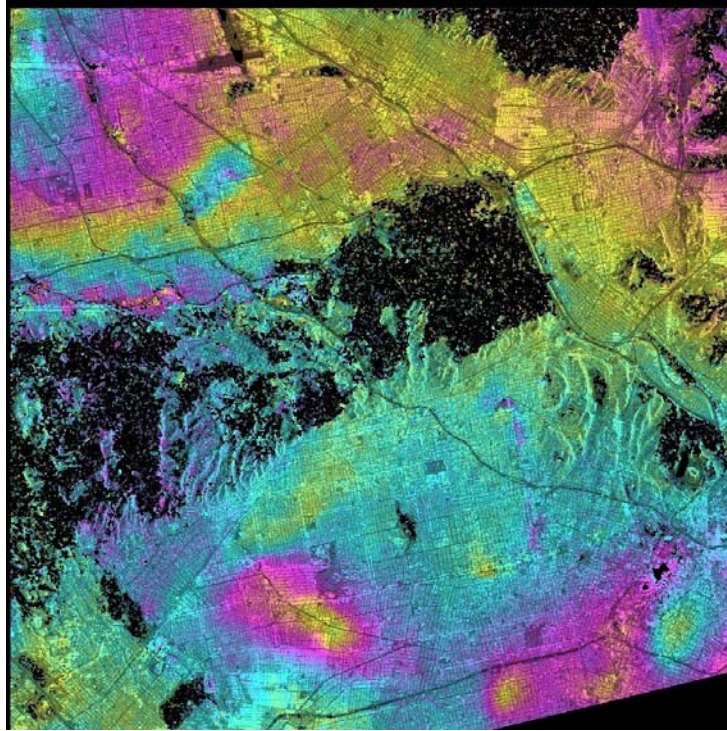
Figure B. 11. Spectral Filter, Window Size 32, 20% Coherence Mask, 1 and 5 Multi-looking.
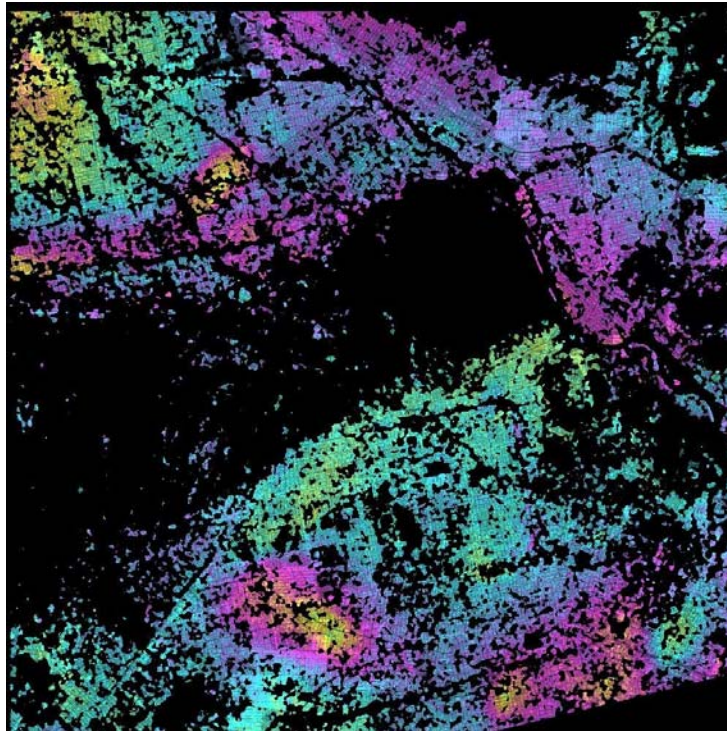
Figure B. 12.. Spectral Filter, Window Size 8, 50% Coherence Mask, 1 and 5 Multi-looking.
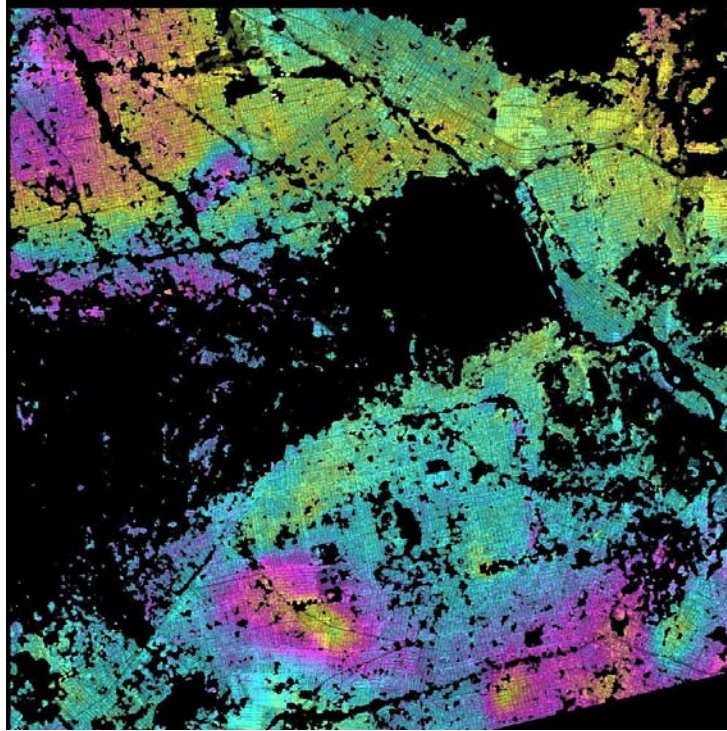
Figure B. 13. Spectral Filter, Window Size 16, 50% Coherence Mask, 1 and 5 Multi-looking.
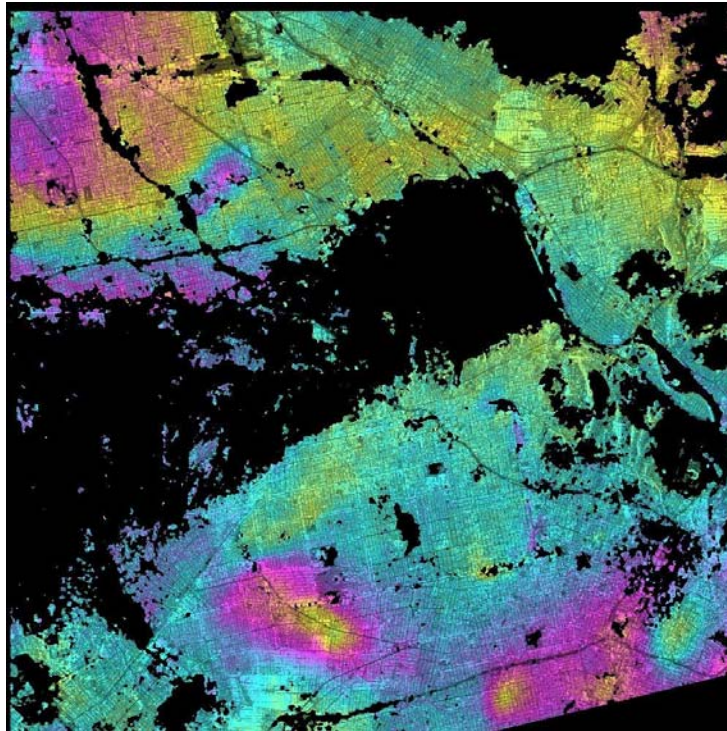
Figure B. 14. Spectral Filter, Window Size 32, 50% Coherence Mask, 1 and 5 Multi-looking.
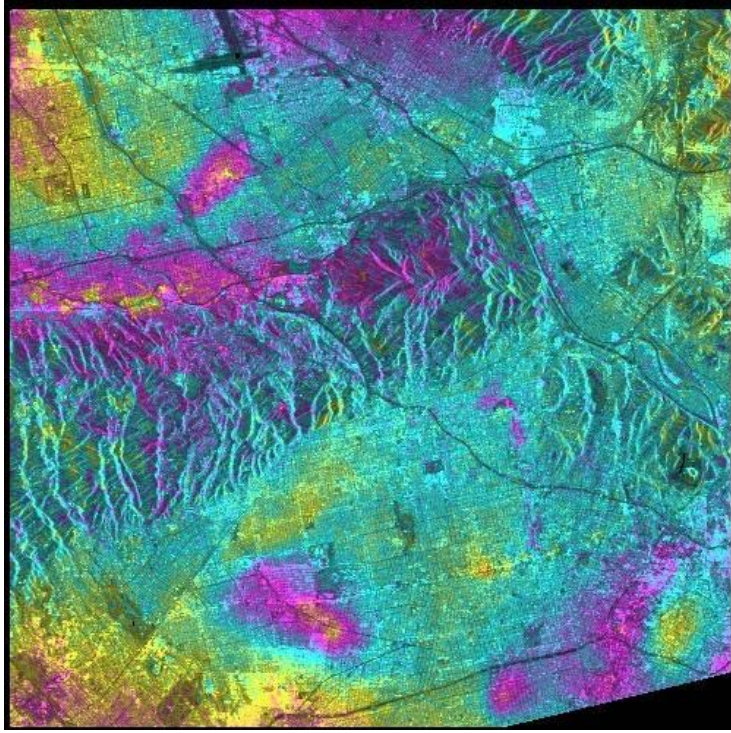
Figure B. 15. Slope Adaptive Filter, Window Size 2, 0% Coherence Mask, 2 and 10 Multi-looking.
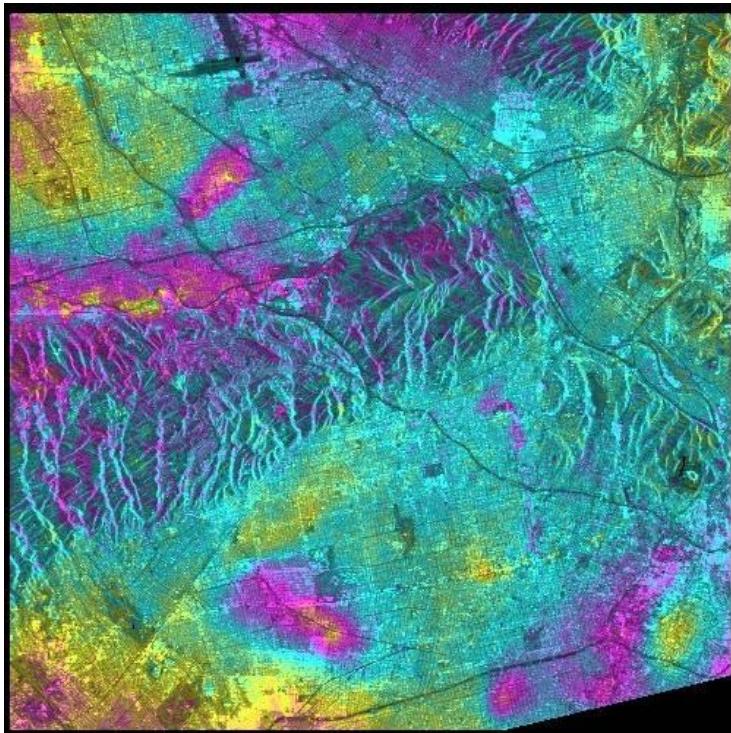
Figure B. 16. Slope Adaptive Filter, Window Size 4, 0% Coherence Mask, 2 and 10 Multi-looking.
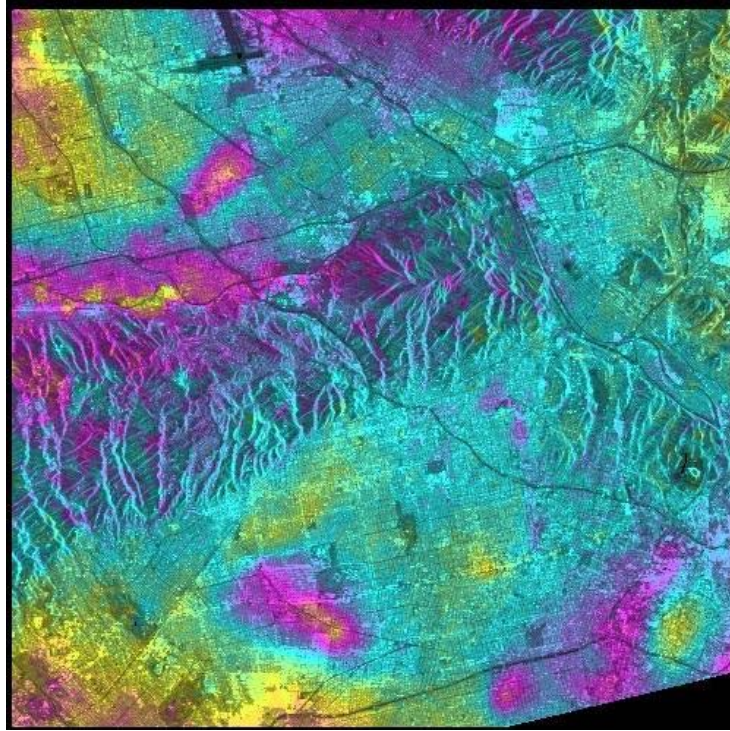
Figure B. 17. Slope Adaptive Filter, Window Size 8, 0% Coherence Mask, 2 and 10 Multi-looking.
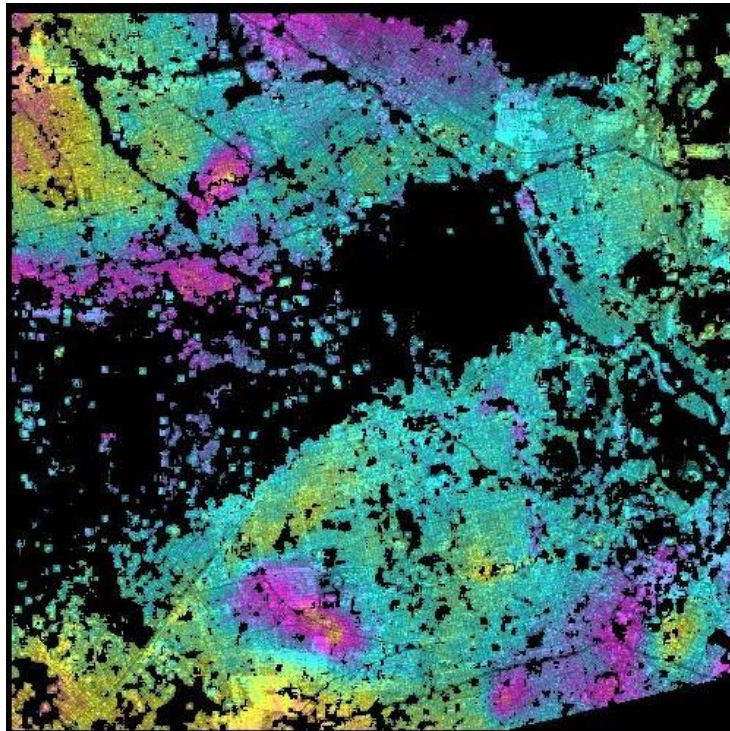
Figure B. 18. Slope Adaptive Filter, Window Size 2, 20% Coherence Mask, 2 and 10 Multi-looking.
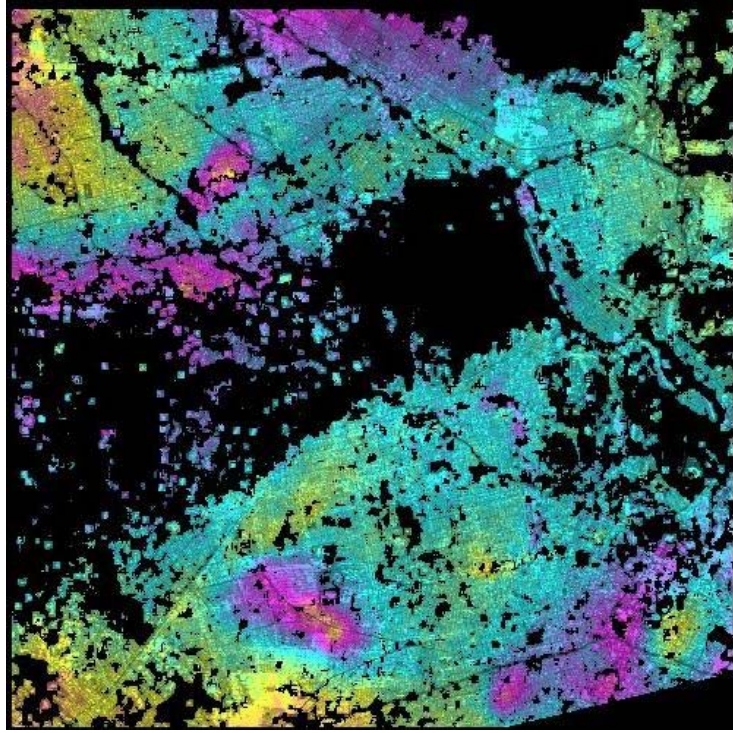
Figure B. 19. Slope Adaptive Filter, Window Size 4, 20% Coherence Mask, 2 and 10 Multi-looking.
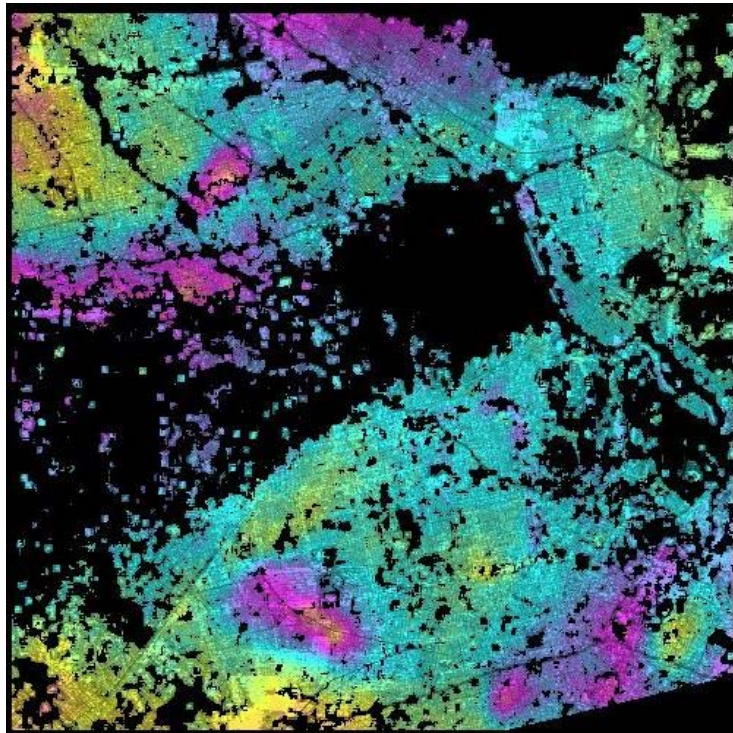
Figure B. 20. Slope Adaptive Filter, Window Size 8, 20% Coherence Mask, 2 and 10 Multi-looking.
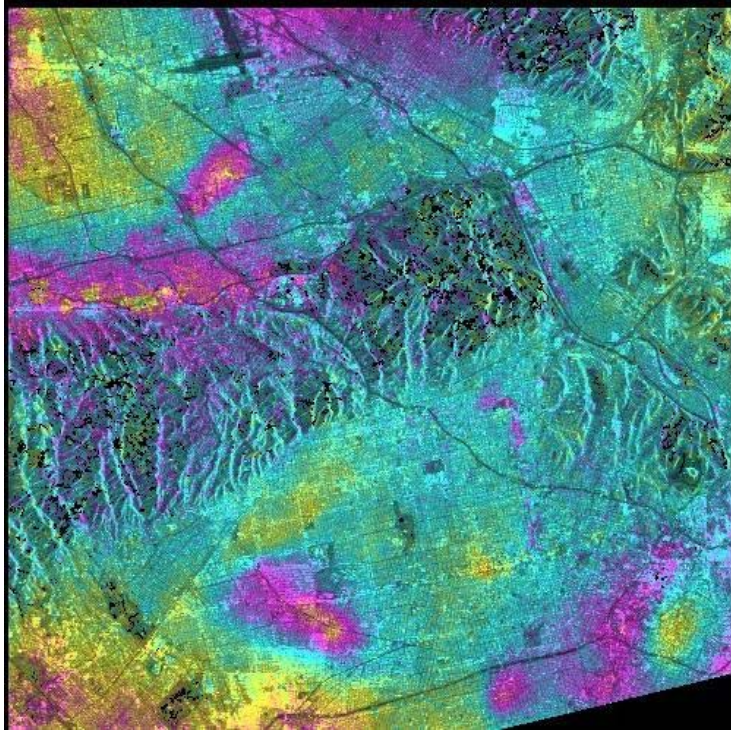
Figure B. 21. Spectral Filter, Window Size 8, 10% Coherence Mask, 2 and 10 Multi-looking.
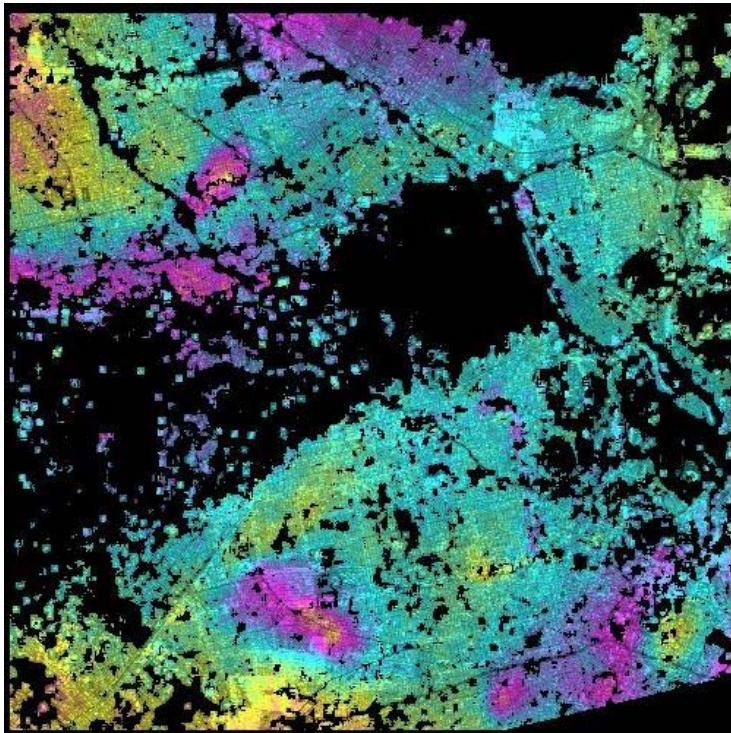
Figure B. 22. Spectral Filter, Window Size 8, 20% Coherence Mask, 2 and 10 Multi-looking.
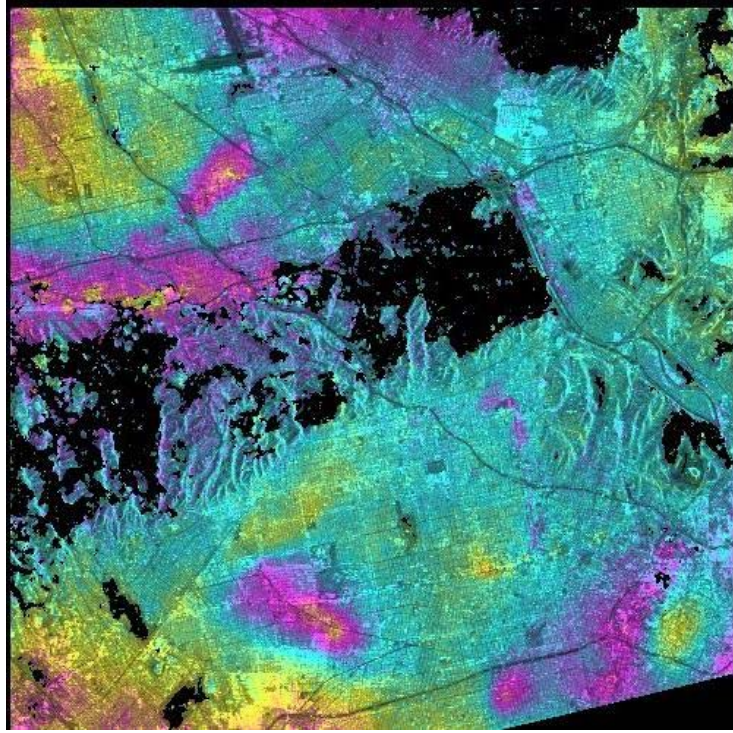
Figure B. 23. Spectral Filter, Window Size 16, 20% Coherence Mask, 2 and 10 Multi-looking.
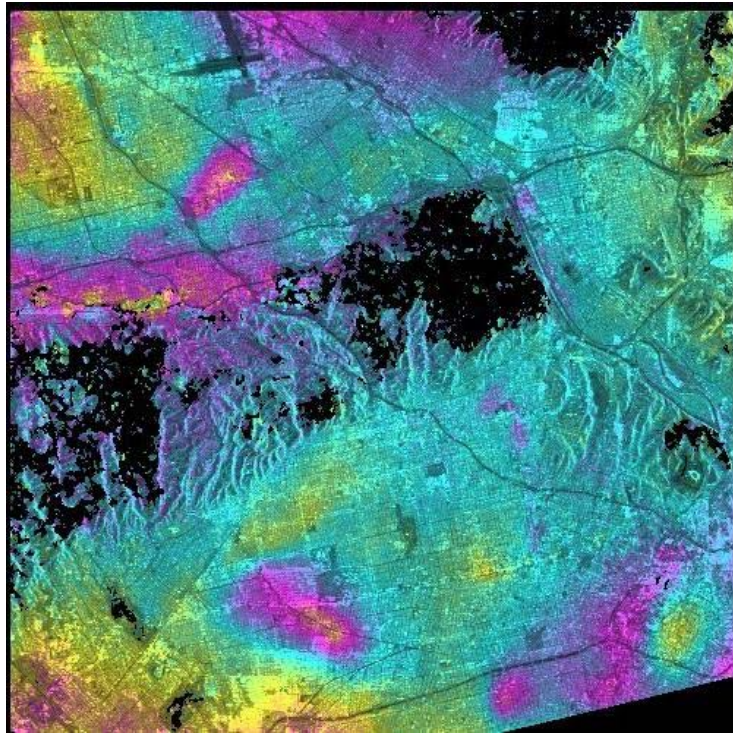
Figure B. 24. Spectral Filter, Window Size 32, 20% Coherence Mask, 2 and 10 Multi-looking.
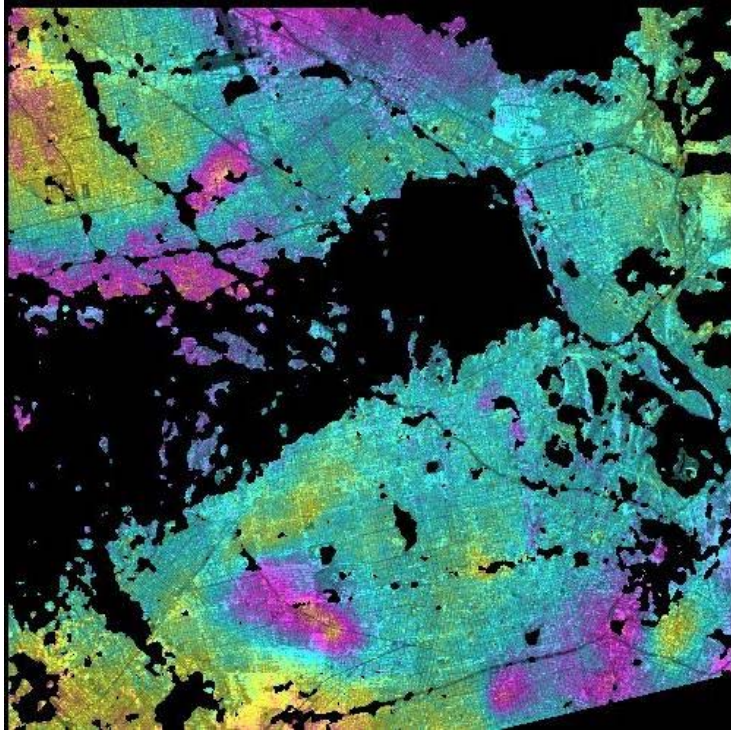
Figure B. 25. Spectral Filter, Window Size 8, 50% Coherence Mask, 2 and 10 Multi-looking.
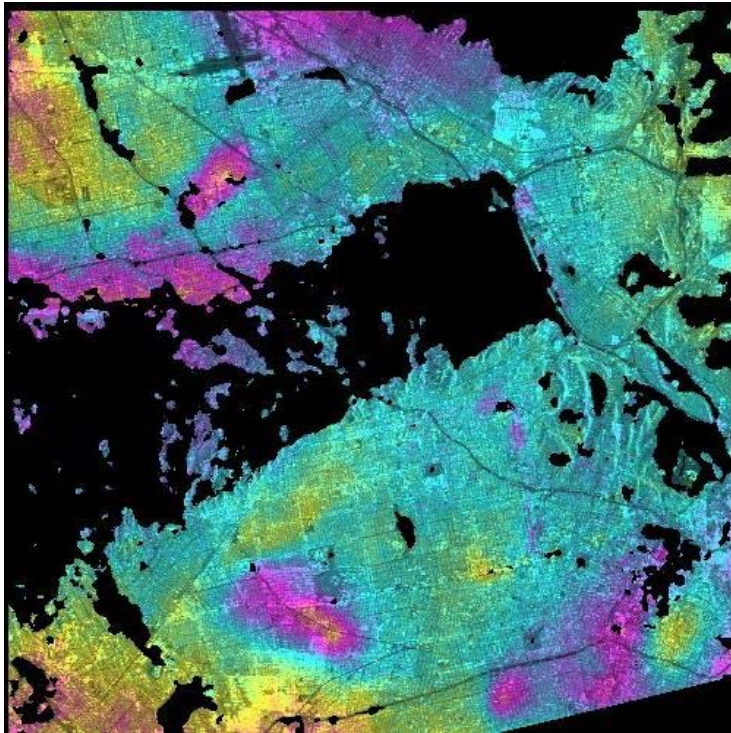
Figure B. 26. Spectral Filter, Window Size 16, 50% Coherence Mask, 2 and 10 Multi-looking.
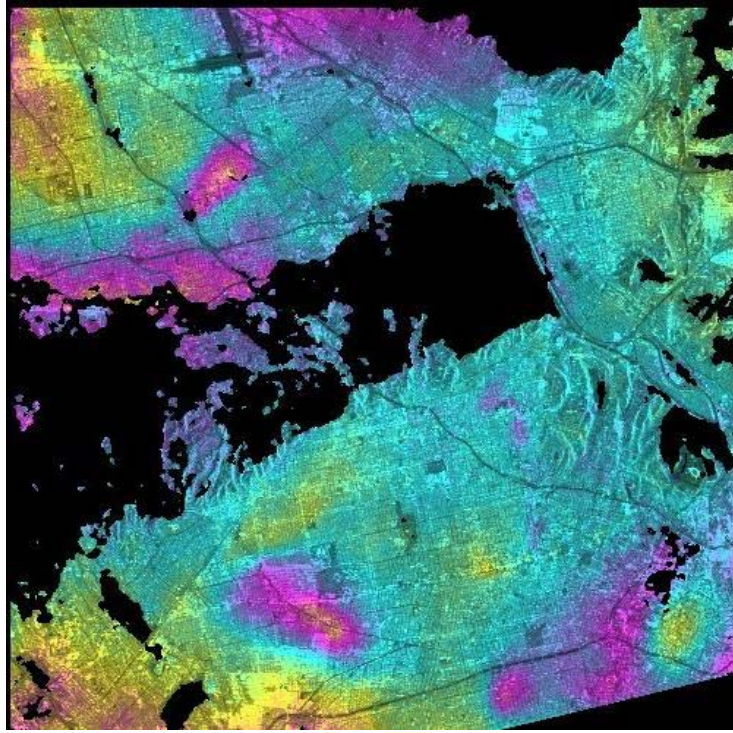
Figure B. 27. Spectral Filter, Window Size 32, 50% Coherence Mask, 2 and 10 Multi-looking.
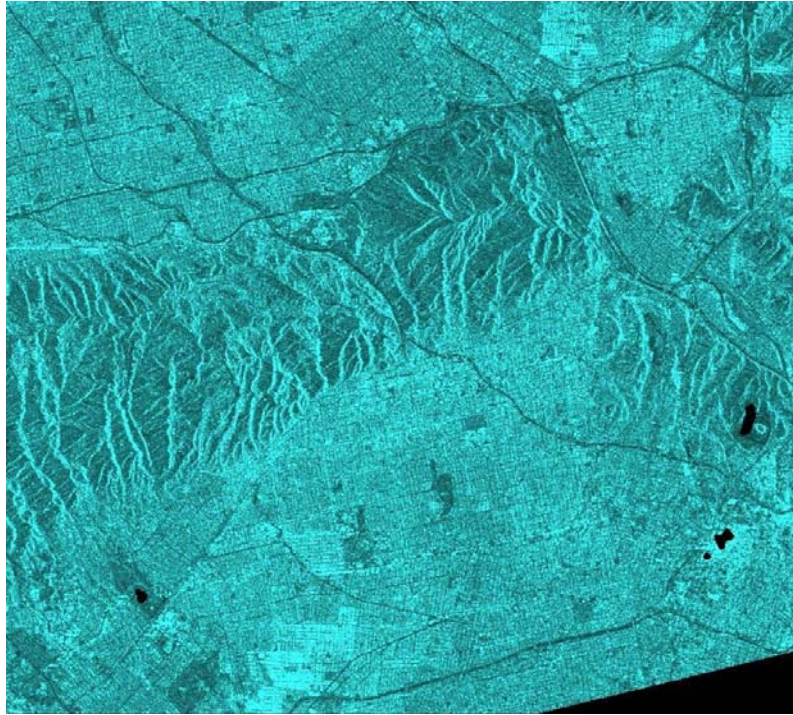
Figure C. 1. June 6, 1992 Cumulative Interferogram from Multi-Baseline Analysis.
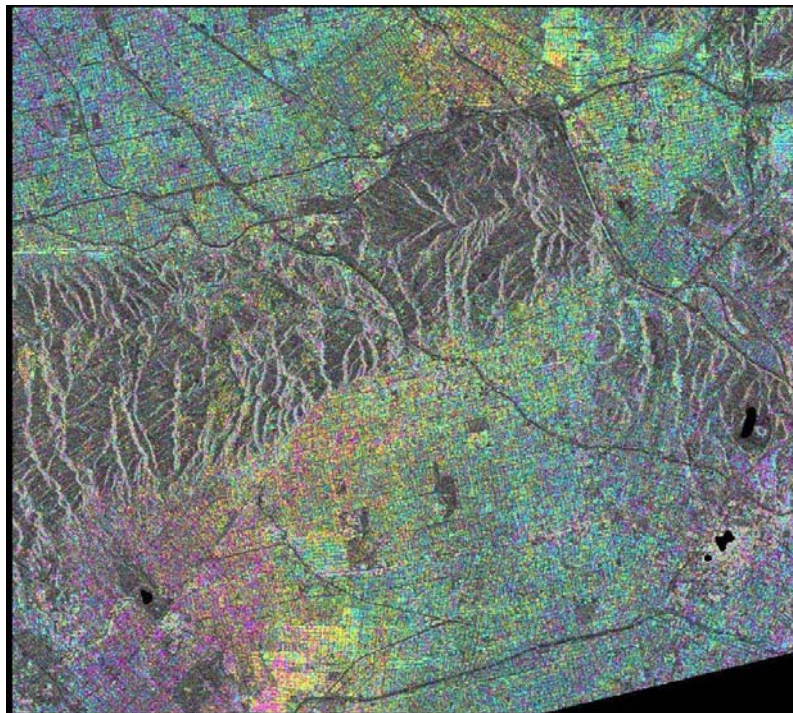
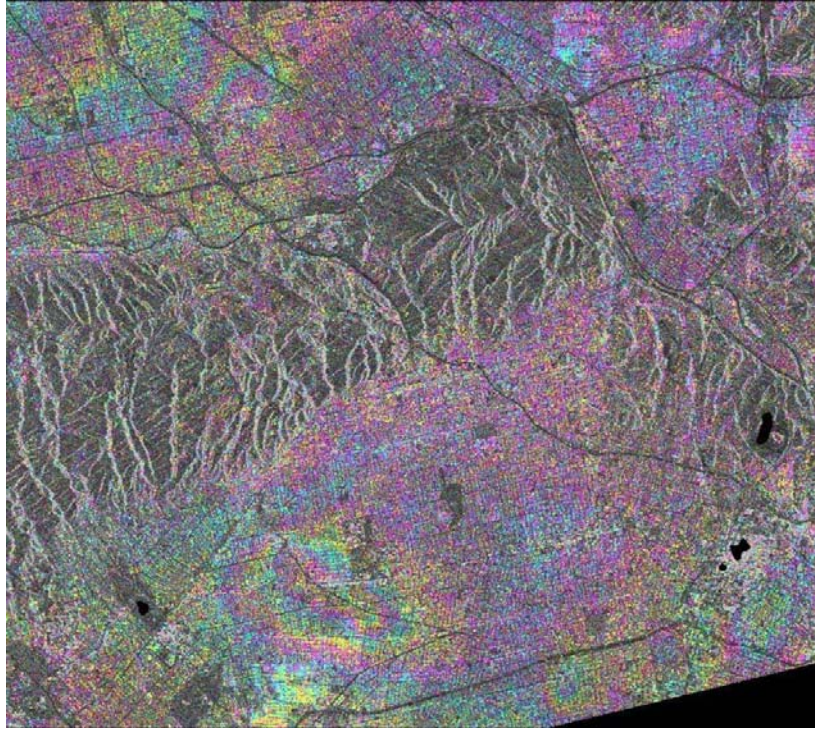**Figure C. 2. September 14, 1992 Cumulative Interferogram from Multi-Baseline Analysis.**
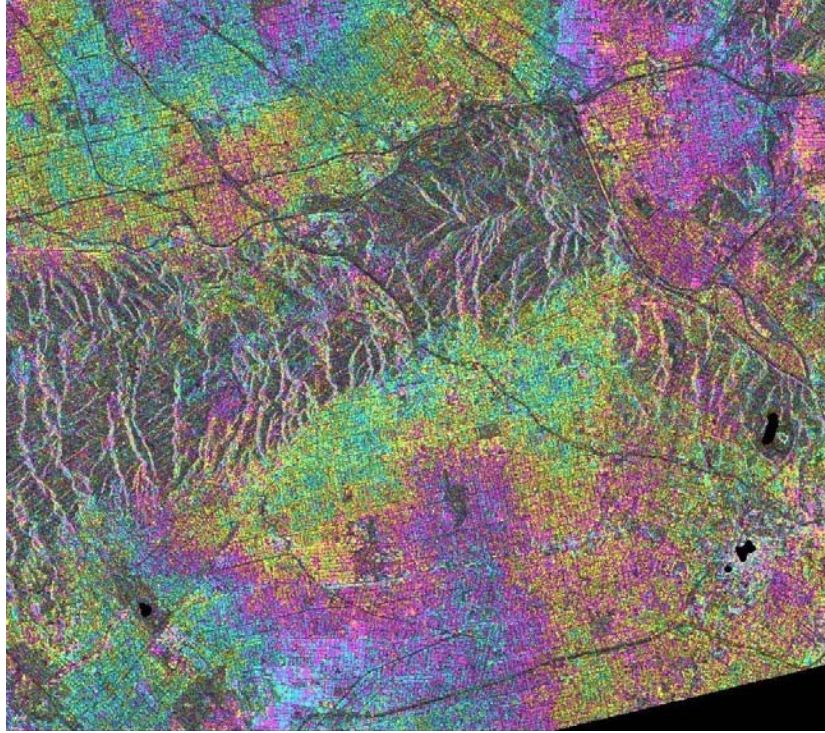
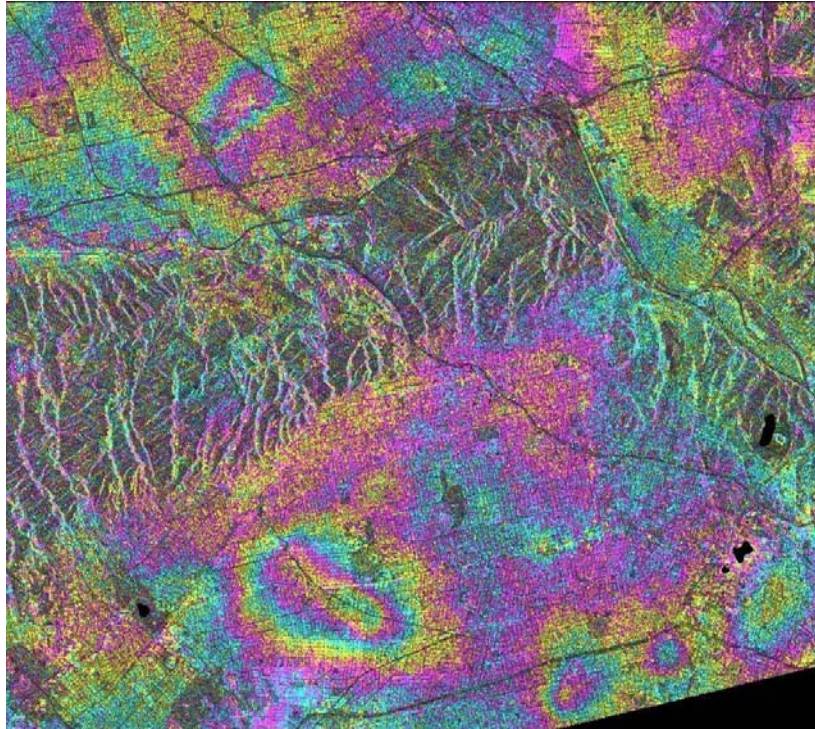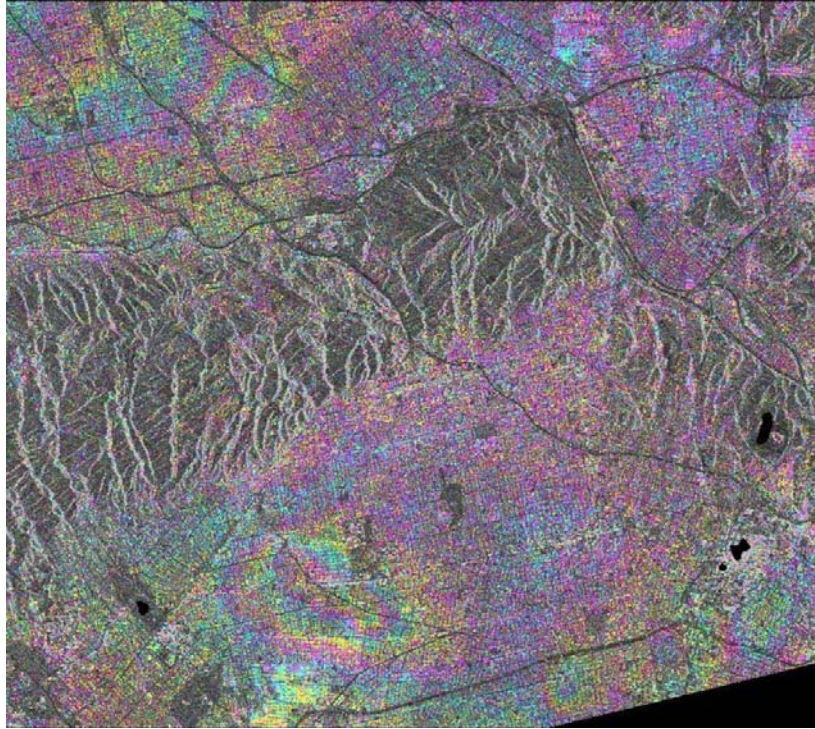**Figure C. 3. October 19, 1992 Cumulative Interferogram from Multi-Baseline Analysis.**
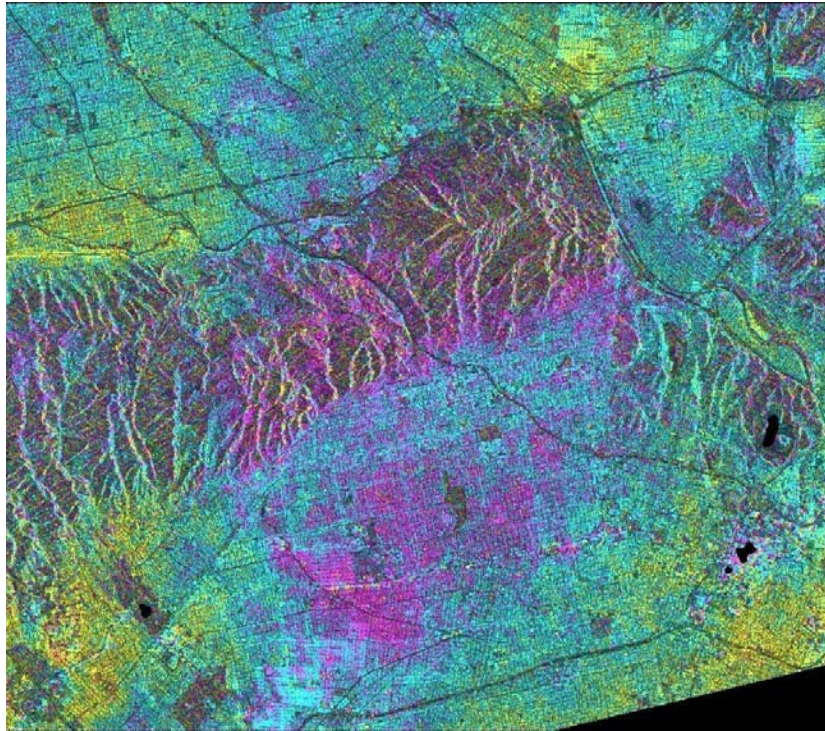
Figure C. 4. November 23, 1992 Cumulative Interferogram from Multi-Baseline Analysis.
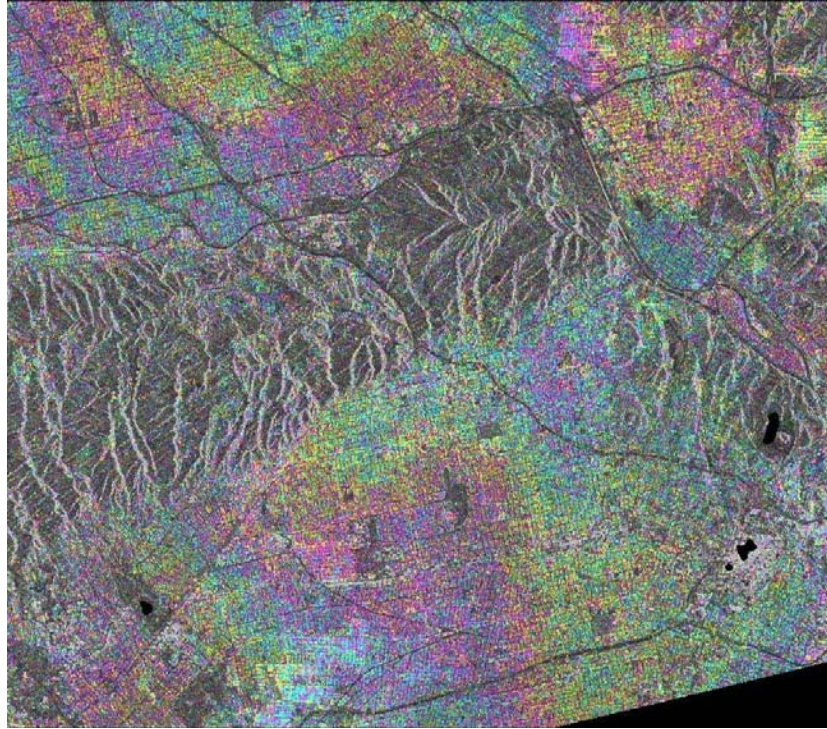
Figure C. 5. December 28, 1992 Cumulative Interferogram from Multi-Baseline Analysis.
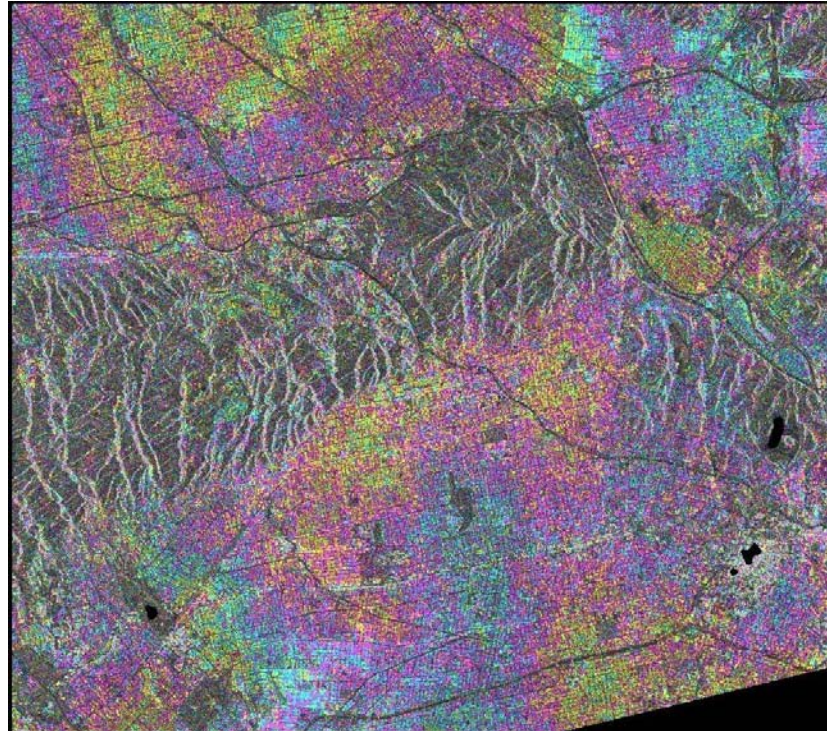
Figure C. 6. August 30, 1993 Cumulative Interferogram from Multi-Baseline Analysis.
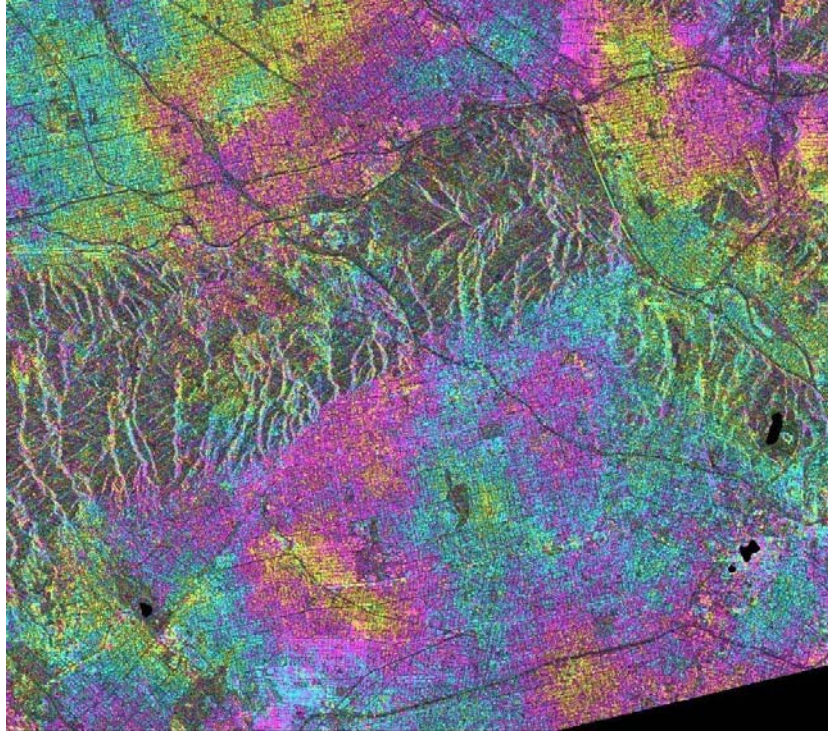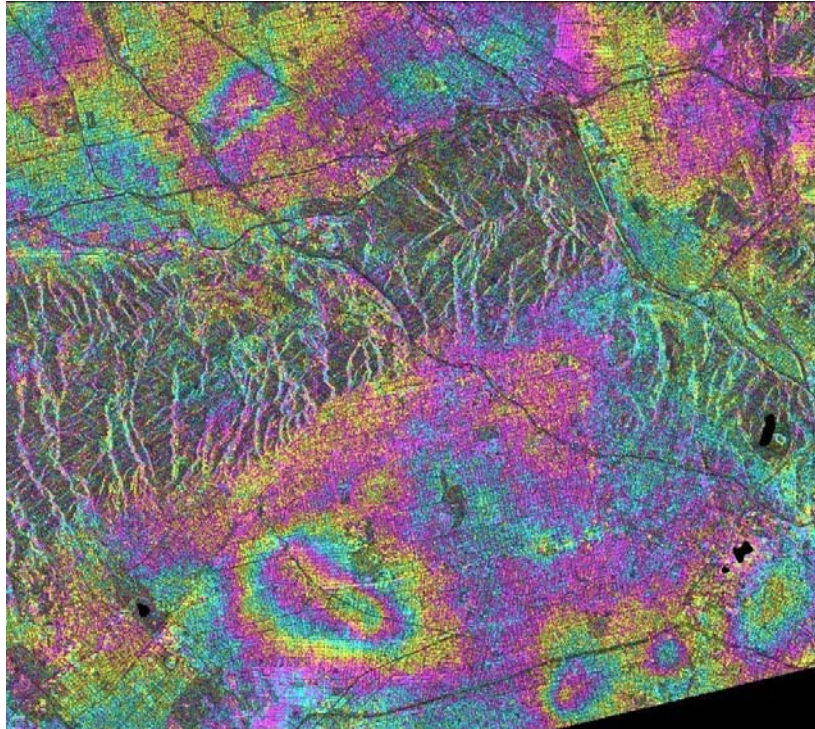
Figure C. 7. October 4, 1993 Cumulative Interferogram from Multi-Baseline Analysis.
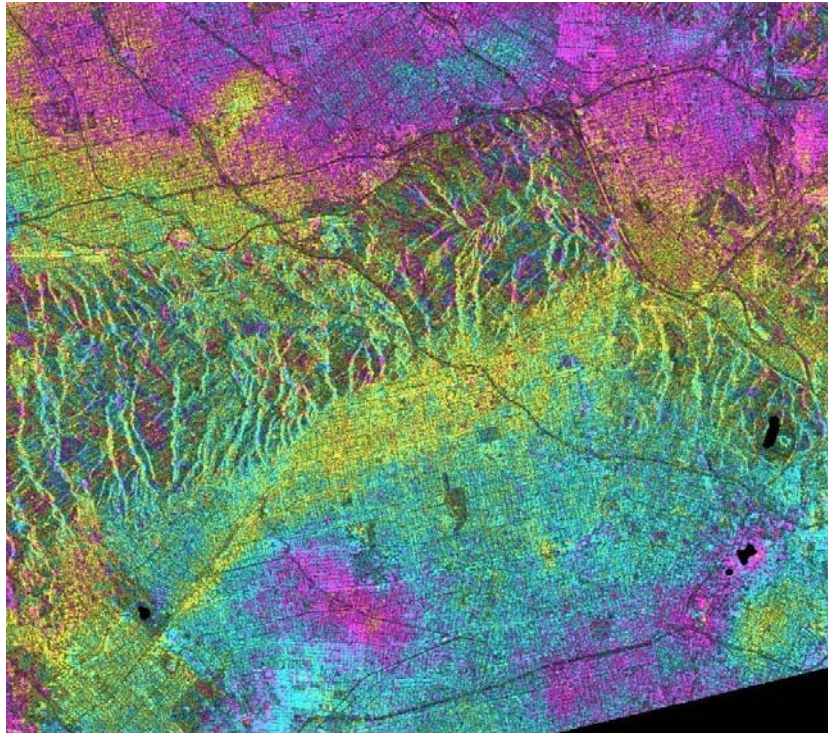
Figure C. 8. November 8, 1993 Cumulative Interferogram from Multi-Baseline Analysis.
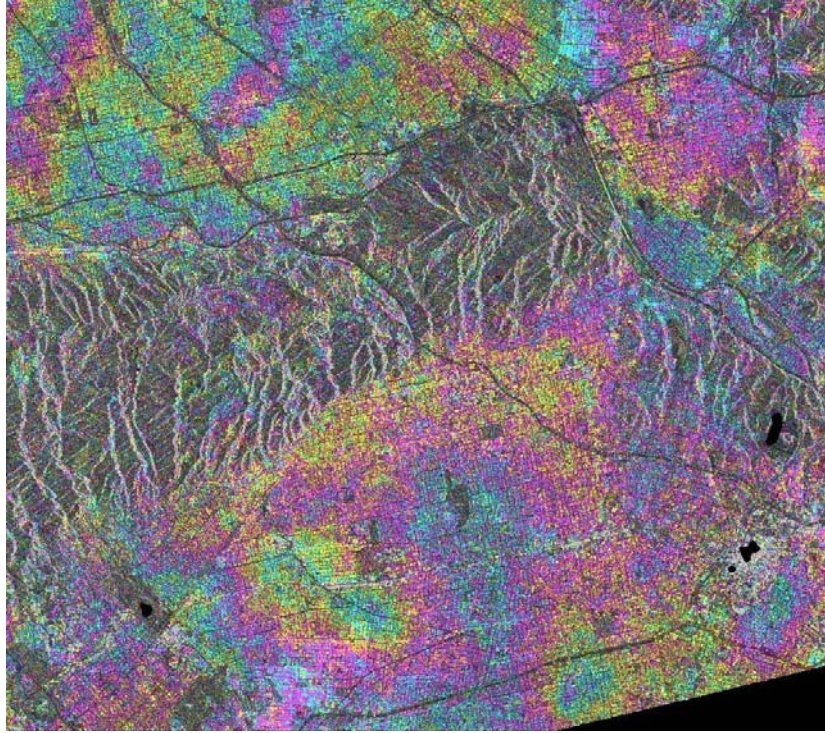
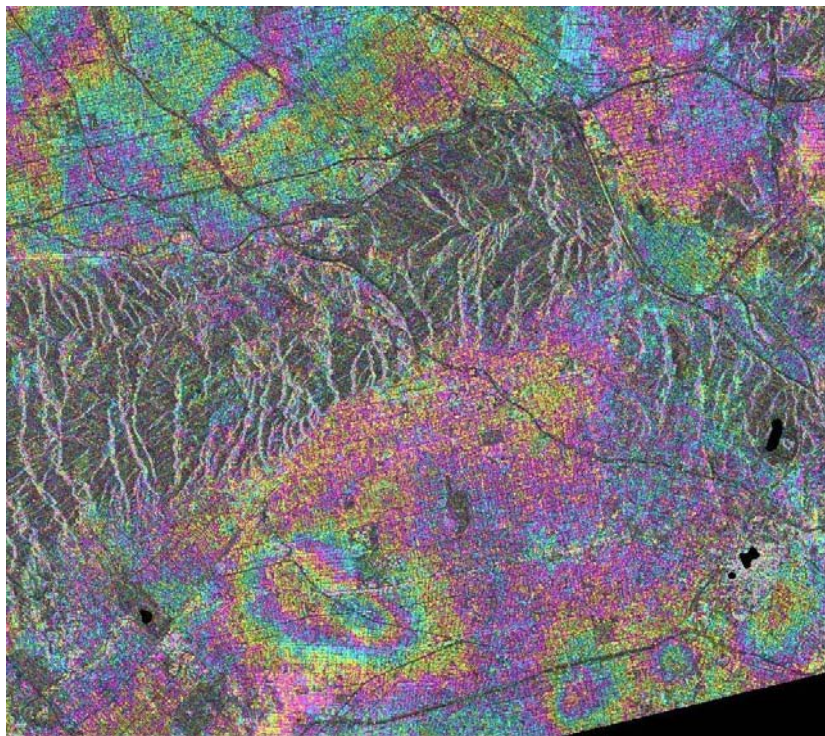**Figure C. 9. April 5, 1995 Cumulative Interferogram from Multi-Baseline Analysis.**
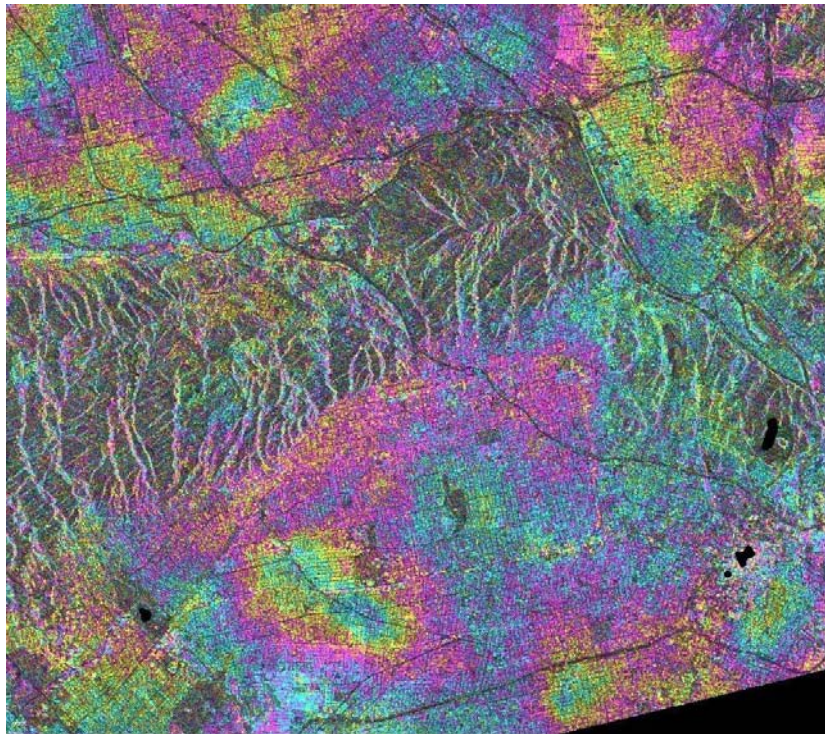
Figure C. 10. June 14, 1995 Cumulative Interferogram from Multi-Baseline Analysis.
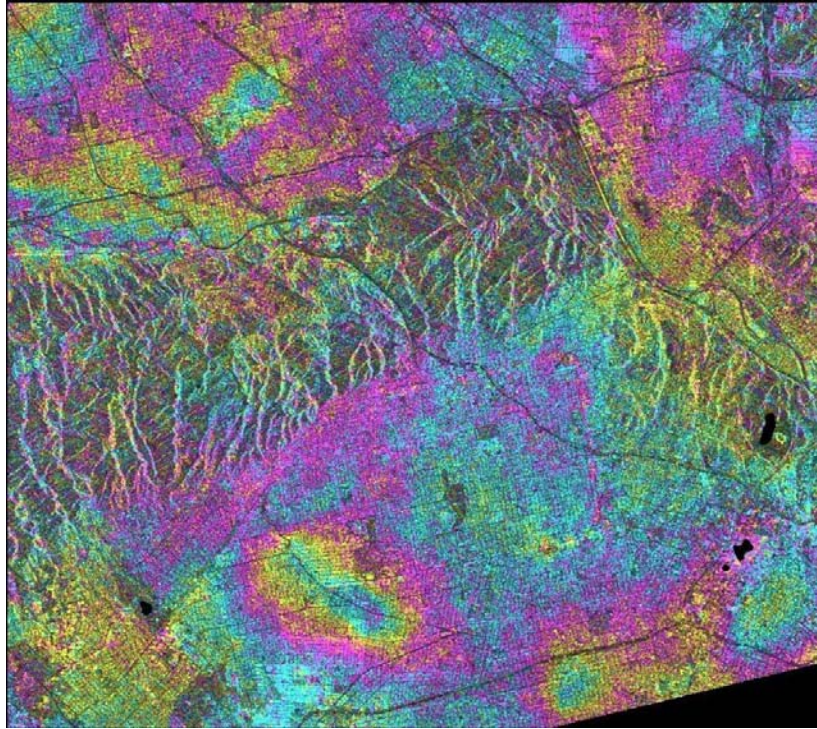
Figure C. 11. July 19, 1995 Cumulative Interferogram from Multi-Baseline Analysis.
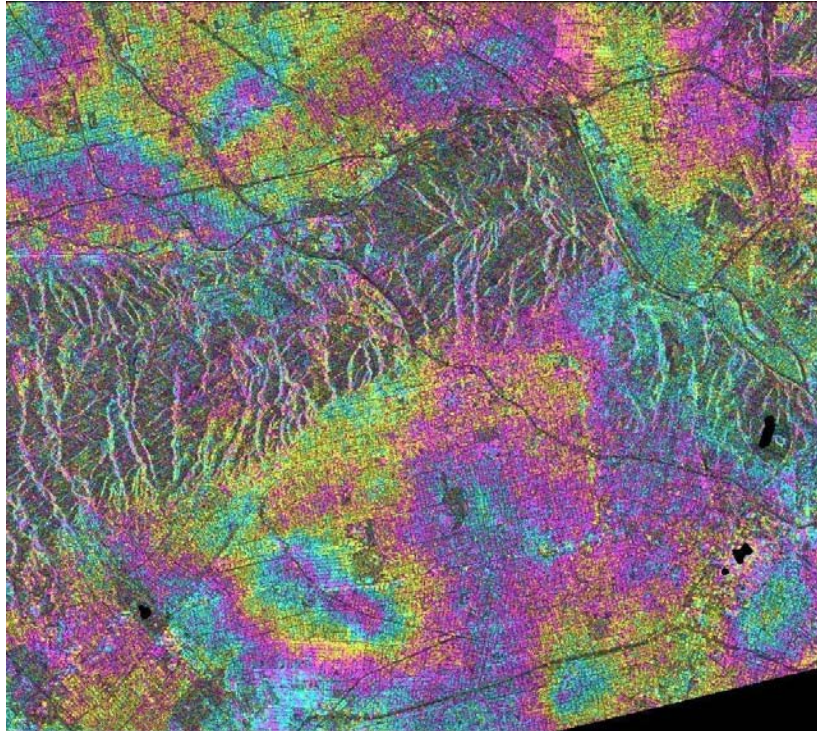
Figure C. 12. August 23, 1995 Cumulative Interferogram from Multi-Baseline Analysis.
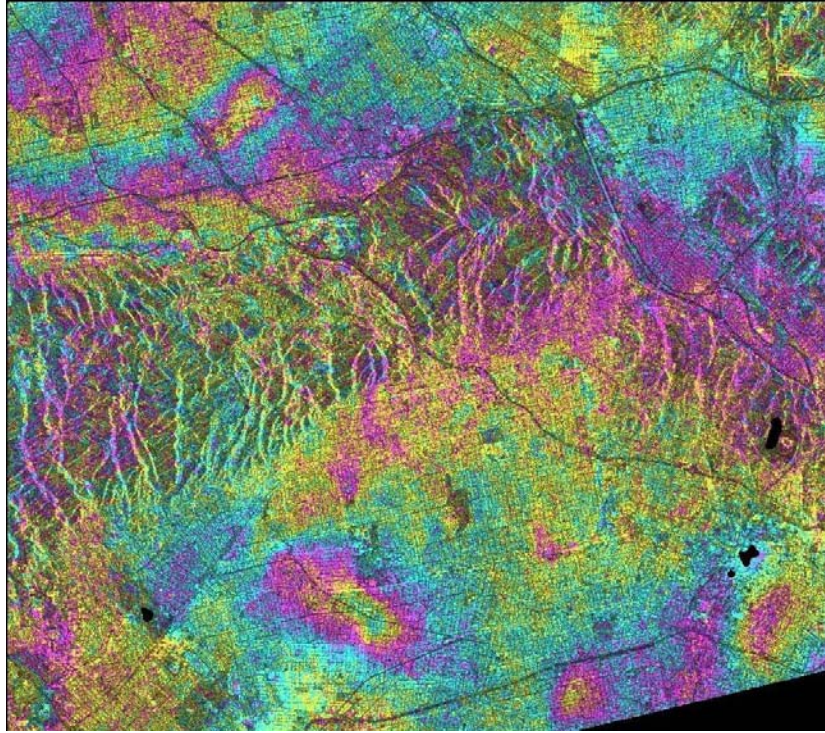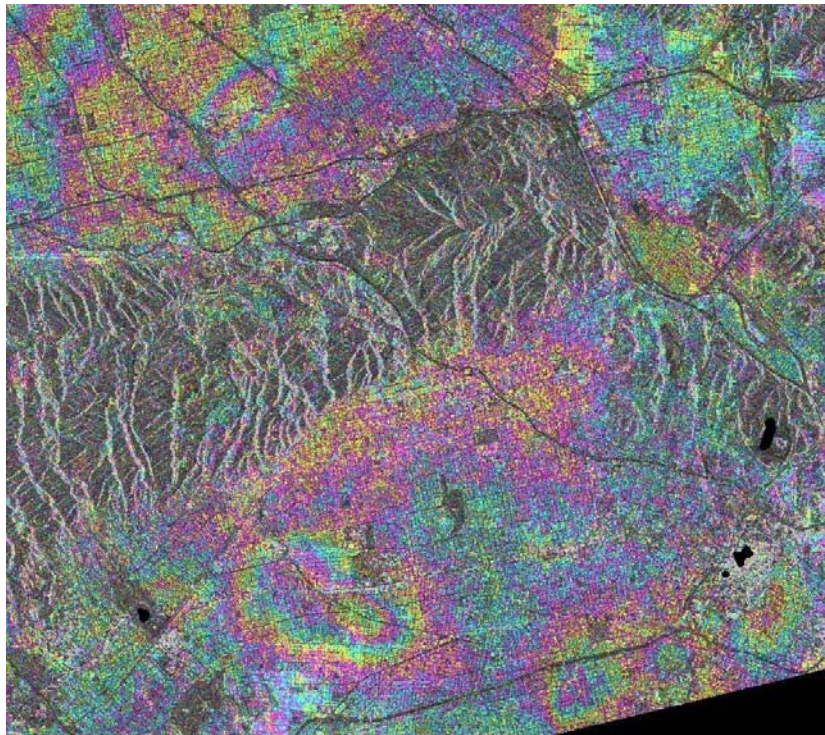
Figure C. 13. September 27, 1995 Cumulative Interferogram from Multi-Baseline Analysis.
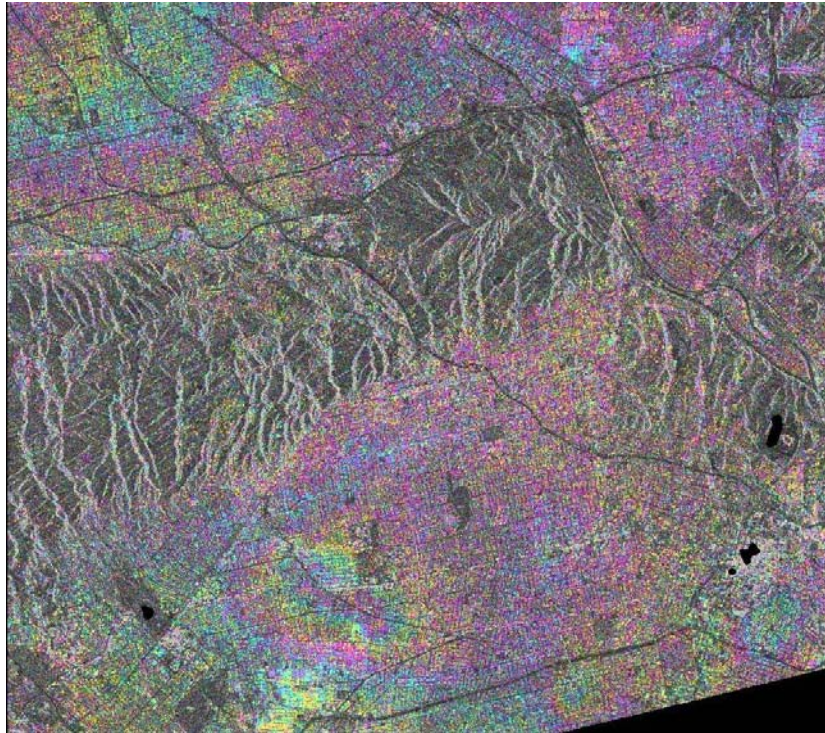
Figure C. 14. November 2, 1995 Cumulative Interferogram from Multi-Baseline Analysis.
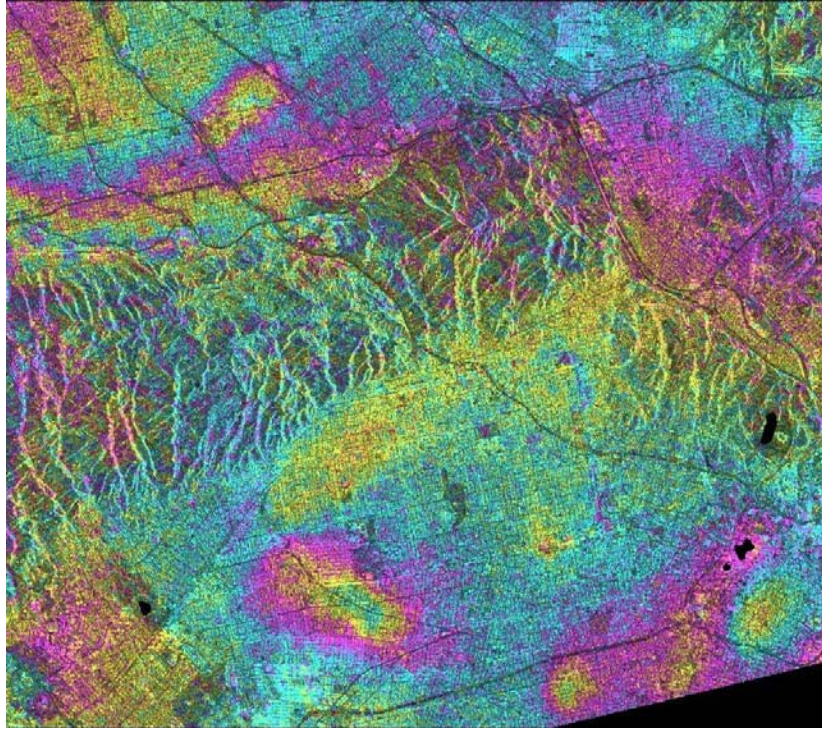
Figure C. 15. December 6, 1995 Cumulative Interferogram from Multi-Baseline Analysis.
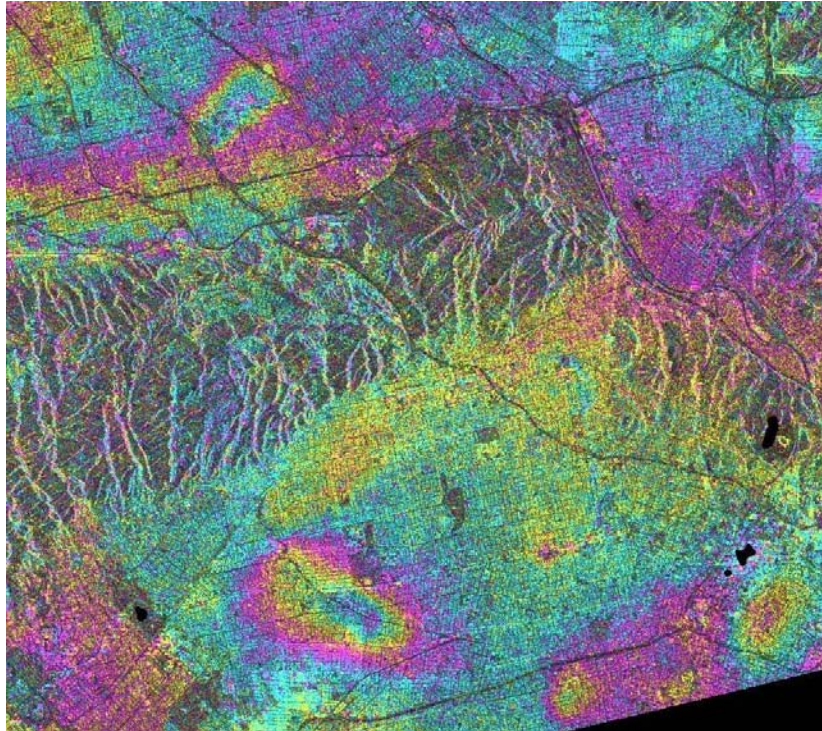
Figure C. 16. December 7. 1995 Cumulative Interferogram from Multi-Baseline Analysis.
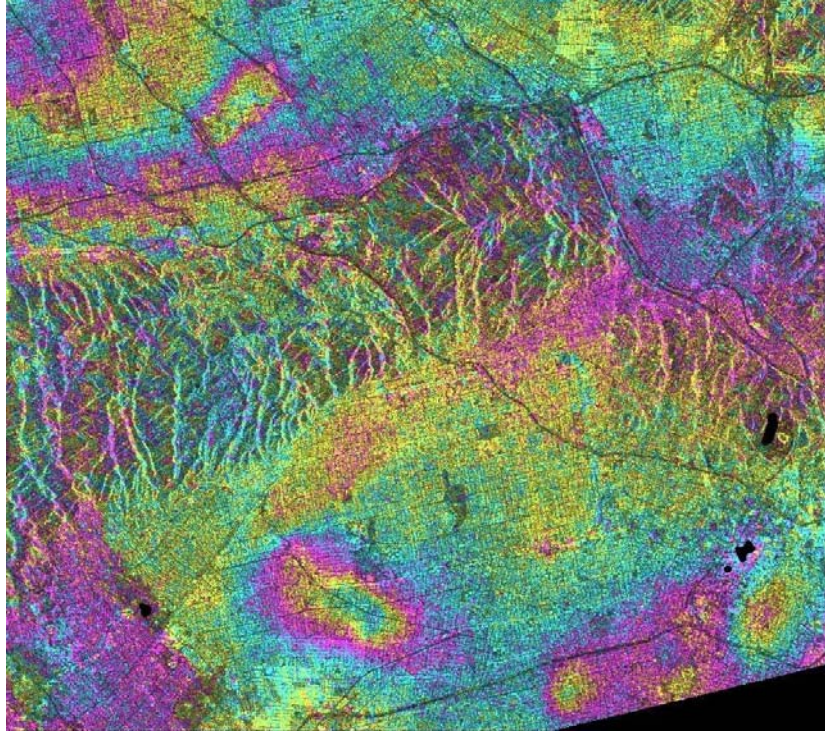
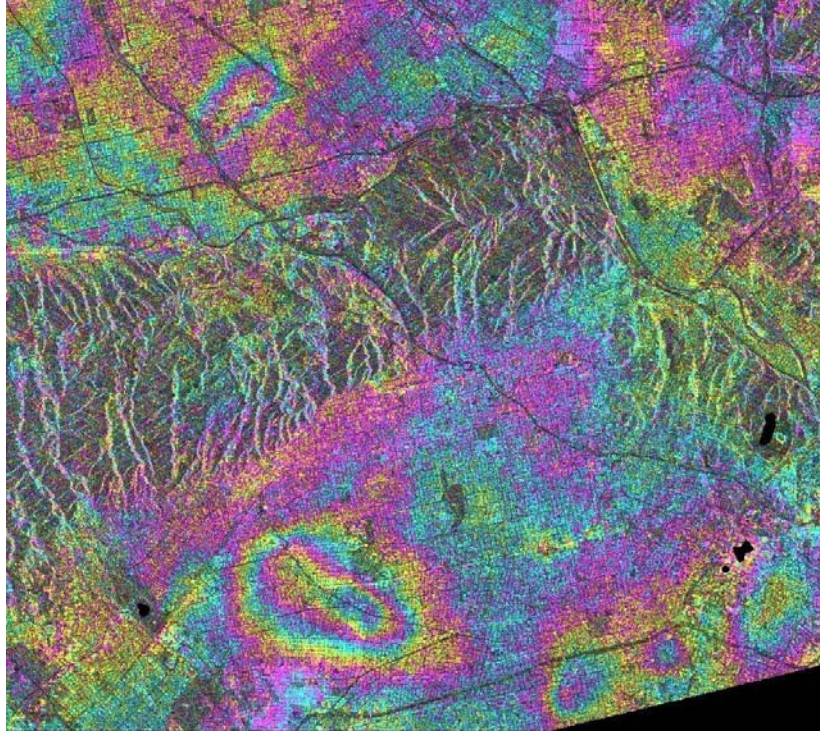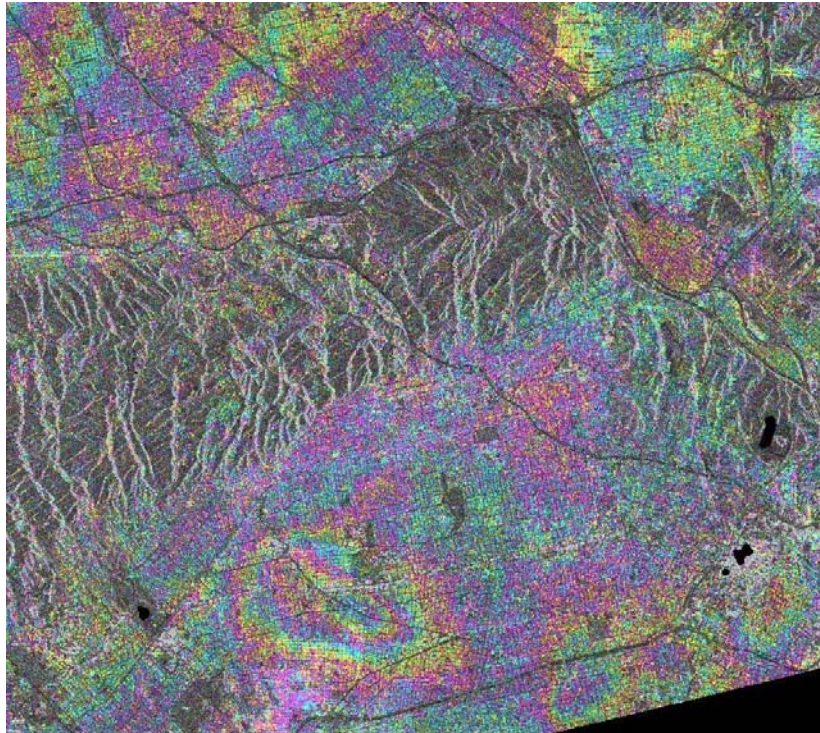**Figure C. 17. January 10, 1996 Cumulative Interferogram from Multi-Baseline Analysis.**
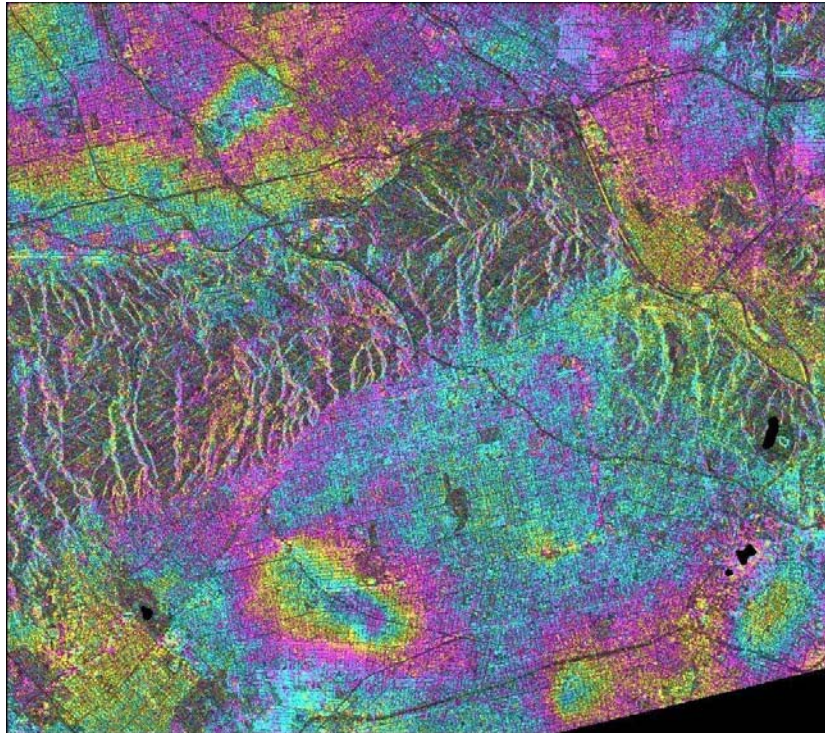
Figure C. 18. January 11, 1996 Cumulative Interferogram from Multi-Baseline Analysis.
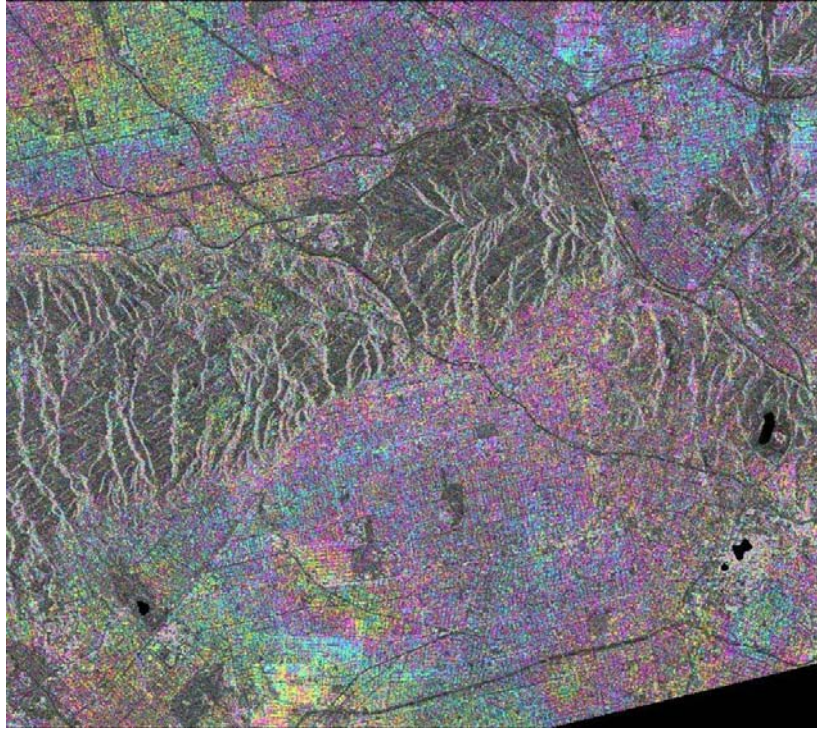
Figure C. 19. February 14, 1996 Cumulative Interferogram from Multi-Baseline Analysis.
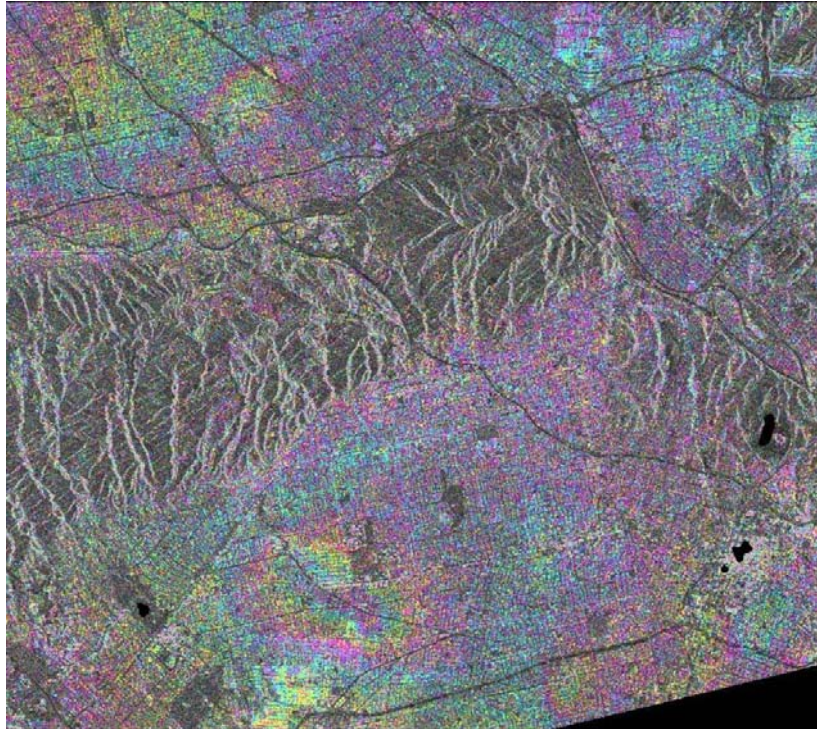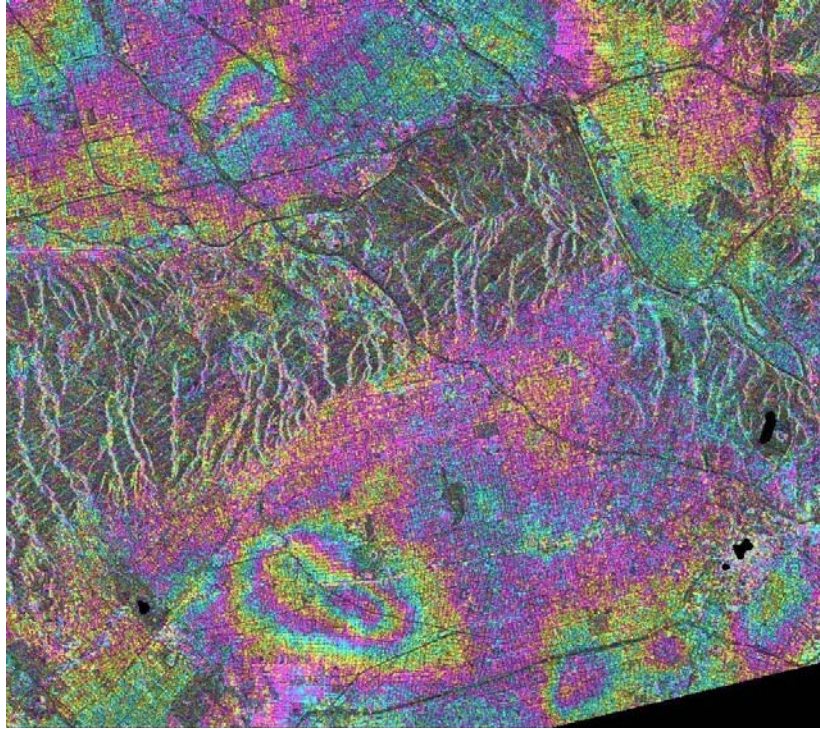

Figure C. 20. February 15, 1996 Cumulative Interferogram from Multi-Baseline Analysis.
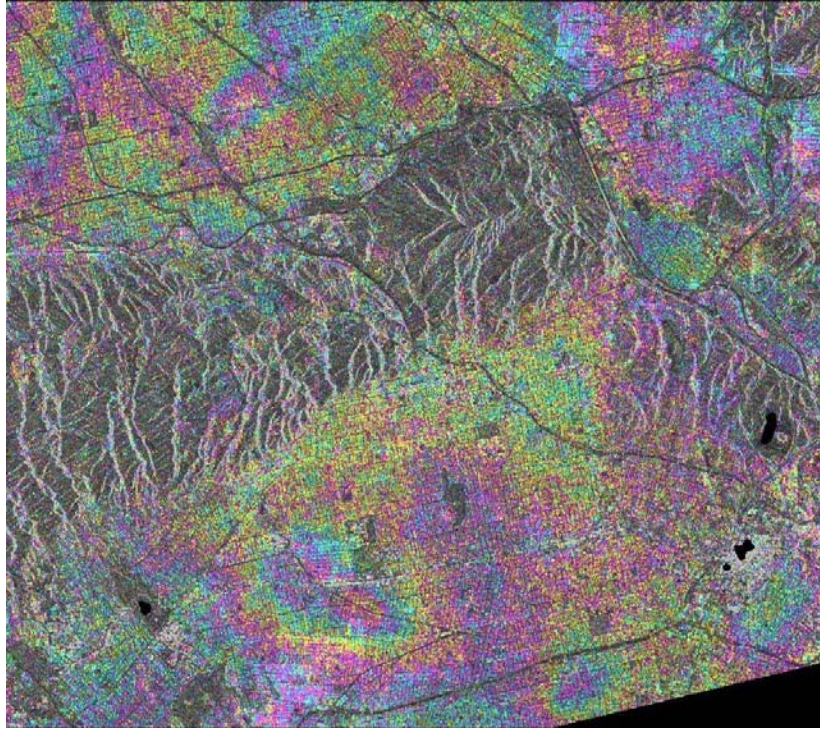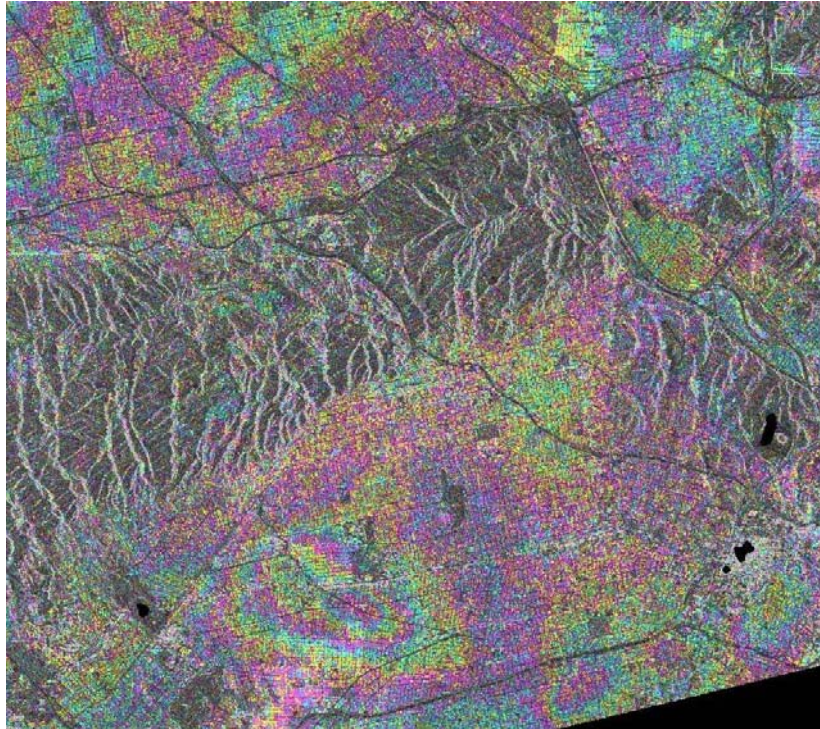
Figure C. 21. May 29, 1996 Cumulative Interferogram from Multi-Baseline Analysis.
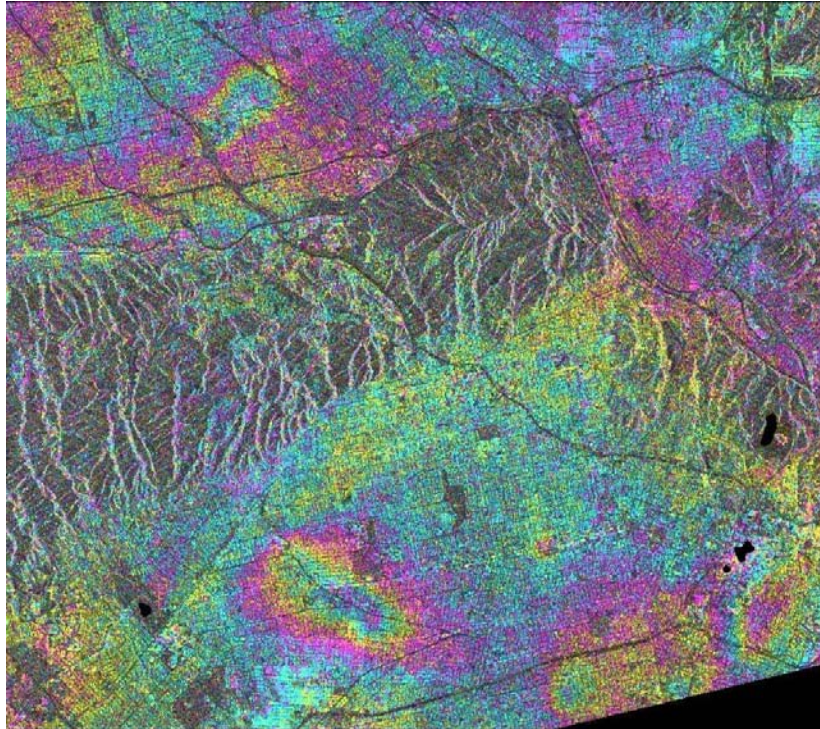
Figure C. 22. July 4, 1996 Cumulative Interferogram from Multi-Baseline Analysis.
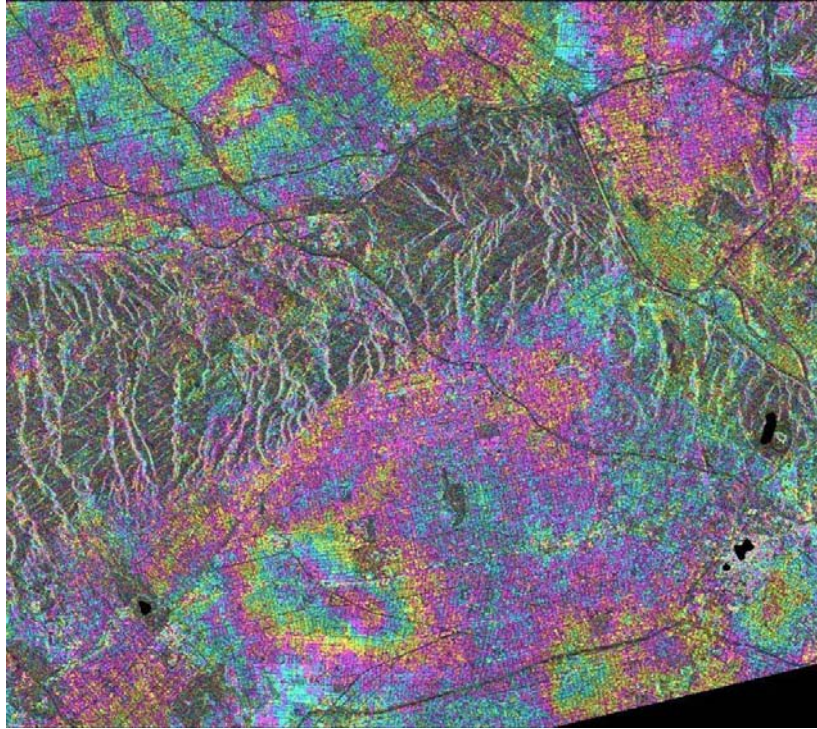
Figure C. 23. September 12, 1996 Cumulative Interferogram from Multi-Baseline Analysis.
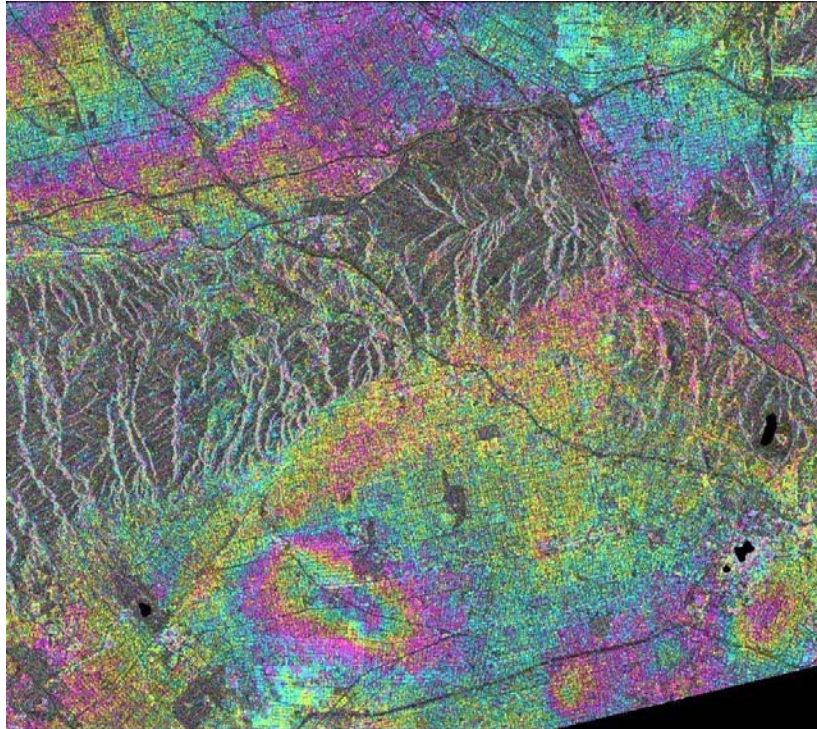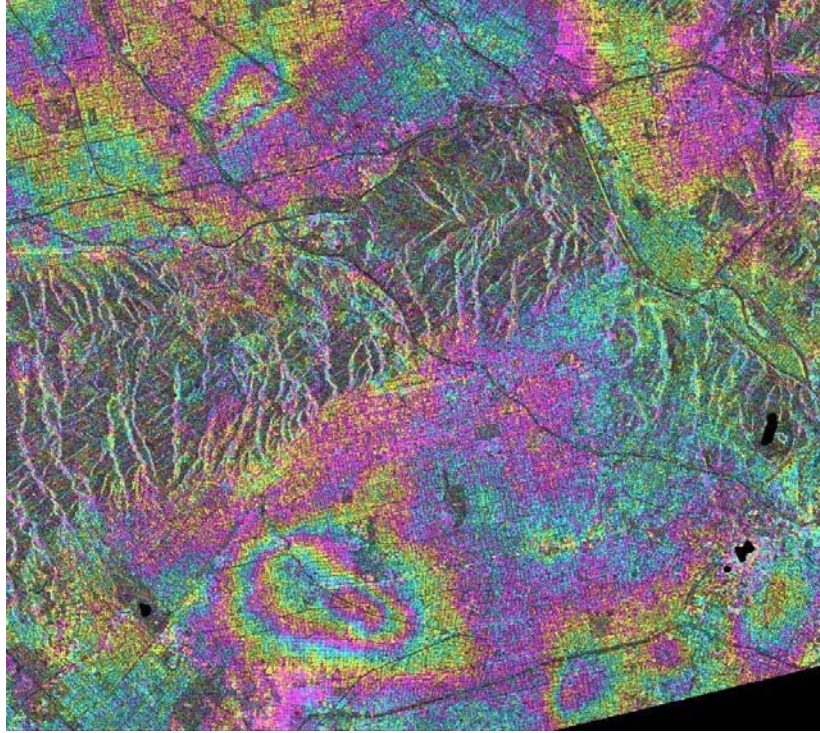

Figure C. 24. October 17, 1996 Cumulative Interferogram from Multi-Baseline Analysis.
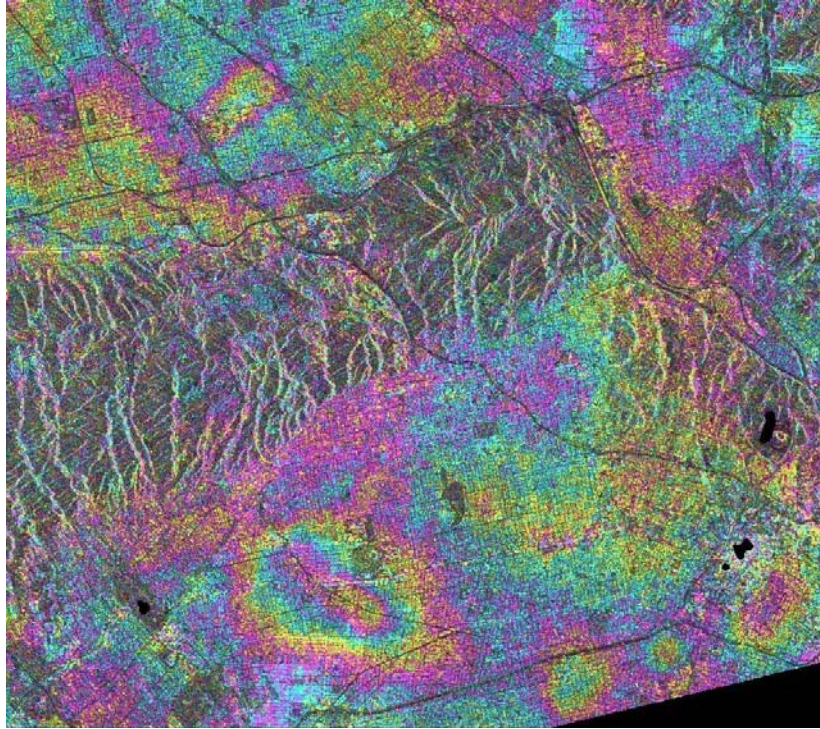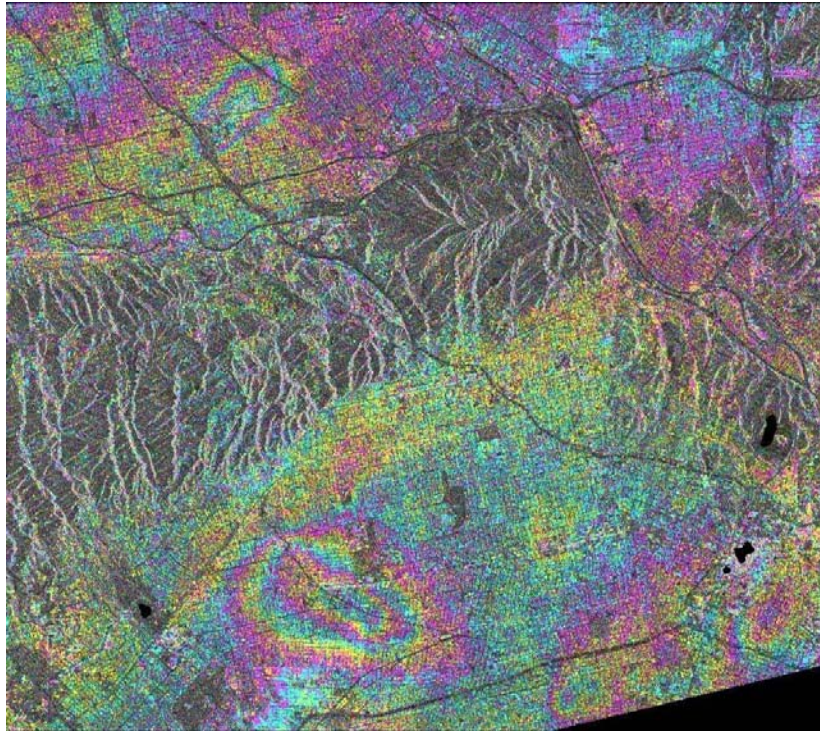
Figure C. 25. December 26, 1996 Cumulative Interferogram from Multi-Baseline Analysis.
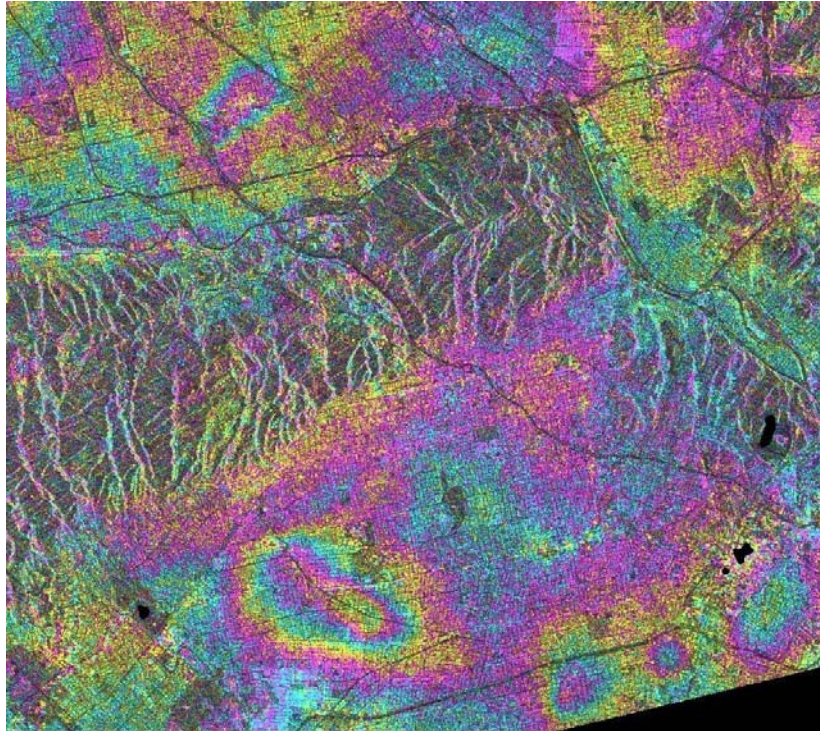
Figure C. 26. March 6, 1997 Cumulative Interferogram from Multi-Baseline Analysis.

Figure C. 27. April 10, 1997 Cumulative Interferogram from Multi-Baseline Analysis.

Figure C. 28. May 15, 1997 Cumulative Interferogram from Multi-Baseline Analysis.

Figure C. 29. June 19, 1997 Cumulative Interferogram from Multi-Baseline Analysis.

Figure C. 30. July 24, 1997 Cumulative Interferogram from Multi-Baseline Analysis.

Figure C. 31. January 15, 1998 Cumulative Interferogram from Multi-Baseline Analysis.

Figure C. 32. February 19, 1998 Cumulative Interferogram from Multi-Baseline Analysis.
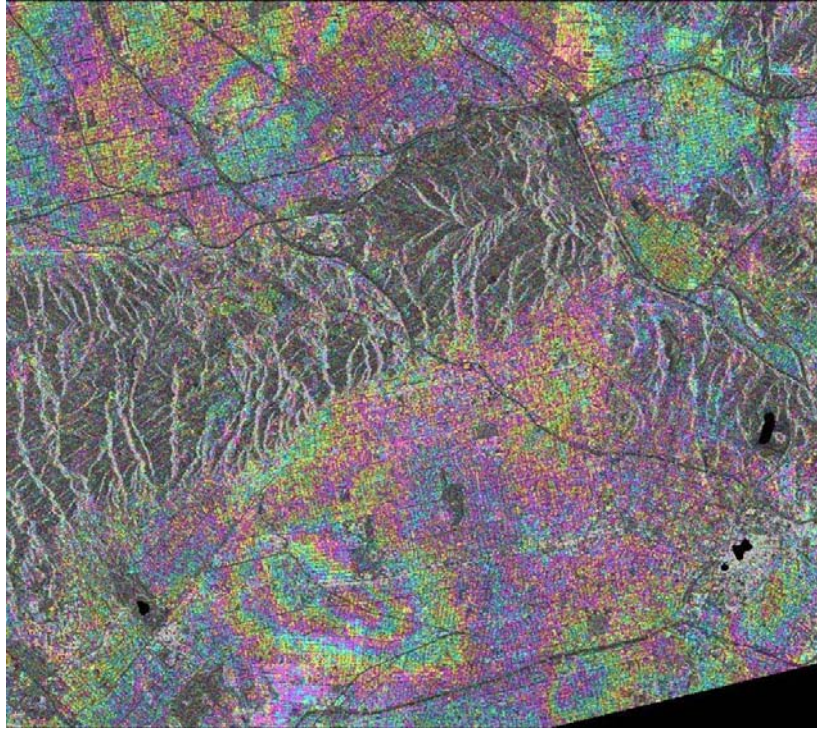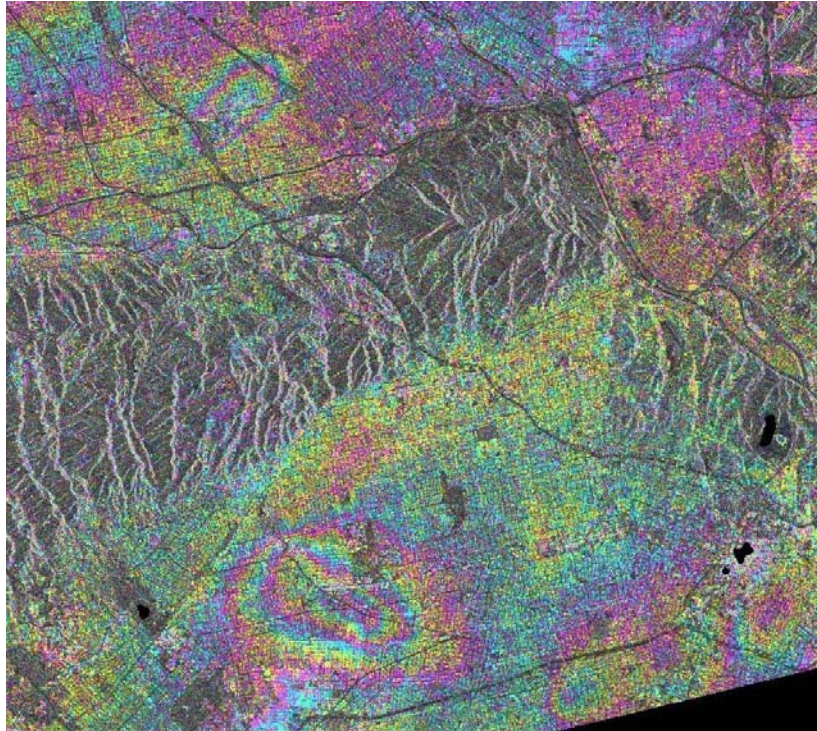
Figure C. 33. August 13, 1998 Cumulative Interferogram from Multi-Baseline Analysis.

Figure C. 34. October 22, 1998 Cumulative Interferogram from Multi-Baseline Analysis.

Figure C. 35. November 26, 1998 Cumulative Interferogram from Multi-Baseline Analysis.

 Figure C. 36. February 4, 1998 Cumulative Interferogram from Multi-Baseline Analysis.

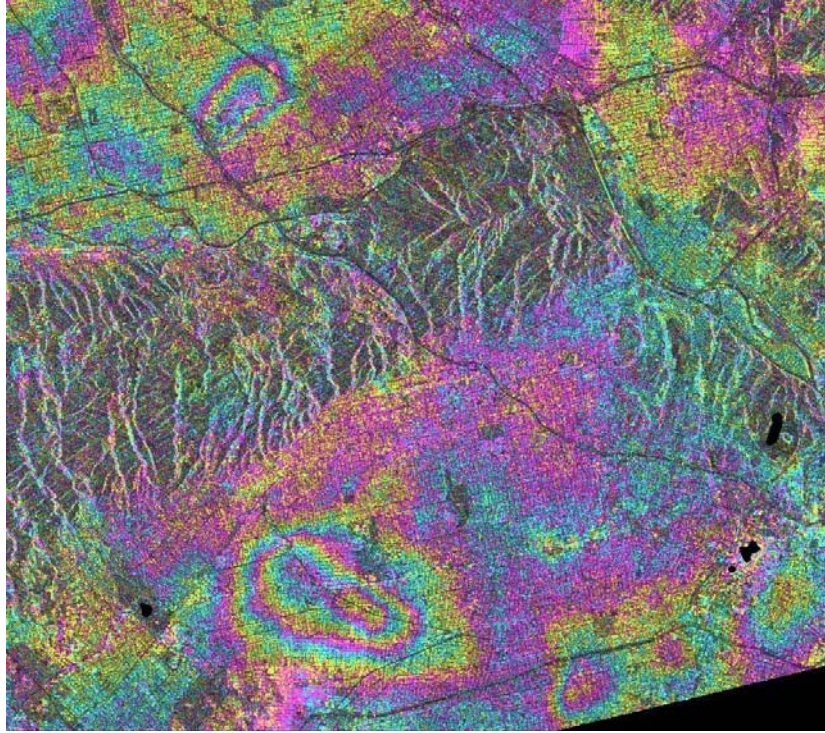**Figure C. 37. March 11, 1999 Cumulative Interferogram from Multi-Baseline Analysis.**

Figure C. 38. June 29, 1999 Cumulative Interferogram from Multi-Baseline Analysis.
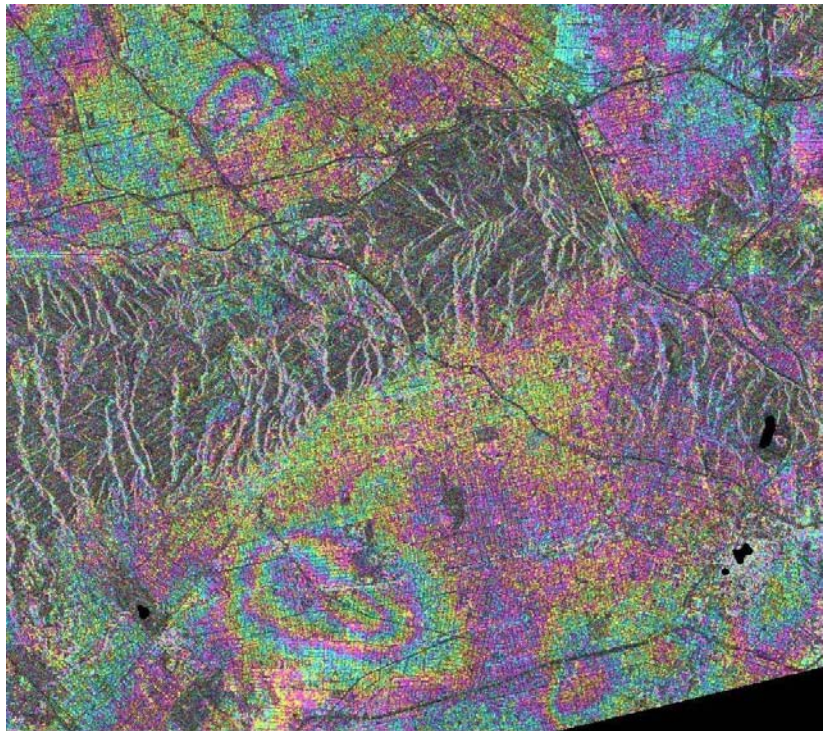
Figure C. 39. October 7, 1999 Cumulative Interferogram from Multi-Baseline Analysis.
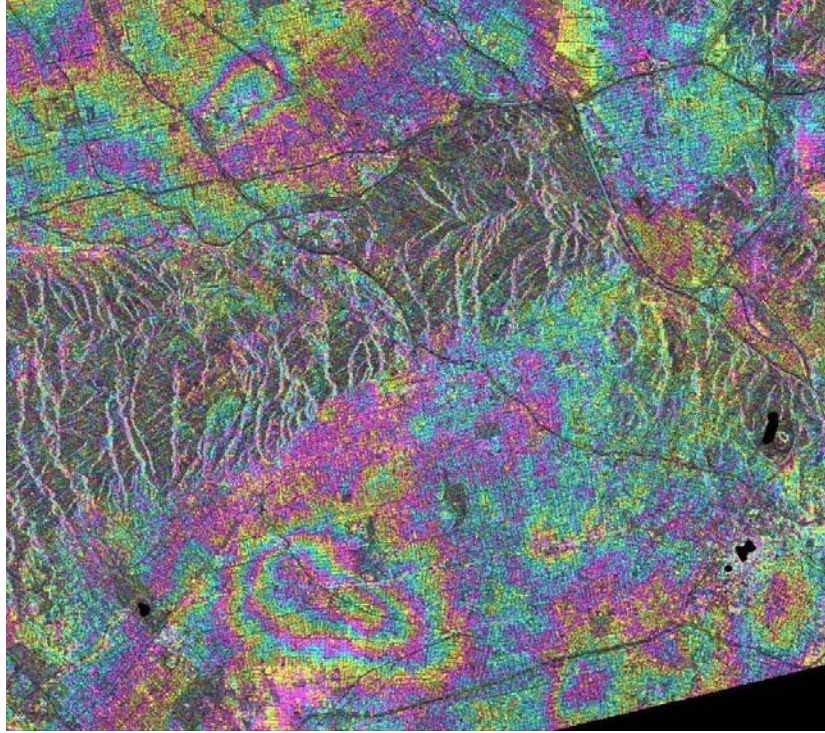

Figure C. 40. December 16, 1999 Cumulative Interferogram from Multi-Baseline Analysis.
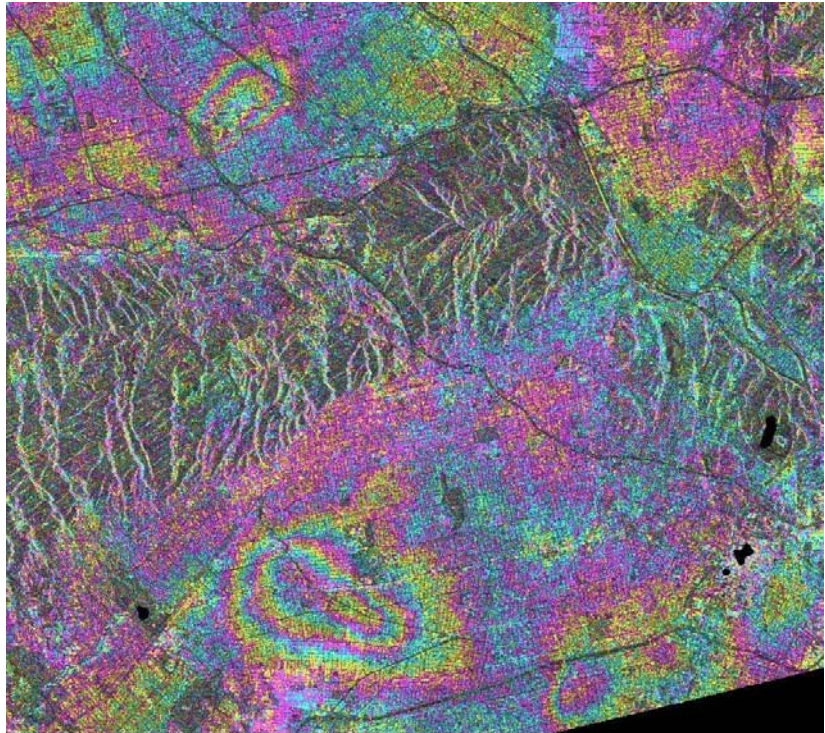
Figure C. 41. May 4, 2000 Cumulative Interferogram from Multi-Baseline Analysis.

 Figure C. 42. June 8, 2000 Cumulative Interferogram from Multi-Baseline Analysis.

Figure C. 43. August 17, 2000 Cumulative Interferogram from Multi-Baseline Analysis.

Figure C. 44. November 30, 2000 Cumulative Interferogram from Multi-Baseline Analysis.

328

VITA

Richard Aaron (Rick) Coffman was born in Denver, Colorado, on September 13, 1980, the son of Glen E. and Peggy L. Coffman. He attended Central High School in Cheyenne, Wyoming, and graduated in May, 1998. In August, 1998, he enrolled in Laramie County Community College, where he studied for one academic year. In May, 1999, he enrolled in the University of Wyoming in Laramie, Wyoming, where the degree of Bachelor of Science in Civil Engineering was conferred in May, 2002. In August, 2002, he entered The Graduate School at The University of Texas at Austin in Austin, Texas, where the degree of Master of Science in Engineering was conferred in December, 2003. From January 2004 to January 2005 he worked as a Geotechnical Engineer for Fugro-McClelland in Houston, Texas. From February 2005 to August 2006 he worked as a Project Engineer and Project Land Surveyor for A Civil Group in Columbia, Missouri. He married his lovely wife Ashley Renee, and became a Professional Land Surveyor in the State of Missouri in June, 2006. He entered The Graduate School at the University of Missouri-Columbia in August, 2006. He became a Professional Engineer in the State of Missouri in June, 2007. He will begin as an Assistant Professor of Civil Engineering (Geotechnical) at the University of Arkansas in August 2009.

Permanent Address: 6316 Moccasin Avenue

Cheyenne, WY 82009

This dissertation was typed by the author.